Development of Probabilistic Finite Element Models for Assessment of Deformation in CANDU Fuel Channels

by

Sreehari Ramachandra Prabhu

A thesis
presented to the University of Waterloo
in fulfillment of the
thesis requirement for the degree of
Doctor of Philosophy
in
Civil Engineering

Waterloo, Ontario, Canada, 2022

Examining Committee Membership

The following served on the Examining Committee for this thesis. The decision of the Examining Committee is by majority vote.

External Examiner: Dr. Wenxing Zhou
Professor, Dept. of Civil and Environmental Engineering
Western University

Supervisor: Dr. Mahesh D. Pandey
Professor, Dept. of Civil and Environmental Engineering
University of Waterloo

Internal Members: Dr. Stan Potapenko
Professor, Dept. of Civil and Environmental Engineering
University of Waterloo

Dr. Marianna Polak
Professor, Dept. of Civil and Environmental Engineering
University of Waterloo

Internal-External Member: Dr. Sanjeev Bedi
Professor, Dept. of Mechanical and Mechatronics Engineering
University of Waterloo

Author's Declaration

I hereby declare that I am the sole author of this thesis. This is a true copy of the thesis, including any required final revisions, as accepted by my examiners.

I understand that my thesis may be made electronically available to the public.

Abstract

Fuel channels (FCs) are one of the most critical components in a CANDU reactor. A FC comprises a Pressure Tube (PT), a Calandria Tube (CT) and four garter springs and it acts as the pressure boundary between the "hot" heavy water reactor coolant and the "cold" moderator. The structural integrity of FCs is affected due to in-reactor deformation caused by irradiation induced creep, irradiation growth and thermal creep. The resulting dimensional changes are a function of reactor operating time and are exhibited as axial elongation, diametral expansion and wall thinning of PTs and the sagging of PTs and CTs, which in turn can lead to PT-CT contact at axial locations between the spacers. These changes can significantly affect PT integrity; for instance, diametral expansion can lead to flow bypass, which may result in the insufficient cooling of the natural uranium fuel and the potential of fuel dry-out. The PT-CT contact can lead to the formation of hydride blisters and the eventual delayed hydride cracking (DHC) of PTs. To ensure a reliable operation and to predict the future dimensional changes of the FC, a comprehensive understanding of the nature of in-reactor deformation and physically based models are necessary. The nuclear industry currently relies on 1D FEA and a limited number of Monte Carlo simulation trials to predict probability of contact and make risk-informed decisions. This thesis critically analyzes the current practices of the industry in assessing PT-CT contact risk and develops computationally efficient and robust probabilistic models based on advanced 3D FEM of FCs for making better risk-informed decisions.

In this study, 1D and 3D finite element models are developed to simulate the in-reactor deformation of a CANDU FC using the finite element analysis (FEA) package ABAQUS, in

which the material deformation models of both the PT and the CT have been implemented as user subroutines using UMAT. The prediction comparison between the two models shows the need of 3D finite element models in correctly predicting the in-reactor deformations. Since the prediction of time to contact is influenced by various uncertainties, such as change in, (i) the dimensions of the FC, and (ii) the material properties and boundary conditions of the FC, probabilistic simulation-based methods have been developed to assess the PT-CT contact risk and establish adherence with provisions of the Canadian Standards Association (CSA) Standard N285.8. An effective calibration approach for diametral creep strain and PT-CT gap profile prediction is also proposed for making better future predictions of inspected channels.

A new approach of coupling multiplicative dimensional reduction method (M-DRM) with polynomial chaos expansion (PCE) method is proposed which significantly reduces the computational cost of probabilistic finite element analysis using expensive-to-evaluate finite element models. The proposed method is applied for probabilistic contact assessment of CANDU FCs by considering 1D and 3D FE models and different PT orientations, which significantly influence probabilistic contact results. Important findings and insights on contact assessment is presented, which would benefit the nuclear industry. The low computational cost and predictive capability of the proposed method is suitable for carrying out full probabilistic assessments of CANDU reactor cores for units with 380 or 480 FCs.

Acknowledgements

I would like to express my sincere gratitude to my supervisor, Professor Mahesh D. Pandey for being very supportive throughout my doctoral program. His consistent guidance, constructive criticism and fruitful discussions has helped me immensely in my research and to grow professionally. He has been very understanding and his support is invaluable for the accomplishment of this research and completion of this thesis.

I wholeheartedly would like to express my deep gratitude to Dr. Nicolas Christodoulou who helped me in understanding the technical details of CANDU fuel channels. His valuable advice, industrial knowledge and prompt responses to my questions has helped me immensely in my research work. His hard working and humble nature are always an inspiration. I would like to express my thanks to Dr. Brian W. Leitch who also helped me with technical details of CANDU fuel channels.

I would like to thank my committee members, Professor Wenxing Zhou, Professor Stan Potapenko, Professor Maria Anna Polak and Professor Sanjeev Bedi for their time, valuable comments and constructive feedback that enhanced my work. Especially, I would like to thank Professor Stan Potapenko for giving me opportunities to work as Course Assistant for his courses, which gave me a lot of confidence in effectively handling course materials and enhancing my knowledge.

Many thanks to all my research group members and friends from University of Waterloo. Special thanks to Eishiro Higo, Nitin Padmanabhan, Ritwik Kodamana, Dileep Ramachandran

and Indranil Hazra who made my days wonderful in Waterloo. I thoroughly enjoyed the time spend together and the discussions we had.

I greatly appreciate and acknowledge the financial support in the form of Research Assistantship by the Natural Science and Engineering Research Council (NSERC) of Canada and University Network of Excellence in Nuclear Engineering (UNENE).

Last but not the least, I am extremely thankful to my ever-loving family circle. I express my sincere gratitude to my Parents S. Ramachandra Prabhu and Usha R Prabhu, my wife Aishwarya Prabhu, my adorable daughter Shreshta S Prabhu, my brother Sreechandra Prabhu, sister-in-law Anupama J Pai, my adorable niece Shrishti S Prabhu, Father-in-law Dr. Ajit Prabhu and Mother-in-law Anupama Prabhu for showing tremendous patience and always loving, supporting and encouraging me. Also special thanks to all my brothers, sisters and family members for your love and affection.

Sreehari Ramachandra Prabhu,

Waterloo, Winter 2022

Dedication

To My Family

Table of Contents

Examining Committee Membership…… ii

Author's Declaration……... iii

Abstract…… iv

Acknowledgements…….. vi

Dedication…….. viii

List of Figures ……. xvii

List of Tables ……. xxvi

List of Abbreviations …… xxvii

Chapter 1 Introduction..... 1

1.1 Background 1

1.2 The CANDU Reactor 3

1.3 Research Motivation 7

1.4 Research Objectives 9

1.5 Outline of the Dissertation 10

Chapter 2 Literature Review 13

2.1 Uncertainty Analysis 13

2.2 Uncertainty Propagation Methods..... 15

2.3 Structural Reliability Methods 17

2.3.1 Monte Carlo Simulation 18

2.3.2 First Order Reliability Method 19

2.4 Spectral Methods..... 21

2.5 Probabilistic Finite Element Analysis 22
2.6 Pressure Tube Deformations in CANDU Reactors 25
2.6.1 Axial elongation 26
2.6.2 Diametral expansion 27
2.6.3 Sag 28
Chapter 3 Computational Modelling of In-Reactor Deformation of CANDU Fuel Channels 30
3.1 Introduction 30
3.1.1 Need for computational models of FC deformation 30
3.1.2 Objective 32
3.1.3 Organization 33
3.2 Design, Operating Conditions and Material Models of a CANDU FC 33
3.2.1 Design of a CANDU FC 33
3.2.2 FC Geometry and Operating Conditions used for FEA 35
3.2.3 Mechanical Deformation Models of PT and CT 37
3.2.3.1 Elastic properties of PT and CT 37
3.2.3.2 Pressure Tube Creep Deformation Equation 38
3.2.3.3 Calandria Tube Creep Deformation Equation 45
3.3 Implementation of PT and CT material models in ABAQUS 47
3.3.1 Explicit Integration Scheme 48
3.3.2 Computational Procedure in ABAQUS using the UMAT 49
3.4 1D Finite Element Analysis of a CANDU FC 52

3.4.1 Modelling details 52
3.4.2 Output of 1D FEA 54
3.4.2.1 Axial elongation 55
3.4.2.2 FC Sag 55
3.4.2.3 PT-CT gap 56
3.4.3 Limitations of 1D FEA 57
3.5 3D Finite Element Analysis of a CANDU FC 58
3.5.1 Modelling Details 58
3.5.2 3D Finite Element Analysis Output 63
3.5.2.1 Fuel Channel Sag 64
3.5.2.2 Axial elongation of PT 65
3.5.2.3 Diametral Expansion of PTs 68
3.5.2.4 Wall Thinning of PTs 71
3.5.2.5 PT-CT Gap 74
3.5.3 3D FEA Results Based on Different FC Configurations 75
3.6 Limitations of 3D FEM Model 77
3.7 Comparison between 3D and 1D FEA Results 78
3.8 Conclusions 80
Chapter 4 Development of Surrogate Models and Calibration Methods for the 3D prediction of In-Service Deformation in CANDU FCs 82
4.1 Introduction 82
4.1.1 Need for Surrogate Model and Calibration 82

4.1.2 Objective 83
4.1.3 Organization 83
4.2 Calibration of 3D FE Model for Diametral Creep Predictions in PTs 84
4.2.1 General 84
4.2.2 Calibration Approach 85
4.2.2.1 Time invariant check 88
4.3 Investigation and Calibration of Diametral Creep with Realistic Flux Profile Inputs 90
4.3.1 Introduction 90
4.3.2 Generation of Realistic Flux Profiles 91
4.3.3 FEA using realistic flux profile inputs 95
4.3.3.1 Creep Strain Prediction at Flux Dip Locations 96
4.3.3.2 Calibration with Diametral Creep Strain Dip 99
4.4 Development of a Surrogate Model for Diametral Creep in PTs 101
4.4.1 Regression model using 3D FEA 101
4.4.2 Surrogate Model Accounting for Material Uncertainty 106
4.5 Development of a Surrogate Model for PT-CT Gap 108
4.5.1 General 108
4.5.2 Variables Affecting PT-CT Gap 109
4.5.3 Understanding the Nature of PT-CT Gap 110
4.5.4 Surrogate model development 113
4.5.4.1 A Study on Model Coefficients 117
4.5.4.2 Surrogate Gap Model Verification 121

4.5.4.3 Comparison of Results from 1D and 3D Surrogate Models 122
4.5.5 Use of Surrogate Model in Calibration of FEM Model 123
4.5.5.1 Calibration using the Surrogate Model 124
4.5.5.2 Calibration Example of a FC 125
4.6 Conclusions 128
Chapter 5 Coupled Multiplicative Dimensional Reduction and Polynomial Chaos Expansion Method 130
5.1 Introduction 130
5.1.1 General 130
5.1.2 Objectives 131
5.1.3 Organization 132
5.2 Polynomial Chaos Expansion 133
5.2.1 Background 133
5.2.2 Mathematical Setting of PCE 135
5.2.3 Construction of polynomial chaos basis 138
5.2.3.1 Univariate orthonormal polynomials 138
5.2.3.2 Multivariate Polynomials 141
5.2.4 Polynomial Chaos Representation of Model Response 142
5.2.4.1 Illustration example 142
5.2.5 Truncation Scheme 144
5.2.6 Computation of PCE Coefficients 144
5.2.6.1 Post-processing using PCE coefficients 146

5.2.6.2 Computational Cost of PCE Coefficients 146
5.2.7 Using PCE for Probabilistic FEA 147
5.3 Multiplicative Dimensional Reduction Method (M-DRM) 148
5.3.1 Background 148
5.3.2 Mathematical Setting of M-DRM 150
5.4 Combining the M-DRM with PCE 151
5.5 Gaussian Quadrature Scheme for One-Dimensional Integration 154
5.6 Probabilistic FEA using the proposed method 158
5.6.1 Application Example 161
5.6.1.1 M-DRM Module 162
5.6.1.2 PCE Module 163
5.6.1.2.1 Computation of response statistics 165
5.6.1.2.2 Sensitivity Analysis 165
5.6.1.2.3 Response Probabilistic Result 166
5.6.2 Accuracy and Limitations of the Coupled Approach 167
5.7 Conclusions 168
Chapter 6 Probabilistic Finite Element Analysis of CANDU Fuel Channels 170
6.1 Introduction 170
6.1.1 Objective 171
6.1.2 Organization 172
6.2 Uncertain Variables Influencing Gap Profile 172
6.3 Probabilistic FEA of CANDU FCs using 1D FEA 174

6.3.1 General 174
6.3.2 Monte Carlo Simulation 174
6.3.3 Application of Coupled M-DRM and PCE Method 175
6.3.3.1 Surrogate Model Form 176
6.3.3.2 Input and Output Grid Generation 176
6.3.3.3 Computation of PCE Coefficients 180
6.3.3.4 Final Surrogate Model based on 1D FE Model 181
6.3.4 Comparison of Statistical Results 182
6.3.5 Computational Time 185
6.3.6 Probabilistic Contact Assessment using 1D Surrogate Model 185
6.4 3D FEA Based on Different PT Orientations 187
6.4.1 Deterministic 3D FEA Results 188
6.4.1.1 Diametral expansion 188
6.4.1.2 Gap profile 189
6.5 Probabilistic FEA of CANDU FCs using 3D FEA 191
6.5.1 General 191
6.5.2 Application of Coupled M-DRM and PCE Method for 3D PFEA 192
6.5.2.1 Implementation of the Method 192
6.5.2.2 Final Surrogate Model based on 3D FE Model 195
6.5.2.3 Gap statistics 196
6.5.2.4 Sensitivity Analysis 197
6.5.3 Probabilistic Contact Analysis using the Surrogate Model 200

6.6 Conclusions 204

Chapter 7 Conclusions and Recommendations..... 207

7.1 Summary 207

7.2 Conclusions 208

7.3 Recommendations for Future Research 211

References..……..……...……..213

Appendix A.……..……229

List of Figures

Figure 1.1: CANDU 6 reactor assembly 5

Figure 1.2: Primary heat transport system of a CANDU reactor 6

Figure 1.3: A section of a FC in CANDU reactors 6

Figure 1.4: Degradation mechanisms leading to failure of a CANDU pressure tube 7

Figure 2.1: General framework for uncertainty analysis of a physical system (Bruno, 2007) 14

Figure 2.2: Classification of uncertainty propagation methods 16

Figure 2.3: Reliability index based on FORM 20

Figure 2.4: A typical diametral profile of a PT from outlet to inlet 28

Figure 2.5: A typical sag profile of a FC after several years of operation, from (Holt, 2008) 29

Figure 3.1: A section of a FC in CANDU reactors 34

Figure 3.2: A schematic of the CANDU FC analyzed 36

Figure 3.3: Variation of fast neutron flux, pressure, and temperature along the PT 36

Figure 3.4: Variation of modulus of elasticity in the PT (temperature-dependent) 38

Figure 3.5: Flowchart of UMAT subroutine implementation for FC deformation modelling 51

Figure 3.6: The CDEPTH FE beam model of a fuel channel (Sauvé et al., 1989) 52

Figure 3.7: A structural beam model representing the FC used in the analysis 54

Figure 3.8: Predicted elongation as a function of fast neutron fluence using 1D FEA (averaged along the length of the PT) compared to experimental data from (Holt, 2008) 55

Figure 3.9: Predicted PT sag profiles at various points in time in the service life of the FC using 1D FEA (kEFPH = thousand equivalent full power hours) 56

Figure 3.10: Predicted PT-CT gap profiles at various time points in the service life of the FC using 1D FEA (PT back end placed at the outlet) 57
Figure 3.11: A section of the 3D FEM model representing the PT, CT and garter spring 59
Figure 3.12: Convergence test result for finding the optimum number of elements for the modelling of a PT 60
Figure 3.13: Convergence test result for finding the optimum number of elements for the modelling of a CT 60
Figure 3.14: Deformed geometry of a FC following 3D FEA at 161615 kEFPH (The left end is the outlet end of PT) 63
Figure 3.15: Predicted profiles of PT sag at various times in the operating life of the FC 64
Figure 3.16: Predicted profiles of CT sag at various times in the operating life of the FC 65
Figure 3.17: Predicted axial strain rates at three different operating intervals 66
Figure 3.18: Contributions of each deformation mechanism towards the axial strain rate at 150 kEFPH 67
Figure 3.19: Calculated axial elongation compared to experimental data from (Holt, 2008) 68
Figure 3.20: Predicted diametral PT profiles at different time intervals (the PT back end was placed at the outlet end) 69
Figure 3.21: Predicted diametral expansion vs. time at five axial locations along the PT (the axial location is measured from the outlet end) 69
Figure 3.22: Contributions of each deformation mechanism to the diametral strain rate at 150 kEFPH 71

Figure 3.23: Predicted wall thickness profiles at various time intervals in the operating life of the FC (PT back end placed at the outlet) 72
Figure 3.24: Predicted wall thickness vs. time at different axial locations along the pressure tube (axial locations measured from the outlet end) 73
Figure 3.25: Calculated wall thickness rate vs. time at different axial locations along the pressure tube (axial locations measured from the outlet end) 73
Figure 3.26: Predicted PT-CT gap profiles at various time intervals in the operating life of the FC (PT back end placed at the outlet) 75
Figure 3.27: Comparison of predicted PT-CT gap profiles at 175 kEFPH for three different boundary conditions (PT back end is always at the outlet) 77
Figure 3.28: Predicted PT-CT gap profiles at 220 kEFPH using 1D and 3D FEM models (PT back end placed at the outlet end) 79
Figure 4.1: Comparison of measured diametral strain against 3D FEA predicted nominal diametral strain of PT1 at 161615 EFPH 87
Figure 4.2: Comparison of measured, nominal, and calibrated diametral strain of PT1 at 161615 EFPH 88
Figure 4.3: Comparison of measured, nominal, and calibrated diametral strain of PT5 at 101,100 EFPH 89
Figure 4.4: Comparison of measured and calibrated diametral strain of PT5 at various time intervals 90
Figure 4.5: Fuel bundle arrangement inside a fuel channel 91

Figure 4.6: Flux data obtained from bundle average power and measured diametral creep strain at 161615 kEFPH for PT2 and PT3 92
Figure 4.7: Fast flux dip in pressure tubes 94
Figure 4.8: Comparison of smooth and realistic flux profile of PT2 94
Figure 4.9: Comparison of smooth and realistic flux profile of PT3 95
Figure 4.10: 3D finite element model of the fuel channel with finer mesh at the flux dip locations 96
Figure 4.11: Nominal diametral strain prediction using 3D FEA and realistic flux profile input of PT2 97
Figure 4.12: Magnified view at maximum diametral strain location of PT2 98
Figure 4.13: Nominal diametral strain prediction using 3D FEA and realistic flux profile input of PT3 98
Figure 4.14: Magnified view at maximum diametral strain location of PT3 99
Figure 4.15: Comparison of measured diametral strain against calibrated diametral strain of PT2 at 161615 EFPH by accounting for flux dip 100
Figure 4.16: Comparison of measured diametral strain against calibrated diametral strain of PT3 at 161615 EFPH by accounting for flux dip 100
Figure 4.17: R-square values obtained following linear regression at axial locations 103
Figure 4.18: Slope obtained from linear regression of diametral strain and operating time 103
Figure 4.19: Comparison of diameter predicted using the regression model and the FEA at 220 kEFPH 105

Figure 4.20: Error in diameter prediction between linear regression model and FEA at various time intervals 105
Figure 4.21: Error in diameter prediction between nonlinear regression model and FEA at various time intervals 106
Figure 4.22: Comparison of measured and surrogate model predicted diametral strain of PT5 at various time intervals 108
Figure 4.23: Predicted reduction in PT-CT gap as a function of time at various axial locations from the outlet end 111
Figure 4.24: Predicted PT-CT Gap vs. creep factor at a fixed location (x =5.267 m) and time 220 kEFPH (the two end-slopes are fixed at 0.002 rad) 112
Figure 4.25: Predicted PT-CT Gap vs. end slope at a fixed location (x =5.267 m) and time 220 kEFPH (the creep factor is fixed at 1) 112
Figure 4.26: Predicted PT-CT gap as function of the creep factor and end slopes (3D surface), at PT axial location x = 5.267 m and 220 kEFPH operating time 114
Figure 4.27: Gap profiles for various values of outlet end slope at 220 kEFPH (CF = 1 and Si = 0.002 rad) 116
Figure 4.28: Gap profiles for various values of inlet end slope at 220 kEFPH (CF = 1 and So = 0.002 rad) 116
Figure 4.29: Variation of the first four coefficients in Equation (4.6) of the PT-CT gap model as a function of the axial location (at a fixed time of 220 kEFPH) 117
Figure 4.30: Variation of some coefficients in Equation (4.7) with axial location and time 120

Figure 4.31: Variation of coefficients b41 and b42 with time at three different PT axial locations 120
Figure 4.32: PT-CT Gap profiles predicted at two different times by the surrogate model and the FEM model 121
Figure 4.33: Gap minimization points and the calibrated gap profile at 148,273 EFPH using the surrogate model 126
Figure 4.34: Comparison of the inspected and predicted gap profiles using the calibrated 3D FEM model at 176,575 EFPH 127
Figure 4.35: Comparison of the measured and predicted diametral profile using the calibrated 3D FEM model at 176,575 EFPH 127
Figure 5.1: Flowchart to conduct PFEA using the proposed method 160
Figure 5.2: Scatter plot and linear fit of internal pressure versus hoop stress 166
Figure 5.3: Comparison of probability of exceedance of hoop stress 167
Figure 6.1: Example of a blister in Zr-2.5Nb PT material (blister depth = 0.25 mm from outside surface to lower end of darker region) (Nadeau, 2012) 171
Figure 6.2: Predicted gap profiles from 1D FEA for selected values of creep factors at 200 kEFPH, (inlet slope and outlet slope fixed at mean values and PT with BEO) 179
Figure 6.3: Predicted gap profiles from 1D FEA for selected values of outlet slopes at t = 200 kEFPH, (creep factor and inlet slope fixed at mean values and PT with BEO) 179
Figure 6.4: Predicted gap profiles from 1D FEA for selected values of inlet slopes at t = 200 kEFPH, (creep factor and outlet slope fixed at mean values and PT with BEO) 180

Figure 6.5: Comparison of gap profiles predicted by the surrogate model and the 1D FEA at different time intervals and parameter values 182
Figure 6.6: Comparison of statistics from MCS and M-DRM + PCE method across the PT axial location at 200 kEFPH 184
Figure 6.7: Comparison of CDF of the minimum gap at 220 kEFPH using MCS and the proposed method based on 1D FEA 184
Figure 6.8: CDF at various time intervals during service of FCs (Based on 1D FEA for PTs with the BEO) 186
Figure 6.9: Comparison of diametral strain profiles in CANDU PTs with back end at the outlet and back end at the inlet 188
Figure 6.10: Predicted diameter profiles for two different PT orientations with respect to coolant flow at 220 kEFPH..... 189
Figure 6.11: Comparison of predicted PT-CT gap profiles at 220 kEFPH for two distinct PT orientations with respect to coolant flow 190
Figure 6.12: Predicted PT-CT gap profiles at various time intervals in the operating life of the FC (PT back end placed at inlet)..... 191
Figure 6.13: Predicted gap profiles from 3D FEA for selected values of creep factors at 200 kEFPH, (inlet slope and outlet slope fixed at mean values and PT with BEO)..... 193
Figure 6.14: Predicted gap profiles from 3D FEA for selected values of outlet slopes at t = 200 kEFPH, (creep factor and inlet slope fixed at mean values and PT with BEO) 194
Figure 6.15: Predicted gap profiles from 3D FEA for selected values of inlet slopes at t = 200 kEFPH, (creep factor and outlet slope fixed at mean values and PT with BEO) 194

Figure 6.16: Comparison of gap profiles predicted by the surrogate model and the 3D FEA at different time intervals and parameter values 196
Figure 6.17: Mean and Variability of the gap profile at 200 kEFPH for PTs with the BEO and the BEI 197
Figure 6.18: Sensitivity indices of the creep factor, outlet slope and inlet slope at 220 kEFPH for a PT with the BEO 198
Figure 6.19: Comparison of creep factor sensitivity index at various time interval for a PT with the BEO..... 199
Figure 6.20: Comparison of outlet slope sensitivity index at various time interval for a PT with the BEO..... 199
Figure 6.21: Comparison of inlet slope sensitivity index at various time interval for a PT with the BEO..... 200
Figure 6.22: Cumulative distribution function (CDF) of minimum gap at two different time intervals for a PT with the BEO..... 201
Figure 6.23: Probability of gap reduction at various time intervals during service of FCs (for PTs with the BEO)..... 202
Figure 6.24: Probability of gap falling below 2mm at various time intervals during service of FCs (for PTs with the BEO) 203
Figure 6.25: Comparison of the probability of gap reduction curves at 220 kEFPH for different PT orientations and type of FE analysis..... 204
Figure A.1: Comparison of measured, nominal, and calibrated diametral strain of PT2 at 161615 EFPH…….229

Figure A.2: Comparison of measured, nominal, and calibrated diametral strain of PT3 at 161615 EFPH…….229

Figure A.3: Comparison of measured, nominal, and calibrated diametral strain of PT4 at 161615 EFPH…….230

List of Tables

Table 3.1: Elastic properties of PT and CT (CSA N285.8, 2015; Northwood et al., 1975; Pan et al., 2010) 37

Table 3.2: Average diametral deformation rate calculated over the design life of a CANDU unit (220 kEFPH). 70

Table 4.1: Scale factor obtained for each FC following calibration 88

Table 4.2: Time predicted to reach 1 mm minimum gap by three different models 123

Table 5.1: Relation between orthogonal polynomials and random variable distributions ... 140

Table 5.2: Gaussian integration formula for one-dimensional integration 157

Table 5.3: Weights and coordinates of the five order Gauss-Hermite quadrature rule 157

Table 5.4: Statistics of random variables related to hoop stress in pipes 162

Table 5.5: Input grid for model evaluation and the corresponding output grid 163

Table 5.6: Two-dimensional Hermite polynomials and computed PCE coefficients 164

Table 5.7: Comparison of statistics of hoop stress based on MCS and proposed method ... 165

Table 5.8: Sensitivity indices 166

Table 6.1: Distribution type and parameters of random variables influencing PT-CT gap profile 174

Table 6.2: Input grid for model evaluation 177

Table 6.3: Statistics of the minimum gap obtained using MCS and coupled M-DRM and PCE method 183

List of Abbreviations

A-DRM	Additive Dimensional Reduction Method
BEO	Back end placed at outlet end
BEI	Back end placed at inlet end
CDF	Cumulative Distribution Function
COV	Coefficient of variation
CSA	Canadian Standards Association
CT	Calandria Tube
DHC	Delayed hydride cracking
EFPH	Equivalent Full Power Hours
FAC	Flow Accelerated Corrosion
FC	Fuel Channel
FEA	Finite Element Analysis
FEM	Finite Element Method
FORM	First Order Reliability Method
GS	Garter Spring
H-DMR	High Dimensional Model Representation
MCS	Monte Carlo Simulation
M-DRM	Multiplicative Dimensional Reduction Method
NOC	Normal Operating Condition
NPP	Nuclear Power Plant
PCE	Polynomial Chaos Expansion

PDF	Probability Density Function
PFEA	Probabilistic Finite Element Analysis
PHTS	Primary Heat Transport System
POC	Probability of Contact
POE	Probability of Exceedance
PT	Pressure Tube
SFEA	Stochastic Finite Element Analysis
SSC	Subsystems, Structures, and Components

Chapter 1

Introduction

1.1 Background

Large engineering systems such as power transmission systems, transportation systems, communication systems, nuclear power systems etc., has played a vital role in the human development and societal advancement. To ensure continuous supply and availability, these systems must be reliable and efficient. With the progress of service time, these systems are subjected to deteriorations, which could affect the serviceability and reliability. Failure of predicting these deteriorations and taking appropriate life-cycle management actions can have a major impact on the safety and economy of the society. For example, the first generation of CANDU[1] reactors in Canada have approached the end of their licensed service life of 30 years and are on the path of life-extension. Nuclear power plants (NPPs) are capital intensive and the life-extension would provide a very significant advantage by bridging the gap between the ageing and new plants. However, the life-extension plans must be executed through a thorough understanding of the ageing mechanisms affecting each component and by careful analysis of the safety concerns.

The nuclear industry has many ageing management programs in which the licensees must perform periodic inspections and demonstrate the fitness-for-service of the components. For example, the

[1] CANDU® (CANada Deuterium Uranium) is a registered trademark of Atomic Energy of Canada Ltd.

pressure tubes (PTs) in CANDU reactors are one of the most critical components operating under extreme conditions, which cause them to deteriorate. The ageing management programs for PTs use extensive research, testing, and modelling development to understand the impact of ageing of PTs. The model predictions are then used for making future decisions on inspections and life-extension. A well validated and an accurate model can assist Engineers in making better predictions on future deformations and minimizing the number of inspections. A powerful tool which the Scientists and Engineers mostly depend on for modelling and simulation is the finite element analysis (FEA). With the advent of powerful computers and accurate analysis of models using FEA, design and analysis has become an everyday tool in the academia and in the industry.

However, despite these advancements, the models will never be able to completely capture the complex behaviour of the real world due to the presence of various uncertainties. This also poses a challenge to the ageing management and life-extension programs as the decisions are to be made under uncertainty. Probabilistic engineering or reliability analysis is the tool used in these scenarios for quantifying the structural safety by considering the uncertainties in input parameters. These tools account for the uncertainties appearing in the modeling of physical systems and then studies the impact of those uncertainties onto the system response. The probabilistic results can be then used for risk-informed decision making. The nuclear industry world-wide is moving towards adopting a risk-informed decision-making framework and probabilistic or stochastic assessment methods for reactor systems are continuously being developed to support this objective (CSA N285.8, 2015). Therefore, the use of probabilistic tools together with finite element (FE) model could give a significant advancement and improvement in making risk-informed decisions of nuclear components and reactor core.

1.2 The CANDU Reactor

The CANDU reactor, like any other nuclear reactor is a complex technical system with various engineered subsystems, structures, and components (SSCs) as shown in Figure 1.1. The CANDU reactor core is a low-pressure cylindrical vessel (Calandria) about 6.0 m long and 7.6 m in diameter, which contains the heavy water moderator at about 70 °C. It is penetrated by 380 or 480 fuel channels (FCs) depending on the reactor power rating. The FCs are an essential part of the primary heat transport system (PHTS) in a CANDU reactor, along with other critical components as shown in Figure 1.2. An important attribute of the CANDU reactor is the use of the heavy water both as moderator and as the heat transporter, which allows a critical chain reaction to be sustained with natural uranium fuel. A typical FC comprises of (i) a cold-worked zirconium 2.5 wt% niobium (Zr-2.5Nb) PT, (ii) a Zircaloy-2 calandria tube (CT) surrounding the PT, (iii) four garter springs and (iv) end-fittings as shown in Figure 1.3. The PTs are the pressure vessels in CANDU reactors, and they are considered as the heart of the reactor, making it one of the most critical components of the reactor. The principal function of PTs is to support and locate the natural uranium dioxide fuel bundles in the reactor core and allow the pressurized heavy water primary coolant to be pumped through the fuel and remove its heat. The ends of each PT are attached to 403 stainless steel end-fittings using roll expanded joints, which then provide a flow path for primary coolant between the PT and rest of the PHTS through the feeder pipe attached to each end fitting. An important function of the CT is to prevent the gross sag of the PT due to irradiation induced deformation that results from its own weight, the weight of the fuel bundles and the heavy water coolant. The annular gap between the PT and CT is maintained using four annulus spacers or garter springs that prevent any contact between the PT and CT. The annulus space is filled with dry CO_2

gas to thermally insulate the “hot” PT from the “cold” CT and to detect any leakage arising in the FC.

The PTs operate under extreme conditions such as high temperatures, fast neutron fluxes (E > 1 MeV) and high applied stresses resulting from the high internal pressure. These operating conditions cause dimensional changes due to irradiation induced creep, irradiation growth and thermal creep (Holt, 2008). The resulting dimensional changes are a function of reactor operating time and are exhibited as axial elongation, diametral expansion and wall thinning of PTs and the sagging of PTs and CTs (Holt, 2008). The sag of PT between the spacers can eventually lead to contact between the PT and CT, termed as PT-CT contact. Direct contact between the PT and CT would result in heat transfer between the two tubes and a substantial decrease in the PT temperature, which in turn leads to the precipitation of hydrogen and the formation of hydride blisters. Blister formation will ultimately lead to delayed hydride cracking (DHC) (Byrne et al., 1991). These changes can significantly affect PT integrity and can pose risk to reactor operation. Figure 1.4 illustrates the degradation mechanisms for CANDU PTs leading to break-before-leak or rupture. The Canadian Standards Association (CSA) Standard N285.8 requires that any such risk to be averted in order to maintain fitness-for-service of the FC and the reactor core (CSA N285.8, 2015).

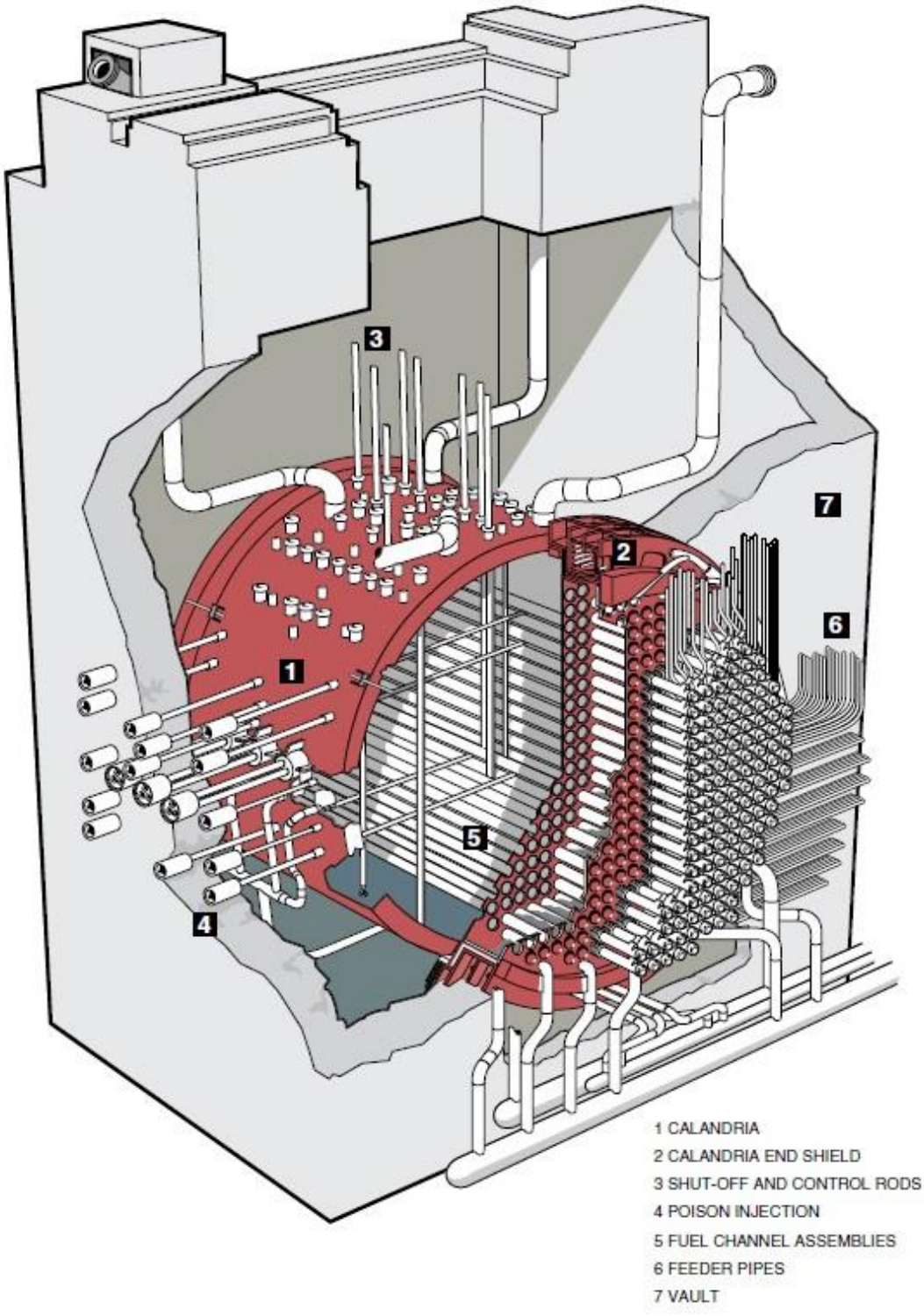

Figure 1.1: CANDU 6 reactor assembly

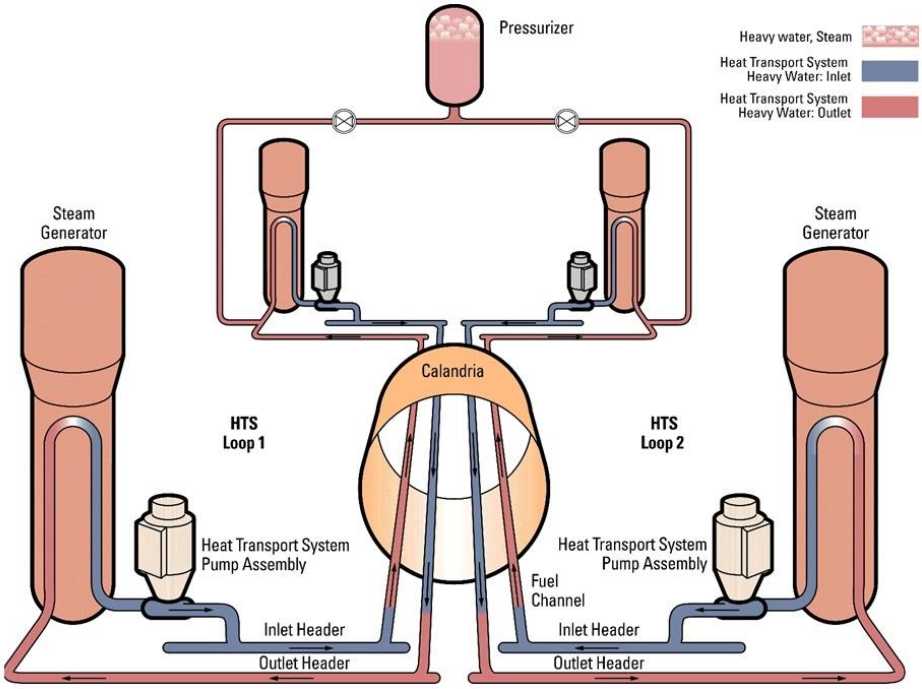

Figure 1.2: Primary heat transport system of a CANDU reactor

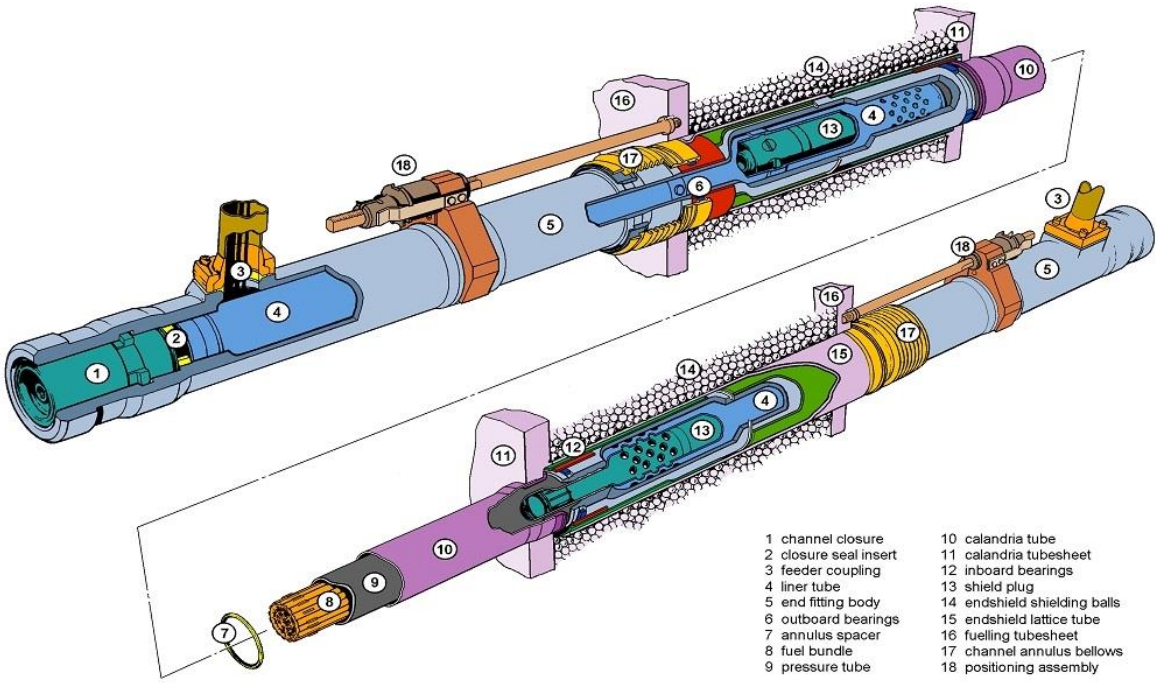

Figure 1.3: A section of a FC in CANDU reactors

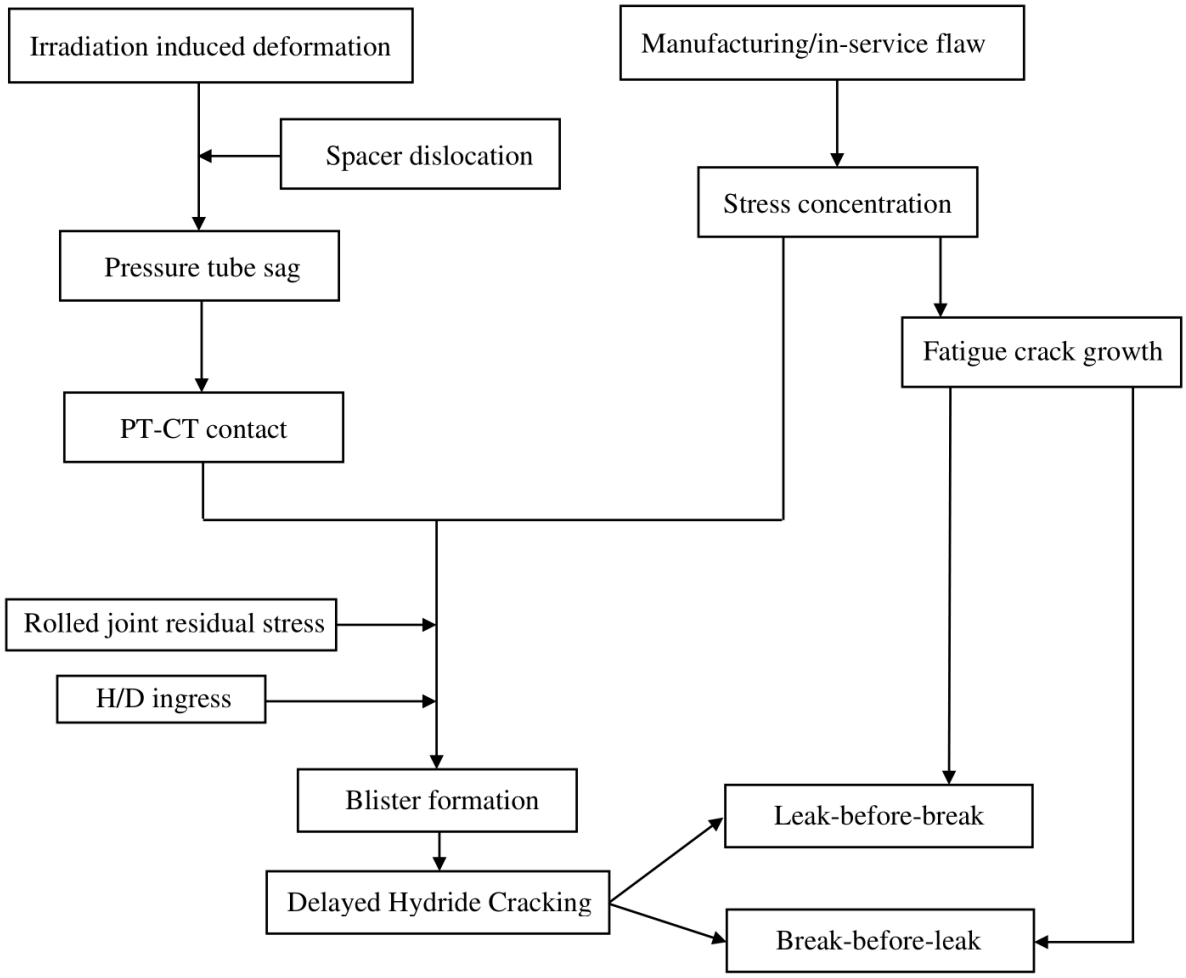

Figure 1.4: Degradation mechanisms leading to failure of a CANDU pressure tube

1.3 Research Motivation

The world is at a crucial juncture now in the fight against climate change. The United Nations considers the climate change as “the most systematic threat to humankind” and suggest immediate reduction in carbon dioxide emissions. Nuclear power plants have a vital role to play against climate change as they produce no greenhouse gas emissions during operation, and they have the potential to be the catalyst for delivering sustainable energy transitions. At the same time, these

systems must be highly reliable, safe and should have a comprehensive plant life management program. In Canada, the CANDU reactors have been operating safely for several years and are now undergoing life-extension programs. Early CANDU reactors were designed with limited knowledge about the material behaviour and ageing related degradation mechanisms. For example, the anisotropic material behaviour of zirconium alloys was not known during the initial manufacturing of the PTs. Significant improvements have been made since then in both design and safety measures from the operating experience, analyzing data from inspection and through rigorous research works.

As mentioned in the previous section, the FCs are the most critical components in a CANDU reactor and the fitness-for-service of PTs must be clearly demonstrated by the licensees. Irradiation induced creep is a degradation mechanism which significantly affects the PT structural integrity. The PTs undergo significant dimensional changes and the sagging of the FC assembly could lead the PT to come into contact with the CT (PT-CT contact), which could then lead to delayed hydride cracking (DHC) of the PT (Byrne et al., 1991). For example, a PT failure occurred in 1983 at Pickering Unit 2 as a result of high levels of deuterium concentration in the Zircaloy-2 PT, and PT-CT contact (Fanjoy, 1984). Following this incident, the Zircaloy-2 tubes were all replaced with Zr-2.5Nb PTs, which have low deuterium pick up rate. Even with the current improvements, the PT integrity is severely affected by PT-CT contact and any such contact risk must be averted in order to maintain fitness for service of the FCs.

Presently, the nuclear industry allows probabilistic assessment methods to assess the PT-CT contact risk and demonstrate adherence to CSA Standard N285.8 provisions. However, there is a significant research gap in the mechanistic models used for predicting the FC dimensional changes

and the probabilistic tools used for making risk-informed decisions. The nuclear industry currently relies on 1D FE model with limited number of Monte Carlo simulations for assessing the PT-CT contact risk. The main motivation behind this research is to critically analyze the current practices of the industry in assessing PT-CT contact risk and to develop computationally efficient and robust probabilistic models based on advanced 3D FE model of FCs for making better risk-informed decisions.

1.4 Research Objectives

The main objective of this research investigation is to develop surrogate models and probabilistic assessment models of in-reactor deformation of CANDU FCs. The thesis includes the development of finite element models of CANDU FCs and development of a general and efficient computational scheme for reliability and sensitivity analysis of structures, which are modeled and analyzed using finite element methods. The specific objectives of this research are:

- To develop 1D and 3D finite element models of a CANDU fuel channel in ABAQUS for the prediction of in-reactor deformation.
- To implement the creep deformation models of PT and CT in ABAQUS using UMAT.
- To compare and analyze the PT-CT gap prediction capability of 1D and 3D Finite element models.
- To study the diametral expansion of PTs and develop a surrogate model for predicting future deformations.
- To develop calibration approaches for diametral creep and PT-CT gap profile predictions.
- To investigate the diametral creep strain dips at the fast flux dip inter-bundle local regions.

- To predict the PT-CT gap and time to contact using 1D and 3D FE model and compare the results with the current nuclear industry practice.
- To study the influence of uncertain variables on PT-CT gap evolution and develop a surrogate model for future PT-CT gap predictions.
- To couple the multiplicative dimension reduction method (M-DRM) with polynomial chaos expansion (PCE) as a computationally efficient method for constructing a surrogate model for expensive computational models (e.g., finite element models).
- To estimate the statistics and complete probability distribution of the structural response using the coupled M-DRM and PCE method and perform reliability analysis.
- To estimate the global sensitivity analysis based on the coupled M-DRM and PCE expansion results.
- To connect uncertainty analysis with deterministic FEA software using programming code.
- To make use of coupled M-DRM and PCE method for the probabilistic contact assessment of CANDU fuel channels.

1.5 Outline of the Dissertation

Chapter 2 provides an extensive literature review on uncertainty analysis and various uncertainty propagation methods, followed by a review on the probabilistic finite element analysis. The chapter closes by discussing the life-limiting pressure tube deformations in a CANDU reactor.

Chapter 3 presents the 1D and 3D finite element modelling details of a CANDU fuel channel in ABAQUS finite element package and the implementation of pressure tube and calandria tube

material deformation equations in ABAQUS using UMAT. The fuel channel deformations are predicted using both models and a comparison on PT-CT gap profile prediction is made.

Chapter 4 presents the importance of surrogate models for replacing the expensive-to-evaluate finite element models. The surrogate models and calibration approaches of diametral creep and PT-CT gap profiles are discussed in detail and the validation of these models are conducted by comparing with measured data.

Chapter 5 presents a computationally efficient method for performing structural reliability and sensitivity analysis by coupling the multiplicative dimensional reduction method (M-DRM) with polynomial chaos expansion (PCE) method. The mathematical formulation of PCE and M-DRM along with Gauss quadrature scheme is presented. The steps required in implementing the proposed method is illustrated and the method is demonstrated by applying on a simple analytical equation. The statistical and sensitivity analysis results obtained from the proposed method is compared with the results obtained from Monte Carlo simulation (MCS), along with the probability of failure results.

Chapter 6 presents a computationally feasible approach for developing a surrogate model of assessing the evolution of PT-CT gap profiles with time and the process to perform probabilistic contact assessments by coupling the multiplicative dimensional reduction method (M-DRM) with the polynomial chaos expansion (PCE). The predictive capability of the proposed method for probabilistic assessments was initially examined using the surrogate model that was developed by using 1D FEA and MCS. The method was then applied to develop a surrogate model based on 3D FEA and conduct a detailed probabilistic contact assessment by considering different PT

orientations. Probabilistic analysis results between 1D and 3D FE models are critically compared and valuable insights to the nuclear industry are presented.

Chapter 7 presents the conclusion of this study and future research recommendations.

Chapter 2

Literature Review

2.1 Uncertainty Analysis

Uncertainty analysis in engineering is a field which is a combination of branches of engineering (e.g. civil, mechanical, aerospace engineering etc.) in one hand and statistics and probability theory on the other hand. A general framework for uncertainty analysis of an engineering system is shown in Figure 2.1 and each of the three steps are described.

- Step A is the step in which the mathematical model is completely defined. For a simple system, the mathematical model can be an analytic expression which could be solved explicitly, whereas a complex model can be an FE model which should be solved implicitly. All the input and output parameters should be clearly identified in this step. In summary, this step collects all the necessary ingredients used for a classical deterministic analysis of the engineering system.
- Step B consists of quantifying the sources of uncertainty in the physical system to be analyzed. This involves identifying all the input parameters that are not well known and modeling them in a probabilistic context. Based on the observations of uncertain input parameters, techniques such as probability paper plots, method of moments, etc., can be used to fit an appropriate distribution to these uncertain input parameters. The end product of this step is a random vector of input parameters with their respective probability

distributions and parameters. When there is a spatial or temporal variability of parameters, it is best to model the variability as a random process or random field.

- Step C is where we propagate the uncertainties in the input through the mechanistic model modeled in Step A and quantify the uncertainty in the output response. This is the core step in the probabilistic engineering analysis. The quantification of the output response is followed by the post processing methods to evaluate the failure probability or reliability of the physical system. Another important information which the analyst seek for is the impact of the random input parameters on the randomness of the output response, which is referred to as the global sensitivity analysis. In summary, Step C involves computing the complete probability distribution and moments of the random output response, failure probability based on a given threshold value of the output response and hierarchization of the input parameters based on sensitivity analysis.

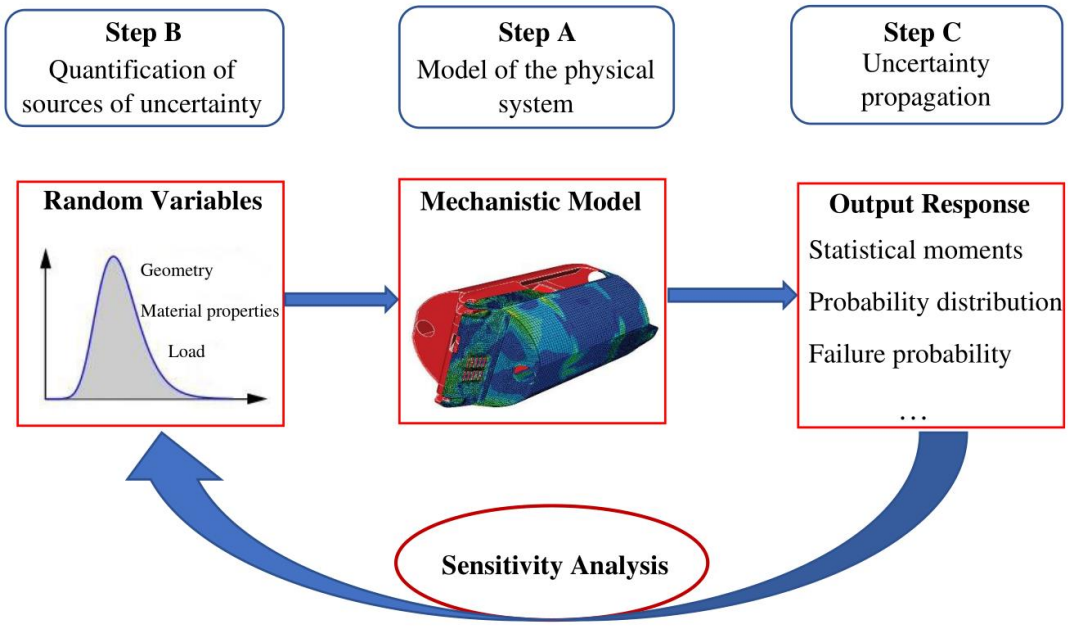

Figure 2.1: General framework for uncertainty analysis of a physical system (Bruno, 2007)

2.2 Uncertainty Propagation Methods

Let us consider a system which can be modelled by a function $\boldsymbol{y} = \mathcal{M}(\boldsymbol{x})$, where $\mathcal{M}(\cdot)$ is an analytical or numeric model, $\boldsymbol{x}$ is the vector of input variables and $\boldsymbol{y}$ is the output vector of the response. For simplicity, let us assume that *y* is a scalar and not a vector to denote the model response. This is the deterministic model we have. Now, when the input variables are having uncertainties, we will have to consider them as random variables, which makes the output response also a random variable. The random response can be then expressed as

$$\boldsymbol{Y} = \mathcal{M}(\boldsymbol{X}) \tag{2.1}$$

where $\boldsymbol{X} = [X_1, X_2, \dots, X_n]^{\mathrm{T}}$ is the vector of input random variables with respective assigned probability distribution and parameters.

The main objective of any uncertainty propagation method is to capture the probabilistic content of the output response, $\boldsymbol{Y}$. The complete probabilistic contents of $\boldsymbol{Y}$ is contained in its probability density function (PDF), $f_{\boldsymbol{Y}}(\boldsymbol{y})$, which depends on the joint PDF, $f_{\boldsymbol{X}}(\boldsymbol{x})$, of the input random vector, $\boldsymbol{X}$, and the model $\mathcal{M}(\cdot)$. However, an analytical computation of the PDF of the output response is only possible in some simple academic cases. In most of the practical cases, an analytical solution is not possible due to the complexity of the model $\mathcal{M}(\cdot)$ and the high dimensionality of input random vector, $\boldsymbol{X}$. This led to the formulation of various uncertainty propagation methods. Based on the specific information on the random output response provided by the methods, they can be categorized as shown in Figure 2.2.

The second moment methods provide only the information on the central part of the response since they deal with only computing the mean and variance of the output response. However, this

information is not much useful while working with real world engineering applications since we are more interested in the tail of probability distributions for computing failure probabilities.

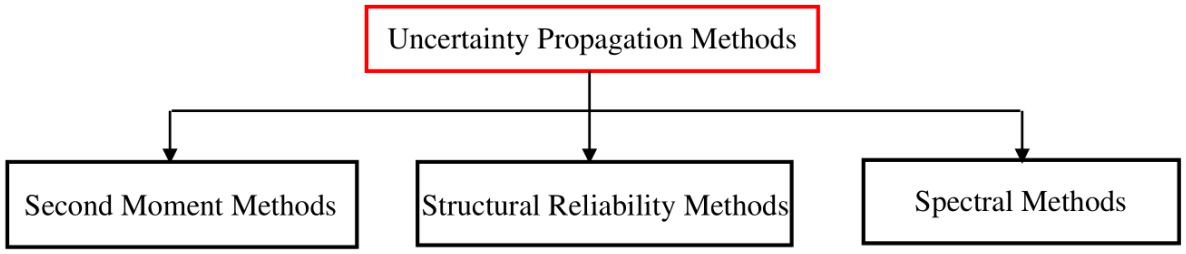

Figure 2.2: Classification of uncertainty propagation methods

The structural reliability methods overcome the disadvantages of second moment methods since they help in the investigation of the tails of the response PDF by computing the probability of exceedance of a prescribed threshold set by the analyst and thus computing probability of failure. However, the structural reliability methods do not provide the whole PDF, $f_{\boldsymbol{Y}}(\boldsymbol{y})$.

The spectral methods use the tools of functional analysis to represent the complete randomness of the model output response in an inherent way. Except the computational cost associated with computing the expansion coefficients on a suitable basis of functions, these methods allow to perform the structural reliability analysis in a straightforward manner following the post-processing of the output. The major advantage of these methods is that it provides an approximate whole PDF $f_{\boldsymbol{Y}}(\boldsymbol{y})$. The post-processing of this PDF information can be used to compute both the statistical moments as well as failure probability, which makes it a combination of both previously discussed methods.

The use of second moment methods in PFEA is of less interest due to the disadvantages of these methods as already discussed. Hence, only structural reliability methods and spectral methods are discussed in detail here.

2.3 Structural Reliability Methods

Structural reliability analysis aims at computing the failure probability of an engineering system with respect to a prescribed failure criterion by accounting for uncertainties arising in the description of the model. These uncertainties in the model may be arising from the strength factors (e.g., material properties, geometric dimensions, etc.) or the load factors (e.g., external load). As a general theory, it started in the early 1950's and the research are still active today. A comprehensive presentation of these topics can be obtained from the textbooks (Ditlevsen & Madsen, 1996; Madsen et al., 2006; Melchers & Beck, 2018).

The probability of failure denotes the probability that a structure fails to perform its intended function at a specific time, while reliability is the complement of the probability of failure. For each of the failure mode, the analyst sets a failure criterion by setting a threshold value for the output response quantity. In a mechanical context, the output response quantities can be displacements, stress or strain components, or quantities computed from these components (e.g., Von Mises stress). Hence, if the output response of a mechanistic model is given as $\boldsymbol{Y} = \mathcal{M}(\boldsymbol{X})$ and its allowable threshold is defined as y_0, the failure criterion is expressed mathematically by using a limit state function $\mathrm{g}(\boldsymbol{X}) = y_0 - \boldsymbol{Y}$. The reliability analysis can be now performed by formulating the limit state function is such a way that:

- $\Omega_s = \{\boldsymbol{X} : \mathrm{g}(\boldsymbol{X}) > 0\}$ is the safe domain in the space of input parameters;

- $\Omega_f = \{\boldsymbol{X} : \mathrm{g}(\boldsymbol{X}) \leq 0\}$ is the failure domain.

The set of points $\{\boldsymbol{X} : \mathrm{g}(\boldsymbol{X}) = 0\}$ defines the limit state surface. Given the joint PDF, $f_{\boldsymbol{X}}(\boldsymbol{x})$, of the input random vector, $\boldsymbol{X}$, the corresponding probability of failure associated with the limit state function can be computed as

$$P_f = \int_{\Omega_f} f_{\boldsymbol{X}}(\boldsymbol{x}) d\boldsymbol{x} = \int_{\mathrm{g}(\mathbf{X}) \leq 0} f_{\boldsymbol{X}}(\boldsymbol{x}) d\boldsymbol{x} \tag{2.2}$$

Except in some academic cases, it is not possible to compute this integral analytically due to the high dimensionality of $\boldsymbol{X}$. It should be also noted that, for the purpose of probabilistic FEA, the failure domain is defined implicitly as a function of $\boldsymbol{X}$, which further complicates the computation of failure probability. Thus, numerical methods must be employed.

2.3.1 Monte Carlo Simulation

The Monte Carlo simulation (MCS) method is a numerical method which solves problems by simulating random variables. It was first presented by Metropolis and Ulam (Metropolis & Ulam, 1949) and soon became popular and widely applicable with the evolution of computers (Sobol, 1994). The MCS method has three basic steps: (1) select the distribution type of each input random variable; (2) generate random numbers based on the selected distribution; (3) compute the output response for each of the generated input random numbers, which is called as simulations.

The probability of failure given in Equation (2.2) is then computed numerically using MCS as

$$P_f \approx \frac{N_f}{N} \tag{2.3}$$

where N is the total number of MCS trials and N_f is the number of trials for which the limit state function indicates a structural failure, i.e., $g(\boldsymbol{X}) \leq 0$. The total number of MCS trials required can be approximated using the binomial distribution as (Ang & Tang, 2007a)

$$N \approx \frac{1}{\left(\mathrm{COV}^2 \times P_f\right)} \tag{2.4}$$

where COV is the desirable coefficient of variation of the output response and P_f is the probability of failure. For most of the applications in mechanical, civil, nuclear and aerospace engineering, the probability of failure is usually between 10^{-2} to 10^{-6} due to high level of reliability (Sudret & Der Kiureghian, 2002a). Suppose that the value of P_f is of the order 10^{-4} and the required COV is 10%, the number of required MCS trials is 10^5. This makes MCS method computationally expensive due to its slow rate of convergence.

2.3.2 First Order Reliability Method

The first order reliability method (FORM) is an approximate method for computing the probability of failure. This method was introduced as an alternative for brute Monte Carlo simulation since the method computes the probability of failure by means of a limited number of functional evaluations. In FORM, the reliability analysis is performed by transforming the correlated or uncorrelated input random variables, $\boldsymbol{X}$, as the independent standard normal variables, $\boldsymbol{Z}$. In the context of structural reliability, this transformation of recasting the problem in the standard normal space is made possible through an isoprobabilistic transformation such as Rosenblatt transform (Hohenbichler & Rackwitz, 1981) or Nataf transform (Der Kiureghian & Liu, 1986).

After the transformation, FORM estimates the reliability index β, which is the shortest distance between limit state function and the origin of the standard normal space (Hasofer & Lind, 1974). The point of the failure domain closest to the origin in the standard normal space is called as design point. Hence, FORM can be formulated as an optimization problem for finding the design points subjected to the constraints of minimizing β subject to $g(\boldsymbol{Z}) = 0$.

Several algorithms are available for solving this optimization problem, e.g., Rackwitz-Fiessler algorithm (Rackwitz & Fiessler, 1978) or using a numerical solver in Matlab or using a solver command in Excel. Once the reliability index, β is obtained by solving the optimization problem, the probability of failure can be computed as

$$P_f \approx \phi(-\beta) = 1 - \phi(\beta) \tag{2.5}$$

where $\phi(\cdot)$ is the standard normal cumulative distribution function.

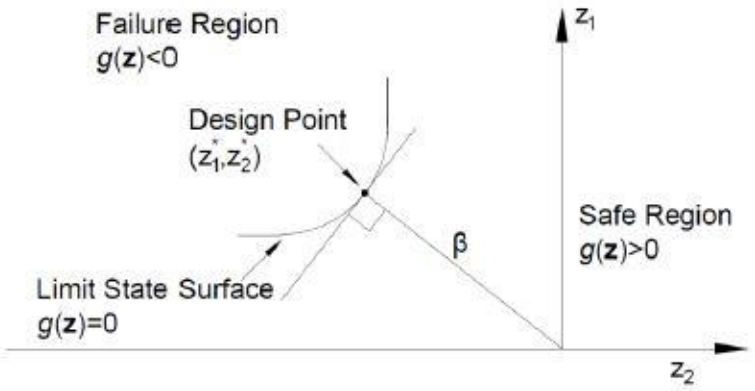

Figure 2.3: Reliability index based on FORM

It should be noted that FORM relies on linearization of the limit state function around the design point and hence can give erroneous results while computing probability of failure. Several improvements are proposed to overcome these disadvantages when the limit state function is highly nonlinear (Koduru & Haukaas, 2010; Zhao & Ono, 1999).

2.4 Spectral Methods

The structural reliability methods such as FORM or its modifications can be used only to solve a specific problem of computing the probability of failure through certain approximations and assumptions. If the analyst is interested in computing the moments of the output response, he should rely on the second moment methods. Thus, the analyst should resort to each type of analysis separately to compute the needed information, which shows the drawbacks of these methods.

As discussed in the MCS method, this method is capable of providing the complete representation of the output response. Once the simulations are performed for the required number of MCS trials, the corresponding output responses can be gathered in a histogram and an empirical cumulative distribution function (CDF) can be constructed. However, the main drawback of this method is the computational cost associated with the evaluation of failure probability due to slow convergence rate.

Spectral method is an efficient method which overcomes the above-mentioned drawbacks of the structural reliability methods. The spectral method uses the tools of functional analysis to represent the complete randomness of the model output response in an inherent way (Maître & Knio, 2010). In the present study, the spectral expansion of an output response quantity onto a bases made of orthogonal polynomials, commonly referred to as polynomial chaos expansion (PCE) are of interest. PCE is a powerful surrogate modeling (or metamodeling) technique that aims at providing a functional approximation of a computational model through its spectral representation on a carefully chosen set of polynomial function bases. PCE alleviates the high computational cost associated with uncertainty analysis by replacing the otherwise expensive-to-evaluate numerical models (e.g., a finite element code) with simple-to-evaluate surrogate models. A Monte Carlo

simulation using the surrogate model can be then used to obtain the complete distribution of the output response and then compute probability of failure. However, computation of the PCE coefficients is expensive when the mechanistic model is expensive-to-evaluate and involve more number of input random variables (Debusschere et al., 2004). Hence, an efficient method is needed to reduce the computational cost associated with using PCE.

2.5 Probabilistic Finite Element Analysis

Many engineering problems are described using partial differential equations and for simple geometry problems, we can arrive at classical analytical solutions. However, when we are having a complex geometry, we must resort to numerical techniques. One of the most widely used numerical approach is the finite element method (FEM), which can solve the partial differential equations approximately (Reddy, 2010). FEM is based on discretizing the problem domain into simpler parts called finite elements and on the calculus of variational methods to minimize an associated error function. With the advent of FEM, it became possible to solve a wide range of complex problems in mechanical, civil, and various other engineering fields.

The starting of finite element approach can be traced back to the work by Hrennikoff in 1941 (Alexander Hrennikoff, 1941) and Courant in 1943 (Courant, 1943), where they both identified a common and essential characteristic of mesh discretization of a continuous domain into sub-domains, usually called elements. The term finite was later coined by Clough in 1960 (Clough, 1960) and since then, FEM became more and more popular in solving various engineering problems. In today's world, FEM is used as a major tool in design and analysis of various complex engineering problems. The progress in the computer technology has immensely aided in the

growth and wide usage of FEM (Haldar & Mahadevan, 2000) and this method now stands as a computational method which permits accurate analysis of any complex engineering problem.

However, when dealing with real world problems, it is natural to understand that the uncertainties are unavoidable (Ang & Tang, 2007b). To deal with these uncertainties, the scientific and engineering communities developed a probabilistic or stochastic approach to engineering problems, which led to the development of probabilistic finite element methods (Stefanou, 2009a). The engineering problems are often focused on understanding the reliability of a structure during its lifetime and computing probability of failure, which led to probabilistic finite element analysis (PFEA), or also called as finite element reliability analysis (FERA) (Haukaas, 2003; Haukaas & Der Kiureghian, 2006, 2007). When the uncertainties are modeled as a random field, i.e., random variables with spatial or temporal correlation, the terminology used is stochastic finite element analysis (SFEA) (Ghanem & Spanos, 1991; Haldar & Mahadevan, 2000; Stefanou, 2009b).

The PFEA is performed by connecting one of the uncertainty propagation methods with the FEA software. At this time, the only commercial software which has the uncertainty analysis capability is ANSYS, which is equipped with ANSYS Probabilistic Design System (PDS). However, the methods available are MCS, which makes it computationally expensive for nonlinear FEA problems and a response surface approach using variational approach, which is not an accurate method (Reh et al., 2006). Hence, for performing a reliable PFEA, the analyst should connect the FE software such as ABAQUS with the existing reliability packages such as NESSUS (Thacker et al., 2006) and COSSAN (Schuëller & Pradlwarter, 2006). These reliability software packages can interact with most of the commercial FEA softwares. The disadvantage of this approach is that the analyst may be performing reliability analysis without having a theoretical background of the

reliability methods and the analyst will have to purchase these reliability platforms separately. A comprehensive review of the reliability packages available to connect with FE softwares can be found in (Pellissetti & Schuëller, 2006) and in the special issue of Structural Safety (Ellingwood, 2006).

Another approach is to link a general purpose FEA software to a numerical computing environment in which the analyst has the flexibility to program more reliability algorithms. The advantage of this approach is that the analyst will have a strong grasp of the theory behind the reliability analysis method, whereas the difficulty is the requirement of advanced programing skills required to connect the reliability analysis module and commercial FE software.

Once the connection between the FE software, e.g., ABAQUS and the computing environment, e.g., MATLAB is established, an uncertainty propagation method must be chosen to perform PFEA. Any method discussed in the previous section can be used for the purpose of reliability analysis. A generally known and an easy to implement method for FERA is the MCS, where the deterministic FEA code is repeatedly called to simulate the structural response (Hurtado & Barbat, 1998). Upon completion of the simulations, MCS provides the statistical properties (mean and standard deviation) as well as the complete distribution of the structural response. However, the computational cost will be extremely high if the required time for each FEA run is not fairly small (Papadrakakis & Kotsopulos, 1999). FORM can be used as a replacement for MCS to compute probability of failure for expensive-to-evaluate FEA codes. FORM can be computationally efficient but the drawbacks are, its accuracy highly depends on the degree of nonlinearity of limit state function (Lopez et al., 2015) and the performance function may not be available in an explicit

form in FEA (Pellissetti & Schuëller, 2006). Also, the analyst must resort on other methods to compute the statistics or to obtain the complete probability distribution of the structural response. Using spectral methods such as polynomial chaos expansion (PCE) for PFEA overcomes the above-mentioned drawbacks of the structural reliability methods. PCE is a powerful surrogate modeling (or metamodeling) technique that aims at providing a functional approximation of a computational model through its spectral representation on a carefully chosen set of polynomial function bases. However, computation of the PCE coefficients becomes expensive when the mechanistic model is expensive-to-evaluate and involves more number of input random variables (Debusschere et al., 2004).

2.6 Pressure Tube Deformations in CANDU Reactors

This section reviews the dimensional changes of PTs resulting from the normal operating conditions under high temperature, pressure and fast neutron flux. These include axial elongation, diametral expansion, wall thinning and sag, which all affect the PT integrity. Three physical mechanisms are considered to be influencing in-reactor dimensional changes: *(i) thermal creep* – changes in shape due to temperature and stress only, but in the absence of fast neutron flux. However, the thermal creep component describes the behaviour of a material that has been hardened by low levels of fast neutron irradiation. *(ii) irradiation creep* - changes in shape at constant volume due to applied stress, temperature and fast neutron flux, and *(iii) irradiation growth* - changes in shape at constant volume due to fast neutron flux and temperature but in the absence of applied stress. These irradiation and thermally induced deformation mechanisms are life-limiting factors in the lifetime of a FC.

2.6.1 Axial elongation

The prime reason for the axial elongation in PTs is due to the anisotropic material properties of Zr alloys. During the initial design of CANDU reactors, the Zr alloys were assumed to be isotropic and any possibility of PT elongation was considered insignificant. But with more reactor operating experience and studies, the contribution of irradiation creep and growth mechanisms were shown to be responsible in enhancing elongation (Christodoulou et al., 1996), which was a result of the hexagonally close packed (hcp) anisotropic crystal structure of Zr and the presence of a strong crystallographic texture that was the result of the manufacturing process. A constant elongation rate was assumed initially for maintenance planning. However, it was later observed that the elongation rate gradually increased with reactor operating time or more specifically with accumulated fast neutron fluence ((Christodoulou et al., 1996; Holt & Wong, 2002), (also see Figure 2.2.1 in (Holt, 2008)). Accommodation of PT elongation is achieved by supporting the end-fittings on sliding bearings. Earlier CANDU reactors were not designed to accommodate large elongation values, however more recent CANDU designs considered increased elongation margins (Holt & Wong, 2002).

To accommodate PT elongation the CANDU design is such that one end of the PT is initially locked and the other end is kept free to axially move. When the reactor reaches about 120,000 Equivalent Full Power Hours (EFPH) or about halfway through the design life, the free and fixed ends are reversed, which is termed as ‘FC reconfiguration’. This is done for the purpose of accommodating elongation at both ends of the channel (Holt & Wong, 2002). The plant life management strategies are based on the monitoring and calculations of elongation rates of each

FC in the reactor. A challenging factor is the variability in elongation rates of different FCs, which requires probabilistic tools for making cost-effective, risk-informed decisions on reconfiguration and maintenance planning. Computational models can be used for predicting the elongation and for the purpose of probabilistic assessments.

2.6.2 Diametral expansion

Another significant dimensional change which can affect the PT integrity is the increase of PT circumference along the length of the tube, termed as diametral expansion. Irradiation creep is the main mechanism that contributes towards diametral expansion, while the contribution from irradiation growth is smaller but negative and therefore beneficial in reducing diametral expansion (Christodoulou et al., 1996). A typical diametral profile of a PT subjected to in-reactor deformation is shown in Figure 2.4. The strains in the inlet and outlet ends of the tube are lower due to the lower fast neutron fluxes there. An additional life limiting outcome of excessive diametral expansion is flow bypass that can lead to fuel dry-out and eventually limit the operating power of the reactor. As seen with axial elongation, diametral expansion also exhibits substantial variability among CANDU FCs (Griffiths et al., 2002). To maintain PT integrity, the maximum diametral expansion must be within allowable design limits.

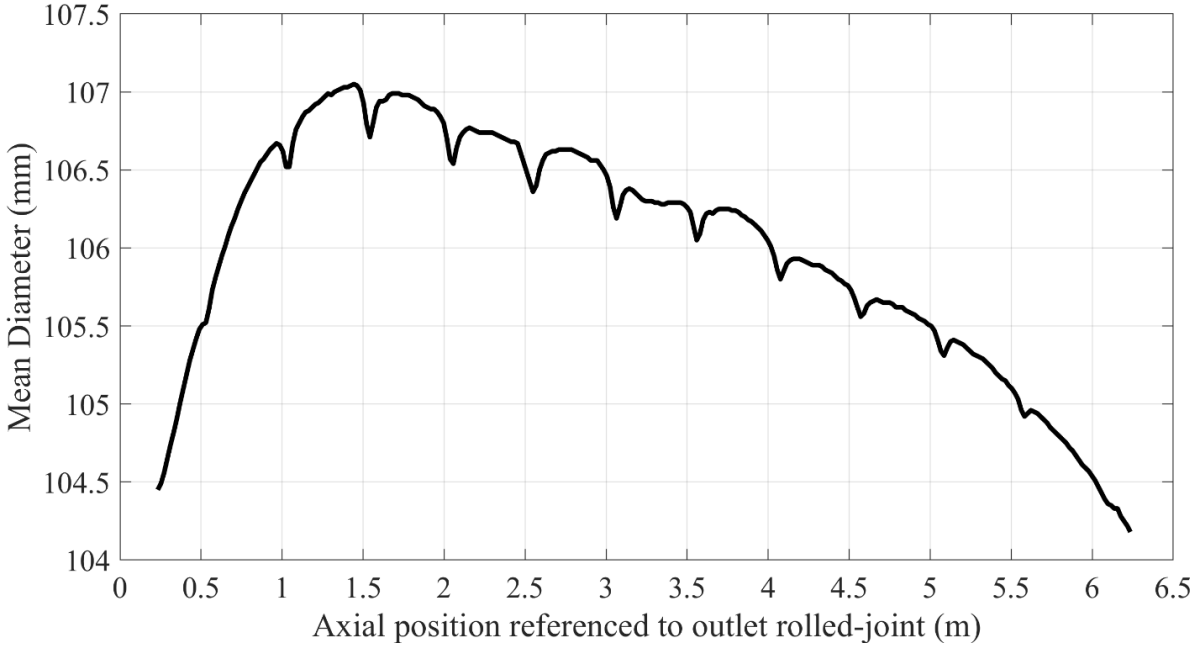

Figure 2.4: A typical diametral profile of a PT from outlet to inlet

2.6.3 Sag

Both the PT and CT sag as a result of in-reactor deformation (Badie et al., 1988; Causey et al., 1985; Kim & Sohn, 2004). Initially the PT sags due to its weight, the weight of the fuel bundles and the weight of the coolant. With additional operating time and when the garter springs had contacted the CT, the FC begins to sag further (i.e., described as "overall sag") due to in-reactor deformation of the CT, as shown in Figure 2.5 (Causey et al., 1985). With additional reactor operating time, the PT continues to sag further between the spacers, a process that can eventually lead to contact between the PT and CT, termed as PT-CT contact. Direct contact between the PT and CT would result in heat transfer between the two tubes and a substantial decrease in the PT temperature, which in turn leads to the precipitation of hydrogen and the formation of hydride blisters. Blister formation will ultimately lead to delayed hydride cracking (DHC) (Byrne et al.,

1991) that severely compromises PT integrity, a risk that must be averted as much as possible. Excessive PT sag may also prevent the passage of fuel bundles when FCs are re-fueled. In addition to these risks, excessive CT sag may result in contact of CTs with horizontal reactor mechanisms that are perpendicular to the FCs (e.g., Liquid Injection Shutdown System or LISS nozzles).

The overall FC sag measurements from in-service inspections provide only crude information on PT sag per se, namely PT sag occurring between the garter springs. More recent techniques have allowed the acquisition of PT sag that is observed between the spacers. This is the reason computational models are needed to predict important information such as PT-CT contact, time to contact and contact location, which are necessary inputs in adopting a more efficient inspection and maintenance planning, and to take end-of-life decisions.

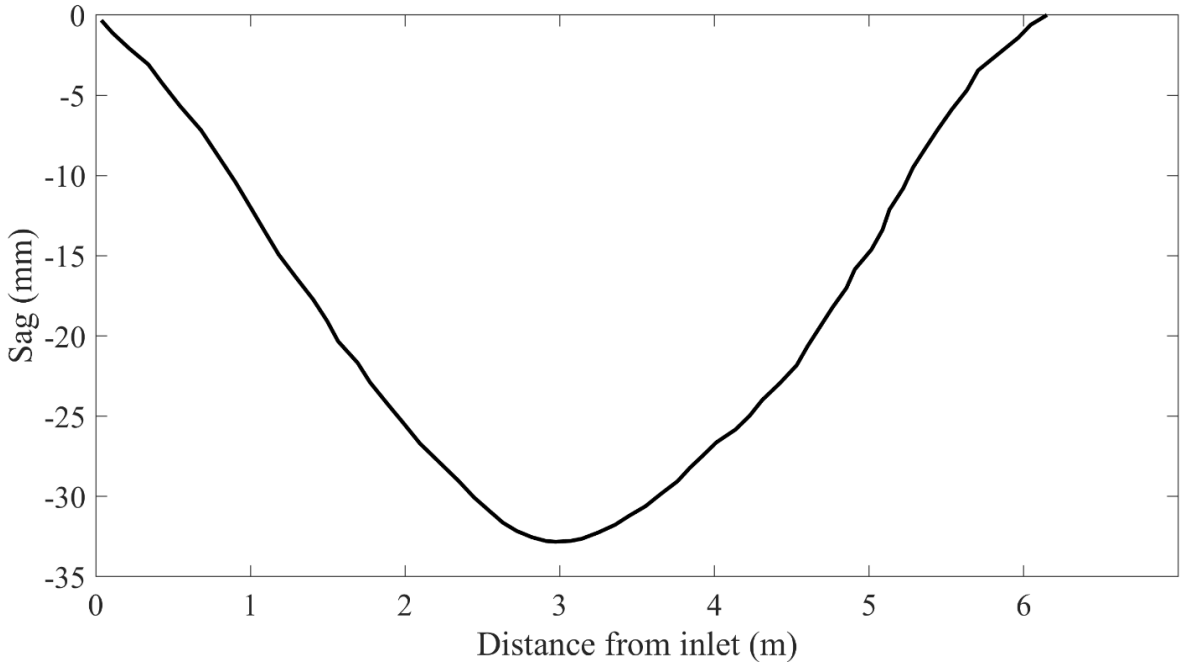

Figure 2.5: A typical sag profile of a FC after several years of operation, from (Holt, 2008)

Chapter 3

Computational Modelling of In-Reactor Deformation of CANDU Fuel Channels

3.1 Introduction

3.1.1 Need for computational models of FC deformation

It is clear from the previous chapters that the FC is the most critical component in a CANDU reactor. The FCs in the reactor core operate under extreme conditions and undergo dimensional changes with reactor operating time. To ensure structural integrity is maintained, it is necessary that these dimensional changes are known and predicted with sufficient confidence levels. For this purpose, computational models of FCs can be developed by using powerful numerical techniques such as finite element methods along with deformation equations, which are based on the understanding of the physical mechanisms that lead to changes in the dimensions, the geometry of the FC and the loading conditions during operation. When Zirconium alloys were initially used for the manufacturing of PTs, the following life limiting issues were not known:

a) Anisotropic material behaviour
b) Irradiation enhancement resulting in irradiation induced creep and growth
c) Formation of hydride blisters leading to Delayed Hydride Cracking (DHC)

d) Neutron irradiation causing reduction in critical material properties (e.g., fracture toughness)

Extensive research conducted over the past 40 years and the experience from operating power reactors has helped in gaining a broad understanding on in-reactor deformation of PTs. The data obtained from in-reactor testing of Zr alloys and periodic non-destructive inspections of PTs have helped in the understanding of various mechanisms responsible for the dimensional changes, and semi-empirical equations were developed for predicting these changes (Christodoulou et al., 1996; Holt, 2008). Utilizing these semi-empirical deformation equations, advanced computational techniques can be developed by incorporating these equations into finite element methods, which can then be used to predict important variables such as axial elongation, diametral expansion, PT and CT sag, PT-CT contact and time to contact. The computational models are therefore necessary due to the following reasons:

- To predict the future dimensional changes in existing reactors, which will aid in the development of optimized inspection and maintenance planning procedures and in ensuring that the regulatory requirements are met.
- To use mechanistic models for probabilistic analysis of FCs, which will aid in a risk-based decision making and end-of-life decisions.
- To simulate the behaviour of new reactor FCs operating at different operating conditions and to improve the future design based on the simulated results.

The nuclear industry currently uses a beam model called as CDEPTH for predicting FC deformation and making risk-informed decisions (Sauvé et al., 1989). These are proprietary

FE codes and are hence unavailable to other investigators. Using the current understanding of the irradiation-induced deformation mechanisms of Zr alloys, this chapter describes the computational modelling of in-reactor deformation of FCs using 1D and 3D finite element analysis using ABAQUS FE package.

3.1.2 Objective

The first objective is to develop a 1D finite element method (1D FEM) model of the FC using beam elements. The main purpose of developing this model is to analyze the prediction accuracy of the beam model currently used by the nuclear industry. Since the PT and CT creep models are not available in the ABAQUS library, these models are incorporated using a user defined subroutine called UMAT. The FE model is then used to predict the axial elongation, sag and PT-CT gap profiles.

The second objective is to develop a complete 3D finite element method (3D FEM) model of the FC using continuum shell elements, which overcomes the limitations and simplifications of a 1D beam model. The PT and CT creep models are incorporated using UMAT and all the life-limiting deformations such as axial elongation, diametral expansion, sag and PT-CT gap profiles are predicted.

The final objective is to compare both 1D and 3D FEA results by analyzing the accuracy and efficiency of these models for predicting the deformations. Special consideration is given to the prediction of PT-CT contact and time to contact, as these are important inputs required for demonstrating fitness-for-service of the PTs and life-extension decisions.

3.1.3 Organization

This chapter is organized as follows. Section 3.2 is a general section applicable to both 1D and 3D FEA, which presents a detailed description of the prerequisites required for the development of a FC FEM model such as the design, geometry, operating conditions, and material models of a typical CANDU FC. Section 3.3 gives a clear description on the implementation of the anisotropic material behaviour of Zirconium alloys and creep models of PT and CT as material models in ABAQUS using UMAT subroutine for both 1D and 3D FEM models. Section 3.4 presents the modelling details of 1D FEA and the corresponding FEA results. In Section 3.5, the modelling details of 3D FEA and the corresponding FEA results is discussed, after which an extended analysis results using different PT boundary conditions are shown. Section 3.6 discusses the limitations of the 3D FE model. Section 3.7 compares the prediction accuracy of PT-CT gap profiles for 1D and 3D finite element models, which will provide a critical insight to the nuclear industry. Finally, conclusions are summarized in Section 3.8.

3.2 Design, Operating Conditions and Material Models of a CANDU FC

3.2.1 Design of a CANDU FC

A typical FC in a CANDU reactor comprises a PT surrounded by a CT and separated by four garter springs as shown in Figure 3.1. PTs and CTs are manufactured using cold-worked zirconium 2.5 wt% niobium (Zr-2.5Nb) and Zircaloy-2, respectively. The PT holds the natural uranium dioxide fuel bundles and operates at a high temperature from about 250 °C at the inlet end to about 310 °C at the outlet end depending on the power rating of the CANDU unit. The internal pressure varies

from about 10.5 MPa at the inlet end to about 9.9 MPa at the outlet end, resulting in a variation in the applied hoop stress across the length of the PT. The initially applied maximum circumferential stress is about 130 MPa at the inlet end to about 122 MPa in the outlet end. It should be pointed out however, that the applied hoop stress tends to increase due to the reduction in the wall thickness and the increase in the diameter of the PT. The internal pressure also generates an initial axial stress of about 65 MPa in the PT wall along with a small axial stress caused due to an end-load of approximately 2220 N resulting from the out-of-core hardware that appears to vary with time from tensile to compressive. The CT operates at a much lower temperature (60-80 °C) due to contact with the heavy water moderator. The annulus gap is filled with dry CO_2 gas for thermal insulation and allowing the detection of any leakage originating from any of the channels. The annular gap between the "cold" CT and the "hot" PT is maintained using the garter springs or annulus spacers, which also help in preventing any contact between the two tubes.

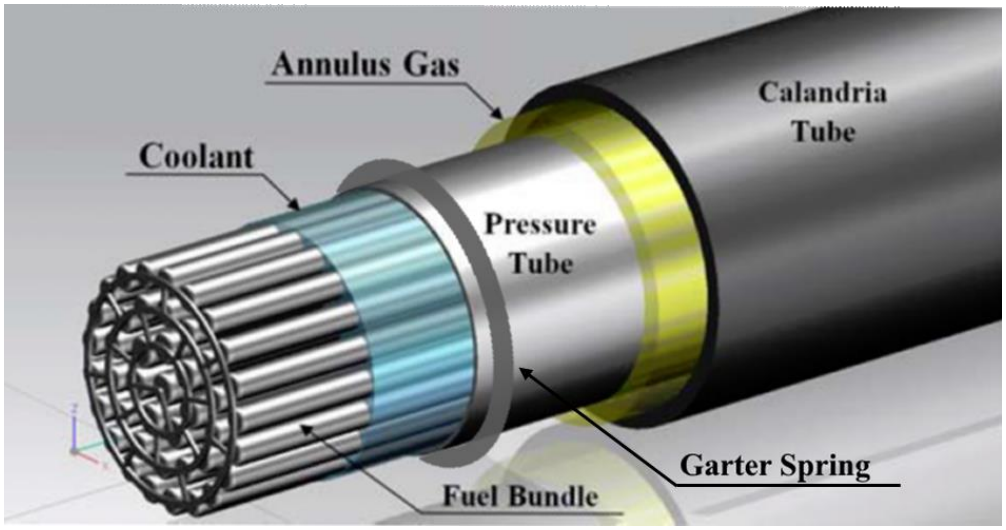

Figure 3.1: A section of a FC in CANDU reactors

3.2.2 FC Geometry and Operating Conditions used for FEA

This section describes the geometry, dimensions and operating conditions of the FC analyzed using both 1D and 3D FEA. A simple schematic of the FC analyzed as an example in this chapter is shown in Figure 3.2. The PT is set as 6163.5 mm in length, 113.2 mm in (outer) diameter and 4.191 mm in thickness; the CT is set as 5944 mm in length, 131.7 mm in (outer) diameter and 1.372 mm in thickness. The PT is divided into five spans based on the positioning of the four tight fitting garter springs. Spans S1, S5 and S3 are identified as the outlet, inlet and central spans, respectively, while Spans S2 and S4 are identified as internal spans. The initial gap between the PT and CT is set as 7.878 mm, which is a nominal value. The right end of the channel is assumed to be the inlet for the coolant and is allowed to be axially free, while the left end is assumed to be the outlet and it is assumed to be the fixed end. It is important to note that the back end of the PT is placed at the outlet end in this example. A note is due here regarding the coolant flow direction as an important factor affecting the deformation profile of PTs in CANDU reactors.

Dimensional changes of PTs are affected by the coolant flow orientation relative to the tube end that appeared first from the hot extrusion press. The tube end emerging first as a result of hot-extrusion is termed as the '*front end*' and the last emerging end is termed as the '*back end*'. The back ends of the PT have a higher ultimate tensile and yield strength than the front ends. This variability in mechanical properties from back to front end and the coolant flow direction with respect to the end of the PT has an influence on the diametral strain profile of PTs (e.g., see Figs. 2.1.1 and 2.1.3 in (Holt, 2008)). In contrast, when the back end is at the inlet end of the channel, the diametral profile has a more symmetrical shape (e.g., see Fig. 2.1.3 in (Holt, 2008)). In this

chapter, the analysis results are based on the back end of the PT being placed at the outlet end of the FC. A more detailed analysis is performed using 3D FEA by considering different boundary conditions to study its influence on gap. The temperature, pressure and fast flux profiles used in the analysis are shown in Figure 3.3.

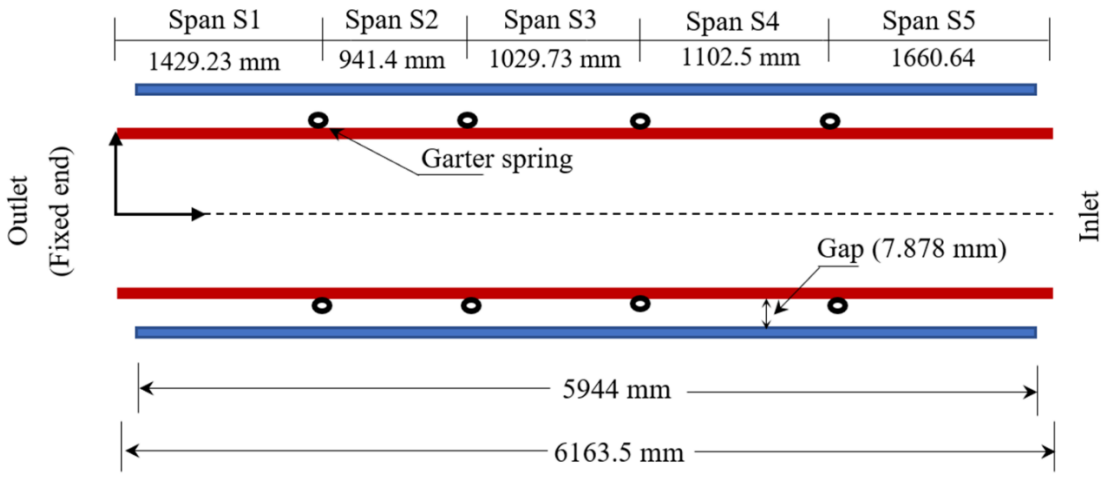

Figure 3.2: A schematic of the CANDU FC analyzed

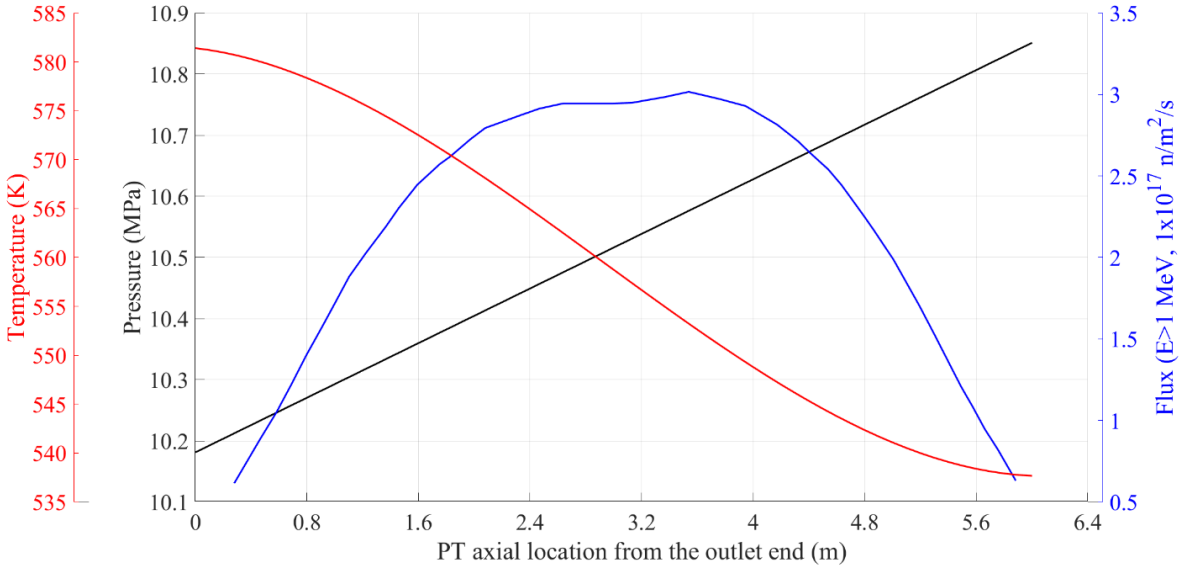

Figure 3.3: Variation of fast neutron flux, pressure, and temperature along the PT

3.2.3 Mechanical Deformation Models of PT and CT

3.2.3.1 Elastic properties of PT and CT

Both Zr-2.5Nb and Zircaloy-2 materials used for the manufacturing of PTs and CTs have anisotropic material properties in the axial, circumferential and radial directions of the tube, respectively (Holt et al., 2003). These anisotropic properties are prominent due to the microstructure and crystallographic texture (i.e., preferred crystallographic orientation) of elongated hexagonal-close-packed (hcp) α-Zr grains developed during the extrusion process (Bickel & Griffiths, 2007, 2008; Saibaba et al., 2013). The elastic properties of these materials are given in Table 3.1.

Table 3.1: Elastic properties of PT and CT (CSA N285.8, 2015; Northwood et al., 1975; Pan et al., 2010)

Elastic properties	FC components	
	Pressure tube, PT	Calandria tube, CT
Elastic modulus (GPa)	Figure 3.4	90.8
Poisson's ratio	0.4	0.4

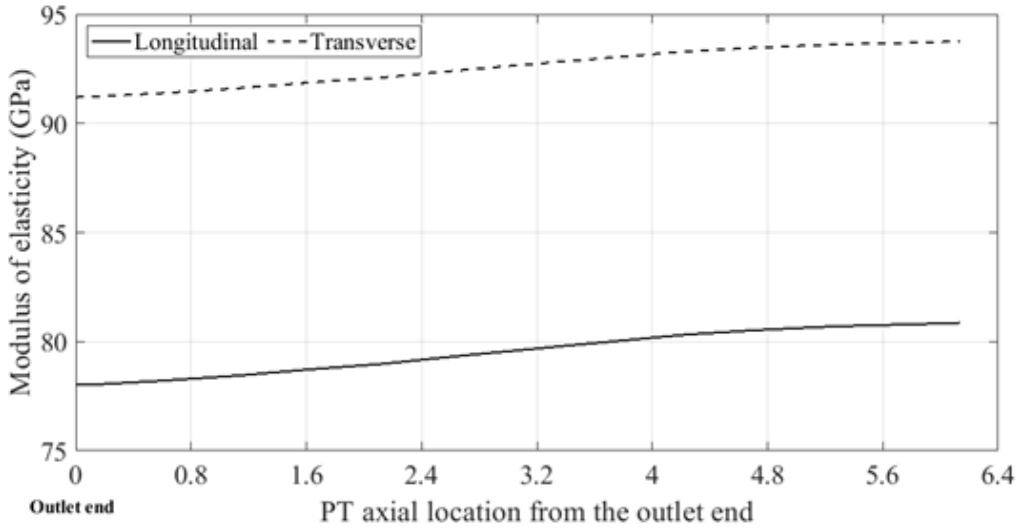

Figure 3.4: Variation of modulus of elasticity in the PT (temperature-dependent)

3.2.3.2 Pressure Tube Creep Deformation Equation

To describe the deformation behaviour of PTs under a multi-axial stress state, an '*anisotropic deformation equation*' is required for anisotropic creep and growth of the material. Combined with the equivalent equation for the CT, such an equation can then be used as input to a finite element model (FEM) to predict the deformation of the fuel channel, and in particular the sag and the potential for PT-to-CT contact. The simplest anisotropic formulation for creep is that derived by Ross-Ross et al. (Ross-Ross et al., 1972) using Hill's method (Hill, 1998). Such an equation contains three independent anisotropy parameters, and thus requires the measurement of three independent deformation rates under at least two different stress states. The parameters for such a model cannot, therefore, be derived solely from the elongation and diametral strain data from a PT.

The first deformation equations separating creep and growth were developed in the late 1970s (Holt, 1979; Ibrahim & Holt, 1980). The anisotropic effects of texture were taken into account by

averaging the behaviour of individual crystals, assuming certain strain-producing mechanisms at the single crystal level in what is referred to as a '*polycrystalline model*'. This was a '*lower bound*' polycrystalline model, which ignores the fact that different orientations of crystals have different strain tensors. The anisotropy of the polycrystal (i.e., the PT) depends on the relative contributions of the strain mechanisms at the single crystal level. This was derived from bent beam uniaxial stress relaxation tests in which the growth component does not contribute to the measured strain (Causey, 1974; Causey et al., 1984; Coleman et al., 1976; Fraser et al., 1973) and allowed the prediction of the creep anisotropy of a PT under biaxial loading. The growth anisotropy was derived again using a lower bound polycrystalline model, by assuming, that at the single crystal level, dislocations were the sinks for SIAs, and grain boundaries were the sinks for vacancies. Once the anisotropy of creep and growth is defined, their contributions to elongation and diametral strain in a given power reactor could be derived from the elongation and diametral strain data for that reactor, and the response of a PT to a multi-axial stress state could be predicted.

In the mid 1980s, an '*upper bound*' approach was used (in which all crystals are assumed to exhibit the same strain tensor) to study the effects of interactions between the crystals (Holt et al., 1989; Holt & Causey, 1997). The approach was developed mainly to explain the irradiation growth response of CT materials (Fidleris et al., 1985; Holt et al., 1989). The parameters of the model were derived by the same methodology as those for the earlier lower bound model, but including data for creep in shear as well as stress relaxation (Causey et al., 1984). At the same time finite element methods were used to calculate the sag more accurately (Sauvé, 1987). Both the upper and lower bound approaches can lead to systematic errors in predictions for stress tensors different from those for which the data are obtained to normalize the model.

The discontinuities of strain or stress at the grain boundaries consistent with the lower bound and upper bound models are due to the lack of self-consistency between the deformation of the individual grains and the deformation of the polycrystal. These discontinuities have successfully been eliminated by the adoption of a self-consistent model that was initially proposed by Woo in 1985 (Woo, 1985) and in 1987 (Woo, 1987) and later by Causey et. al. (Causey et al., 1988) and Tomé et. al.(Tomé et al., 1993). Based on the work of Woo and in particular by Tomé (Tomé et al., 1993) a '*self-consistent polycrystalline model*' called SELFPOLY, was developed, which allowed for individual crystals to deform differently, but under constraints imposed by the surrounding matrix of crystals with different orientations. The single crystal creep compliances and growth tensor are derived from in-reactor data for polycrystalline PT and PT-like materials tested with a range of stress tensors including uniaxial tension, biaxial tension and shear (Christodoulou et al., 1993; Tomé et al., 1994). For the first time the single crystal growth parameters could be based on growth data obtained from tests in high flux reactors (Holt et al., 2000; Holt & Fleck, 1991). This model, which is currently in use, represents the behaviour of the tubes quite well over a narrow range of textures close to those of PTs. However, there are inconsistencies in the predicted creep anisotropy when the texture is changed significantly (Causey et al., 1994).

The self-consistent approach offers a powerful tool to predict polycrystalline behaviour from single crystal properties taking into account material parameters such as crystallographic texture, elastic properties, grain morphology etc. However, the basic physical parameters in the single crystal level that are needed to construct reliable mechanistic models to predict the deformation of even a pure Zr single crystal are not known (e.g., mobility and anisotropy, configuration, and

elastic properties of point defects, structures of dislocation cores and the influence of impurity atoms on these characteristics). Therefore, reliance on a phenomenological approach is still required.

The in-reactor deformation rate of PTs is based on the equation described in (Christodoulou et al., 1996) that assume that long term steady-state deformation consists of separable, additive components from three physical mechanisms, namely: thermal creep, irradiation creep and irradiation growth. The in-reactor deformation rate is approximated as the linear sum of individual contributions from these mechanisms, namely:

$$\dot{\varepsilon}_d^c = \dot{\varepsilon}_d^{tc} + \dot{\varepsilon}_d^{ic} + \dot{\varepsilon}_d^{ig} \tag{3.1}$$

where $\dot{\varepsilon}$ is strain rate, subscript d indicates the tube direction (axial, transverse and radial) and superscripts c, tc, ic and ig indicate total creep, thermal creep, irradiation creep and irradiation growth, respectively. As was mentioned previously, the directionality dependence is due to the anisotropic nature of these mechanisms (Causey, 1981; Holt et al., 2003; Ross-Ross et al., 1972), which contribute to length, thickness as well as diametral changes. The contributions to the total strain rate from each of these mechanisms are functions of operating variables such as applied stress from the internal pressure, temperature and fast neutron flux as given:

$$\dot{\varepsilon}_d^{tc} = [K_1 C_1^d \sigma_1 + K_2 C_2^d \sigma_2^2] e^{-Q_1/T} + K_3 C_1^d \sigma_1 e^{-Q_3/T} \tag{3.2}$$

$$\dot{\varepsilon}_d^{ic} = K_c K_4(x) C_4^d(x) \sigma(x) \phi \left[e^{-Q_4/T} + K_5 \right] \tag{3.3}$$

$$\dot{\varepsilon}_d^{ig} = K_g K_6(x, \phi t) C_6^d(x) \phi e^{-Q_6/T} \tag{3.4}$$

The in-reactor thermal creep component has two terms that dominate at temperatures above and below 570 K, respectively. The terms in the equations above are defined as follows:

K_1, K_2 are constants for high temperature in-reactor thermal creep

K_3 is constant for low temperature in-reactor thermal creep

K_c and K_g are constants defining the material creep and growth rate due to irradiation

$K_4(x)$ is a function describing the variation of irradiation creep due to microstructure variations along the tube length

x is the distance from the back end of the tube

$K_6(x, \phi t)$ is a function describing the variation of irradiation growth due to variation of microstructure along the tube length as a function of fluence

C_1^d, C_2^d are the anisotropy factors due to texture for in-reactor thermal creep in a given direction d for stress exponents of 1 and 2, respectively.

$C_4^d(x)$, $C_6^d(x)$ are anisotropy factors due to texture for irradiation creep and growth, respectively, in a given direction d at position x along the tube length

$Q_1, Q_2, Q_3, Q_4, Q_6, K_5$ are activation temperatures and constant, respectively

σ_1, σ_2 are the effective stresses for thermal creep and stress exponents *n* of 1 and 2, MPa

$\sigma(x)$ is the effective stress for irradiation creep, MPa

T is temperature, *K*

ϕ is fast flux, $n/m^2/s$ (E>1 MeV)

t is the irradiation time, *s*

The equivalent stresses σ_1, σ_2 and $\sigma(x)$ are related to the radial, axial and transverse stress σ_r, σ_a and σ_t, respectively, by means of the Hill's anisotropy constants:

$$\sigma_i = [F_i(\sigma_a - \sigma_t)^2 + G_i(\sigma_t - \sigma_r)^2 + H_i(\sigma_r - \sigma_a)^2]^{1/2} \quad (3.5)$$

The subscript *i* stands for 1, 2 or $\sigma_i = \sigma(x)$ in the case of irradiation creep. The Hill's anisotropy constants for irradiation creep depend on the distance, *x*, from the back end of the tubes, and for a 6m tube this dependence is given by:

$$\begin{aligned} F(x) &= F^b + (F^f - F^b)\, x/6 \\ G(x) &= G^b + (G^f - G^b)\, x/6 \\ H(x) &= 1.5 - F(x) - G(x) \end{aligned} \tag{3.6}$$

where F^f, F^b, G^f and G^b are the values of Hill's anisotropy constants *F* and *G* at the front and back end of the tube. The method used to obtain the values of the Hill's anisotropy coefficients for irradiation creep is described in detail in (Christodoulou et al., 1996). These are average values derived from the crystallographic textures of power reactor PTs using the self-consistent polycrystalline model, SELFPOLY (Tomé et al., 1993), based on single crystal creep compliances. The eigenvalues of the single crystal creep compliance tensor describing pyramidal, prismatic and basal climb-assisted glide of dislocations in PT materials during in-reactor deformation were derived in (Christodoulou et al., 1993) and they are given in (Christodoulou et al., 1996). In (Christodoulou et al., 1993) experimental data from internally pressurised capsules, stress relaxation specimens and data from the Pickering NGS were used to derive the eigenvalues of the single crystal creep compliance tensor.

The anisotropy factors due to texture for in-reactor irradiation or thermal creep are given by:

$$\begin{aligned} C_i^r &= [H_i(\sigma_r - \sigma_a) - G_i(\sigma_t - \sigma_r)]/\sigma_i \\ C_i^t &= [G_i(\sigma_t - \sigma_r) - F_i(\sigma_a - \sigma_t)]/\sigma_i \\ C_i^a &= [F_i(\sigma_a - \sigma_t) - H_i(\sigma_r - \sigma_a)]/\sigma_i \end{aligned} \tag{3.7}$$

where i = 1, 2 or (x). The end-to-end effect of irradiation creep and irradiation growth along the length of the tube is described using the coefficients given by:

$$K_4(x) = K_{41} + K_{42}x$$
$$K_6(x, \phi t) = (K_{61} + K_{62}x)(1 + C/B\,[\phi t]) \tag{3.8}$$

where the parameters K_{41} and K_{42} are derived from experimental tests and, K_{61} and K_{62} are constants derived from the average end-to-end variation in grain thickness and from a theoretical model for the effect of grain thickness on growth (Fidleris, 1988). The constants C and B are related to the dependence of growth rate on fluence.

The growth anisotropy factors are given by

$$C_6^a(x) = G_a^b + \left(G_a^f - G_a^b\right) x/6$$
$$C_6^t(x) = G_t^b + \left(G_t^f - G_t^b\right) x/6 \tag{3.9}$$
$$C_6^r(x) = -C_6^a(x) - C_6^t(x)$$

Here G_a^b, G_a^f, G_t^b and G_t^f are anisotropy parameters derived from polycrystalline irradiation growth data from Osiris (R. G. Fleck et al., 1994). The single crystal growth strain rate tensors are deconvoluted from the polycrystalline data using SELFPOLY and the single crystal creep compliance coefficients mentioned above. SELFPOLY is then used to calculate K_g, G_a^b, G_a^f, G_t^b and G_t^f. The temperature dependence of growth represented by Q (~3000 K) is derived from the growth data from Osiris.

Once the growth and thermal creep parameters are established, the irradiation creep rates can be extracted from the power reactor data (in this case data from the pressure tubes in Pickering A

were used to obtain biaxial data comprising only irradiation creep). Values of K_c, Q_4 (~9900 K) and K_5 (1.1×10^{-7}) could then be derived.

3.2.3.3 Calandria Tube Creep Deformation Equation

The deformation equation describing the in-reactor deformation of Zircaloy-2 CTs operating at moderator temperature and stresses (e.g., ~340 K and axial stresses in the range of -10 to +40 MPa) was proposed by Fidleris in (Fidleris et al., 1985). The CTs are exposed to fast neutron fluxes E > 1 MeV of ~77% of the flux that the PTs experience. From creep, stress relaxation and irradiation growth experiments, the total in-reactor creep rate of CT material can be expressed as:

$$\dot{\varepsilon}_d^c = \dot{\varepsilon}_d^{ic} + \dot{\varepsilon}^{ig} \tag{3.10}$$

where $\dot{\varepsilon}$ is strain rate, subscript d indicates the direction (axial, transverse and radial) and superscripts $c,\ ic$ and ig indicate total creep, irradiation creep and irradiation growth, respectively. The irradiation creep rate is given as:

$$\dot{\varepsilon}_d^c = K_c C_d \sigma \phi \tag{3.11}$$

The creep constant K_c is given by $K_c = K_1 e^{-B\phi t} + K_2$, where K_1 and K_2 are material constants for transient and steady-state creep in units (n .m^{-2}.s^{-1}× MPa × h)$^{-1}$, ϕ is fast flux, $n/m^2/s$ (E > 1 MeV), C_d is the creep anisotropy factor in direction *d* given in terms of Hill's constants *F*, *G*, and *H*, as

$$\begin{aligned} C_r &= [H(\sigma_r - \sigma_a) - G(\sigma_t - \sigma_r)]/\sigma \\ C_t &= [G(\sigma_t - \sigma_r) - F(\sigma_a - \sigma_t)]/\sigma \\ C_a &= [F(\sigma_a - \sigma_t) - H(\sigma_r - \sigma_a)]/\sigma \end{aligned} \tag{3.12}$$

Here σ_r, σ_t and σ_a are the radial, transverse and axial components of the applied stress tensor (MPa) and σ is the effective stress, given by

$$\sigma = [F(\sigma_a - \sigma_t)^2 + G(\sigma_t - \sigma_r)^2 + H(\sigma_r - \sigma_a)^2]^{1/2} \quad (3.13)$$

The growth deformation rate is given by:

$$\dot{\varepsilon}^{ig} = \left(G_1 e^{-B\phi t} + G_2\right)\phi \quad (3.14)$$

where B is the transient decay constant (n .m^{-2}.s^{-1}×h)$^{-1}$, and G_1 and G_2 are material constants for transient and steady-state growth, (n .m^{-2}.s^{-1}×h)$^{-1}$. The exponential term ($B\phi t$) refers to the integrated fast neutron fluence up to the given time. The material parameters depend on microstructural factors, namely, K_1, K_2 and B on the crystallographic texture and dislocation density, G_1 and G_2 on residual stresses as well as texture and dislocation density and the Hill's constants on texture. Derivation of the values of these parameters for the different types of CTs used in CANDU reactors were derived by fitting these expressions to the measurements of gross sag from these units.

The creep parameters were based on the results from stress relaxation tests and the observation that the creep rate depends on the dislocation density by the relationship $\dot{\varepsilon}^c \propto \rho^n$ where n is ~0.4. Moreover, the dependence of the Hill's coefficients on crystallographic texture was analysed by means of self-consistent model that relates the creep behaviour of a polycrystal to that of single crystals. This is achieved by taking into account the crystallographic texture, dislocation density, grain shape and the intergranular stresses generated due to the crystallographic anisotropy (Christodoulou et al., 1993). Three independent creep compliances describing the behaviour of polycrystalline samples were obtained from creep tests on a reference material. Subsequently,

these polycrystalline creep compliances were used to derive the single crystal creep compliances that are consistent with the polycrystalline behaviour of the reference material. Once this step was carried out, the single crystal creep compliances were used to calculate the polycrystalline creep compliances for the remaining materials. It should be noted that the self-consistent model was used in two different ways. Firstly, it was used to establish the values of single creep compliances that are consistent with measured values from a reference material and then used in the opposite direction by employing these single crystal values to calculate the polycrystal creep compliance of other materials. It was shown that the predicted polycrystalline creep compliances agreed well with the measured values. The observed behaviour was consistent with a climb-assisted glide mechanism in which the creep strain is accommodated mainly by prismatic slip with smaller contributions from basal and pyramidal slip systems.

3.3 Implementation of PT and CT material models in ABAQUS

Along with the FC geometry, loading and boundary conditions, the material response to the fast neutron flux, applied pressure and temperature has to be properly modelled using the respective material deformation models. ABAQUS has a built-in library of phenomenological models that describe the deformation of many common materials, but it does not include models of specific materials that deform in an anisotropic fashion such as the in-reactor creep of Zr alloys. However, ABAQUS allows the incorporation of code describing a user-defined deformation model as a user defined subroutine called UMAT (ABAQUS). The UMAT is coded in FORTRAN programming language, and it describes the deformation model of each of the materials involved in the calculation. An elastic-viscoplastic analysis is used to model material response due to elastic

deformation and inelastic deformation due to creep of PT and CT. The anisotropic material behaviour was accounted for by using a linear elastic orthotropic model, and the creep equations of both the PT and CT were coded in the UMAT to simulate both the elastic and creep material responses. An explicit integration scheme was then used to solve the rate form of the deformation equation of PT and CT.

3.3.1 Explicit Integration Scheme

In addition to coding the material deformation models in UMAT, the user is also required to program a time-integration scheme for solving the rate form of those models. The goal is to compute the updated strain and stress at the end of each time increment. These updated values are then used in the equilibrium equations to solve for the element nodal displacements. An explicit time-integration scheme was used, and the stability condition was satisfied by taking appropriate smaller time steps. The implementation of this scheme in UMAT is as follows:

The classical additive decomposition of strain approach similar to that used in metal plasticity problems was used, where the total strain increment is expressed as the sum of the elastic strain increment and of the plastic strain increment. As the problem at hand experiences creep deformations, using the classical additive decomposition of strain approach, the total strain increment is expressed as the sum of the elastic strain increment and of the creep strain increment:

$$\Delta\varepsilon_d^T = \Delta\varepsilon_d^e + \Delta\varepsilon_d^c \tag{3.15}$$

where $\Delta\varepsilon$ is the strain increment, subscript d indicates the direction (axial, transverse and radial) and superscripts T, e and c indicate total, elastic and creep.

For each time increment, Δt, (note that the unit of time increment in this problem is in equivalent full power hours, EFPH) the creep rate was computed using Equation (3.1) for the PT and Equation (3.10) for the CT. The creep strain increment for a particular time increment can be then computed as:

$$\Delta\varepsilon_d^c = \dot{\varepsilon}_d^c \, \Delta t \tag{3.16}$$

Knowing the total strain increment, the elastic strain increment and stress increments can be computed as:

$$\Delta\varepsilon_d^e = \Delta\varepsilon_d^T - \Delta\varepsilon_d^c \tag{3.17}$$

$$\Delta\sigma_d = D \, \Delta\varepsilon_d^e \tag{3.18}$$

where D is the orthotropic linear elastic matrix in plane stress condition.

Suppose the stress tensor at the start of a time step t_n was $(\sigma_d)_{t_n}$, the updated stress $(\sigma_d)_{t_n+\Delta t}$ after the time increment Δt can be computed as:

$$(\sigma_d)_{t_n+\Delta t} = (\sigma_d)_{t_n} + \Delta\sigma_d \tag{3.19}$$

3.3.2 Computational Procedure in ABAQUS using the UMAT

For the specific problem at hand, the end objective of FEA is to compute the nodal displacements. In the process of solving for the displacements, the finite element formulation in ABAQUS (or any other finite element package) requires the computation of stress tensor at the Gauss integral points using the respective constitutive models, which are provided here by the UMAT. The UMAT includes the elastic and the in-reactor creep deformation equations of both the PT and CT.

The FC creep deformation analysis is completed in two steps. The first step (Step 1) involves the incremental application of internal pressure and all the gravitational loads using the appropriate material density of each FC component, which deforms the FC elastically (This step is described in detail for 1D and 3D FEM models in later sections). The second step (Step 2) involves the calculation of the deformation increment due to in-reactor creep and growth of the FC, which is the permanent component of the total deformation. The flowchart of the UMAT subroutine for in-reactor deformation of FCs is shown in Figure 3.5 and is briefly described here:

1) At the start of a time step t_n, the ABAQUS main program provides the UMAT with the stress tensor σ_{t_n}, the total strain, the total strain increment, the time increment Δt, and other problem specific information such as temperature and flux in this example.
2) After entering the UMAT subroutine, the UMAT code first checks for the material name ('MAT1' for Zr-2.5Nb material of PT and 'MAT2' for Zircaloy-2 material of CT) and then for the step number (1 or 2). Based on these inputs, the corresponding models (i.e., elastic or creep) in the UMAT code are used to compute the strain increment.
3) An explicit integration scheme is used to update the stress at the end of each time increment as $(\sigma_d)_{t_n+\Delta t} = (\sigma_d)_{t_n} + \Delta\sigma_d$.
4) The updated stress tensor is passed to ABAQUS main code for solving for the nodal displacements.

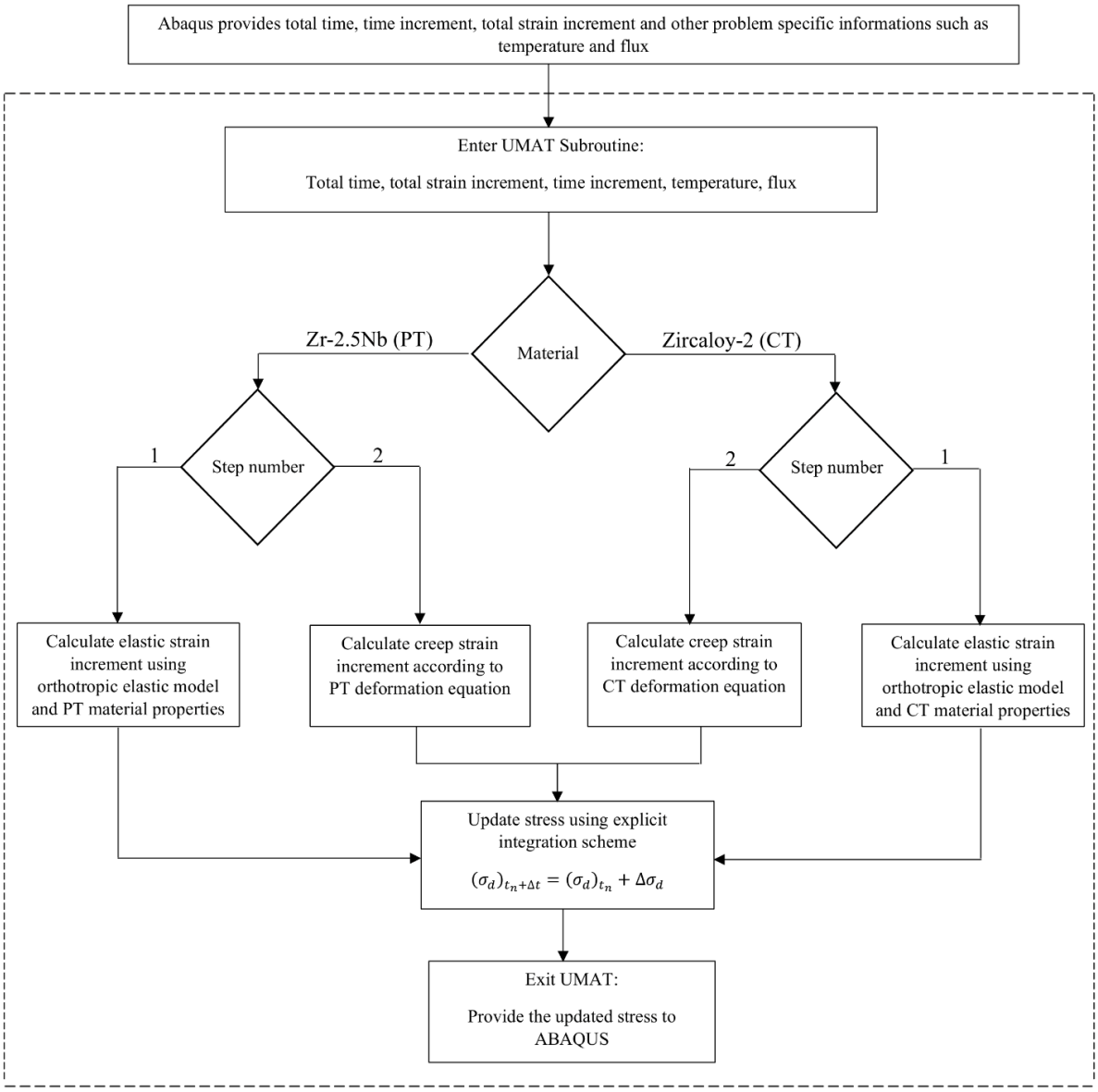

Figure 3.5: Flowchart of UMAT subroutine implementation for FC deformation modelling

3.4 1D Finite Element Analysis of a CANDU FC

3.4.1 Modelling details

The main aim of developing a 1D beam model is to make a model as close as the FE beam model currently used by the nuclear industry, called as CDEPTH (Sauvé et al., 1989). The developed 1D beam model can be then used as a suitable replacement to the beam model currently used by the nuclear industry and to analyze the prediction accuracy of this model. Figure 3.6 shows the CDEPTH FE beam model of a FC taken from Sauvé et al. (Sauvé et al., 1989). These are proprietary FE codes and are hence unavailable to other investigators.

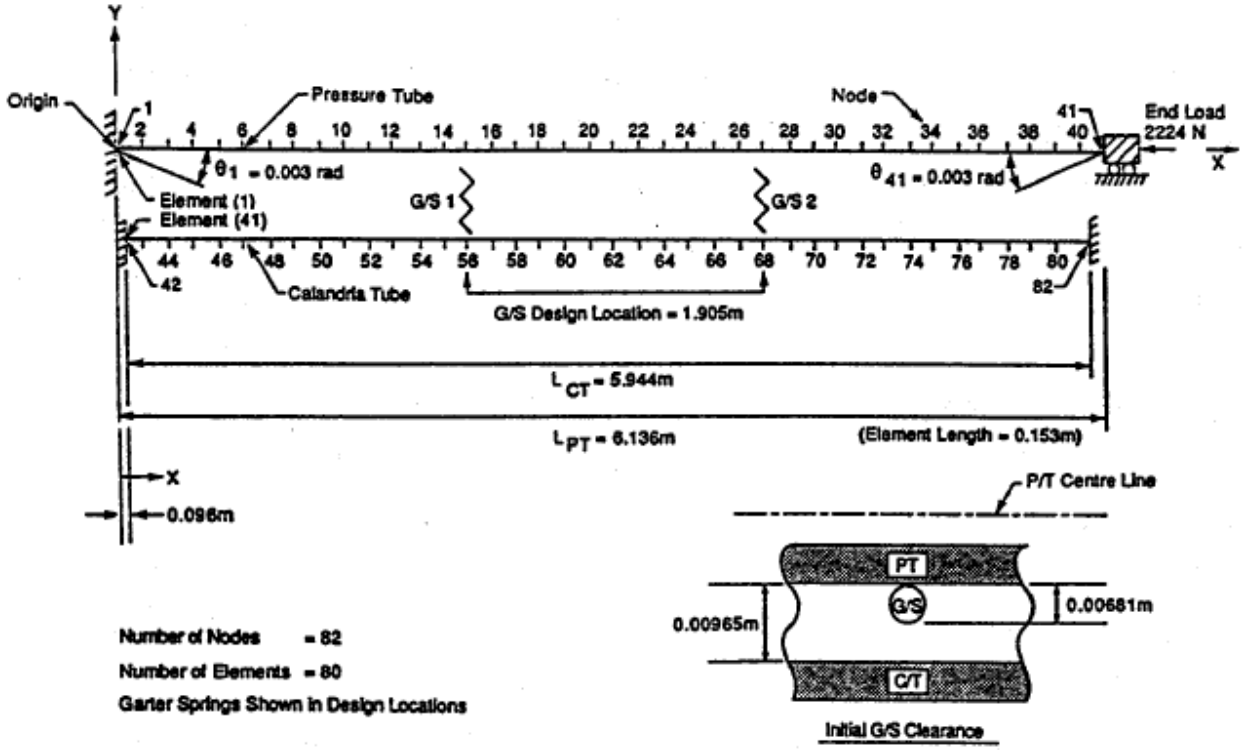

Figure 3.6: The CDEPTH FE beam model of a fuel channel (Sauvé et al., 1989)

Therefore, in this section, a similar 1D FEM beam model of the CANDU FC was developed in ABAQUS software using the geometric details given in section 3.2.2, as shown in Figure 3.7. PIPE31 element was chosen from the Abaqus finite element package element library to model both the PT and CT. A PIPE31 element is a 2-noded linear Timoshenko beam element capable of modeling the combined effect of axial and bending deformation and is best suited to model thick or thin-walled hollow circular sections. Apart from generating axial and bending stresses, the pipe elements also generate the hoop stresses due to internal pressure. A total of 239 pipe elements were used to model the fuel channel assembly of which 121 elements were used to model the PT and 118 elements to model the CT. The contact between the garter springs and the CT (GS-CT contact) were modeled using ITT31 elements, which are best suited to use with pipe elements and to model tube-to-tube contact. They are into contact when the GS-CT gap is reduced to zero. The initial PT-CT gap is taken as 7.878 mm, which is a nominal value.

Figure 3.7 shows the loading conditions and boundary conditions used in the analysis.

The following loading conditions are used:

a) End slopes of nominal values are applied to both ends of the PT
b) An axial force, $F = -2220N$ applied at the inlet of the PT
c) Uniformly distributed loads of $q_{PT} = -0.605\ {}^{N}/_{mm}$ and $q_{CT} = 0.109\ {}^{N}/_{mm}$ applied on the PT and CT, respectively. q_{PT} includes weight of PT, fuel bundles and D2O; whereas q_{CT} includes weight of CT and buoyancy force.
d) Temperature and pressure profiles are applied on the PT (Figure 3.3).
e) Fast neutron flux profiles applied on the PT (Figure 3.3).
f) Fast neutron flux profile applied on the CT is assumed to be 77% of the PT.

The boundary conditions are:

a) The left end of PT is fixed (outlet end) whereas the right end (inlet end) of PT is axially free.

b) Both ends of the CT are fixed.

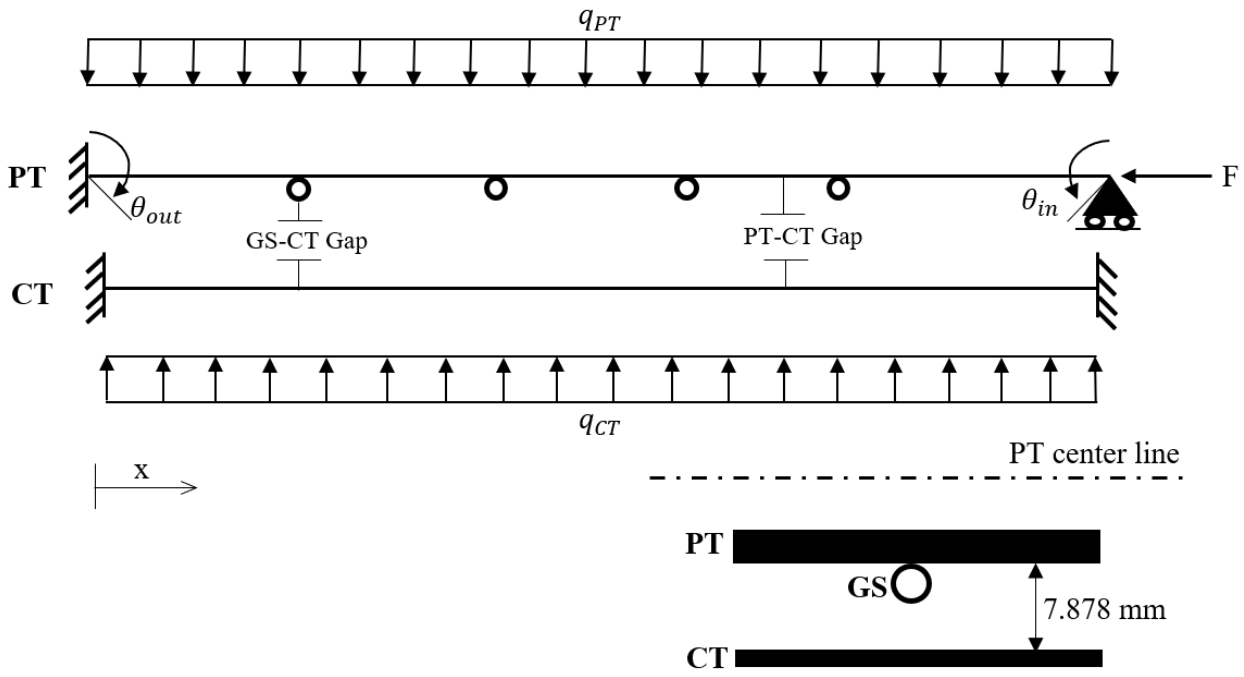

Figure 3.7: A structural beam model representing the FC used in the analysis

Using the 1D FE model and the corresponding UMAT, the analysis was performed up to 220 kEFPH (thousand effective full power hours), which is the design life of a CANDU reactor.

3.4.2 Output of 1D FEA

A typical output of the 1D FEA of the FC is the axial elongation of the PT and the overall sag (or total vertical displacement) of PT and CT at any specified time.

3.4.2.1 Axial elongation

The axial elongation of PT obtained from 1D FEA is plotted as a function of the neutron fluence in Figure 3.8, along with the data obtained from Figure 2.2.1 in (Holt, 2008). The slight bend in the predicted elongation is because the elongation rate increases gradually with time as was shown in (Christodoulou et al., 1996; Holt, 2008). From Figure 3.8, it is also evident that the calculated elongation is approximately equal to the average of that observed from in-service measurements, thus validating the prediction capability of the model.

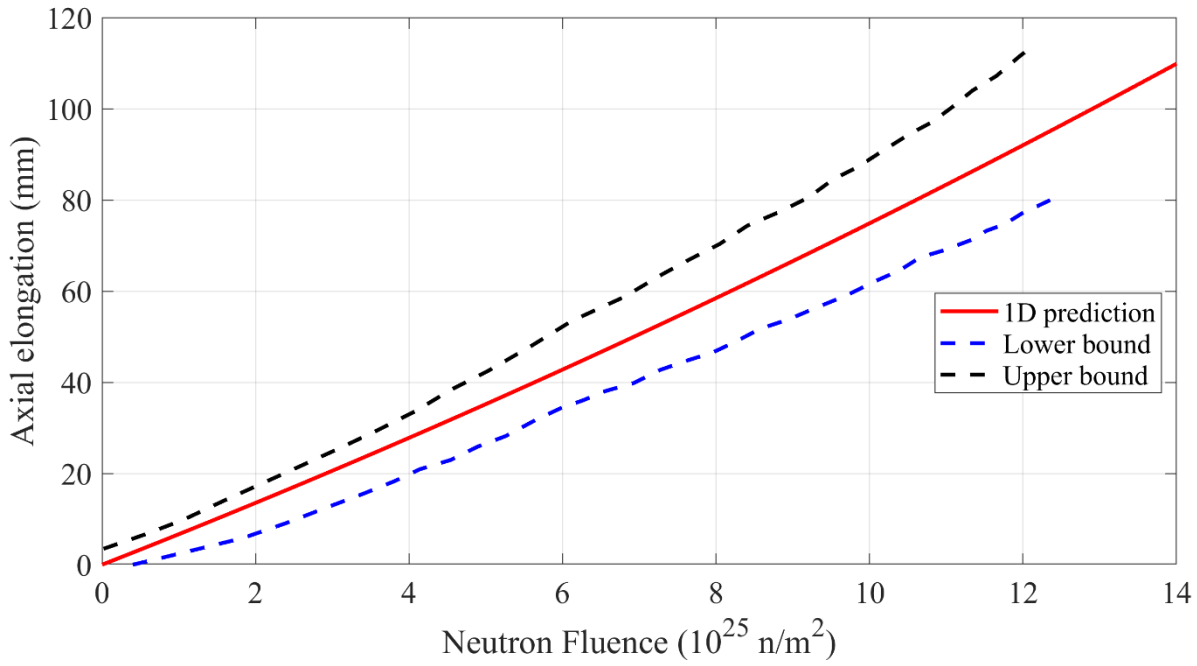

Figure 3.8: Predicted elongation as a function of fast neutron fluence using 1D FEA (averaged along the length of the PT) compared to experimental data from (Holt, 2008)

3.4.2.2 FC Sag

Figure 3.9 shows the PT sag profile, which continues to increase with time as expected. The maximum sag due to the application of gravitational loads is approximately 10 mm. The sag

continues to increase with reactor operating time, reaching a maximum of 56 mm by the FC end-of-life.

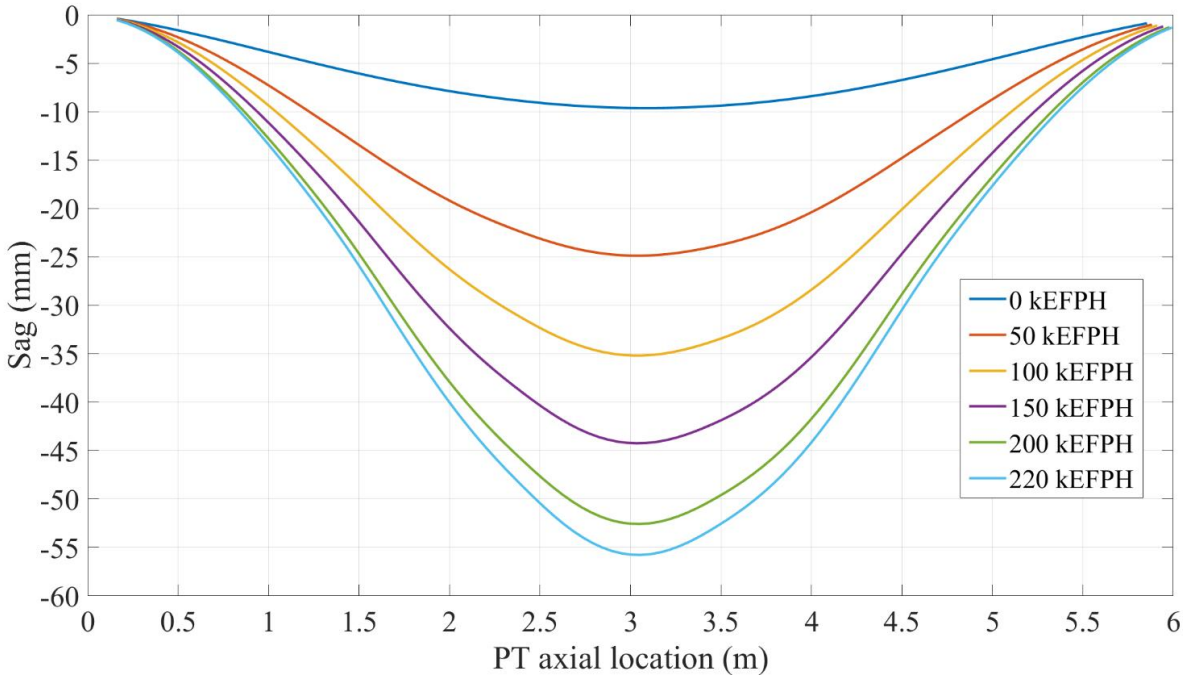

Figure 3.9: Predicted PT sag profiles at various points in time in the service life of the FC using 1D FEA (kEFPH = thousand equivalent full power hours)

3.4.2.3 PT-CT gap

The prediction of PT-CT gap is one of the main results obtained by using FEA for in-reactor deformation. The PT-CT gap along any axial location on the PT axis can be computed using the PT and CT sag profiles. Figure 3.10 shows the PT-CT gap profiles for various time points and as expected, the gap continues to reduce with time. The initial locations of the four garter springs are indicated by black down arrows shown at the top of this figure. The spans S1-S5 are also shown. A red arrow at the right side of the figure shows the garter spring thickness, which is the PT-CT gap at the contact location of the garter springs with the CT.

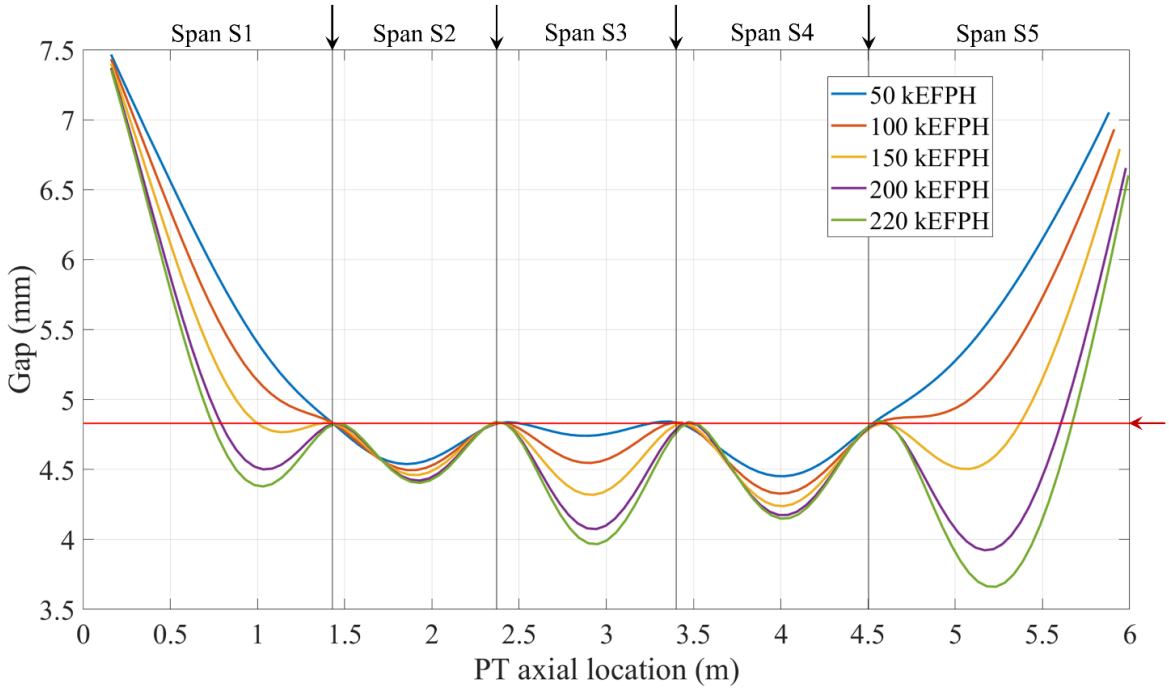

Figure 3.10: Predicted PT-CT gap profiles at various time points in the service life of the FC using 1D FEA (PT back end placed at the outlet)

3.4.3 Limitations of 1D FEA

The 1D FE model can predict the axial elongation with good accuracy. However, the main limitation of 1D beam models is its incapability in simulating diametral expansion and wall thinning of the PT. Apart from sag, the diametral expansion also influences the PT-CT gap significantly. Therefore, a beam model is incapable of predicting the diametral expansion, which in turn introduces error in PT-CT gap predictions. These limitations indicate the need of a 3D FE model for predicting all the life-limiting deformations in a CANDU FC.

3.5 3D Finite Element Analysis of a CANDU FC

3.5.1 Modelling Details

The 3D FEM model of the CANDU FC was developed in ABAQUS software using the geometric details given in section 3.2.2. To accurately model the deformation behaviour of the PT and CT, the SC8R continuum shell element was chosen as a suitable element type from the ABAQUS element library. It is an 8-noded hexahedron continuum shell element, which considers the topology of the element as continuum (similar to continuum solid elements), but its kinematic and constitutive behaviors are similar to conventional shell elements. Therefore, this element type has the following advantages:

(1) The bending behaviour (sag) of both the PT and CT can be accurately modelled using a smaller number of elements that reduce the computational cost,

(2) the model takes into account the 3D nature of the problem by considering the wall thickness of both the PT and CT (i.e., the presence of nodes at both inner and outer diameter) thus significantly increasing the accuracy of the gap and contact predictions, which was otherwise not possible using a conventional shell element, and

(3) the model allows for the change in the thickness of the finite element due to Poisson effect, which significantly improves the prediction of diametral expansion and gap along the length of the PT.

Conventional shell elements were used to model garter springs as rigid elements. A short section of the meshed PT, CT and a garter spring is shown in Figure 3.11.

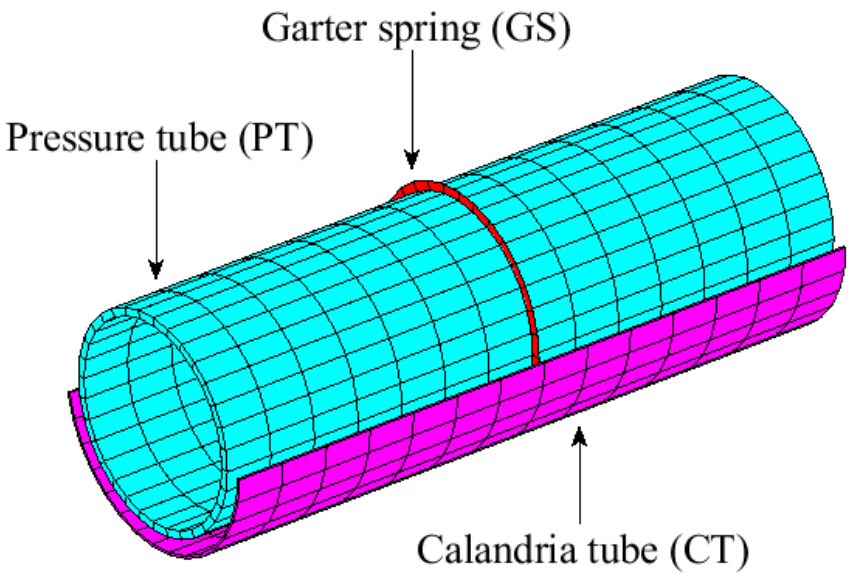

Figure 3.11: A section of the 3D FEM model representing the PT, CT and garter spring

Convergence tests were conducted to determine the optimal size of the finite elements. For this purpose, convergence of maximum sag of PT and CT subjected to gravitational loads was used. Figure 3.12 and Figure 3.13 show the results of a monotone convergence with increased mesh size used for modelling the PT and the CT, respectively. The PT is modelled with 7808 finite elements with a maximum aspect ratio of 2.7, whereas the CT is modelled with 7680 finite elements with a maximum aspect ratio of 2.

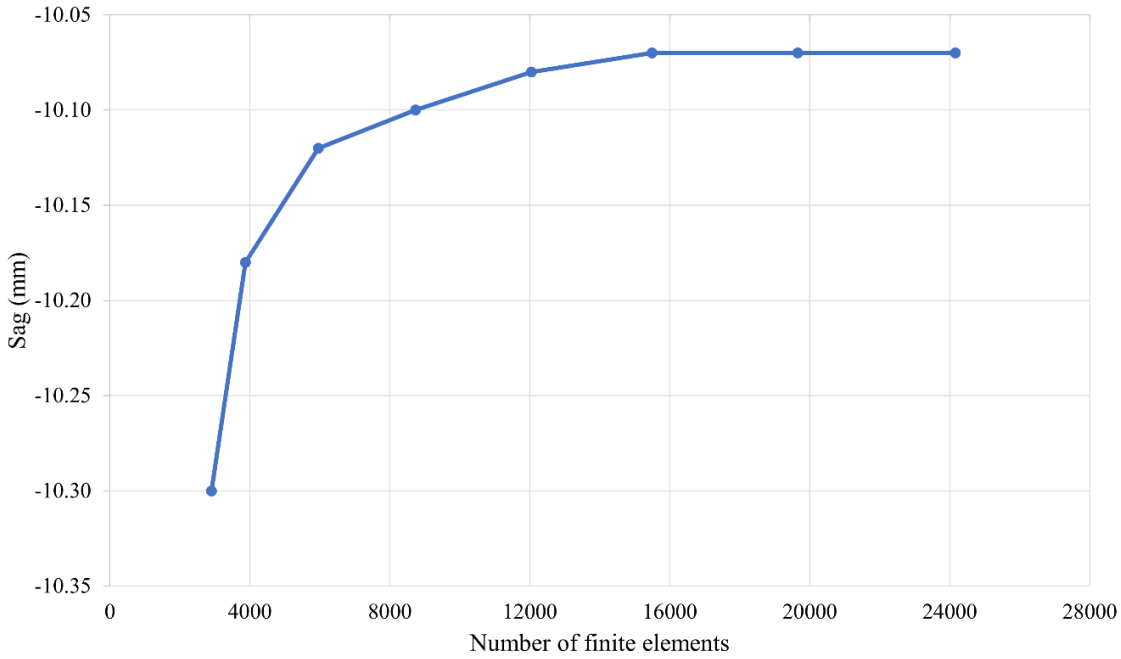

Figure 3.12: Convergence test result for finding the optimum number of elements for the modelling of a PT

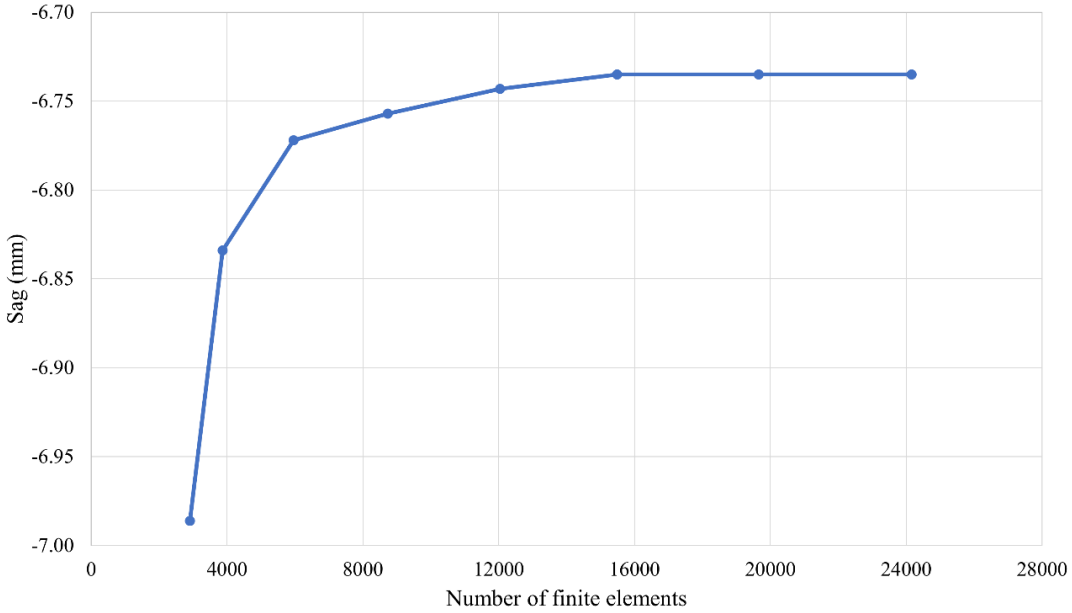

Figure 3.13: Convergence test result for finding the optimum number of elements for the modelling of a CT

The following loading conditions were used in the analysis:

a) end slopes of the PT (the end-slopes were incorporated in the model by assigning a rigid body reference node at the centre of ends of the PT. ABAQUS allows these rigid nodes to be pinned with the nodes at the ends of the PT. The end-slopes were then applied by assigning respective end-slope values to a rotational degree of freedom in the downward direction to these nodes leading to a tilt at the ends.),

b) a compressive force applied axially at the inlet end of the PT, $F = -2200$ N resulting from the out-of-core hardware that appears to vary with time from tensile to compressive,

c) gravitational loads were applied by assigning appropriate densities to the PT material using the PT weight (~56 kg), the weight of fuel string (300kg) and the weight of D_2O (~ 4.6 kg). Similarly, an appropriate material density was applied to the CT material to account for the weight of the CT and the buoyancy force acting on the CT, and

d) fast neutron flux (E > 1 MeV), pressure and temperature profiles applied on the PT as shown in Figure 3.3. The fast neutron flux profile applied on the CT is assumed to be 77% of the fast neutron flux profile applied on the PT. This value is based on the analysis of properties of a CT removed from Pickering Unit 2 after 86,880 EFPH and an accumulated fast neutron fluence of 6×10^{25} n/m^2 (Ells et al., 1985). The PTs in Pickering Unit 2 were exposed to a maximum fast neutron flux of ~ 2.5×10^{17} n/m^2/s. Therefore, the accumulated fast neutron fluence of the PT would be 7.8×10^{25} n/m^2 and the ratio 6.0/7.8 ~ 0.77.

The boundary conditions are:

a) the right side of the PT (inlet end) is axially free, and

b) the left side of the PT (outlet end) is fixed in all directions

c) both ends of the CT are fixed in all directions

The following key assumptions were made in the 3D modelling:

- The principal axes of the tubes are coincident with the axes of anisotropy due to the observed in-reactor deformation.
- An orthotropic material in plane stress condition is considered.
- The deformation of garter springs was considered insignificant compared to the deformation of PT and CT (Previous studies show that the assumption of garter springs as rigid is valid (Leitch, 2004)).
- Tight-fitting garter springs
- The width of garter spring was considered insignificant

The contact between the CT and garter springs was modelled using the pressure-overclosure relation and a frictionless contact was assumed. This relation defines the amount of contact pressure generated in the normal direction for a certain amount of overclosure (or penetration). At the start of the analysis, the overclosure is zero since there is no contact between the garter springs and CT. With the application of gravitational loads and creep deformation, the PT starts to sag and applies a contact pressure on CT through the garter springs. The garter springs come into contact with CT at different time points and exert different pressure.

Using the developed 3D FE model and the corresponding UMAT, the analysis was performed up to 220 kEFPH.

3.5.2 3D Finite Element Analysis Output

This section deals with a detailed discussion of the FEA results of the in-reactor FC deformation analysis. The analysis is carried out in terms of axial elongation, diametral expansion, wall thinning and sag of both the PT and CT results. A typical deformed shape of the FC following 3D FEA is shown in Figure 3.14 along with reported logarithmic strain measure in circumferential direction. The sag results are further post-processed to obtain PT-CT gap. As was mentioned previously, five spans are defined in a FC configuration with four spacers. The span S1 is the outlet span defined between the outlet end and the first spacer; likewise, the span S5 is the inlet span defined between the fourth spacer and the inlet end. Spans S2 and S4 are internal spans, while S3 is the central span.

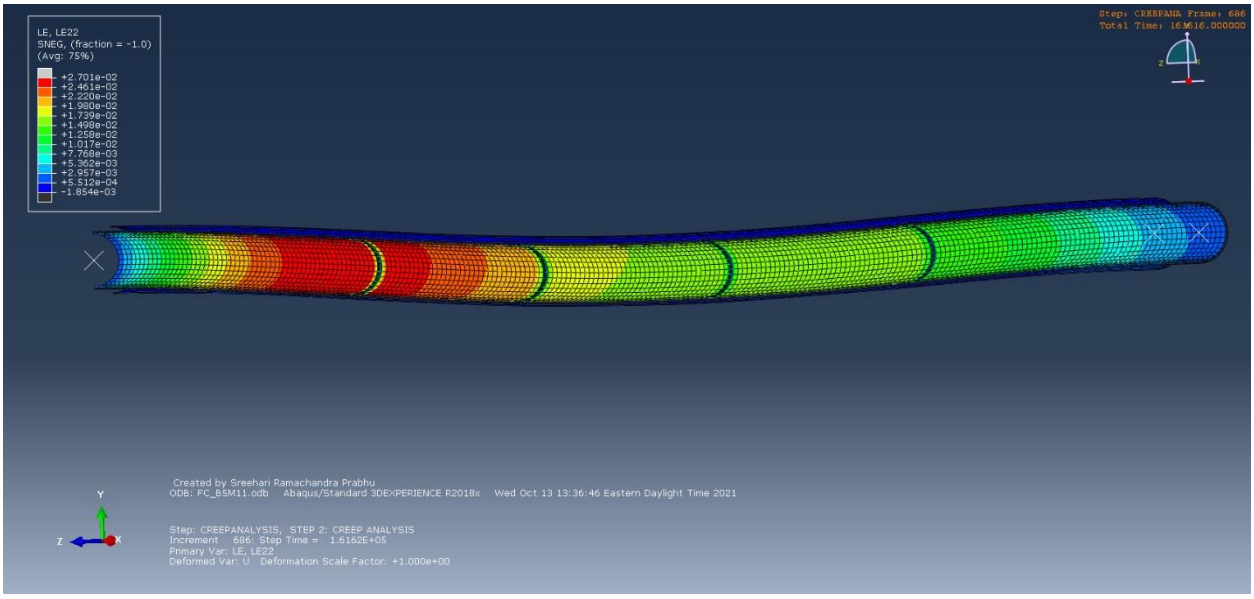

Figure 3.14: Deformed geometry of a FC following 3D FEA at 161615 kEFPH (The left end is the outlet end of PT)

3.5.2.1 Fuel Channel Sag

The prediction of PT and CT sag is one of the crucial outputs obtained from the FEA. The FC sag is the total vertical displacement of both tubes due to the initial gravitational loads and the in-reactor creep. The predicted sag profiles of PT and CT are shown in Figure 3.15 and Figure 3.16, respectively. Initially, the PT starts to sag due to gravitational loads. In time, the garter springs come into contact with the CT initiating the sag of the CT. Therefore, the PT sag is equal to CT sag plus the (Initial PT-CT gap – GS diameter) at the contact locations. Namely, PT sag will be greater than that of the CT, since the PT starts to sag before the CT. In the example here, the initial PT-CT gap is 7.878 mm, the GS diameter is 4.83 mm and their difference is 3.048 mm. As a result, at contact locations PT sag is equal to CT sag + 3.048. This can be verified in Figure 3.15 and Figure 3.16. With additional reactor operating time, the overall sag continues to increase due to in-reactor creep and growth.

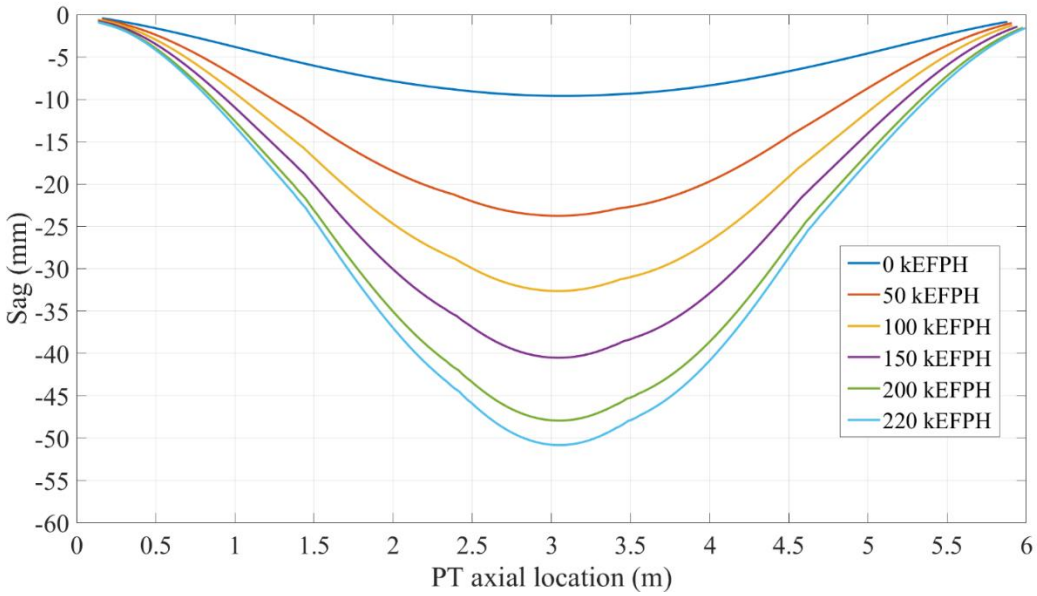

Figure 3.15: Predicted profiles of PT sag at various times in the operating life of the FC

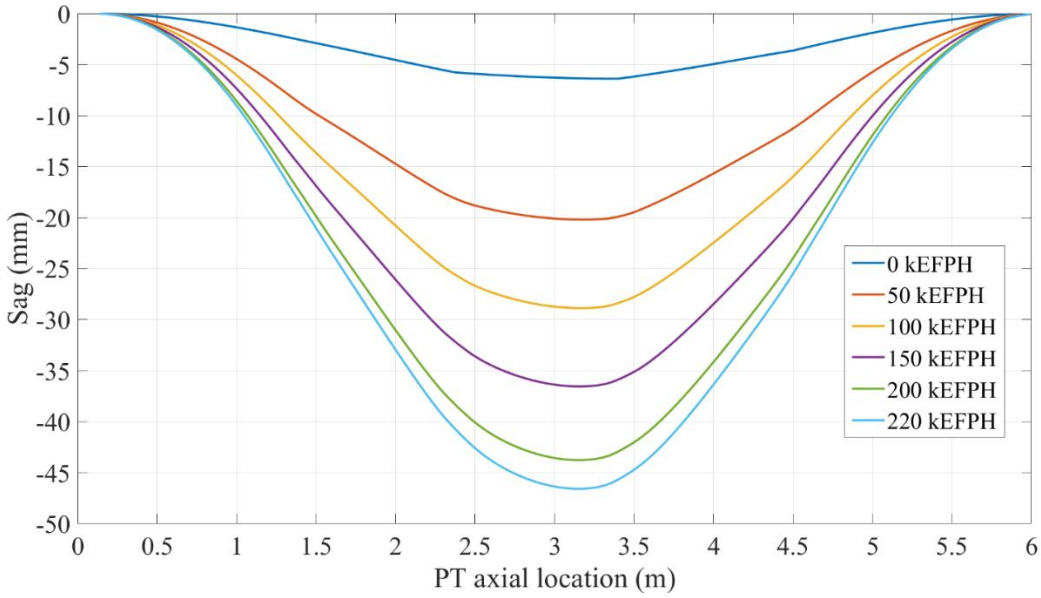

Figure 3.16: Predicted profiles of CT sag at various times in the operating life of the FC

3.5.2.2 Axial elongation of PT

The total strain rate and the strain rate contribution from individual deformation mechanisms can be extracted from the UMAT. Figure 3.17 shows the axial strain rate along the pressure tube computed at three different operating intervals. It is interesting to observe that the axial strain rate profile resembles the variation of the fast neutron flux experienced by the PT (Figure 3.3). The axial deformation rate varies along the PT length and increases gradually with reactor operating time. However, the total length of the PT at any given time (namely, the total axial strain) is the weighted sum of all the local axial creep rates along the length of the tube times the elapsed time. Note that the ripples at 4 different axial locations are due to the presence of the garter springs. The average value of the axial deformation rate at 50, 150 and 220 kEFPH can be calculated from these profiles and they are 1×10^{-7}, 1.17×10^{-7} and 1.3×10^{-7} /h, respectively. Given that 7 kEFPH is

approximately the number of full power hours in one calendar year, the axial rates mentioned above correspond to strain increments of 7×10^{-4}, 8.2×10^{-4} and 9.1×10^{-4}, respectively. In terms of axial elongation, these stain increments correspond to 4.3, 5 and 5.6 mm/year, namely values consistent with those that are observed in current CANDU units.

The contribution of the individual deformation mechanisms towards the total axial strain rate at 150 kEFPH is shown in Figure 3.18. As expected, the most significant contribution towards axial elongation is from irradiation creep, followed by irradiation growth, whereas there is a very small contribution from thermal creep.

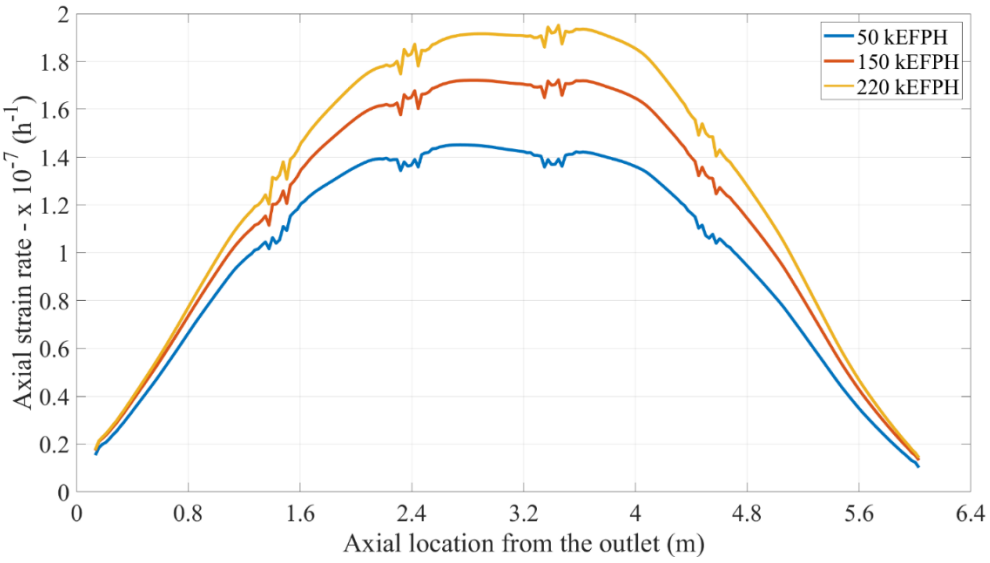

Figure 3.17: Predicted axial strain rates at three different operating intervals

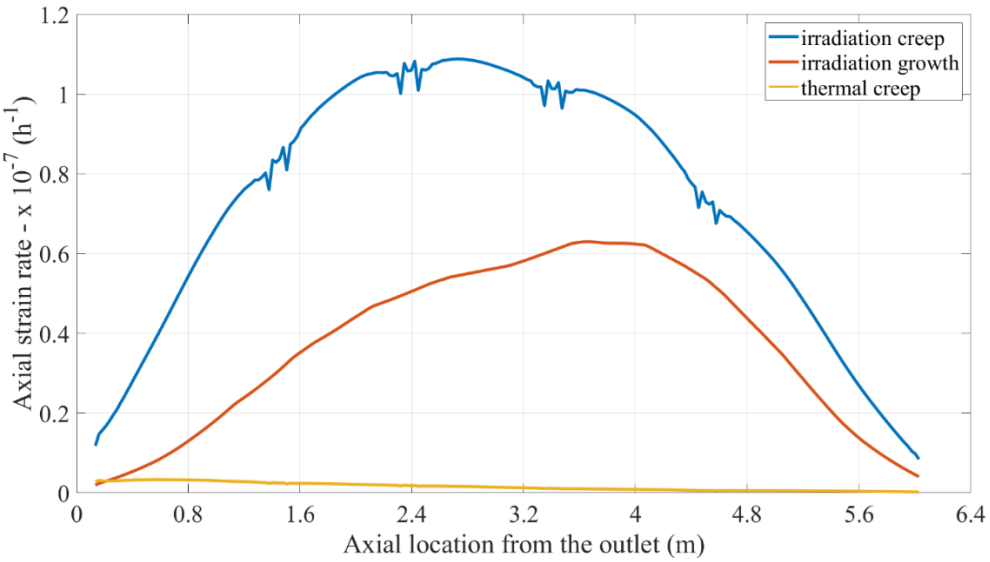

Figure 3.18: Contributions of each deformation mechanism towards the axial strain rate at 150 kEFPH

Figure 3.19 shows the comparison of the calculated axial elongation (solid red line) as a function of fast neutron fluence compared to the data (dotted lines) obtained from Fig. 2.2.1 in (Holt, 2008). The slight upward bend in the calculated elongation is because the elongation rate increases gradually with time as was shown in (Christodoulou et al., 1996; Holt, 2008; Holt & Wong, 2002). It is also evident that the calculated elongation is approximately equal to the average of the values observed from in-service measurements.

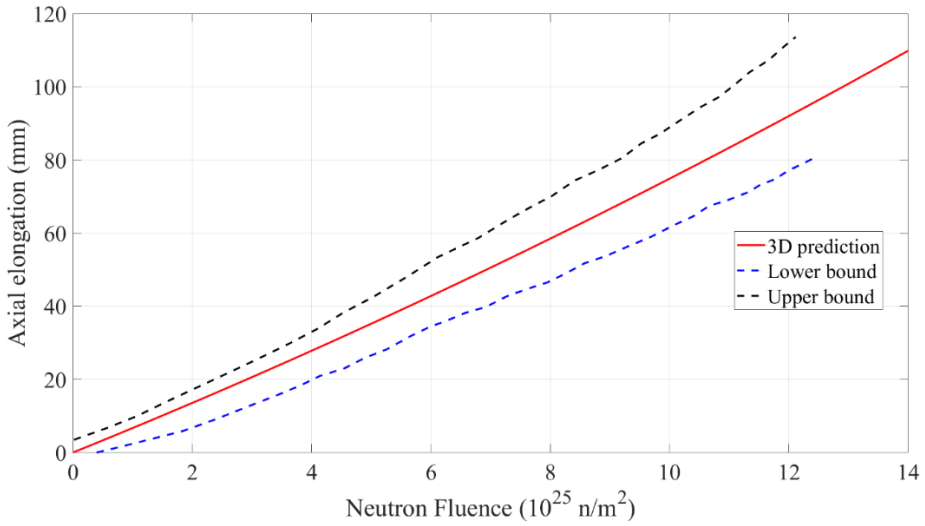

Figure 3.19: Calculated axial elongation compared to experimental data from (Holt, 2008)

3.5.2.3 Diametral Expansion of PTs

Diametral profiles of the PT at different time intervals are presented in Figure 3.20. The diameter exhibits a peak toward the outlet end, which is characteristic of tubes with their back end located at the outlet. The diameter of the PT tends to a nominal value (ID = 104.818 mm) at the ends of the tubes, as expected. The position of the four spacers is clearly evident in this figure. The diameter at a given axial location along the length of the PT increases linearly with time as is shown in Figure 3.21, which shows the variation of the diameter with time at five axial locations of the PT. These axial locations are approximately in the middle of each of the five spans and they are measured from the outlet end. The diametral deformation rate at each location is then determined as the slope of the best fit straight line as presented in Table 3.2. The calculated peak diametral rate is approximately 1.4×10^{-7} /h. This value compares well with (albeit somewhat lower than) the peak rate obtained from Figure 2.1.1 in (Holt, 2008) at 130 kEFPH, i.e. 1.5×10^{-7} /h.

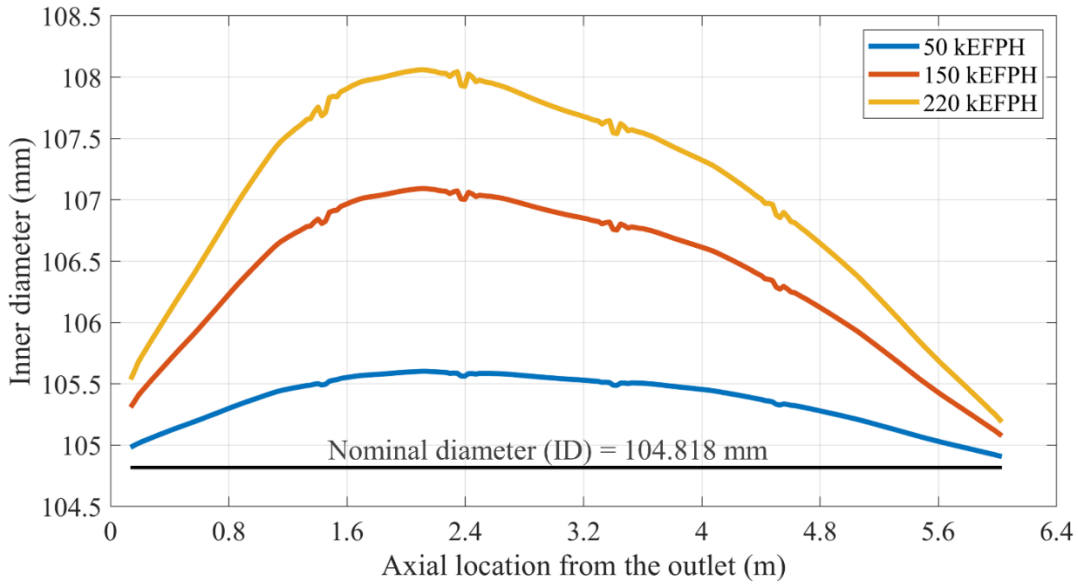

Figure 3.20: Predicted diametral PT profiles at different time intervals (the PT back end was placed at the outlet end)

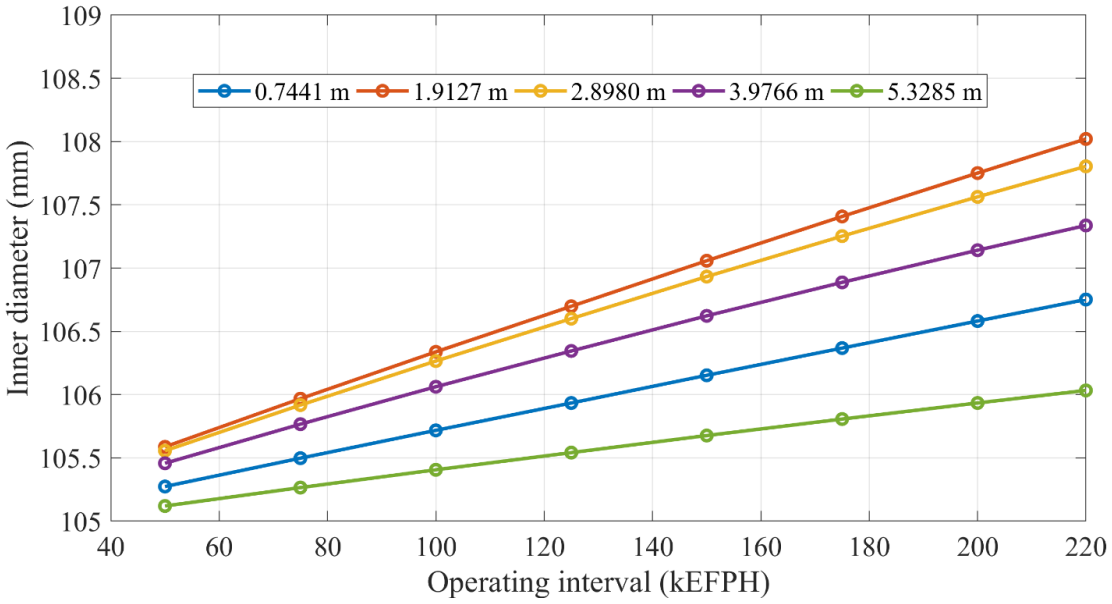

Figure 3.21: Predicted diametral expansion vs. time at five axial locations along the PT (the axial location is measured from the outlet end)

Table 3.2: Average diametral deformation rate calculated over the design life of a CANDU unit (220 kEFPH).

Axial location from the outlet end (m)	Diametral rate × 10^{-2} (mm/kEFPH)	Coefficient of correlation
0.74 (outlet span S1)	0.86	0.999954
1.93 (internal span S2)	1.45	0.999561
2.9 (central span S3)	1.3	0.998906
4.0 (internal span S4)	1.06	0.998001
5.3 (inlet span S5)	0.52	0.999236

The contribution of individual deformation mechanisms towards the total diametral strain rate at 150 kEFPH is shown in Figure 3.22. Irradiation creep has the most significant contribution to the diametral strain, while thermal creep has only a very small effect. Irradiation growth has a negative contribution to the diametral strain, which is beneficial because it reduces the peak diametral strain rate by about 13% (i.e., from about 1.6×10^{-7} /h to about 1.4×10^{-7} /h, see Figure 3.20 above).

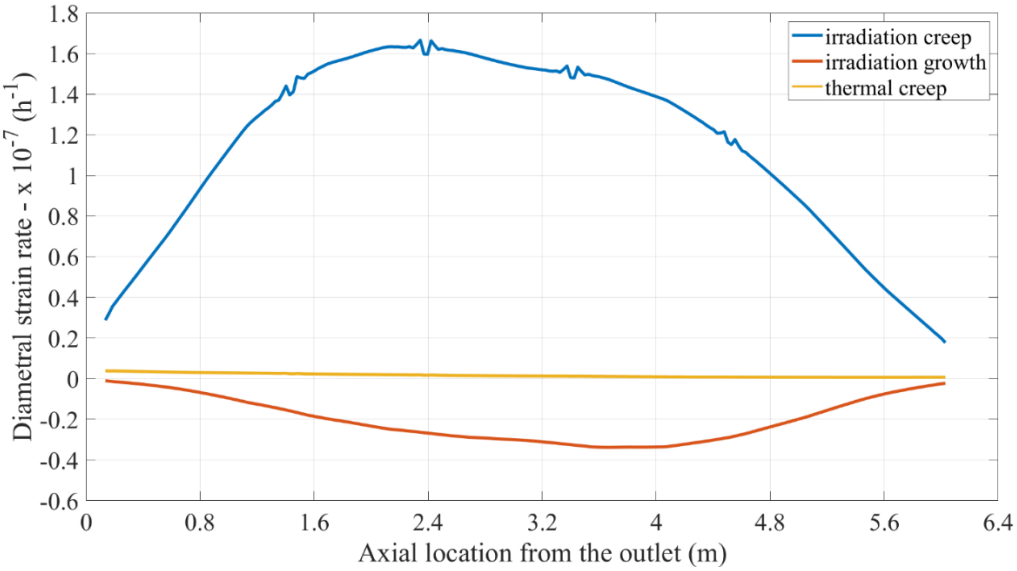

Figure 3.22: Contributions of each deformation mechanism to the diametral strain rate at 150 kEFPH

3.5.2.4 Wall Thinning of PTs

In-reactor deformation of FCs occurs at constant volume, namely the sum of strains in the three main PT directions adds to zero. Therefore, as the diametral expansion and axial elongation are positive, this results in a gradual decrease of the wall thickness with time, as shown in Figure 3.23. Note that the shape of wall thickness profiles appears to be the mirror image of the diametral profiles.

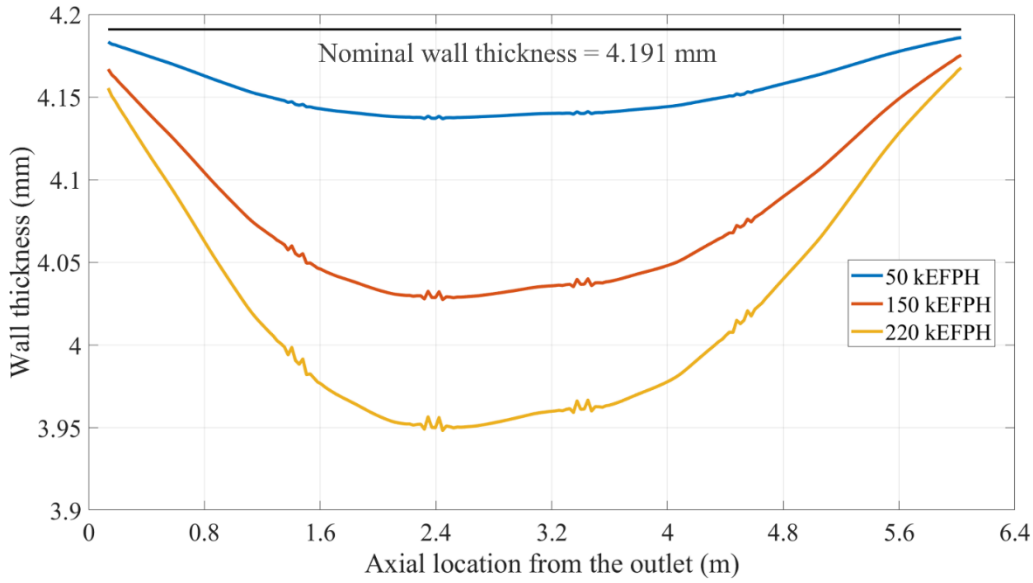

Figure 3.23: Predicted wall thickness profiles at various time intervals in the operating life of the FC (PT back end placed at the outlet)

Figure 3.24 shows the variation of wall thickness with time at five different axial locations along the PT. In general, the wall thickness shows a gradual non-linear temporal variation. The absolute wall thickness reduction rate increases slightly with time as shown in Figure 3.25 (note that the rate is negative). In general, the variation in rate is very close to linear. The apparent small increase in the absolute value of the thickness rate is due to the dependence of the irradiation growth rate on fast fluence. While the thickness rate exhibits this slight increase with fluence, the elongation rate exhibits a somewhat lower rate in the early stages of the operating life.

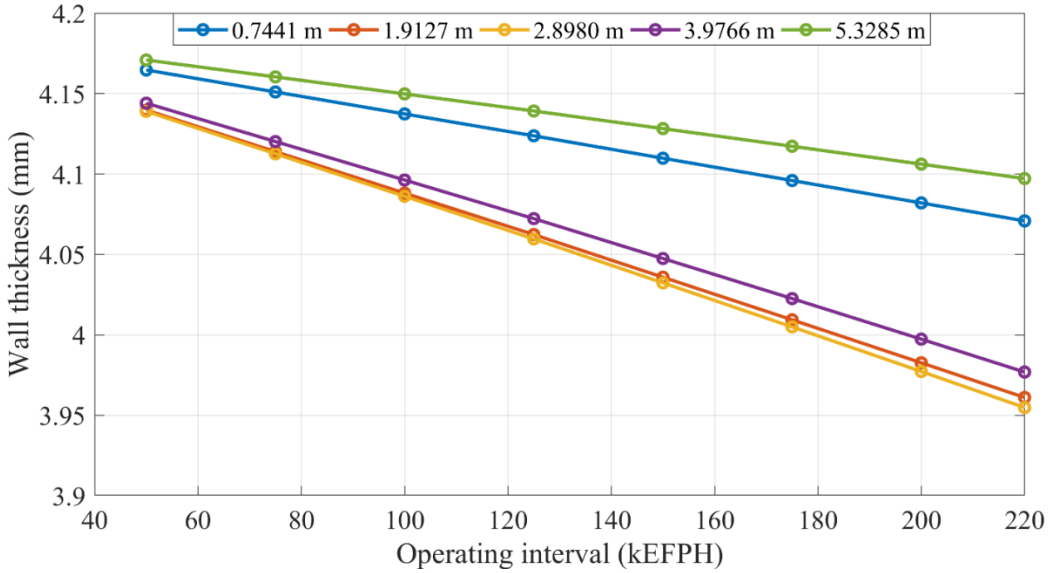

Figure 3.24: Predicted wall thickness vs. time at different axial locations along the pressure tube (axial locations measured from the outlet end)

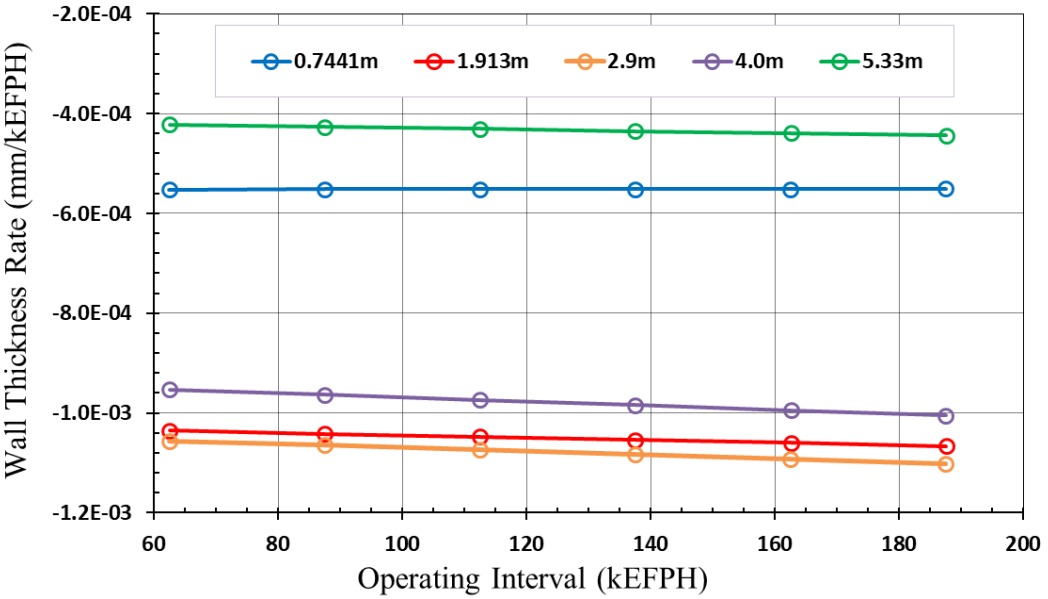

Figure 3.25: Calculated wall thickness rate vs. time at different axial locations along the pressure tube (axial locations measured from the outlet end)

3.5.2.5 PT-CT Gap

The prediction of PT-CT gap is one of the main results obtained by using FEA for in-reactor deformation. The PT-CT gap along any axial location on the PT axis can be computed using the PT and CT sag profiles. Accurate computation of the gap profile is made possible by taking into account the wall thickness of both PT and CT, the vertical displacement (sag) of outer nodes of PT and inner nodes of CT is used. The gap profiles at various reactor operating intervals are shown in Figure 3.26. It can be clearly seen that the gap is reducing over time as a result of the increasing PT sag. The red arrow on the right side of the figure shows the garter spring thickness, which is the PT-CT gap at the contact location of the garter springs with the CT. As the unit reaches its end-of-life time (i.e., times > 200 kEFPH), Span S5 (inlet span) turns out to be the most critical one since the gap is minimum in this region. The gap results can also be used for establishing the time to contact or time to reach a specific value of minimum gap for the purpose of deciding the optimum time for in-service inspections.

The profile of PT-CT gap from outlet to inlet is fairly asymmetric due to the following reasons: (1) the anisotropy in the mechanical properties of the Zr-2.5 Nb alloy, which varies from the back end to the front end, (2) an increment in the coolant temperature from inlet to outlet, (3) a decrease in the internal pressure from the inlet to the outlet, (4) the different lengths of the five spans, and (5) the different boundary conditions at the outlet and inlet ends, which influence the axial movement of the FC.

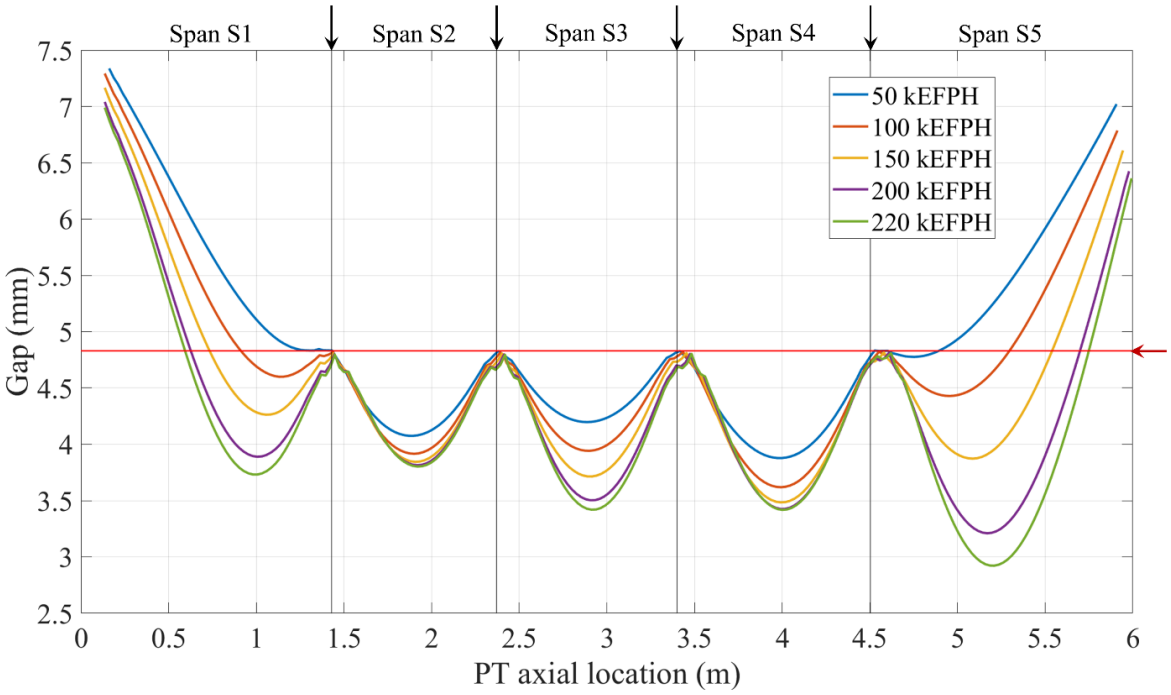

Figure 3.26: Predicted PT-CT gap profiles at various time intervals in the operating life of the FC (PT back end placed at the outlet)

3.5.3 3D FEA Results Based on Different FC Configurations

The example analyzed in the previous section was based on two criteria: 1) the outlet end of the PT is fixed, and inlet end is free, 2) the PT back end is placed at the outlet end. It must be clearly mentioned here that this arrangement of boundary conditions and PT orientation is not the same for all FCs in a reactor core. They vary from unit to unit and affect the maintenance and operating history of FCs in CANDU reactors. Moreover, the FCs are "reconfigured" to accommodate the axial elongation at both ends of the PT, a process that takes place approximately at halfway of operating life. Each of these factors can significantly affect the PT-CT gap, the location of contact and the time to contact. Therefore, the FEM must be able to model all these scenarios. This section

discusses the results based on different combinations of boundary conditions and shows the differences in gap predictions.

To determine the difference in gap profiles based on various boundary conditions, the following analyses were conducted:

a) The gap profile at 175 kEFPH was predicted by keeping the outlet end fixed and the inlet end free (similar to the previously described analysis).
b) The gap profile at 175 kEFPH was predicted by keeping the inlet end fixed and the outlet end free.
c) The gap profile at 175 kEFPH was predicted by keeping the outlet end fixed and the inlet end free up to 120 kEFPH and then changing the boundary conditions to simulate the inlet end fixed and the outlet end free for the rest of 100 kEFPH operating time (i.e., reconfiguration was done at 120 kEFPH).

It is important to note that the back end of the PT was placed at the outlet end for all these analyses. Figure 3.27 shows the comparison of gap profiles at 175 kEFPH for these three cases. The changes made to the boundary conditions have a significant effect on the gap profile. The outlet span (S1) becomes the most critical span instead of the inlet span in the case of free-end outlets and reconfigured FCs as they approach end-of-life. This example shows the influence of boundary conditions on PT-CT gap and the importance of considering the configuration of a FC in PT-CT gap computations, location of contact and time to contact.

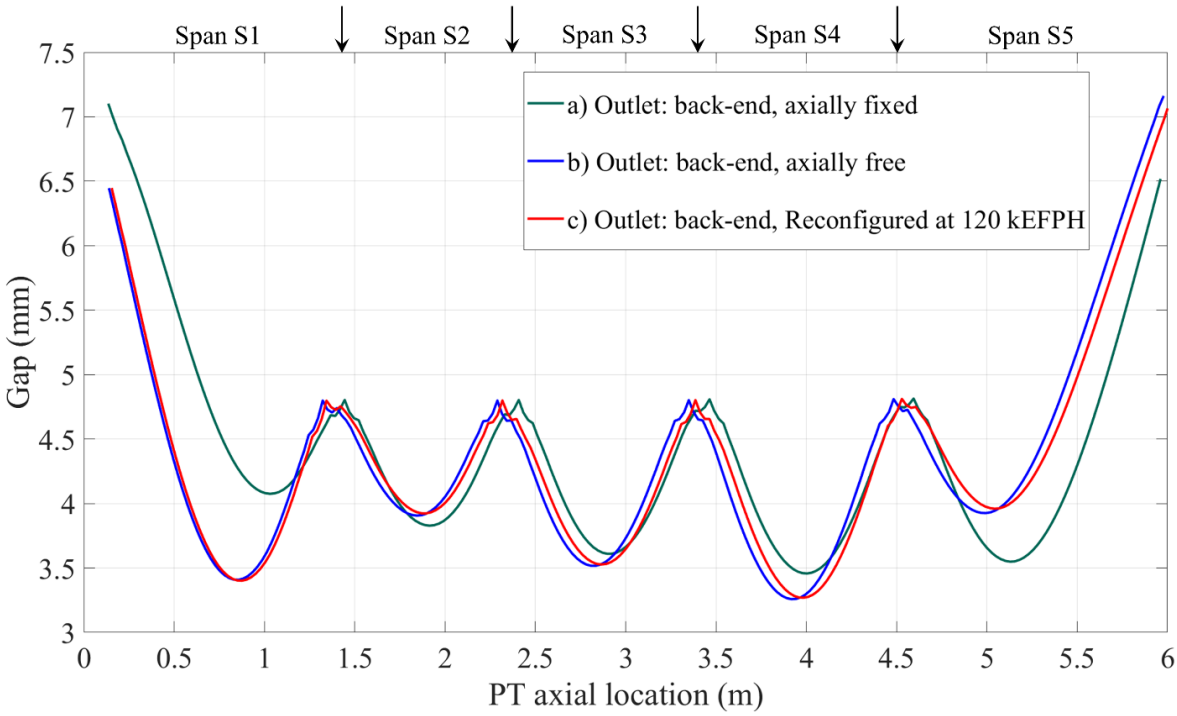

Figure 3.27: Comparison of predicted PT-CT gap profiles at 175 kEFPH for three different boundary conditions (PT back end is always at the outlet)

3.6 Limitations of 3D FEM Model

The current 3D FEM model predicts only the mean diameter and doesn't give a significant ovality at locations other than the locations of the spacers. The ovality in pressure tubes is obtained due to the variation in flux and temperature along the circumference of the tube and also due to local deformation at spacer locations. With diametral expansion, the fuel bundle sits at the bottom part of the tube. Therefore, the bottom part of the tube is exposed to more flux and temperature compared to the upper part, which introduces variation in diametral strain along the circumference and contribute to ovality, which gives minimum, mean and maximum diameter. To incorporate this behavior in the FE model, the relation between time and variation in flux and/or temperature

must be understood, which can be then coded in UMAT. The current model considers constant temperature and flux distribution around the circumference which deforms all the material points equally, and therefore no diametral strain variations along the circumference. Therefore, the model predicts only the mean diameter.

Due to the mean diameter estimation, the PT-CT gap is computed only from 6-o'clock position. However, the inspection results have shown that the minimum gap is not always at the 6-o'clock position. As already mentioned, when the variation in diameter along the circumference is accounted for, the minimum gap is possible at location other than 6 o'clock position. As this variation in diameter is not accounted for, the minimum gap is possible only at 6 o'clock position and all the PT-CT gap results discussed in this thesis were computed only from 6-o'clock position.

3.7 Comparison between 3D and 1D FEA Results

This section discusses the difference between the 1D and 3D FEA results for PT-CT contact assessment. The nuclear industry currently relies on 1D FEM for modelling the deformation response of FCs and making end-of-life decisions. A significant advantage of the 1D model over the 3D model is the computational cost. A 1D FEA can be completed in about 18 minutes, whereas a 3D FEA can take up to 3 hours. Therefore, it is important to compare both these models and to check for any significant differences in the deformation predictions.

As already discussed in section 3.4.3, the 1D beam model cannot predict diametral expansion and wall thinning, which is a major drawback in obtaining a comparison of predictions with all the data obtained from the in-service gauging of the tubes. Figure 3.28 shows the comparison of gap profiles at 220,000 EFPH predicted by the 1D and 3D FEM models. It is important to note that the

1D FEM substantially underestimates the gap along the whole length of the tube. The nuclear industry should take into account this aspect, particularly at a time when there are plans to extend the operating life of reactors well beyond the initial design target of 210,000 EFPH. Making end-of-life, and beyond, decisions based on 1D FEM results may therefore not be the most reliable of methods.

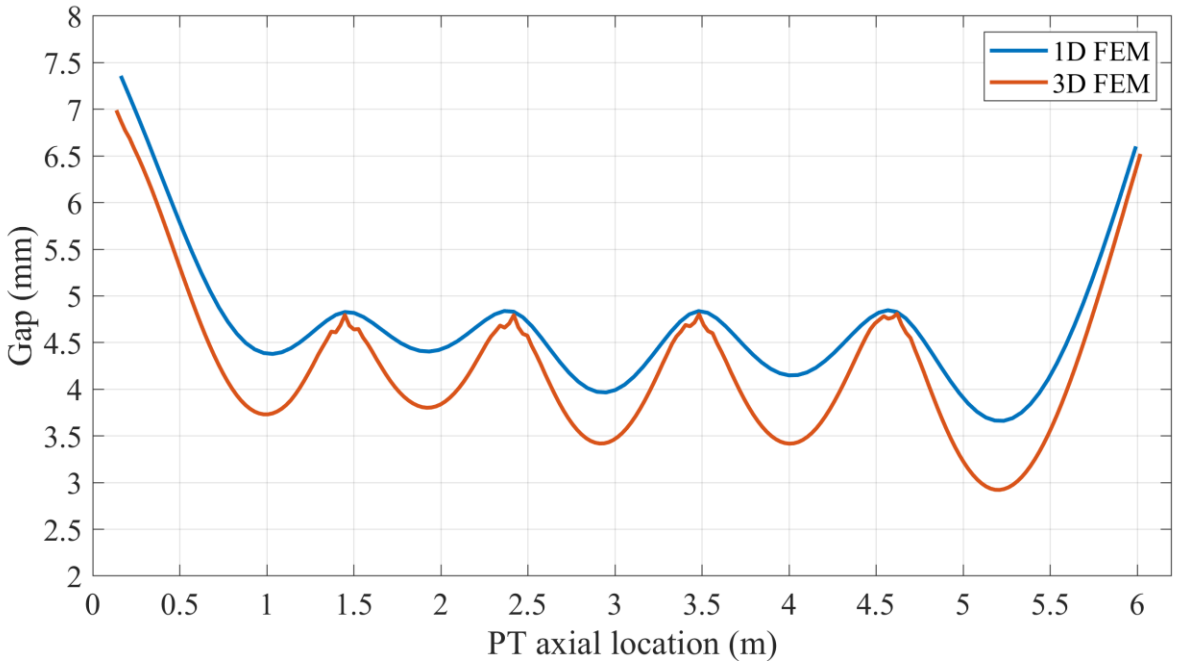

Figure 3.28: Predicted PT-CT gap profiles at 220 kEFPH using 1D and 3D FEM models (PT back end placed at the outlet end)

The underestimation of the gap profile can be further shown by predicting the time to reach a minimum gap of 1 mm. The 1D and 3D models predicted a time of 299 kEFPH and 261 kEFPH, respectively. Namely, the 1D model over-predicts the time by 38 kEFPH, which is equivalent to about 5.5 calendar years (assuming that one calendar year is about 7 kEFPH, or that a CANDU unit operates at roughly 80% full power over a calendar year). These results show the disadvantage

of using 1D FEM results to make end-of-life decisions. Therefore, it is evident that a 3D model is required for accurately predicting the in-reactor FC deformation when end-of-life decisions are required.

3.8 Conclusions

This chapter discusses the computational modelling of in-reactor FC deformation using 1D and 3D FEM models in ABAQUS and the implementation of elastic and creep deformation models describing the in-reactor behaviour of PT and CT materials by means of UMAT subroutines in ABAQUS. The 1D FEM beam model was developed as a similar FE beam model used by the nuclear industry. The 3D FEM model can capture the complex nature of in-reactor deformation and can accurately predict the in-reactor dimensional changes. The use of continuum shell elements significantly improves the prediction of PT and CT sag, and most importantly the prediction of PT-CT gap by taking into account the tube thickness and diametral expansion of PT. The 3D FEA results obtained using different boundary conditions showed the capability of the model to correctly predict the FC dimensional changes in any FC configuration.

The following observations are made based on the FEA results:

- A full 3D FEM model is required for accurately modelling in-reactor deformation and predicting PT-CT gap, contact location and time to contact.
- A comparison between the 1D and 3D FEA results showed a significant underestimation of gap by the 1D model. Making end-of-life decisions based on 1D FEM results would therefore be a less reliable estimate.
- The boundary conditions significantly influence the PT-CT gap profiles.

In short, the developed 3D FEM can accurately simulate the dimensional changes of CANDU FCs and can be a useful tool for the nuclear industry in making confident and cost-effective decisions.

Chapter 4
Development of Surrogate Models and Calibration Methods for the 3D prediction of In-Service Deformation in CANDU FCs

4.1 Introduction

4.1.1 Need for Surrogate Model and Calibration

The ageing mechanisms of CANDU FCs limit the useful operating life and the maximum power output of CANDU power reactors. For optimising the plant life management (PLiM) of existing power reactors, the prediction of future in-reactor deformation of PTs using physically based models is necessary. As shown in the previous chapter, a 3D FEM model can be used to predict the in-reactor deformation with sufficient confidence level. However, these models are computationally expensive, and it becomes cumbersome to use these models frequently, especially as a quick access tool for making decisions in the industry. The nuclear industry often prefers to have models which are readily accessible, and which predict the quantity of interest using a simple equation or model (e.g., use of closed form equations to predict peak stress at a blunt flaw). These closed form equations or models are developed based on the understanding of physical mechanisms and parameters influencing the quantity of interest and through proper validation. A similar approach can be used to develop simple-to-evaluate surrogate models by utilizing the simulation results of an expensive-to-evaluate 3D FEM model. Once the surrogate model is validated and verified, it can replace the computationally expensive 3D FEM model. Therefore, surrogate models can be used as approximate models which could mimic the behaviour of the FEM

model as close as possible while being computationally cheap to evaluate. The surrogate models can be then used for the purpose of predictions, calibration of FEM models and performing probabilistic analysis, which would give a significant reduction in the computational cost of performing these analyses.

4.1.2 Objective

The main objective of this chapter is to develop surrogate models for diametral creep in PTs and surrogate models of PT-CT gap profiles. The first objective is to study the diametral creep behaviour from 3D FEA leading to diametral expansion of PTs and to utilize the understanding in developing a calibration and surrogate modelling approach by accounting for the observed variability in diametral strains due to material uncertainties. The surrogate model predictions are then validated by comparing against inspection data. The second objective is to investigate and predict the diametral creep strain using 3D finite element analysis with realistic flux profile inputs. The third objective is to develop a surrogate model of PT-CT gap by studying the influence of important variables (creep factor and end-slopes) on PT-CT gap. The surrogate models are then validated and are checked for the application of calibration purpose.

4.1.3 Organization

The organization of this chapter is as follows. Section 4.2 discusses the calibration of 3D FE models for diametral creep predictions of PTs by introducing a scale parameter to account for the material uncertainty. Section 4.3 presents the investigation and calibration result of diametral creep strain predictions with realistic flux inputs. Section 4.4 presents the development of a surrogate model for diametral creep in PTs, which can be used to replace the 3D FE model. Section 4.5

presents the surrogate model development of PT-CT gap and the use of surrogate model in calibrating for PT-CT gap. Finally, conclusions are summarized in Section 4.6.

4.2 Calibration of 3D FE Model for Diametral Creep Predictions in PTs

4.2.1 General

The previous chapters discussed the issues due to diametral expansion in PTs and the prediction of these life-limiting dimensional changes using 3D FEA. However, the deterministic 3D FE model does not account for the observed variability in the measured diametral strains. Previous studies have shown that in addition to variations in operating conditions, the observed deformation rates are significantly influenced by as-fabricated microstructural variables, which are mainly crystallographic texture and grain thickness (Bickel & Griffiths, 2007, 2008; Walters et al., 2015). The variability in these microstructural variables is due to variations in temperature and pressure occurring during PT manufacturing (Bickel & Griffiths, 2007, 2008; Walters et al., 2015), and they are also factors that affect the evolution of the microstructure in response to the irradiation damage occurring during operation (Griffiths et al., 2002). These variables affect both the anisotropy as well as the magnitude of the observed strain and are responsible for the tube-to-tube variability in deformation rates of PTs operating within the same reactor (Griffiths et al., 2002). Moreover, the crystallographic texture and grain structure also vary gradually from one end of the tube to the other due to the temperature and pressure changes occurring during the extrusion process, thus affecting the deformation profile along the length of the tube (Bickel & Griffiths, 2008).

The parameters accounting for these microstructural factors in the PT deformation equation are obtained such that the model predicts the average deformation behaviour. Therefore, the 3D FE model predicts only the mean behaviour of the tube deformation and needs an approach to calibrate the FE model to make comparisons against the measured diameter. A well calibrated model can be used to make future predictions and can be used as an efficient tool for assisting in optimized inspections. For example, CSA N285.4 Standard requires the dimensional examination of maximum internal diameter, the location of the maximum internal diameter, the maximum change in internal diameter since the previous examination, and the rate of change in diameter (CSA N285.4, 2010). The capability of a calibrated FE model for predicting these changes is analyzed in this section.

4.2.2 Calibration Approach

A CANDU reactor has 380 or 480 FCs depending on the reactor power rating. Each of these FCs have different operating conditions depending on the location inside the reactor core. The CSA N285.4 Standard requires the PTs to be inspected at regular intervals. As the large-scale inspections are difficult and capital intensive, only a handful of PTs are inspected from each quarter of the reactor (A reactor is divided into four quarters). An analyst should confirm that the diametral strain rate is as expected and safe to operate until next inspection. A 3D FE model can be used to model these channels and predict the dimensional changes. However, it is important to study how the material variability is influencing the diametral strains. This can be studied by comparing the 3D FE predictions with the inspection data and use the understanding of prediction variability for making probabilistic decisions on uninspected population of FCs. A calibration approach can be

used in these scenarios to quantify the variability in predictions and measured quantities, as discussed next.

The measured diametral data from 4 PTs (Hereby called as PT1, PT2, PT3 and PT4) located at various locations in a single quarter of the reactor core at 161615 EFPH were available. In this section, these FCs are analyzed using 3D FE model and the diametral strain at 161615 EFPH is predicted. The corresponding operating conditions of these FCs were used in the analysis. As already mentioned, the 3D FE model can simulate only the mean behaviour of a tube and the material uncertainty is not accounted for. Therefore, the diametral strain predicted by the 3D FE model using mean parameters is hereby called as a "*nominal model*". The nominal model accounts for the contribution of operating conditions such as fast flux, temperature and internal pressure to the diametral strain. Therefore, any difference between the measured diametral strain and the predicted diametral strain by the nominal model is assumed to be from the material variability.

For example, Figure 4.1 shows the comparison of measured diametral strain vs 3D FEA predicted diametral strain for PT1. It is clear that the 3D FEA overpredicts the diametral strain for this channel. The difference is due to the deviation of the microstructural parameters from the average. To make future predictions, the 3D FE model must be calibrated such that it correctly predicts the diametral strain of a given FC. For this purpose, a simple and effective approach is used here by introducing a factor called as a "*scale factor*", which is defined as the ratio of the maximum measured diametral strain to the maximum 3D FEA nominal diametral strain. For a calibrated model, the scale factor is multiplied with the nominal diametral strain at all axial locations, such that the nominal model is scaled by the multiplied factor, which significantly reduces the error at all axial locations and a zero error at the maximum diametral strain location which is of prime

interest. Therefore, the scale factor can be considered as a factor accounting for the material uncertainties.

Figure 4.2 shows the comparison of measured, nominal and calibrated diametral strain for PT1. The scale factor was calculated as 0.8 for this channel. The calibrated model gives a very good agreement with the measured diametral strain. The scale factors obtained for PT2, PT3 and PT4 are given in Table 4.1 and the diametral strain comparison plots are given in Appendix A.

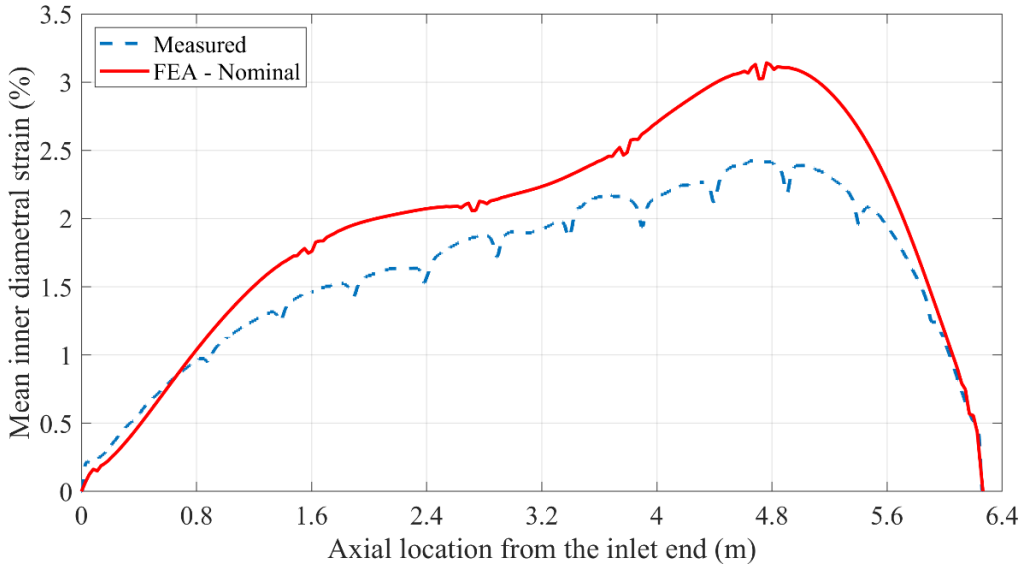

Figure 4.1: Comparison of measured diametral strain against 3D FEA predicted nominal diametral strain of PT1 at 161615 EFPH

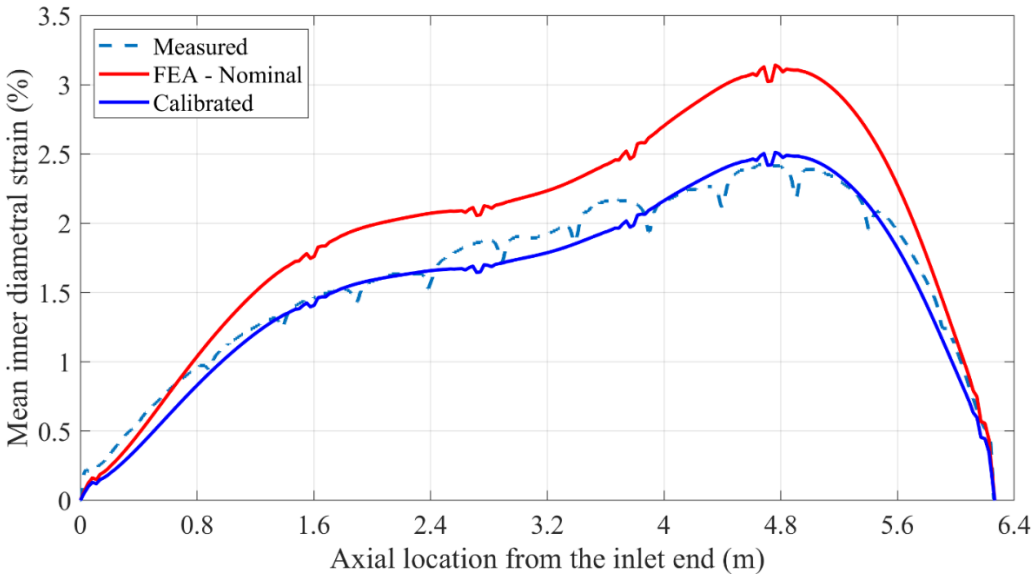

Figure 4.2: Comparison of measured, nominal, and calibrated diametral strain of PT1 at 161615 EFPH

Table 4.1: Scale factor obtained for each FC following calibration

Fuel Channel	Scale factor
PT1	0.795
PT2	0.87
PT3	0.94
PT4	0.981

4.2.2.1 Time invariant check

A scale factor can aid in calibrating a 3D FE model prediction and therefore give good agreement with the measured data. However, it is important to check the validity of using this approach for making future predictions (i.e., to check whether the scale factor is dependent or invariant with time). For this purpose, a PT (Hereby called as PT5) with the availability of multiple diametral measurements was used. The diametral strain measurements are available at four different time

intervals (101,100 EFPH, 124,944 EFPH, 148,273 EFPH and 176,575 EFPH, respectively). The nominal prediction was initially made using 3D FEA at 101,100 EFPH and the model was then calibrated by finding the scale factor. A scale factor of 0.96 was obtained for this PT at 101,100 EFPH. The nominal and calibrated predictions against the measured data is shown in Figure 4.3.

The same scale factor was then used to make predictions of diametral strains at other operating intervals (i.e., at 124,944 EFPH, 148,273 EFPH and 176,575 EFPH, respectively) as shown in Figure 4.4. It is observed that the scale factor is time invariant as the same scale factor gives very close predictions at other time intervals. Therefore, a once calibrated 3D FE model can be confidently used to make future predictions.

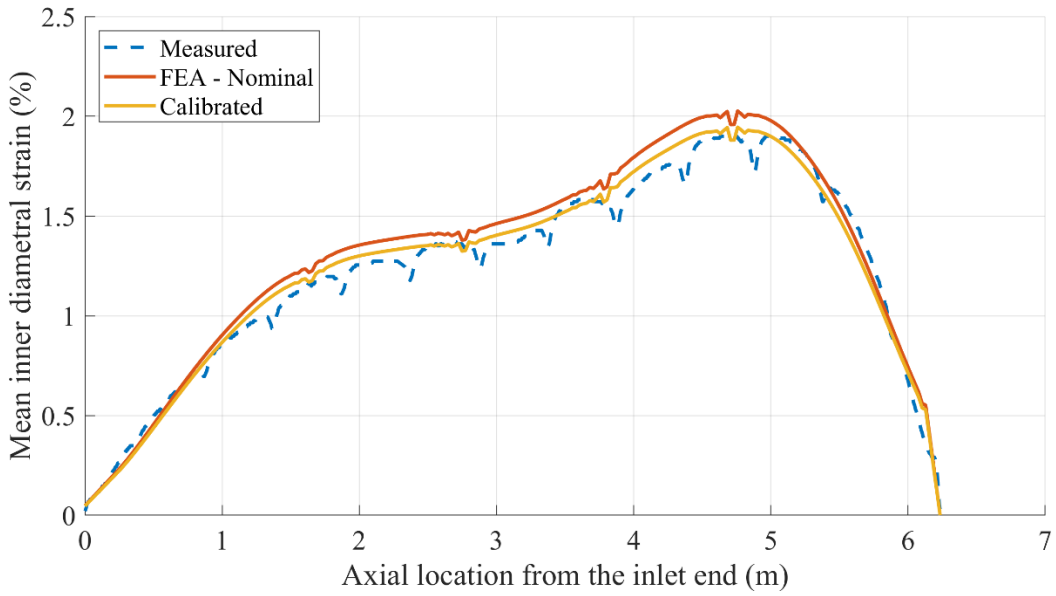

Figure 4.3: Comparison of measured, nominal, and calibrated diametral strain of PT5 at 101,100 EFPH

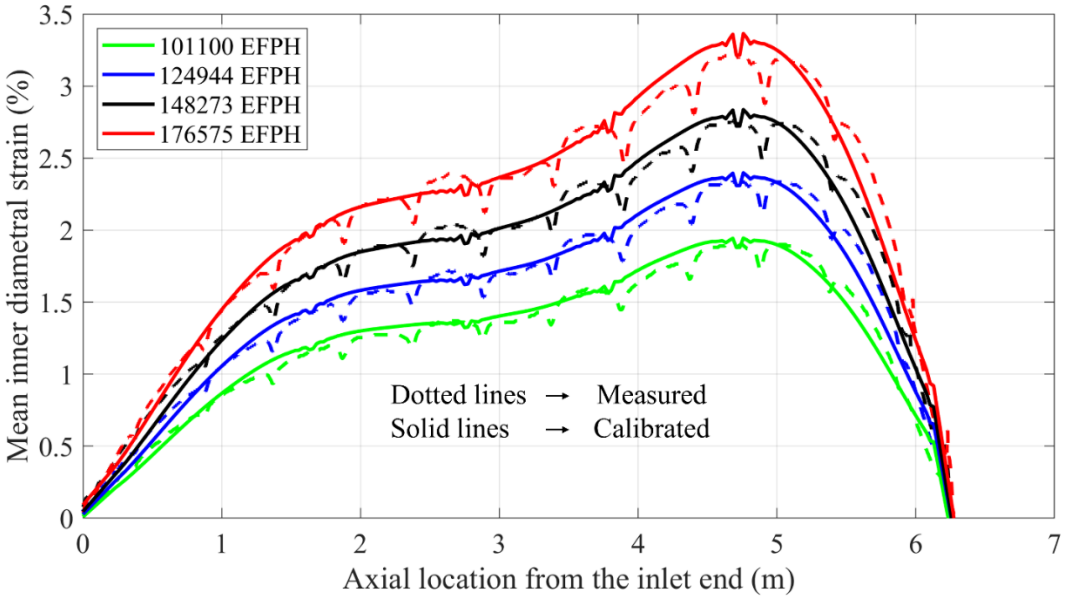

Figure 4.4: Comparison of measured and calibrated diametral strain of PT5 at various time intervals

4.3 Investigation and Calibration of Diametral Creep with Realistic Flux Profile Inputs

4.3.1 Introduction

By referring to the measured diametral profiles in the previous section (eg., Figure 4.3), it can be observed that the diametral profiles has dips along the axial locations. These dips are generated because of dips in flux profiles at these respective locations as a result of gaps in the fuel bundle arrangement. The previous FEA results were based on a smooth flux profile input which resulted in a smooth diametral profile prediction. Even though a smooth diametral profile result would suffice for the prediction and calibration purpose, this section specifically investigates the diametral creep strain at the dips using 3D FEA and realistic flux profile inputs. The flux profiles

are considered as a direct descriptor of diametral creep strains and are found to be scaled proportionally. However, the creep strain dip amplitudes at these local dip regions do not scale proportionally with flux. In this section, the 3D FEA results are used to analyze the scale of flux dip and diametral creep strain dip at these local regions. The predicted profiles are then calibrated and compared with measured data using the same approach as discussed in previous section.

4.3.2 Generation of Realistic Flux Profiles

The arrangement of fuel bundles in a FC is shown in Figure 4.5. A typical FC has 12 fuel bundles, each with a length of 49.53 cm. As shown in Figure 4.5, the arrangement of fuel bundle is not continuous as there are gaps at the inter-bundle regions. This gap is called as stack-to-stack gap, which is the distance from a fuel stack end in one bundle to the nearest fuel stack end in an adjacent bundle. The absence of the fuel at these gaps causes a dip in fast neutron flux at these respective locations called as fast flux dip, which in turn introduces a dip in diametral creep profiles.

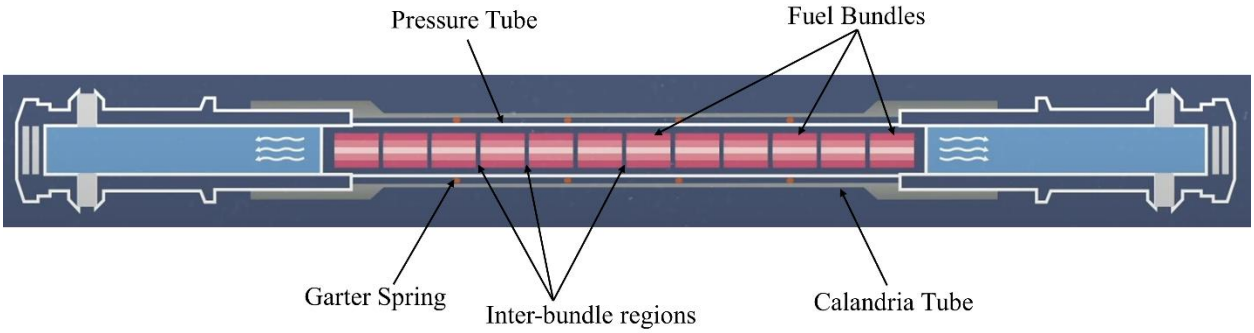

Figure 4.5: Fuel bundle arrangement inside a fuel channel

In this study, the same fuel channels discussed in section 4.2.2 are analyzed and the realistic flux profile generation of PT2 and PT3 are discussed in detail here. The reactor operator provides only the fast flux data obtained from bundle average power at 12 or 13 axial locations along the PT.

The flux data obtained from bundle average power for PT2 and PT3 are shown in Figure 4.6 along with the measured diametral creep strain profiles. It is clear from this figure that the low density of flux profile data compared to creep data requires careful modeling of a complete flux profile. In Figure 4.6, the vertical solid lines show the mid-bundle location of each fuel bundle and the dotted lines show the ends of each fuel bundle. In CANDU FCs, there are two general types of fast flux profile, an M-profile and a cosine profile. From Figure 4.6, PT2 has an M shaped flux profile whereas PT3 has a cosine shaped flux profile. The M shaped flux profiles are generated at the centre of the reactor core, whereas the cosine shaped flux profiles are generated when moving further away from the reactor core centre. An M shaped profile is formed generally due to the presence of reactor mechanisms (these mechanisms are for reactor control or for parts of the shutdown system) normal to the channel that absorb neutrons.

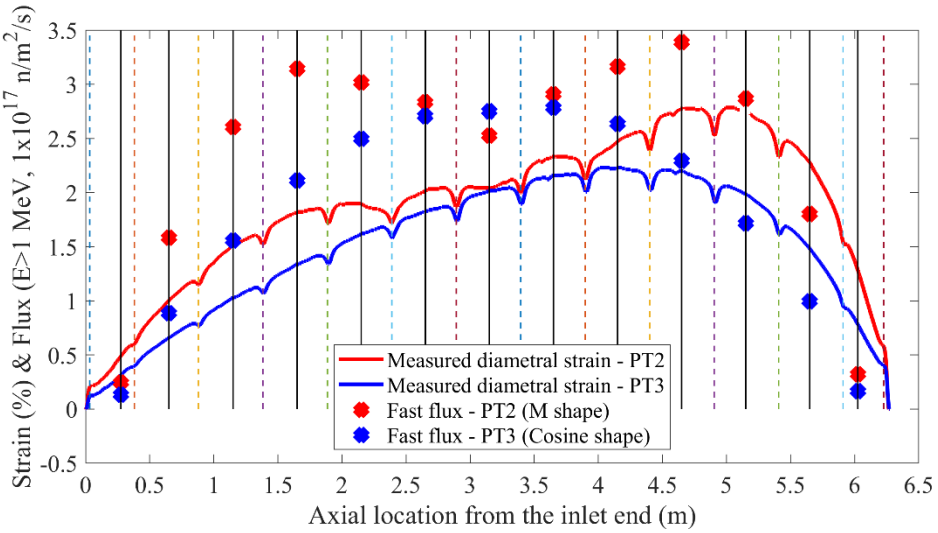

Figure 4.6: Flux data obtained from bundle average power and measured diametral creep strain at 161615 kEFPH for PT2 and PT3

A realistic flux profile is now generated from the available 13 flux data. The fast flux should be smoothly varying across fuel bundles. Therefore, an approach is used to construct a realistic fast flux profile by first fitting a sixth-degree polynomial to the mid-bundle flux data to create a smooth flux profile and then the flux dips were introduced at respective locations. A report from the nuclear industry was available which detailed the modelling of flux dips. The fast flux dip is taken as ~85% for the bundle joints with a stack-to-stack width of 1.437 cm. Although the stack-to-stack gap is only 1.437 cm (or 0.7185 cm in each bundle), the flux dip appeared to be significantly wider, over ~5 cm at the end of each bundle. Figure 4.7 shows variation in the fast flux dip as a function of the distance from the bundle joints. Based on this model, it is computed that the fast flux reaches to 100% at a distance of ~10 cm from the bundle joints.

From the smoothly varying flux profiles generated using the fitted polynomial, a realistic fast flux profile was generated by introducing the dips at the respective locations of the bundle joints as shown in Figure 4.8 and Figure 4.9 for two different flux profile shapes. These flux profiles were used as an input to the FE model. Note that the analysis in Section 4.2.2 was based on a smooth flux profile obtained using the polynomial fit.

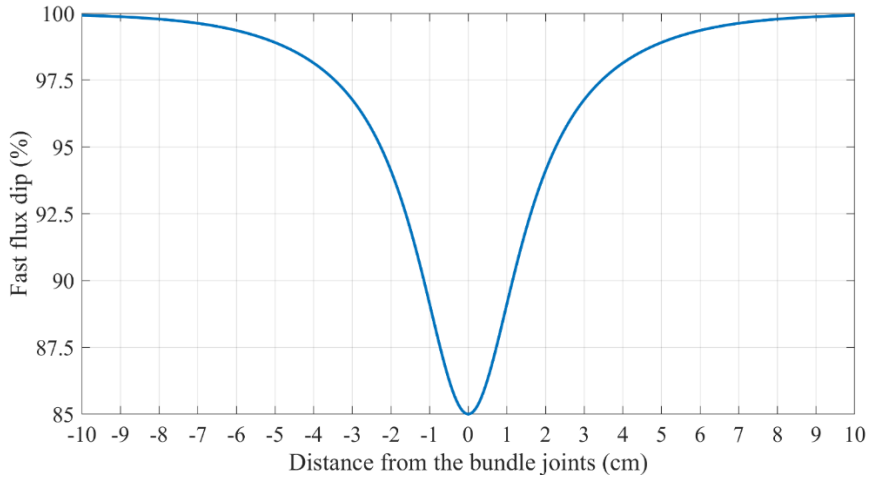

Figure 4.7: Fast flux dip in pressure tubes

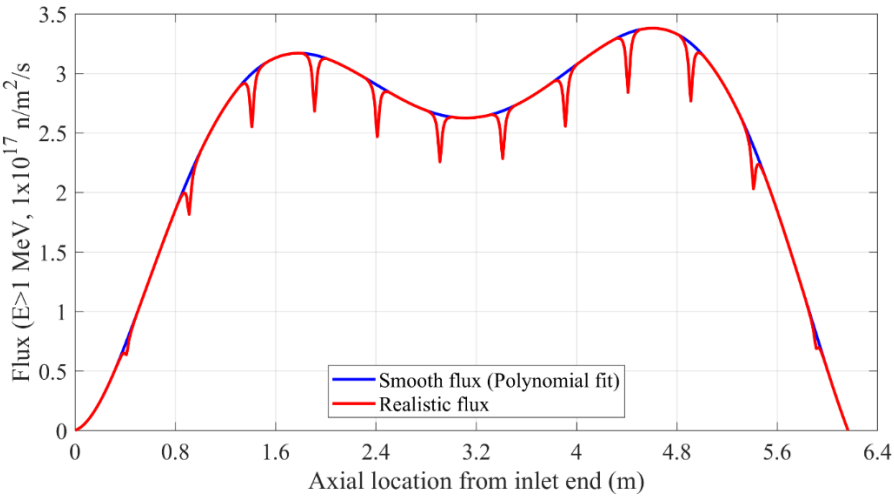

Figure 4.8: Comparison of smooth and realistic flux profile of PT2

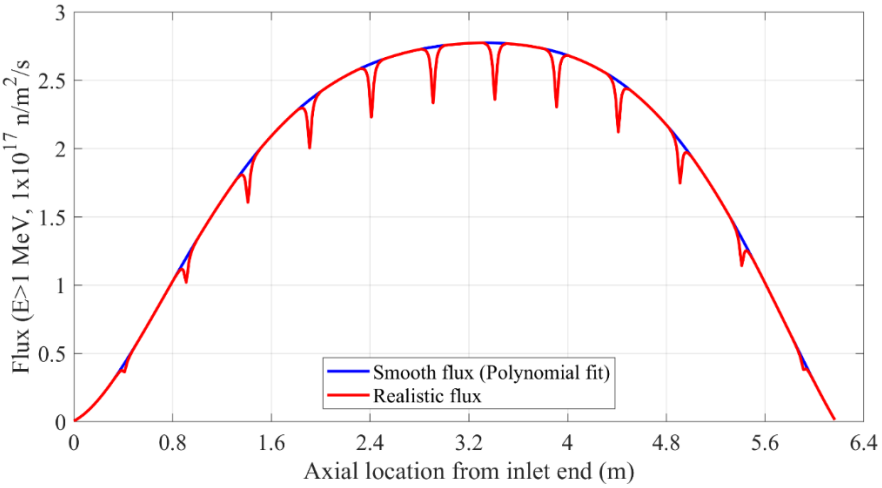

Figure 4.9: Comparison of smooth and realistic flux profile of PT3

4.3.3 FEA using realistic flux profile inputs

3D FEA is used to predict the diametral creep of PT2 and PT3 using realistic flux profile inputs. The 3D meshed cross section of the FC with finer mesh at the flux dip locations is shown in Figure 4.10. A Python script was developed to write the Abaqus input file for carefully discretizing and meshing the PT by considering the axial locations of each of the bundle joints, such that the flux dips are assigned to the appropriate nodes. A finer mesh of 4mm is used at the flux dip locations to accurately capture the diametral creep at these local regions. A total of 12 fuel bundles are arranged axially in the PT with each fuel bundle having a length of 49.53 cm. The current FE model had more than three times the number of elements when compared to the FE model used in the previous section, and therefore a higher computational cost.

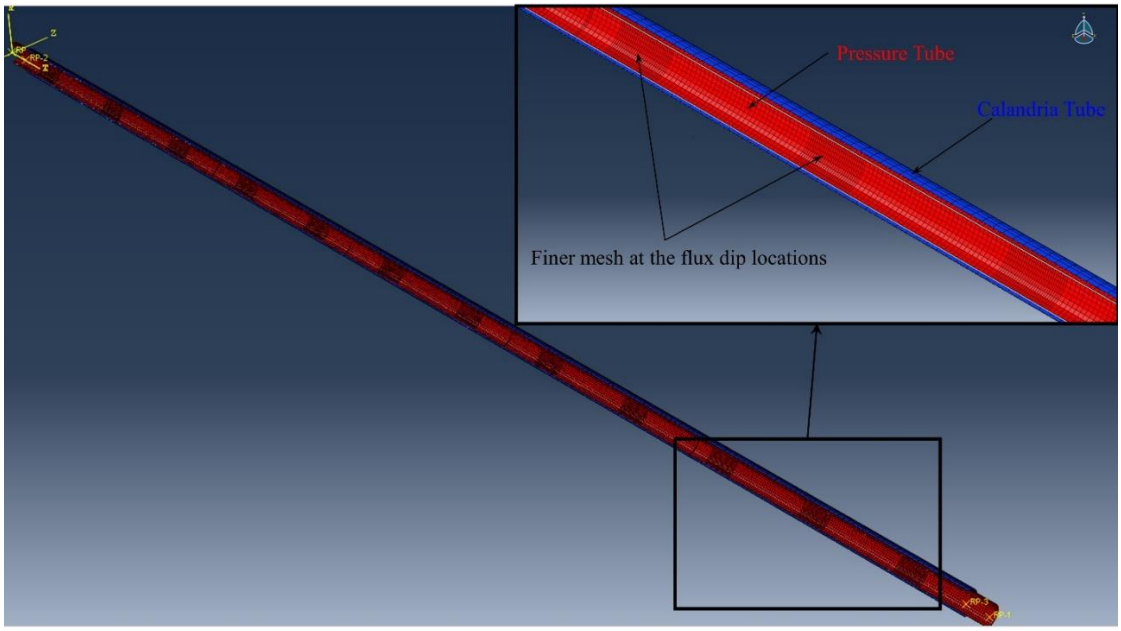

Figure 4.10: 3D finite element model of the fuel channel with finer mesh at the flux dip locations

4.3.3.1 Creep Strain Prediction at Flux Dip Locations

As was mentioned in section 4.2.2, the parameter values accounting for the microstructural factors in the PT deformation equation are such that the model predicts the average deformation behaviour, which was called as a "*nominal model*". The nominal model results are used to estimate the creep strain reduction at the flux dip locations. Figure 4.11 shows the nominal model diametral creep strain prediction of PT2 and Figure 4.12 shows a magnified figure of the maximum diametral strain location. Similarly, Figure 4.13 shows the nominal model diametral creep strain prediction of PT3 and Figure 4.14 shows a magnified figure of the maximum diametral strain location. By taking the second dip (at around axial location of 4.95 m) in Figure 4.12, the diametral strain at the dip location is ~ 2.875. In the absence of a flux dip, the diametral strain at this location is ~ 3.2. Therefore, the strain dip at this location can be estimated as 0.898 (89.8%). Similarly, by taking

the second dip (at around axial location of 4.4 m) in Figure 4.14, the diametral strain at the dip location is ~ 2.13. In the absence of a flux dip, the diametral strain at the same location is ~2.38 from the smooth curve. Therefore, in the absence of a flux dip, the diametral strain at this location is ~ 2.38 and the strain dip at this location can be computed as 0.895 (89.5%).

Even though the flux dip at the bundle joints is ~15%, the diametral creep does not drop by the same scale. From the FE results, the maximum diametral creep strain dip is ~10%. This trend was observed at all the flux dip locations with diametral creep strain dip varying around 10%. This is due to the effect that the material at the flux dip is restricted from freely reducing the diameter by the adjacent material points that is exposed to higher values of flux that result at higher diametral reductions. The FE model clearly captures this short-range effect at the inter-bundle locations. Therefore, the non-scale creep strain dip amplitudes at the local flux dip regions are because of material continuity.

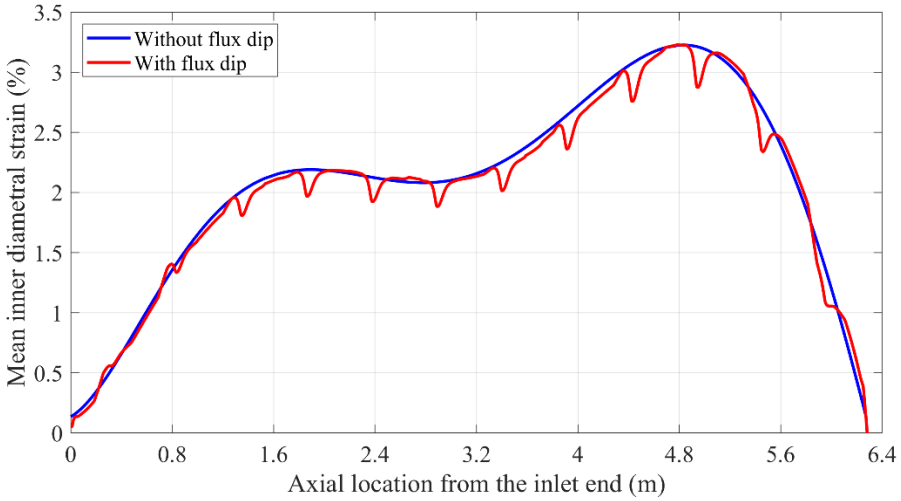

Figure 4.11: Nominal diametral strain prediction using 3D FEA and realistic flux profile input of PT2

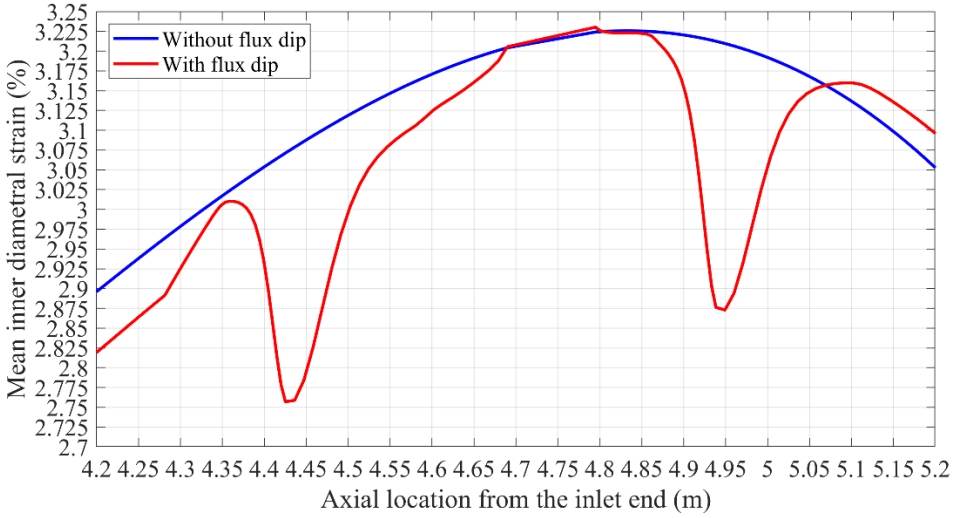

Figure 4.12: Magnified view at maximum diametral strain location of PT2

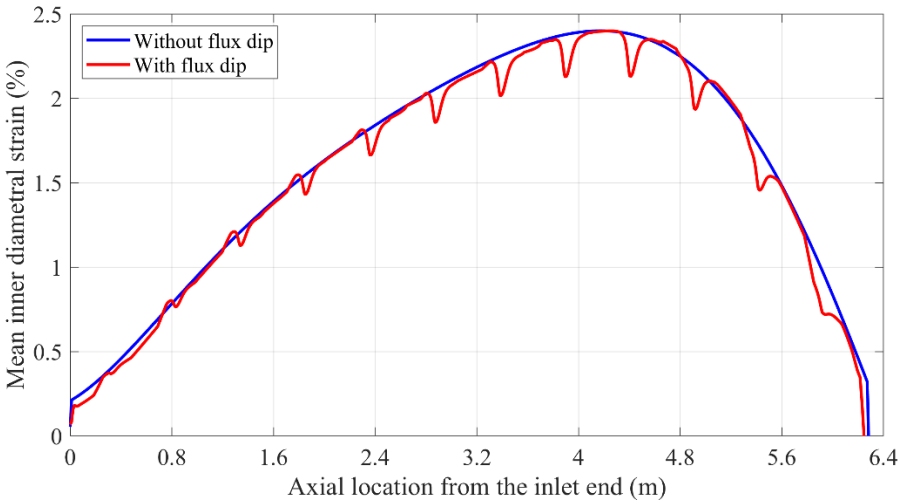

Figure 4.13: Nominal diametral strain prediction using 3D FEA and realistic flux profile input of PT3

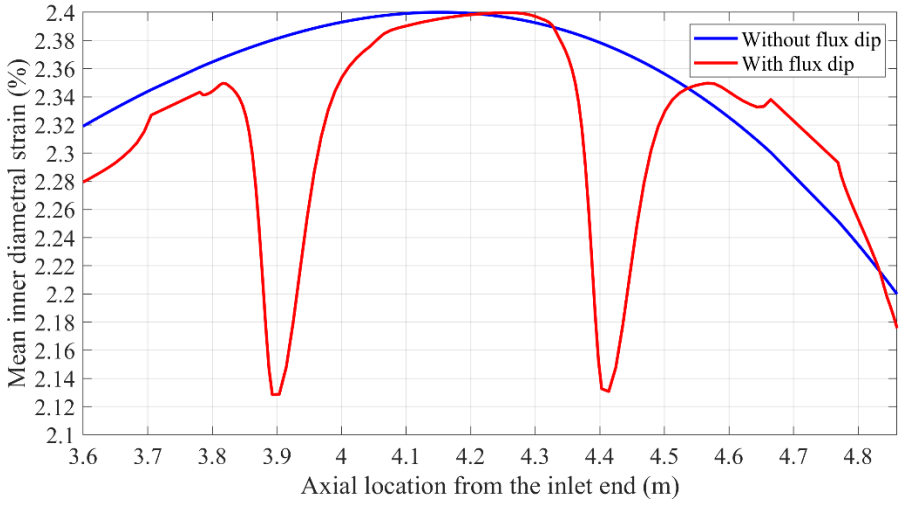

Figure 4.14: Magnified view at maximum diametral strain location of PT3

4.3.3.2 Calibration with Diametral Creep Strain Dip

For calibration, the same approach as used in section 4.2.2 was used and the scale factors were computed to be the same as reported in Table 4.1. Figure 4.15 and Figure 4.16 shows the measured and the calibrated model predictions obtained by multiplying a scale factor to the diametral strain of the nominal model with dips. The calibrated model gives a very good agreement with the measured diametral strain and captures well the diametral creep along most of the axial locations. Another important finding is on the diametral strain at inter-bundle locations. As was observed for the measured data, the FE model successfully predicts the local diametral creep dips and demonstrates it to be not in scale with the flux dip.

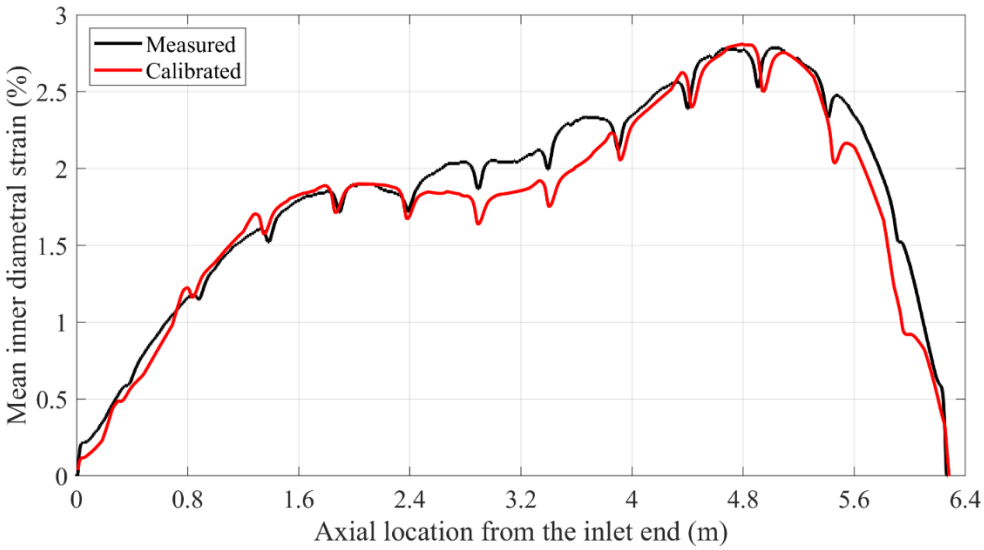

Figure 4.15: Comparison of measured diametral strain against calibrated diametral strain of PT2 at 161615 EFPH by accounting for flux dip

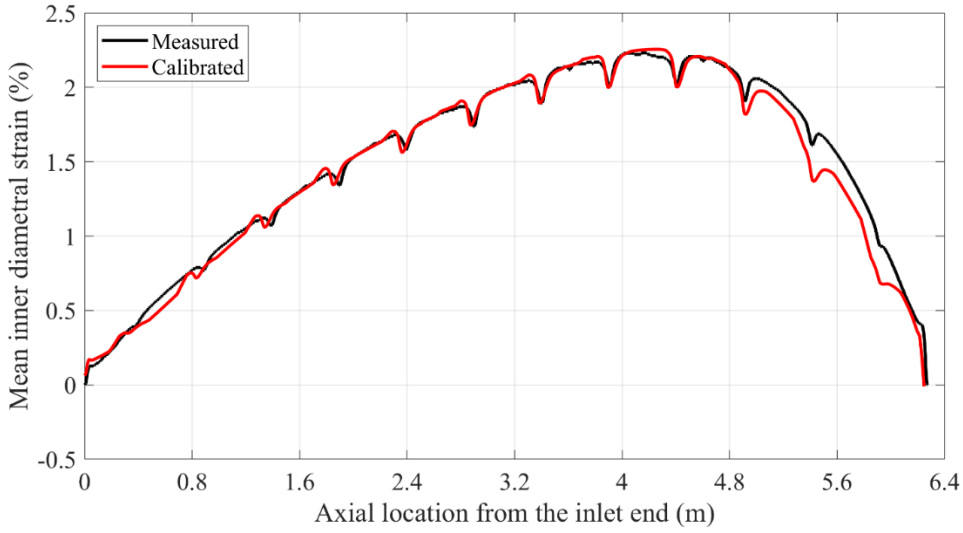

Figure 4.16: Comparison of measured diametral strain against calibrated diametral strain of PT3 at 161615 EFPH by accounting for flux dip

4.4 Development of a Surrogate Model for Diametral Creep in PTs

4.4.1 Regression model using 3D FEA

The main inspiration for developing a regression model for diametral creep in PTs is based on the observations from Figure 3.21 and Table 3.2, which shows a linear trend for diametral expansion with operating time along five axial locations. These axial locations were approximately in the middle of each of the five spans and they were measured from the outlet end. In this section, the analysis is extended to check the generality of this trend along the entire PT length. If the linear trend is observed at all axial locations, a regression model can be developed using linear regression of diametral strain vs operating time, and the slope would be giving the diametral strain rate at each axial location. For this purpose, the prediction from 3D FEA were initially used. The following steps were used to develop and verify the regression model of diametral strain as a function of operating intervals:

i. Fit a line using linear regression for diametral strain vs operating interval up to 150 kEFPH for each axial location.
ii. Save the respective slope (strain rate) and intercept values obtained at each axial location in a matrix form. These are the coefficients for the regression model.
iii. Use the regression model and predict the diametral strain or diameter for future time points.
iv. Compare the regression model prediction of the diametral strain at a future time point with the FEA prediction.

Each step given above was performed to check the development of a regression model. Initially, linear regression was performed for each axial location for an operating interval up to 150 kEFPH

using the 3D FE model. The R-square values at respective axial locations are shown in Figure 4.17 and these values confirm high degree of linearity at all axial locations of the PT. The slope obtained following the linear regression analysis can be considered as the diametral strain rate along each axial location as shown in Figure 4.18. As expected, the slope along the PT length takes the shape of the diametral strain and the peak diametral strain rate is about 1.46 x 10^{-7} at around 1.6 m. Therefore, the regression model for the diametral strain can be modelled as

$$\varepsilon(x,t) = b(x) * t \; + \; b_2\left(x, t_{ref}\right) \tag{4.1}$$

where ε is the diametral strain, x is the axial location, t is the operating interval in EFPH, b_1 is the slope and b_2 is the intercept of the nominal profile at a time $t_{ref} < t$. A nominal profile is the diametral strain profile obtained from 3D FEA using the mean deformation equation (i.e., no parameter to account for material uncertainty). It is important to mention here that the coefficients in the model are directly dependent on the operating conditions of a PT, mainly fast flux and temperature. The shape of the diametral profile is highly influenced by these parameters. Therefore, each PT in the reactor core will have the same regression model form but with different coefficient values along the length of the PT. The prediction capability of the regression model for a future time point is analyzed next.

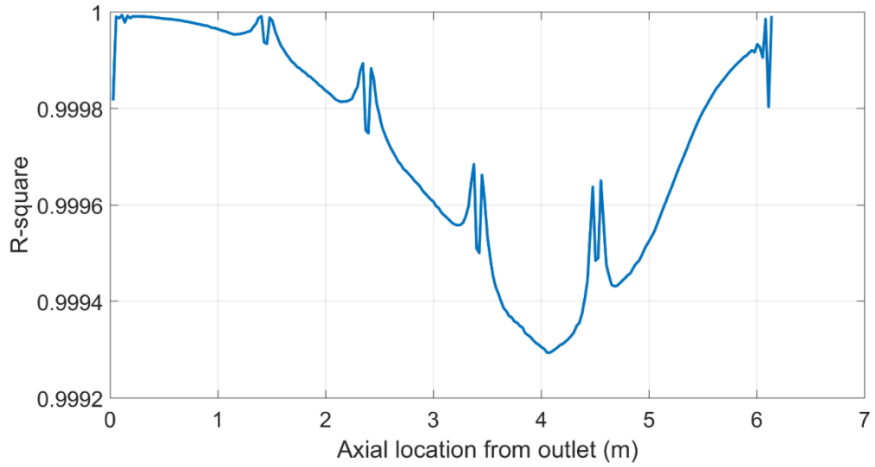

Figure 4.17: R-square values obtained following linear regression at axial locations

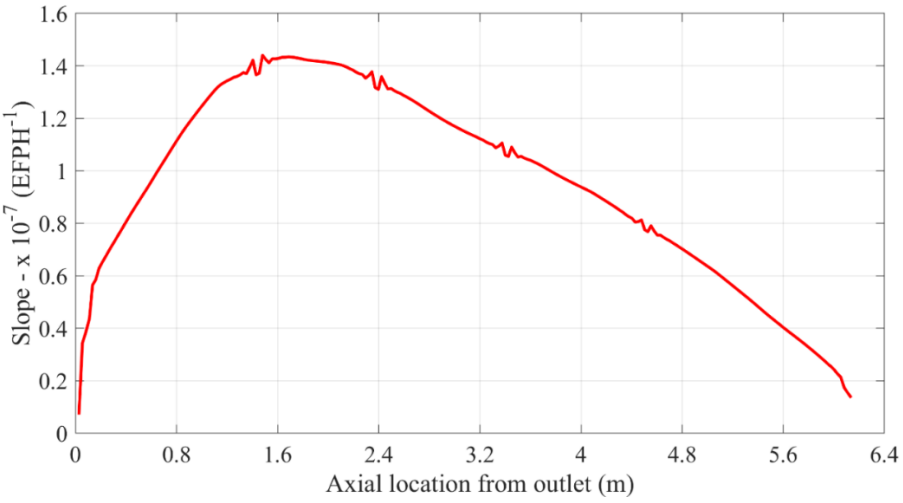

Figure 4.18: Slope obtained from linear regression of diametral strain and operating time

The diametral strain was predicted using the linear regression model for 220 kEFPH. The diameter was then computed from diametral strain and compared with the FEA prediction as shown in Figure 4.19. The error in prediction was computed as the difference in prediction between the regression model and 3D FEA ($Error = Surrogate\ model\ diameter - FEA\ diameter$). The error for three different time interval predictions is plotted in Figure 4.20. The prediction error

increases with increase in time interval for a regression model using linear regression. This shows that the diametral increase is not strictly linear and not increasing at the same strain rate. The mechanism leading to the deviation from linearity is the irradiation growth strain rate dependence on fluence. The growth rate in PTs is negative and decreases with fluence. Since the regression model couldn't account for the negative growth rate with time, this model always overpredicts the diametral strain by a small factor. To minimize the prediction error, a nonlinear form of regression model was developed as:

$$\varepsilon(x,t) = b_1(x) * t^2 + b_2(x) * t + b_3\left(x, t_{ref}\right) \tag{4.2}$$

where ε is the diametral strain, x is the axial location, t is the operating interval in EFPH, b_1, b_2 and b_3 are the coefficients obtained from nonlinear regression of the nominal profile at a time $t_{ref} < t$. The same procedure of computing the coefficients for linear regression was performed using nonlinear regression up to 150 kEFPH, which gave an R-square value approximately equal to one. Using the obtained coefficients, the nonlinear form of regression model was used to predict the diameter at various time intervals and the corresponding error is shown in Figure 4.21. Compared to linear regression model, the nonlinear form of regression model significantly reduces the prediction error at all axial locations. Unlike linear model, the nonlinear model prediction error remains almost constant with increase in time interval, showing that the nonlinear model accounts for nonlinearity introduced by irradiation growth. Therefore, the nonlinear form of regression model was used as an appropriate model for diametral creep modelling.

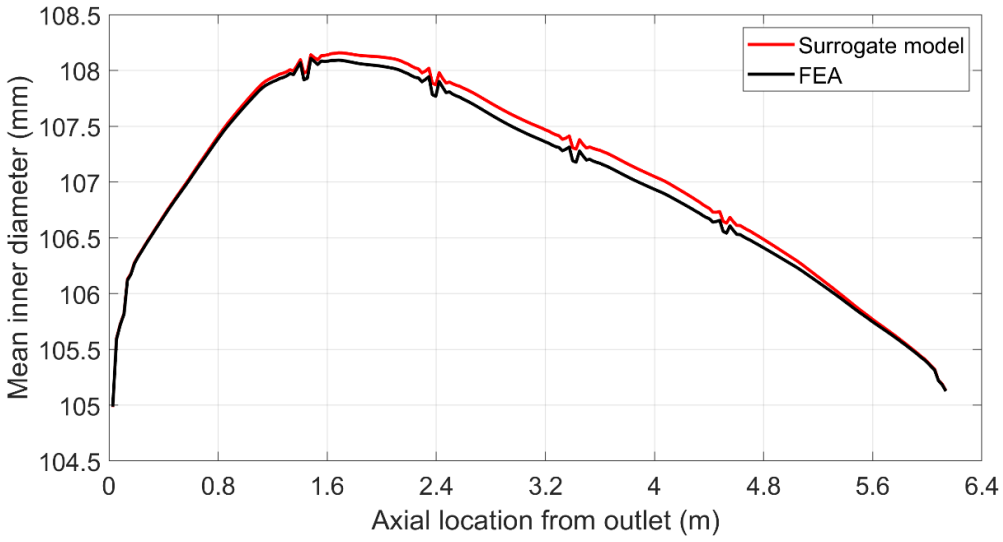

Figure 4.19: Comparison of diameter predicted using the regression model and the FEA at 220 kEFPH

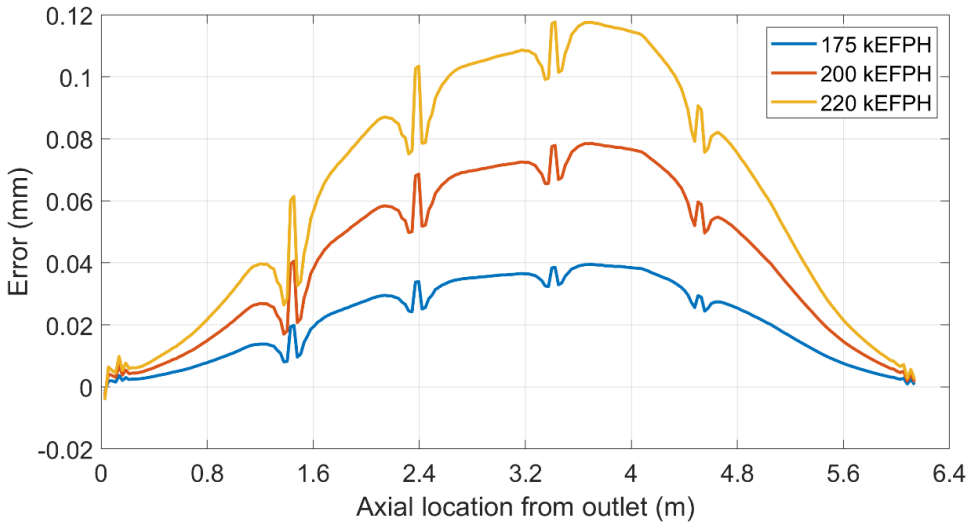

Figure 4.20: Error in diameter prediction between linear regression model and FEA at various time intervals

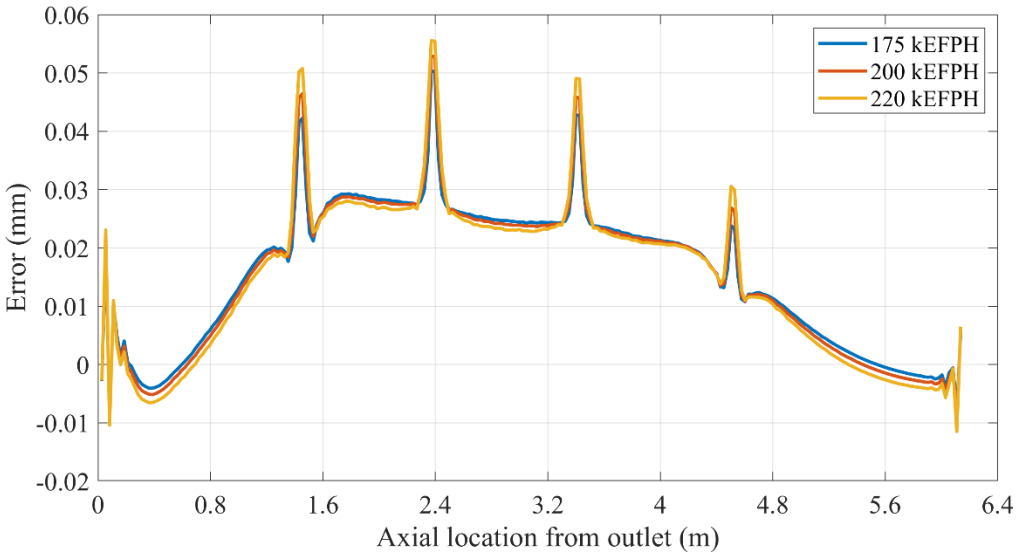

Figure 4.21: Error in diameter prediction between nonlinear regression model and FEA at various time intervals

4.4.2 Surrogate Model Accounting for Material Uncertainty

A significant advantage in the developing process of regression model is that it requires to run the 3D FE model only up to a small operating time (e.g., up to 100 kEFPH or less) to obtain the fitting parameters. Once a regression model is developed based on the given operating conditions, it can be used to replace the 3D FE model for making future predictions. As described in section 4.2, the diametral strain is affected by material uncertainties and hence required a calibration approach. Therefore, for developing a regression model for practical use, it should be able to account for these uncertainties. The introduction of scale factor into the regression model will give a complete model, which can be then considered as a surrogate model. As the diametral strains along the entire axial location is multiplied by the same scale factor, the regression model in Equation (4.2) can be expressed in a calibrated form as:

$$\varepsilon_{cal}(x,t) = SF * \left[b_1(x) * t^2 \ + b_2(x) * t \ + \ b_3\left(x, t_{ref}\right)\right] \tag{4.3}$$

where ε_{cal} is the calibrated diametral strain, SF is the scale factor, x is the axial location, t is the operating interval in EFPH, b_1, b_2 and b_3 are the coefficients obtained from nonlinear regression of the nominal profile at a time $t_{ref} < t$. The scale factor can be calculated for any inspected channel by comparing the measured data with the nominal prediction. For uninspected channels, a probabilistic approach can be used by using the probability distribution of scale factor for making risk-informed decisions.

The predictive capability of the surrogate model was validated by applying it to PT5, the PT which was used to validate the calibrated 3D FE model prediction in section 4.2.2.1. Nonlinear regression was performed up to 101,100 EFPH and the coefficients were saved in a matrix form. The scale factor was obtained as 0.96 as described in section 4.2.2.1. The surrogate model was then developed using the model in Equation (4.3) and the diametral strains were predicted for future time intervals and compared to the measured as shown in Figure 4.22. The nonlinear form of surrogate model gives a very good approximation of the diametral strains, and this shows the efficiency of the surrogate model. This simple form of surrogate model can now replace the computationally expensive 3D FE model for making diametral creep predictions.

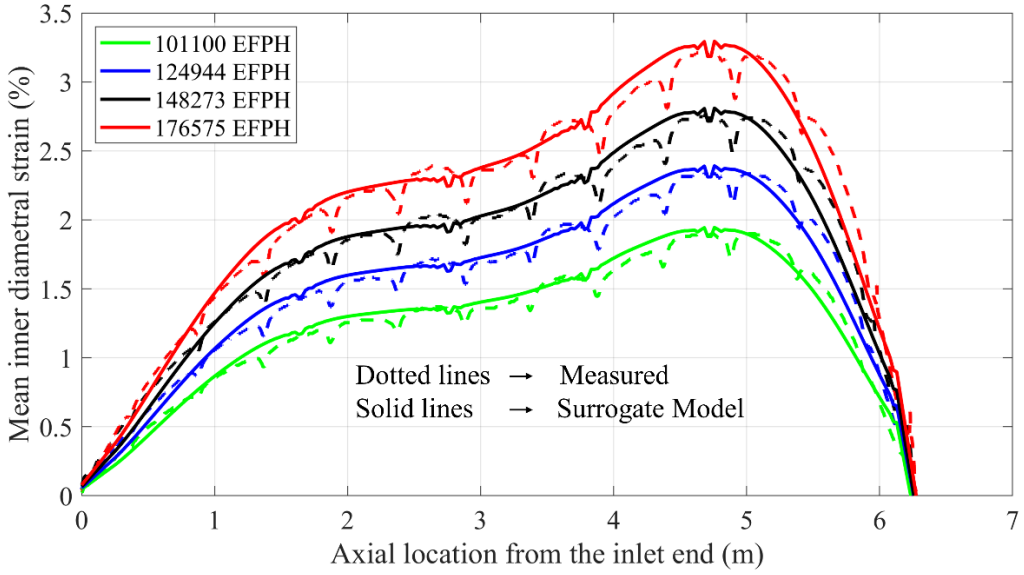

Figure 4.22: Comparison of measured and surrogate model predicted diametral strain of PT5 at various time intervals

4.5 Development of a Surrogate Model for PT-CT Gap

4.5.1 General

This section discusses the development of a surrogate model for PT-CT gap based on 3D FEA. The 3D FE model described in Chapter 2 is a deterministic model with nominal values of model parameters, and therefore predicts the nominal gap profile. However, the PT-CT gap is influenced by various uncertainties emanating from material properties and boundary conditions. The variability assessment in these parameters is established by comparing the predictions with data obtained from the in-service gauging of FCs and the statistical study of material inspection data (Nadeau, 2012; Nadeau et al., 2007). It is important to understand how the variability in these parameters influence the PT-CT gap. Using 3D FEA, this section studies the nature of PT-CT gap

evolution and the contribution of uncertain parameters towards the gap evolution. Based on the findings, a surrogate model is developed as a function of these uncertain parameters. The surrogate model is validated and the applicability of these models for PT-CT gap calibration is studied.

4.5.2 Variables Affecting PT-CT Gap

PT-CT gap is affected by several model parameters (Holt, 2008), which include the FC dimensions, loading history, material properties, coefficients of the various mechanisms in the analytical expressions describing PT and CT creep, and boundary conditions such as end slopes at the inlet and outlet ends of the channel. However, some variables do not exhibit any significant variation from their nominal design values, and so they are not likely to contribute to the risk of PT-CT contact in any appreciable manner. For example, the elastic modulus of zirconium alloys, weight of nuclear fuel and length of FC are modelled as deterministic constants due to insignificant variations. In this manner, most variables can be removed from the probabilistic analysis, except the two groups described next.

The first group involves variables related to the deformation equations describing the in-reactor deformation of CT and PT alloys. A simplified approach is used to model the variation in deformation rates due to the unavailability of statistical information of various parameters involved in the creep deformation equation. A scaling factor called the creep factor is used to scale the overall creep strain computed by the nominal deformation equation (Nadeau, 2012). In the FE model, the creep factor was incorporated in the UMAT subroutine, and the scaling was performed by multiplying the creep strain increment computed by the corresponding deformation equation with the creep factor at each time increment.

The second most influential variable is the slope of the FC centre line at the inlet and outlet ends of the channel. Note that inlet and outlet ends are modelled as fixed ends with respect to the bending of FC, but the end slopes are not necessarily zero due to tilting of the end fittings caused by fueling operation (Nadeau, 2012). The end-slopes were applied by assigning respective end-slope values to the rotational degree of freedom in the downward direction to the rigid nodes at the centre of the PT ends, leading to a tilt at the ends.

4.5.3 Understanding the Nature of PT-CT Gap

This section focuses on evaluating the nature of gap variation and its dependence on the input variables using 3D FEA. The decrease in PT-CT gap as a function of time at various fixed axial locations (on the PT axis) for a nominal model is shown in Figure 4.23. It is interesting to note that after about 40 kEFPH the gap versus time is almost linear. Therefore, for an FE model with no uncertainty accounted, a similar linear regression model given in Equation (4.1) is applicable. The PT-CT time to contact (i.e., zero gap) at any given location is the time at which the PT first contacts the CT, and it can be estimated by extrapolating the linear portion of the gap versus time curve. It is clear from Figure 4.23 that the time to contact at the given axial locations exceeds 220 kEFPH.

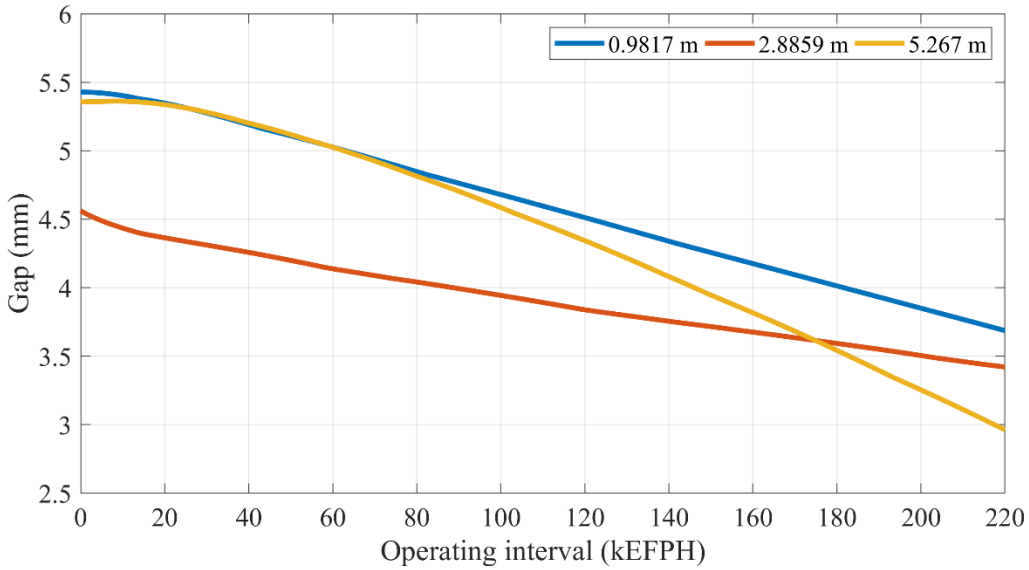

Figure 4.23: Predicted reduction in PT-CT gap as a function of time at various axial locations from the outlet end

As discussed in the previous section, the PT-CT gap is most sensitive to the creep factor and end slopes of the FC and the nature of variation of the gap with these two variables is investigated. As shown in Figure 4.24, the PT-CT gap at a given time and location can be modelled as a linearly decreasing function of the creep factor, while the end slope at both ends is fixed at 0.002 radians (downward). Similarly, Figure 4.25 shows that the gap decreases linearly with the end slope as well, when the creep factor is fixed at 1. This trend in gap evolution was observed for all axial locations and time.

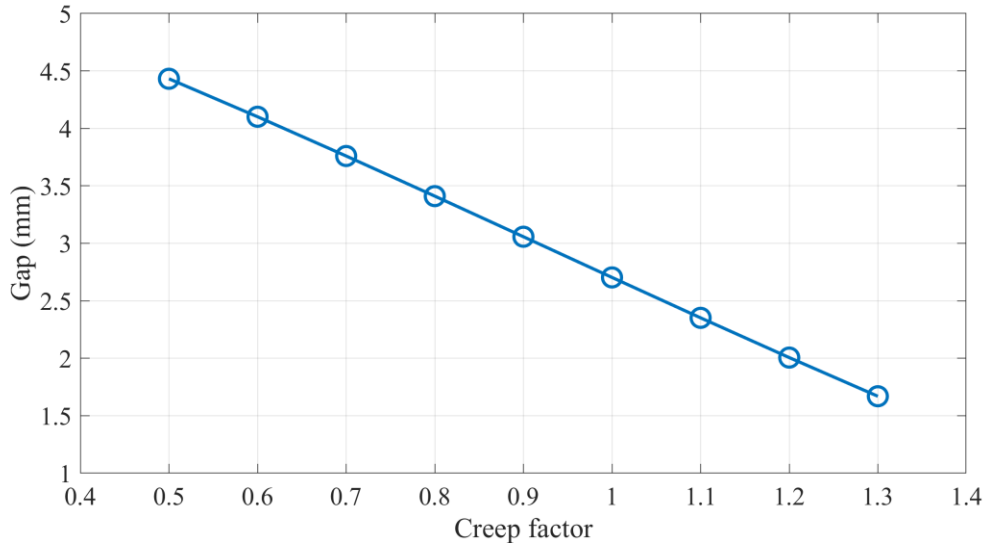

Figure 4.24: Predicted PT-CT Gap vs. creep factor at a fixed location (x =5.267 m) and time 220 kEFPH (the two end-slopes are fixed at 0.002 rad)

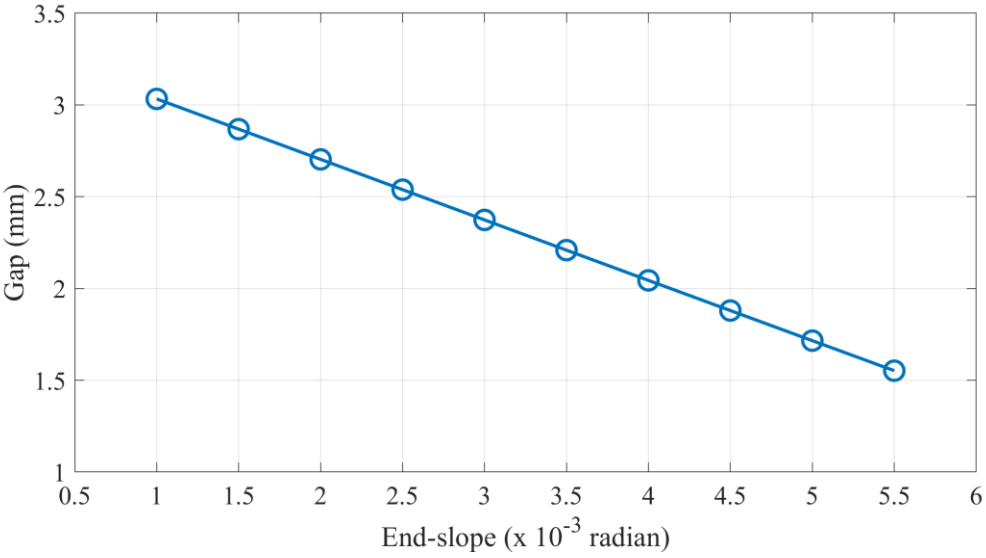

Figure 4.25: Predicted PT-CT Gap vs. end slope at a fixed location (x =5.267 m) and time 220 kEFPH (the creep factor is fixed at 1)

4.5.4 Surrogate model development

The inspiration for the development of the surrogate model was drawn from the Dimensional Reduction Method (DRM), which can be used to approximate any complex and multivariate function by a sum of univariate functions of the form (Zhang & Pandey MD, 2014):

$$G(x,t) \approx b_0 + b_1(x,t)A_1 + b_2(x,t)A_2 + \cdots + b_n(x,t)A_n \quad (4.4)$$

$$\text{or,} \quad G(x,t) \approx b_0 + \sum_{i=1}^{n} b_i(x,t)A_i$$

where $G(x,t)$ is the PT-CT gap at an axial location x and time t, $b_i(x,t),\ i = 0, 1, \ldots n$, are the surrogate model coefficients to be determined in a suitable manner and $A_1, \ldots, A_n$ are n random parameters used in the FEM.

The results presented in Figure 4.24 and Figure 4.25 showed a linear variation of PT-CT gap at a given axial location and time. To investigate the generalization of this observation, the PT-CT gap was recorded for various combinations of creep factor and end-slopes at a particular time interval and axial location. Figure 4.26 shows a 3D plot of the PT-CT gap after 220 kEFPH operating time and an axial location of 5.267 m from the outlet.

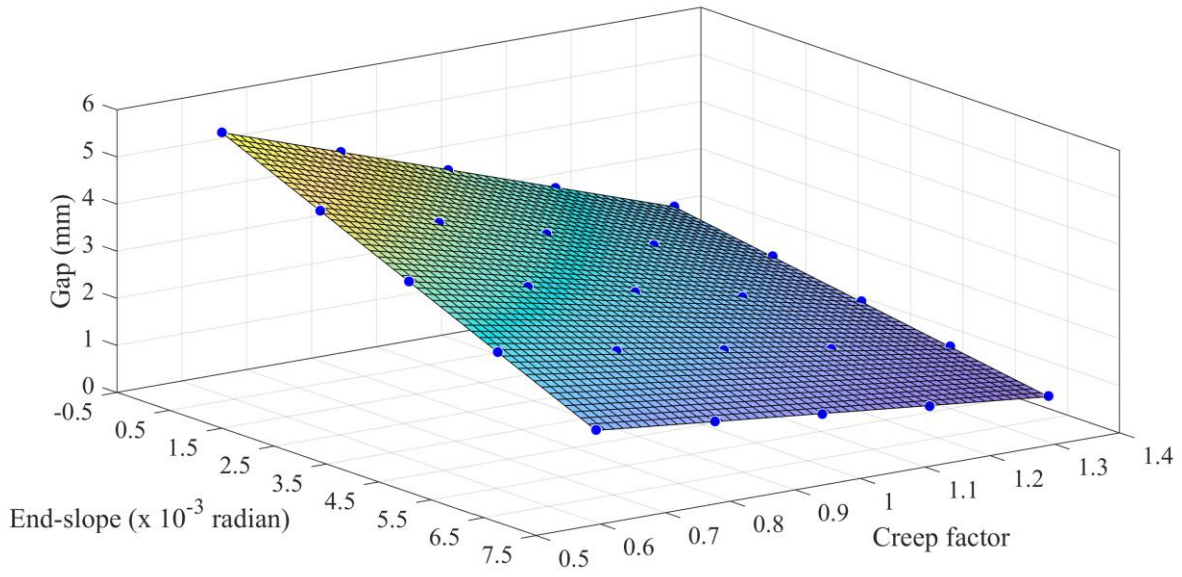

Figure 4.26: Predicted PT-CT gap as function of the creep factor and end slopes (3D surface), at PT axial location x = 5.267 m and 220 kEFPH operating time

It is interesting to note that these results can be accurately described by a quadratic surface, which can be expressed by the following equation:

$$G(x,t) = b_0 + b_1 * C + b_2 * S + b_3 * C^2 + b_4 * C * S + b_5 * S^2 \qquad (4.5)$$

Here the variables C and S are the creep factor and end slope, respectively. For location x = 5.267 m and time t = 220 kEFPH, a quadratic surface was fitted to the FEM results using multiple linear regression. An R-square value of 1.00 was obtained for the quadratic fit, whereas 0.93 was obtained for a linear fit. This indicates an excellent goodness-of-fit for the quadratic surface. Only 25 FE simulations were required to effectively fit the surface and develop an accurate surrogate model. The derived values of the coefficients of the gap model were $b_0 = 7.838$, $b_1 = -4.62$, $b_2 = -759.2$, $b_3 = 0.1402$, $b_4 = 430$ and $b_5 = 228.3$. It is important to note here that a quadratic fit indicates that the gap varies non-linearly when the creep factor and end-slopes take

extreme values, as compared to a perfect linear fit when one of the variables is fixed to the average value. Since the gap varies along the length of the PT, the PT-CT gap model coefficients will also vary as a function of axial location. Using a similar approach as shown in Figure 4.26, a quadratic surface was fitted to PT-CT gap values for each of the 235 axial locations along the PT axis and the coefficients were recorded in a matrix form as a function of axial location.

The surrogate model in Equation (4.5) requires both end slopes to be the same and therefore couldn't be used for practical applications. To consider the individual influence of each end slope on the gap profile, additional FEA simulations were run by varying one end slope at a time and fixing the other at a constant value as shown in Figure 4.27 and Figure 4.28. The outlet end slope mainly influences the gap at Span S1 and S2. Similarly, the inlet end slope has a significant influence on Span S5 and S4. Both end slopes have minor influence on the middle span. The effect of end slope at the inlet (S_i) and at the outlet (S_o) on the gap can be expressed as the superposition of the effect of individual slopes. Equation (4.5 can be then rewritten as:

$$\begin{aligned} \mathrm{G}(x,t) = \mathrm{b}_0 + \mathrm{b}_1 * \mathrm{C} + \mathrm{b}_{21} * S_o + \mathrm{b}_{22} * S_i + \mathrm{b}_3 * \mathrm{C}^2 + \mathrm{b}_{41} * \mathrm{C} \\ * S_o + \mathrm{b}_{42} * \mathrm{C} * S_i + \mathrm{b}_{51} * S_o^2 + \mathrm{b}_{52} * S_i^2 \end{aligned} \tag{4.6}$$

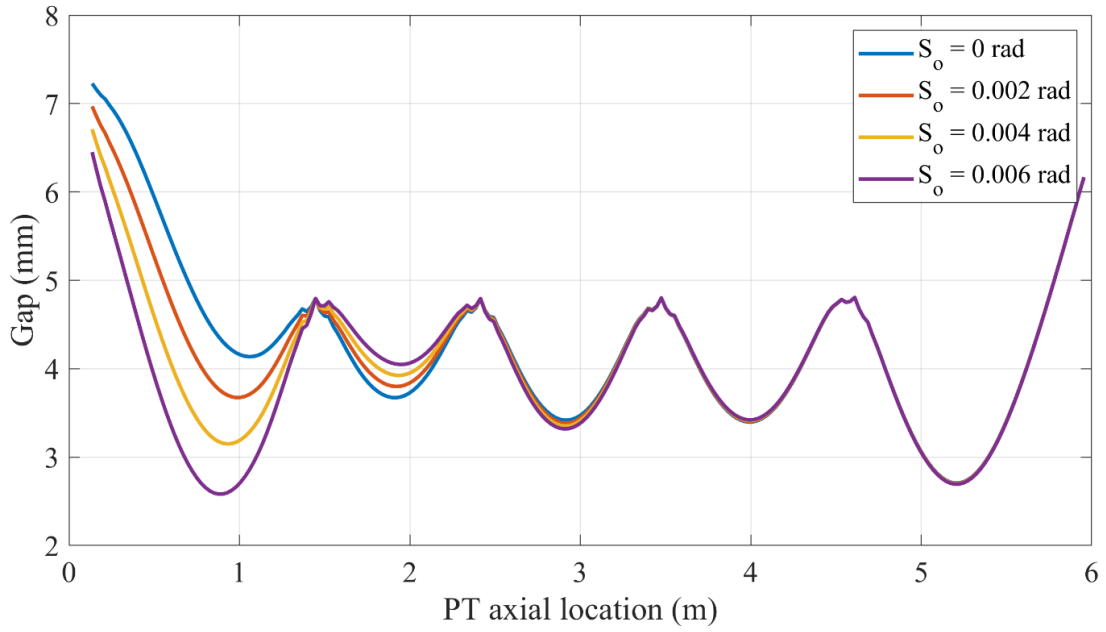

Figure 4.27: Gap profiles for various values of outlet end slope at 220 kEFPH (CF = 1 and $\boldsymbol{S_i}$ = 0.002 rad)

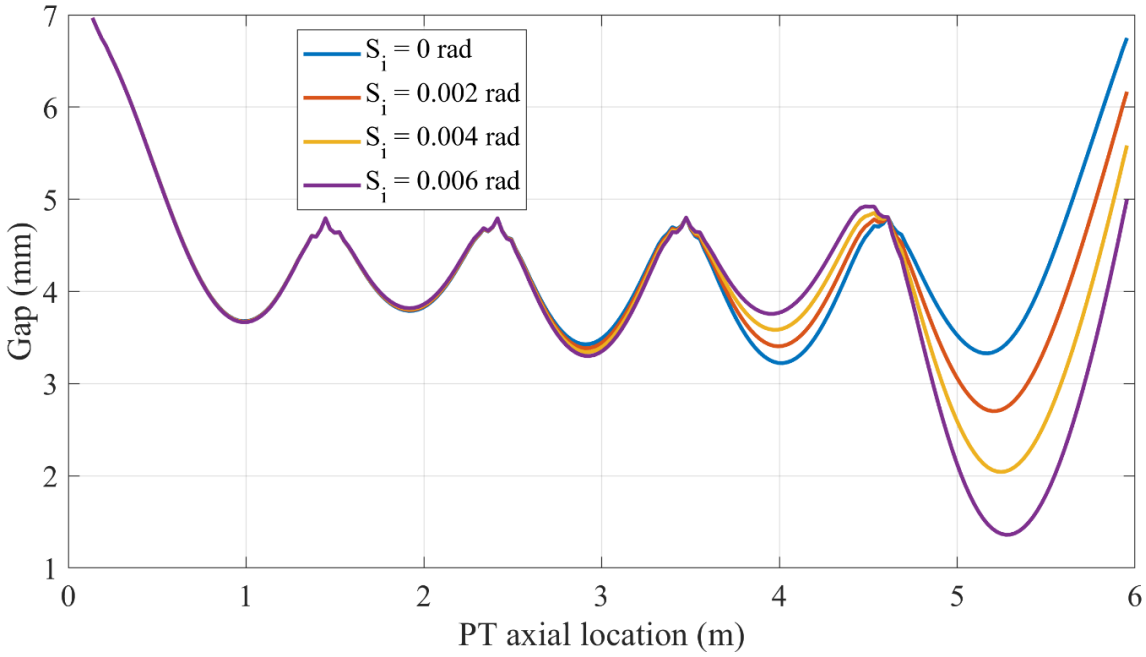

Figure 4.28: Gap profiles for various values of inlet end slope at 220 kEFPH (CF = 1 and $\boldsymbol{S_o}$ = 0.002 rad)

4.5.4.1 A Study on Model Coefficients

The first four coefficients in Equation (4.6) are plotted as a function of the axial location at a fixed time of 220 kEFPH in Figure 4.29. The magnitude of variation in the model coefficients reflects the effect of a particular variable on the PT-CT gap. For example, the end slope coefficients (i.e., b_{21} *and* b_{22}) in the inlet and outlet spans are considerably higher, and their values in the internal spans are close to zero. This suggests that the end slopes mostly affect the gap in the outer (inlet and outlet) spans.

Similarly, the variation of creep coefficient shows that creep has a pronounced effect on the gap in the outer spans and a modest effect in the central span. The PT-CT gap in the inlet span (the right most span), being axially free, is the most sensitive to the creep factor as well as the end slopes of the FC.

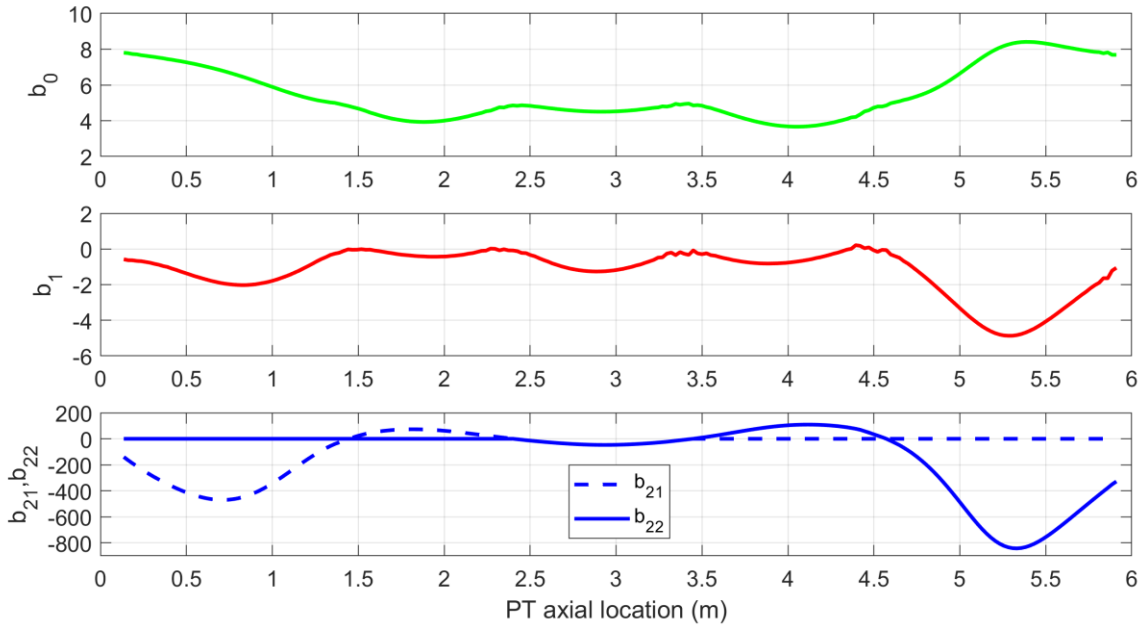

Figure 4.29: Variation of the first four coefficients in Equation (4.6) of the PT-CT gap model as a function of the axial location (at a fixed time of 220 kEFPH)

The Coefficients of the Surrogate Gap Model as a Function of Time

It was shown in the previous section that the PT-CT gap can be expressed as an additive combination of the creep factor and end slopes. Since the sag and gap profiles change with time, the coefficients of the surrogate model would also change with time. Thus, the surrogate model of PT-CT gap can be expressed in a more general form as

$$\begin{aligned} \mathrm{G}(x,t) = {} & \mathrm{b}_0(x,t) + \mathrm{b}_1(x,t) * \mathrm{C} + \mathrm{b}_{21}(x,t) * S_o + \mathrm{b}_{22}(x,t) * S_i \\ & + \mathrm{b}_3(x,t) * \mathrm{C}^2 + \mathrm{b}_{41}(x,t) * \mathrm{C} * S_o + \mathrm{b}_{42}(x,t) * \mathrm{C} * S_i \\ & + \mathrm{b}_{51}(x,t) * S_o^2 + \mathrm{b}_{52}(x,t) * S_i^2 \end{aligned} \qquad (4.7)$$

Model coefficients versus axial location plots, similar to Figure 4.29, were computed again for different time intervals ranging from 50 kEFPH to 220 kEFPH. For reasons of brevity, only the coefficients that have the most significant effect on the gap profile will be further discussed in detail here. Results of this analysis are presented in Figure 4.30. From Figure 4.30, coefficient b_1 (i.e., the coefficient related to the creep factor) is a strong function of reactor operating time. The gap in the outlet and inlet spans S1 and S5, as well as in the central span S3 is strongly influenced by the creep factor. The values of this coefficient in the two internal spans, S2 and S4, are comparatively less affected by the creep factor for the type of FC analyzed here. For other types of FC configurations, the effect of the creep factor can be however different.

Regarding the dependence of coefficients b_{21} and b_{22} (i.e., the coefficients related to end-slopes) on axial location and time, a significant variation of the gap due to changes in the end slopes is observed in spans S5 and S1, as expected. Since the profiles of b_{21} for various times (from 50 to 200 kEFPH) are almost identical in all the spans, b_{21} can be considered as time invariant.

However, the axial variation of b_{22} is significant in span S5 indicating the strong dependence of the minimum gap in this span on the inlet end slope (S_i).

The variation of coefficients b_{41} and b_{42} accounts for the combined contribution of the creep factor and end-slopes. As expected, the combined effects are significant in the outer spans with the largest variation observed in Span S5. Coefficient b_{42}, which expresses the combined effect of the creep factor and inlet end-slope on the minimum gap, contributes the most in the inlet span. It is the contribution of coefficients b_{41} and b_{42} that accurately approximates the gap profile when the various parameters acquire extreme values.

The next question is in regard to the nature of variation of the coefficients with time. Since all the coefficients showed a similar trend, only the results based on b_{41} and b_{42} are discussed here. These coefficients plotted versus time for two axial locations along the PT are shown in Figure 4.31. Only two axial locations were chosen in Figure 4.31 because these coefficients appear to be independent of operating time and axial location for the inner spans.

It is evident from this figure that coefficient b_{42} in the inlet span (solid red line) varies as a function of both axial location and time, whereas this coefficient is zero in the outlet span (solid blue line). In contrast, coefficient b_{41} varies less with time and axial location in the outlet span (dotted blue line) but it is also zero in the inlet span (dotted red line). This is indicative of the variability in the gap in the outer spans being larger compared to that in the inner spans. Another important observation is that the coefficient b_{42} in the inlet span appears to increase exponentially with time, indicating the increased likelihood of PT-CT contact in this span.

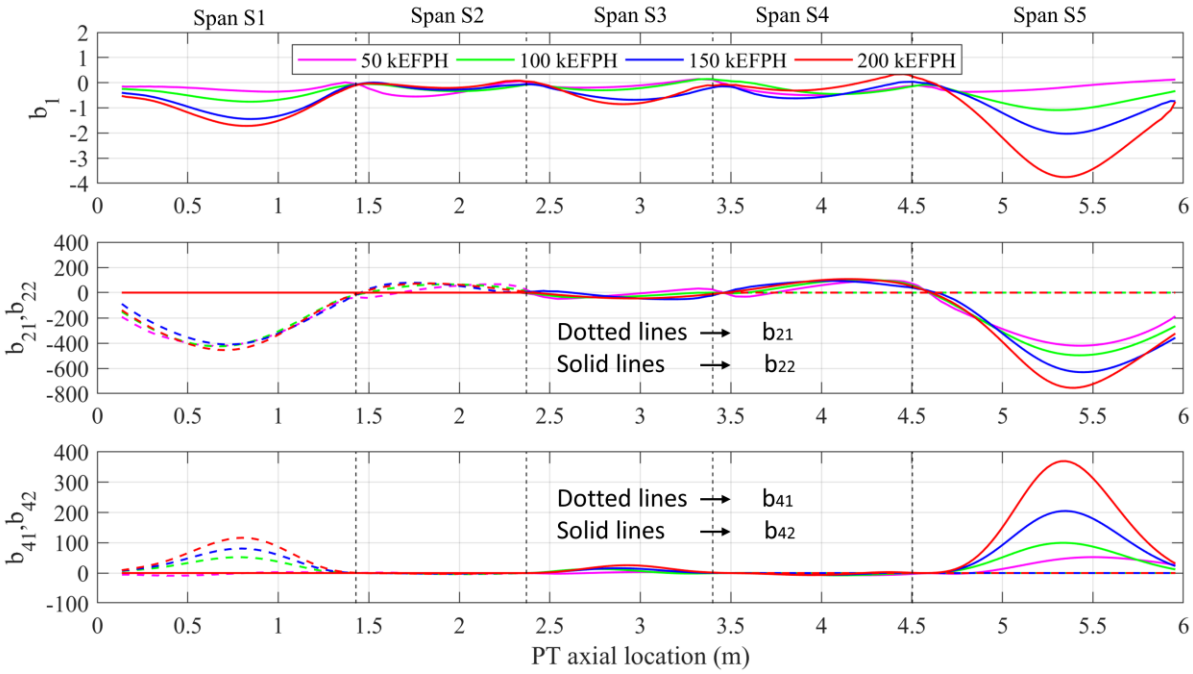

Figure 4.30: Variation of some coefficients in Equation (4.7) with axial location and time

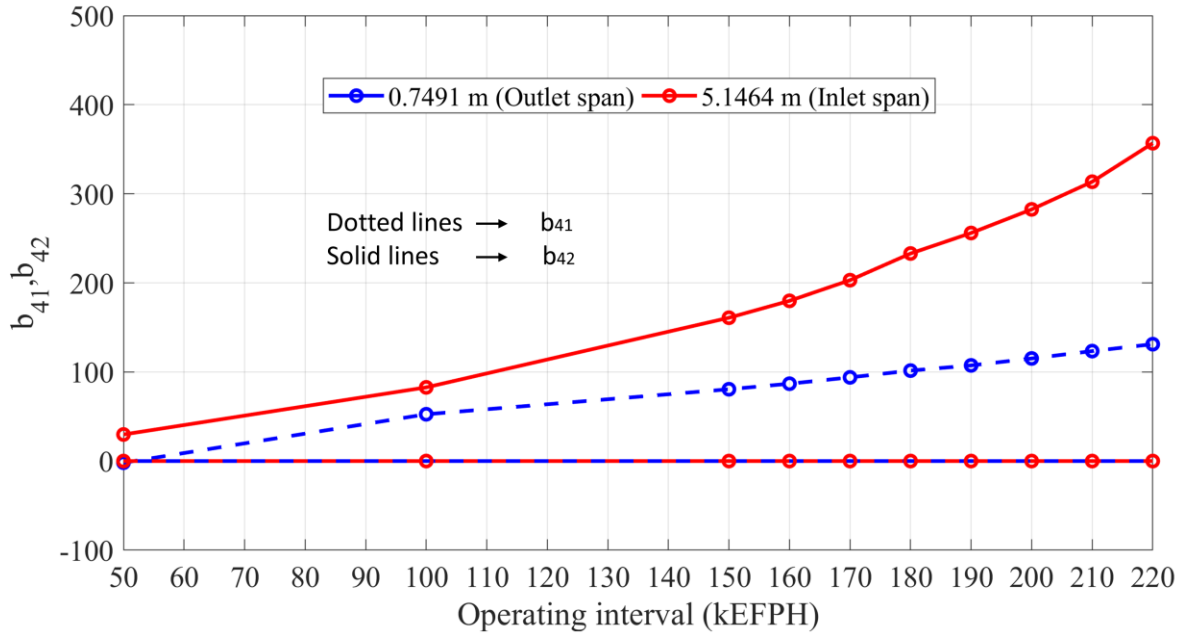

Figure 4.31: Variation of coefficients b41 and b42 with time at three different PT axial locations

4.5.4.2 Surrogate Gap Model Verification

The coefficients in Equation (4.7) obtained through the quadratic fitting were saved in a matrix form as a function of the PT axial location and time. This surrogate model can then replace the full 3D FEM model in the ABAQUS code. To evaluate the accuracy of the proposed surrogate model, PT-CT gap profiles at (i) 150 kEFPH with $\mathrm{C} = 0.822$, $S_o = 0.001$ rads and $S_i = 0.002$ rads and, (ii) 220 kEFPH with $\mathrm{C} = 1.212, S_o = 0.003$ rads and $S_i = 0.005$ rads, were predicted by the surrogate model and compared to those calculated by the 3D FEM code as shown in Figure 4.32. The maximum gap error was computed as 0.063 mm in the central span whereas the gap error for the minimum gap was 0.009 mm. This confirms that there is a strong agreement between the surrogate formulation and the predictions using the full 3D FEM code.

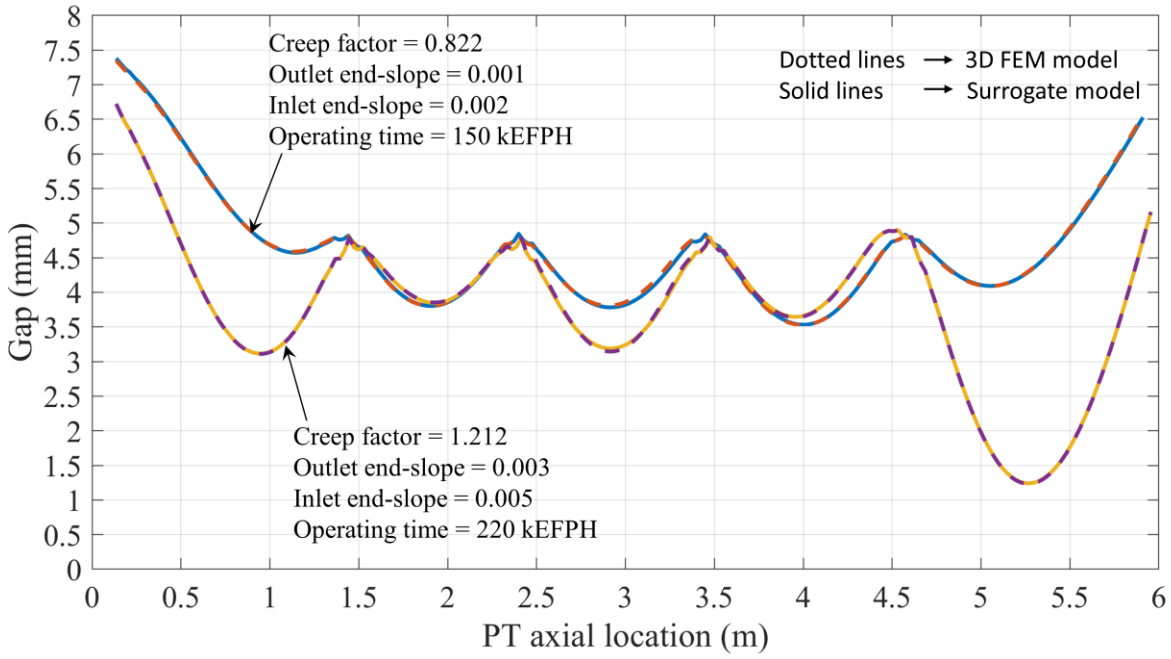

Figure 4.32: PT-CT Gap profiles predicted at two different times by the surrogate model and the FEM model

4.5.4.3 Comparison of Results from 1D and 3D Surrogate Models

In this section, the time to reach a minimum gap of 1 mm is predicted by using different surrogate models and compared to the ABAQUS 3D FEM result. The creep factor, outlet end slope and inlet end slope were set as 1.1, 0.002 and 0.004, respectively. The following surrogate models were used:

1) Model 1 - The current surrogate model with quadratic fit based on 3D FEM (Equation (4.7))
2) Model 2 - The surrogate model with linear fit based on a 1D FEM (Equation 7 in (Pandey et al., 2018))
3) Model 3 - The surrogate model with linear fit based on a 3D FEM (This model was developed using the same approach as given in (Pandey et al., 2018) using 3D FEM results).

The results are shown in Table 4.2. Models 1 and 3 slightly over predict and under predict the time to reach 1mm gap, but the prediction error is low. However, Model 2, which is based on the 1D FEM, significantly over-predicts this time. This shows the disadvantage of using a 1D FEM in PT-CT contact analyses. Given that 7 kEFPH is approximately the number of EFPH in one calendar year, the 1D model overpredicts the time to contact by 38 kEFPH or almost 5.5 calendar years.

A further analysis using Model 1 and Model 3 showed a better prediction of minimum gap using Model 3, especially when the variables take extreme values. The error in Model 3 is primarily due to the use of linear form of surrogate model. However, the advantage of Model 1 is that it has the time parameter in the surrogate model form, whereas Model 1 is more accurate in gap prediction

but does not include the time parameter.

Table 4.2: Time predicted to reach 1 mm minimum gap by three different models

Model	**Time predicted to reach 1mm gap (kEFPH)**	**Prediction error (%)**
Result using the 3D ABAQUS FEM	261	N/A
Model 1	265	+ 1.53
Model 2	299	+14.56
Model 3	255	-2.30

4.5.5 Use of Surrogate Model in Calibration of FEM Model

For practical purposes, the FEM must be calibrated by comparing the FEM predictions with inspection results. Once the FEM of a given FC is calibrated, it can be used successfully to predict future behaviour and optimize inspection and maintenance schedules or make end-of-life decisions. For example, the acceptance standard for PT-CT contact in CSA N285.4 requires to meet the condition that no PT-CT contact predicted to exist at the end of the next periodic inspection interval, considering the as-found annulus spacer locations (CSA N285.4, 2010). A well calibrated model would be of great advantage to demonstrate these conditions are met, and it would aid in optimizing the inspection intervals.

The development of the 3D FEM model in Chapter 3 was based on the mean behaviour of FC deformation and the predictions agreed well with the measurements (Figure 3.19 and Figure 3.20), an observation that provides a degree of validation of the FEM approach. However, there is significant variability in the in-reactor behaviour of FCs, which is responsible for the observed

variation in the measured gap and diametral profiles. Therefore, the calibration of the FEM must involve the identification of the factors that are mainly responsible for the observed behaviour and the determination of their variability range. Two main issues were identified while calibrating the FE model:

1) The determination of the appropriate parameter values in the FEM that require adjustment until a satisfactory agreement of the prediction with measurements is obtained. For instance, the parameters that were adjusted were chosen such that the predicted PT-CT gap fit reasonably well compared to inspection results.
2) The 3D FEA is a computationally expensive task (a single run takes up to 3 hours). Therefore, the calibration process must be completed with a minimum number of FEA runs.

As is discussed next, a computationally efficient approach was developed to overcome both of these issues in order to successfully calibrate the FEM model.

4.5.5.1 Calibration using the Surrogate Model

The first issue stated above was solved by choosing the creep factor and the two end slopes as appropriate parameters to be adjusted for calibrating for the gap profile. The second issue was solved by replacing the 3D FEM model by the surrogate model, which requires only a few FEM model runs in the process of developing. The calibration procedure is as follows:

1) Compare the PT-CT gap obtained from the surrogate model to the inspection gap data at three axial locations, namely, location of minimum gap with the highest weightage, location were the inlet and outlet slopes are reasonable influenced.

2) Find the optimized values of the creep factor, the inlet slope and the outlet slope by minimizing the gap error at the three selected axial locations.
3) Input the optimized parameter values to the 3D FEM model and verify the accuracy of the gap prediction by comparing with the inspected gap data.

4.5.5.2 Calibration Example of a FC

The aim here is to calibrate and verify the PT-CT gap profile obtained from the calibrated 3D FEM model with those obtained from the in-service inspection of a FC. Note that the garter spring locations and the operating conditions of the FC analyzed for validation here are different than the one analyzed in Chapter 3 as an example. The details of the FC used for calibration are as follows:

1) The PT inlet is on the left and outlet is on the right.
2) The back end of the PT is placed at the outlet
3) The reactor unit was reconfigured at 124,944 EFPH
4) Prior to reconfiguration, the inlet end (left end) was fixed and the outlet end (right end) was axially free. After reconfiguration, the boundary conditions are reversed.

Two sets of inspection data were available. The first set included the PT-CT gap profile at 148,273 EFPH and the second set included the PT-CT gap measurements at 176,575 EFPH. The FEM model was initially calibrated for the PT-CT gap profile at 148,273 EFPH using the steps described above. Using the surrogate model for calibration, the optimum values of the creep factor, inlet end slope (left end) and the outlet end slope (right end) were obtained as 0.99, -0.004 rad and 0.000 rad. The three minimization points chosen, and the calibrated gap profile are shown in Figure 4.33. The calibrated model (i.e., the model which uses the creep factor, 0.99, inlet end slope -0.004 and

outlet end slope 0.000) was then used to predict the gap profile and diametral profile at 176,575 EFPH using the 3D FEM in ABAQUS as shown in Figure 4.34 and Figure 4.35. The predicted values are in good agreement with the measurements obtained from inspection and also accurately predict the minimum gap.

This is a powerful tool for the nuclear industry as the approach will help in confidently predicting future gap profiles. This will assist in reducing the expensive inspection tasks, which would be a significant economic benefit for the industry.

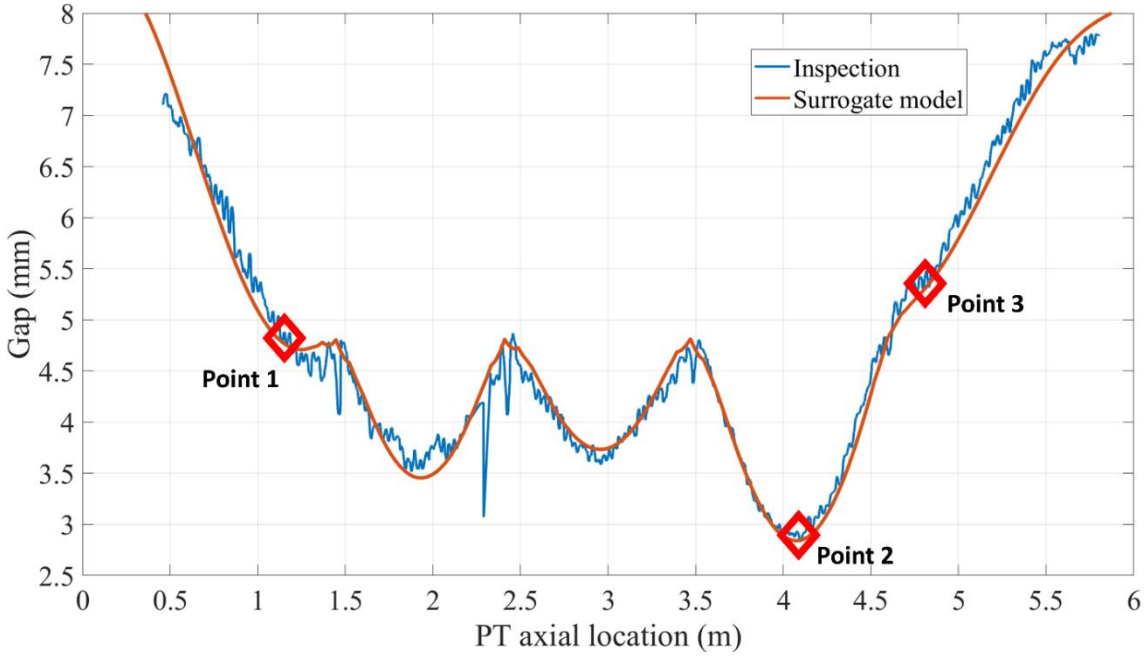

Figure 4.33: Gap minimization points and the calibrated gap profile at 148,273 EFPH using the surrogate model

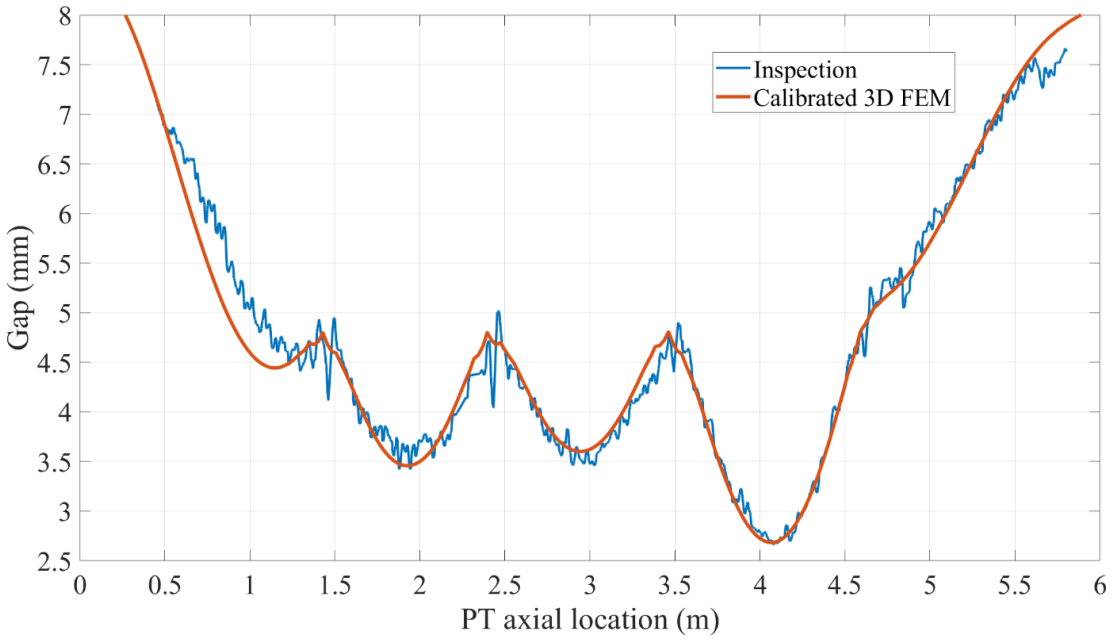

Figure 4.34: Comparison of the inspected and predicted gap profiles using the calibrated 3D FEM model at 176,575 EFPH

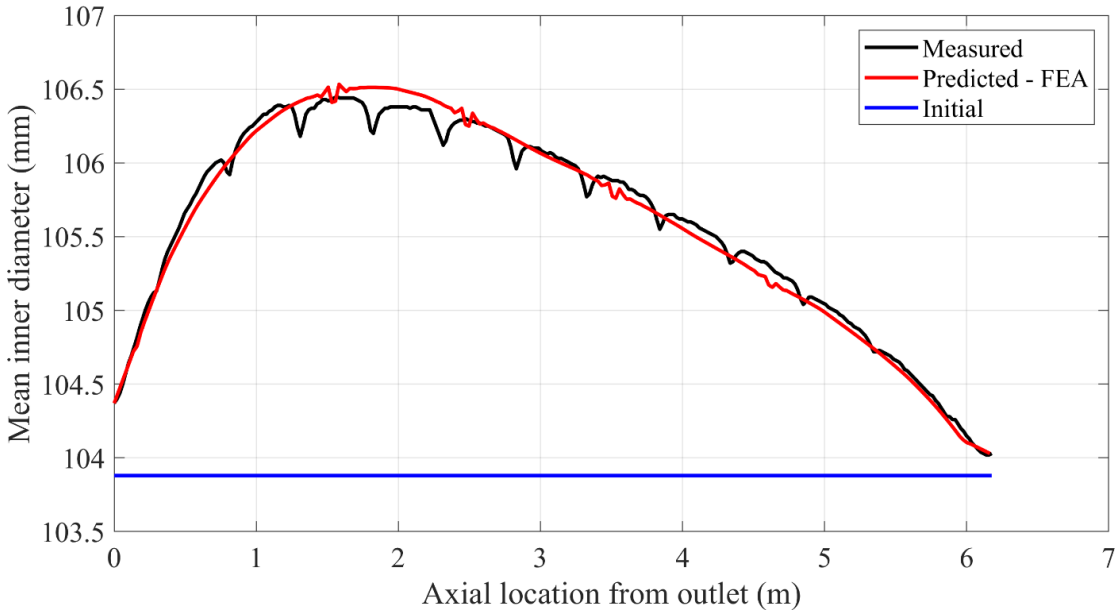

Figure 4.35: Comparison of the measured and predicted diametral profile using the calibrated 3D FEM model at 176,575 EFPH

4.6 Conclusions

This chapter presented the development of surrogate models and calibration approaches for diametral creep and PT-CT gap profiles. The 3D FE model of in-reactor deformation of FCs is a computationally expensive model, and therefore a surrogate model is of significant advantage. The material uncertainty in diametral creep was captured by introducing a parameter called as “scale factor”, which was successful in calibrating the 3D FE model. A more detailed analysis was then performed using 3D FEA and realistic flux profile inputs for investigating the diametral creep strain at the flux dip locations. It was concluded that even though the flux dip at the bundle joints is ~15%, the diametral creep drop by only ~10% because of material continuity, which agrees well with measured creep strain data.

A surrogate model was then developed by using a nonlinear relation between the diametral strain and the axial location and time. Together with the nonlinear form and scale factor, a calibrated surrogate model was developed which predicts the future deformation with good accuracy. This surrogate model, which is computationally cheaper than a 3D FEA, can be used as an easy-to-use and efficient tool by the industry.

Similarly, a surrogate model was developed for the prediction of PT-CT gap profile. The surrogate model is a quadratic function of two variables that substantially affect the deformation profiles, namely the creep factor and end slopes. This form of the surrogate model can capture the non-linear behaviour of the evolution of the PT-CT gap occurring when the creep factor and end slopes acquire extreme values. The surrogate model coefficients depend on the axial location along the PT axis and the operating time. These coefficients are saved as a function of location and time in a matrix form for subsequent use. A computationally efficient approach using a surrogate model

was developed for the calibration of the 3D FEM to incorporate the variability observed in FC in-service measurements. The calibration approach was successfully validated by accurately predicting the PT-CT gap and diametral expansion using the calibrated model. A calibrated 3D FEM can be successfully used to predict future dimensional changes and make risk-informed decisions on inspection and maintenance schedules as well as obtain end-of-life predictions. Similarly, fuel channels with different operating conditions can be analysed to develop a database of the best suited surrogate models for the performance of probabilistic assessments of an entire CANDU reactor core in a computationally efficient and inexpensive way.

The development of the model is supported by the following observations made from carrying out finite element analyses of the problem:

- The PT-CT gap at a given axial location and time is a linear function of the creep factor if the end-slopes are maintained at their average values.
- The PT-CT gap at a given axial location and time is also a linear function of the end slopes if the creep factor is maintained at its average value.
- The PT-CT gap at a given axial location and time becomes a non-linear function of the creep factor and end slopes when these parameters approach extreme values.

The surrogate model based on a 1D FEM appears to significantly over-predict (by 14.6 %) the time for PT-CT contact. Given that 7 kEFPH is approximately the number of EFPH in one calendar year, the 1D model overpredicts the time to contact by 38 kEFPH or almost 5.5 calendar years.

Chapter 5

Coupled Multiplicative Dimensional Reduction and Polynomial Chaos Expansion Method

5.1 Introduction

5.1.1 General

The uncertainty propagation methods are methods of propagating the uncertainty in the input parameters through a model (e.g., analytical or numerical) and computing the random model output. The uncertainty propagation using FE models paved the way for the integration of reliability analysis with the FEA, which is often termed as probabilistic finite element analysis (PFEA), stochastic finite element analysis (SFEA) or finite element reliability analysis (FERA). These methods are now becoming more popular in the engineering practice. The basic issues in the context of PFEA or SFEA are: (1) to minimize the functional evaluations, especially when the evaluation of the model is expensive, such as in a nonlinear FEA; (2) to accurately estimate the probability distribution of the output response, especially when the response function is defined in an implicit form as in the case of an FEA.

Regarding the first issue, the primary concern is the computational cost associated with the reliability analysis. We can use a very well understood and easy to implement method called Monte Carlo Simulation (MCS) but this will require an enormous amount of FEA simulations to be run.

This leads to an immense computational cost, especially when we solve expensive-to-evaluate FE problems. Hence, the practical application of PFEA using MCS is not a viable choice.

Regarding the second issue, it is of great interest that the entire probability distribution of the response be obtained, and the tail of the distribution is also known for computing failure probability. This becomes easy if the structural systems contain only a small number of random variables and the limit state functions are formulated analytically, i.e., in an explicit form. However, in the FEA, the output response is obtained through an implicit relation with the input random variables. Thus, even if we are able to compute the statistics of the response, i.e., mean, standard deviation, etc., we do not have enough knowledge about the entire probability distribution of the response. This means that we do not have knowledge of the tail of the probability distribution, which has the information about the failure probability.

Spectral methods such as polynomial chaos expansion (PCE) has proved to be a replacement for the traditional structural reliability methods. PCE alleviates the high computational cost associated with uncertainty analysis by replacing the otherwise expensive-to-evaluate numerical models (e.g., a finite element code) with simple-to evaluate surrogate models. However, computation of the PCE coefficients is expensive when the mechanistic model is expensive-to-evaluate and involve more number of input random variables (Debusschere et al., 2004). Hence, an efficient method is needed to reduce the computational cost associated with using PCE.

5.1.2 Objectives

The main objective of this chapter is to develop a general and efficient computational scheme for reliability and sensitivity analysis of structures, which are modeled and analyzed using

expensive-to-evaluate finite element models by considering the uncertainties in geometry, material properties, loads, etc. To achieve this objective, multiplicative dimensional reduction method (M-DRM) is coupled with polynomial chaos expansion (PCE) method, which significantly reduces the computational cost of PCE coefficient computation, and therefore the construction of surrogate model using PCE. The Monte Carlo Simulation (MCS) can be then performed using the surrogate model for obtaining the statistics and the entire probability distribution of the output response of interest.

5.1.3 Organization

The organization of this chapter is as follows. Section 5.2 firstly presents the necessary background on PCE, the formulation for developing a surrogate model using PCE and the limitations in using this method for probabilistic FEA due to the computational cost associated with PCE coefficient computation. Section 5.3 presents the mathematical formulation of M-DRM and its potential use in minimizing the computational effort of a multidimensional integral. Section 5.4 shows how M-DRM can be combined with PCE (coupled M-DRM and PCE method) to achieve a significant reduction in the computational cost of PCE coefficient computation and therefore use it as an efficient method for surrogate model development of expensive-to-evaluate FE models for performing probabilistic FEA. Section 5.5 presents the Gauss quadrature scheme, which is an important tool required before applying the coupled M-DRM and PCE method. Section 5.6 illustrate the implementation of the proposed method through a simple example and the obtained probabilistic results are compared against the MCS results for validation. Finally, conclusions are summarized in Section 5.7.

5.2 Polynomial Chaos Expansion

5.2.1 Background

The term polynomial chaos was first introduced by Wiener in 1938 to model stochastic processes with Gaussian random variables (N Wiener, 1938). In his work, he used Hermite polynomials to serve as orthogonal basis and the validity of this approach was later proved by Cameron and Martin (Cameron & Martin, 1947). After drawing inspiration from the theory of Wiener-Hermite polynomial chaos, Ghanem and Spanos introduced polynomial chaos expansion into stochastic mechanics by 1991 (Ghanem & Spanos, 1991). They considered a boundary value problem by modeling the input parameters as random fields and employed Hermite polynomials as a complete base to represent these random fields. The output random quantities of interest were the displacement and stress fields. Following their work, this approach was successfully applied to other practical engineering problems (Ghanem, 1998; Le Maˆıtremaˆıtre et al., 2002). Thus, the use of PCE has been closely associated with spatial variability and was considered as a separate topic with respect to structural reliability for a while, until it was illustrated for the first time by Sudret and Der Kiureghian (Sudret & Der Kiureghian, 2002b).

Albeit the mathematical soundness of Hermite polynomials with Gaussian distribution, difficulties arose in applications involving the convergence and probability approximations for non-Gaussian problems (Orszag & Bissonnette, 1967). The work by Xiu helped in overcoming these difficulties. In his work, he generalized the result of Cameron-Martin to various continuous and discrete probability distributions using the so-called Askey-scheme of orthogonal polynomials (Xiu & Karniadakis, 2002). This is proposed in literature as generalized polynomial chaos and based on

this framework, it depends on the probability distribution of an input variable to select the representative orthogonal polynomial. Fast and optimal convergence can be obtained by choosing a proper basis for each random variable and the effectiveness of using the generalized polynomial chaos was later demonstrated (Xiu & Em Karniadakis, 2002; Xiu & Karniadakis, 2003).

Once a suitable basis is chosen based on the distribution of random variables, the next step is to compute the PCE coefficients through a numerical technique. It should be noted that the basic idea of PCE is the polynomial decomposition of the uncertain variables, where the uncertainty is concentrated in the polynomials and the unknown coefficients of the decomposition become deterministic.

In the initial works of PCE coefficient computation, Ghanem used the Galerkin method which minimized the error of a finite-order expansion by an orthogonal projection (Ghanem & Spanos, 1991). This method is called the stochastic Galerkin approach and has been called “intrusive” in the sense that it requires the governing equations to be altered for each problem. It was used to solve elliptic stochastic partial differential equations. Once the variational form of the equations are given, the stochastic problem is solved by a Galerkin strategy in a tensor product Hilbert space, which is formed based on a tensor product of approximation space in deterministic finite element analysis (i.e., element basis functions) and the space of random variables with finite second moments (i.e., polynomial chaos basis). Hence, this method requires the modification of the basic governing equations, which is not practical while solving finite element problems using softwares or when dealing with complicated forms of mechanistic models. Another disadvantage of this method is that it requires additional efforts to compute derived quantities (e.g., stress components

and strain components) by projecting them onto the PC basis (Bruno, 2007). This led to the development of non-intrusive methods to compute the PCE coefficients.

Instead of depending on a Galerkin type computation, the non-intrusive methods allow the analyst to compute the PCE coefficients from a series of calls to the deterministic model. The advantage of this method is that it requires no need to modify the deterministic code and hence is best suitable with analysts using finite element softwares as a black-box. Two main non-intrusive methods in the literature are namely projection and regression, in which the projection method is of interest.

One of the widely used projection scheme is the tensor Gauss quadrature. Although the tensor product construction makes the mathematical analysis more accessible, the total number of function evaluation grows exponentially fast with respect to the number of input variables, which is known as the curse of dimensionality (Debusschere et al., 2004; Hosder et al., 2007). This makes the computation of PCE coefficients expensive while considering a full tensor product quadrature (Debusschere et al., 2004). An alternative for a full tensor product quadrature, called the sparse quadrature scheme was originally introduced by Smolyak (SA Smolyak, 1963) and was proposed to solve the curse of dimensionality by Gerstner and Griebel (Gerstner & Griebel, 1998). Even with the use of Smolyak quadrature, the cost of this technique strongly increases with the number of input parameters (Blatman & Sudret, 2010b). Hence, PCE currently lacks a computationally efficient method for the meta-model construction.

5.2.2 Mathematical Setting of PCE

Let us consider a mechanistic model represented by a deterministic mapping

$$\boldsymbol{y} = \mathcal{M}(\boldsymbol{x}) \tag{5.1}$$

where $\boldsymbol{x} = [x_1, x_2, \dots, x_n]^{\mathrm{T}} \in \mathbb{R}^{\boldsymbol{n}}, n \geq 1$ is the vector of the input variables and $\boldsymbol{y} = [y_1, y_2, \dots, y_m]^{\mathrm{T}} \in \mathbb{R}^{\boldsymbol{m}}, m \geq 1$ is the vector of output response of quantities of interest. Now, let us consider that the input vector $\boldsymbol{x}$ is uncertain, which requires the introduction of probabilistic framework.

Let $(\Omega, \mathcal{F}, \mathcal{P})$ be a probability space, where Ω is the sample space containing set of all possible outcomes, $\mathcal{F}$ is the set of events, where each event is a set containing zero or more outcomes and $\mathcal{P}$ is the probability measure assigned to each event, i.e., a function which maps from events to probabilities. From now on, the random variables will be denoted by upper case letters, X, and their realizations will be denoted by the corresponding lower case letters, x. Consequently, bold upper case letters (e.g., $\boldsymbol{X} = [X_1, X_2, \dots, X_n]^{\mathrm{T}}$) will be used to denote random vectors and bold lower case letters (e.g., $\boldsymbol{x} = [x_1, x_2, \dots, x_n]^{\mathrm{T}}$) will be used to denote their realizations, respectively. Let us also denote by $f_{\boldsymbol{X}}(\boldsymbol{x})$ its joint PDF and by $\mathcal{P}_{\boldsymbol{X}}$ the associated probability measure such that $\mathcal{P}_{\boldsymbol{X}}(d\boldsymbol{x}) = f_{\boldsymbol{X}}(\boldsymbol{x})d\boldsymbol{x}$.

The mechanistic model response as a random vector $\boldsymbol{Y}$ can be then expressed as:

$$\boldsymbol{Y} = \mathcal{M}(\boldsymbol{X}) \tag{5.2}$$

To properly characterize the random properties of $\boldsymbol{Y}$, suitable function spaces must be defined. For the sake of simplicity, let us consider that we have only one quantity of interest and hence a scalar output response, $Y = \mathcal{M}(\boldsymbol{X})$. Let us suppose that its random response is a second-order random variable:

$$\mathrm{E}[Y^2] < +\infty \tag{5.3}$$

Let us denote $\mathcal{H} = \mathcal{L}^2_{f_{\boldsymbol{X}}(\boldsymbol{x})}$, the Hilbert space of square integrable real-valued functions (i.e., the basis functions) of $\boldsymbol{X}$ with respect to the weight function $f_{\boldsymbol{X}}(\boldsymbol{x})$, equipped with the inner product:

$$\langle u, v \rangle_{\mathcal{H}} = \int_{\mathbb{R}^{\boldsymbol{n}}} u(\boldsymbol{x}) v(\boldsymbol{x}) f_{\boldsymbol{X}}(\boldsymbol{x}) d\boldsymbol{x} \tag{5.4}$$

Equation (5.3) is equivalent to:

$$\mathrm{E}[\mathcal{M}^2(\boldsymbol{X})] = \langle \mathcal{M}, \mathcal{M} \rangle_{\mathcal{H}} < +\infty \tag{5.5}$$

Consequently, considering model responses that are second-moment random variables is equivalent to considering models that belong to the Hilbert space, $\mathcal{H}$. In polynomial chaos expansion, the Hilbert space is spanned by square integrable real-valued functions of $\boldsymbol{X}$ with respect to the weight function $f_{\boldsymbol{X}}(\boldsymbol{x})$, called the polynomial chaos basis functions. The weight function is equivalent to the probability distribution function (PDF) of the respective random variable. Hence, one of the important steps in PCE is to set up the suitable PC basis based on the distribution of the random variables. Once the PC basis is set up, the output response Y can be represented as (Soize & Ghanem, 2005):

$$Y = \sum_{j=0}^{\infty} a_j \Psi_j(\boldsymbol{X}) \tag{5.6}$$

where $\Psi_j(\boldsymbol{X})$ are the basis functions and a_j are the coordinates of Y in this basis, called as PCE coefficients. The aim of PCE is to compute these coefficients to develop a surrogate model of the mechanistic model given in Equation (5.2) using Equation (5.6). In PCE, it is important to note that the basis terms $\Psi_j(\boldsymbol{X})$ are always orthonormal polynomials and it is the properties of orthonormal polynomials which are utilized to efficiently compute the PCE coefficients.

5.2.3 Construction of polynomial chaos basis

5.2.3.1 Univariate orthonormal polynomials

The primary step in PCE is to set up a suitable basis based on the distribution type of random variables. For the sake of simplicity, let us assume that the input random variables are independent. The joint probability distribution can be then written as the product of marginal distributions as:

$$f_{\boldsymbol{X}}(\boldsymbol{x}) = \prod_{i=1}^{n} f_{X_i}(x_i), \quad x_i \in \mathfrak{T}_{X_i} \tag{5.7}$$

where $\mathfrak{T}_{X_i}$ is the support of X_i. For any two functions ξ_1, ξ_2 and for each single random variable X_i, we can define a functional inner product by the following integral:

$$\langle \xi_1, \xi_2 \rangle_i = \int_{\mathfrak{T}_{X_i}} \xi_1(x)\xi_2(x) f_{X_i}(x)dx \tag{5.8}$$

Equation (5.8) is nothing but the expectation $\mathrm{E}[\xi_1(X_i)\xi_2(X_i)]$ with respect to the marginal distribution $f_{X_i}(x)$. Two such functions are said to be orthogonal with respect to the probability measure $\mathcal{P}(dx) = f_{X_i}(x)dx$ if

$$\mathrm{E}[\xi_1(X_i)\xi_2(X_i)] = \int_{\mathfrak{T}_{X_i}} \xi_1(x)\xi_2(x) f_{X_i}(x)dx = 0 \tag{5.9}$$

Utilizing this property, one can build a family of orthogonal polynomials $\left\{\phi_k^{(i)},\ k \in \mathbb{N}\right\}$ satisfying

$$\begin{aligned} \langle \phi_j^{(i)}, \phi_k^{(i)} \rangle_i &= \mathrm{E}\left[\phi_j^{(i)}(X_i)\phi_k^{(i)}(X_i)\right] \\ &= \int_{\mathfrak{T}_{X_i}} \phi_j^{(i)}(x)\phi_k^{(i)}(x) f_{X_i}(x)dx = \alpha_j^i\, \delta_{jk} \end{aligned} \tag{5.10}$$

where δ_{jk} is the Kronecker symbol equal to 1 when $j = k$ and 0 otherwise, and α_j^i corresponds to the squared norm of $\phi_j^{(i)}$, defined as:

$$\alpha_j^i = \left\| \phi_j^{(i)} \right\|_i^2 = \langle \phi_j^{(i)}, \phi_j^{(i)} \rangle_i \tag{5.11}$$

To implement PCE effectively, we need family of orthogonal polynomials which are orthogonal with respect to the probability distribution functions. It was Weiner who first formulated the chaos polynomial with the standard Normal variables and Hermite polynomials as a finite dimensional Wiener polynomial chaos (N Wiener, 1938). However, the use of Hermite polynomials with distribution functions other than standard Normal distribution gives a slower convergence rate of mean and second order moment. This means that more expansion terms are required to minimize the error in mean and second order moment. The faster convergence rate of standard Normal distribution is due to the reason that the weighting function of Hermite polynomials is the same as the probability density function of standard Normal variables.

Xiu and Karniadakis used the Askey scheme of polynomials, which are an important class of orthogonal polynomials to extend the idea to other classical distributions (Xiu & Karniadakis, 2002). Hermite polynomials are a subset of the Askey scheme. Each subset of the orthogonal polynomials in the Askey scheme has a different weighting function in its orthogonality relationship. It has been realized that some of these weighting functions are identical to certain probability distribution functions as shown in Table 5.1.

Table 5.1: Relation between orthogonal polynomials and random variable distributions

Type of distribution	Weight or PDF	Support	Orthogonal polynomials	Orthonormal basis
Normal	$\frac{1}{\sqrt{2\pi}} e^{-x^2/2}$	$(-\infty, \infty)$	Hermite $H_{e_k}(x)$	$H_{e_k}(x) \,/\, \sqrt{k!}$
Uniform	$1/2$	$[-1,1]$	Legendre $P_k(x)$	$P_k(x) \,/\, \sqrt{\frac{1}{2k+1}}$
Beta	$(1-x)^a(1+x)^b$	$[-1,1]$	Jacobi $J_k^{a,b}(x)$	$J_k^{a,b}(x) \,/\, C_{\text{Jacobi}}$
Exponential	e^{-x}	$[0,\infty)$	Laguerre $L_k(x)$	$L_k(x) \,/\, \frac{\Gamma(k+1)}{k!}$
Gamma	$\Gamma(x, a+1, 1)$	$[0,\infty)$	General Laguerre $L_k^a(x)$	$L_k^a(x) \,/\, \frac{\Gamma(k+a+1)}{k!}$

where the normalization constant of Jacobi polynomial is $C_{\text{Jacobi}} = \frac{2^{a+b+1}}{2k+a+b+1} \frac{\Gamma(k+a+1)\Gamma(k+b+1)}{\Gamma(k+a+b+1)\Gamma(k+1)}$

It should be noted that the family of polynomials are only orthogonal and are usually not orthonormal. To use them as a suitable basis, the normalization is enforced and a family of orthonormal polynomials, $\left\{\psi_j^{(i)}\right\}_{j=0}^{\infty}$ is obtained from Equations (5.10) and (5.11) as:

$$\psi_j^{(i)} = \frac{\phi_j^{(i)}}{\sqrt{\alpha_j^i}} \quad i = 1, \dots, n, \quad j \in \mathbb{N} \tag{5.12}$$

If a random variable following a particular distribution is not listed in Table 5.1, it is possible to employ a non-linear mapping such that the generalized PCE can be still applied (Der Kiureghian

& Liu, 1986; Rosenblatt, 1952). For example, a Lognormal random variable can be recast as a function of standard normal variable, which then allows to use Hermite polynomials.

5.2.3.2 Multivariate Polynomials

In most of the mechanistic models, the output response will be a function of multiple input random variables, $\boldsymbol{X} = [X_1, X_2, \dots, X_n]^{\mathrm{T}}$. Hence, we will need to construct an n-dimensional polynomial chaos which will require the tensor product of univariate orthonormal polynomials to build a suitable basis. For this purpose, let us define multi-indices $\boldsymbol{\lambda} \in \mathbb{N}^n$, which are an ordered list of integers.

$$\boldsymbol{\lambda} = (\lambda_1, \dots, \lambda_n), \qquad \lambda_i \in \mathbb{N} \tag{5.13}$$

One can now associate a multivariate polynomial $\boldsymbol{\Psi_\lambda}$ to any multi-index $\boldsymbol{\lambda}$ by

$$\boldsymbol{\Psi_\lambda}(\boldsymbol{x}) = \prod_{\boldsymbol{i=1}}^{\boldsymbol{n}} \psi_j^{(i)}(x_i) \tag{5.14}$$

where $\boldsymbol{\Psi_\lambda} = \{\Psi_{\lambda_i},\ \lambda_i \in \mathbb{N}\}$ is obtained from the tensor product of the univariate polynomials $\left\{\psi_j^{(i)},\ j \in \mathbb{N}\right\}$ defined according to the i-th marginal distribution. By virtue of Equation (5.10) and the tensor product construction in Equation (5.14), the multivariate polynomials in the input vector $\boldsymbol{X}$ are also orthonormal. Hence, this set of multivariate polynomials span the Hilbert space, $\mathcal{H} = \mathcal{L}^2_{f_{\boldsymbol{X}}(\boldsymbol{x})}$, which is the space of square integrable real-valued functions of $\boldsymbol{X}$ with respect to the joint PDF $f_{\boldsymbol{X}}(\boldsymbol{x})$, equipped with the inner product:

$$\langle \Psi_\lambda, \Psi_\eta \rangle = \mathrm{E}\left[\Psi_\lambda(\boldsymbol{X})\Psi_\eta(\boldsymbol{X})\right] = \int_{\mathfrak{X}_{\boldsymbol{X}}} \Psi_\lambda(\boldsymbol{x})\Psi_\eta(\boldsymbol{x}) f_{\boldsymbol{X}}(\boldsymbol{x}) d\boldsymbol{x} = \delta_{\lambda\eta} \tag{5.15}$$

where $f_{\boldsymbol{X}}(\boldsymbol{x})$ is the joint PDF as given in Equation (5.7) and $\delta_{\lambda\eta}$ is the Kronecker symbol equal to 1 when $\lambda = \eta$ and 0 otherwise.

5.2.4 Polynomial Chaos Representation of Model Response

From Equation (5.14), we have a complete basis of multivariate polynomials which are orthonormal with respect to the joint PDF of the input random variables. Let us assume that the mechanistic model response Y has a finite variance as given in Equation (5.3), i.e., $Y \in \mathcal{L}^2(\Omega, \mathcal{F}, \mathcal{P})$. Consequently, we can represent $Y = \mathcal{M}(\boldsymbol{X})$ using the chaos representation as (Soize & Ghanem, 2005):

$$Y(\boldsymbol{X}) = \sum_{\lambda=0}^{\infty} a_\lambda \Psi_\lambda(\boldsymbol{X}) \tag{5.16}$$

Equation (5.16) can be viewed as an intrinsic representation of the random response Y in an abstract space through an orthonormal basis, $\Psi_\lambda(\boldsymbol{X})$, and the coefficients, a_λ as the projections of Y on each of these basis.

Instead of using the multi-index $\boldsymbol{\lambda}$ for expressing the polynomial chaos representation, one can also write Equation (5.16) using a condensed notation as:

$$Y(\boldsymbol{X}) = \sum_{k=0}^{\infty} a_k \Psi_k(\boldsymbol{X}) \tag{5.17}$$

where $k \in \mathbb{N}$. Throughout the discussion, this condensed form of PCE will be used.

5.2.4.1 Illustration example

The following example illustrates the polynomial chaos representation of a two-dimensional function $Y = \mathcal{M}(X_1, X_2)$ by assuming both the random variables as standard Normal variables.

From Table 3.1, the Hermite polynomials are the best suitable polynomials for a standard Normal variable. Let the family of orthogonal basis functions for X_1 be defined as $\{\phi_k(X_1),\ k \in \mathbb{N}\}$ and for X_2 be defined as $\{\phi_l(X_2),\ l \in \mathbb{N}\}$. By using Equation (5.14) for tensor product of the basis functions and using Equation (5.16) for chaos representation, a surrogate model for $Y = \mathcal{M}(X_1, X_2)$ can be written as

$$\begin{aligned}\mathcal{M}(X_1, X_2) = {} & a_{00}\phi_0(X_1)\phi_0(X_2) + a_{10}\phi_1(X_1)\phi_0(X_2) \\ & + a_{01}\phi_0(X_1)\phi_1(X_2) + \\ & a_{20}\phi_2(X_1)\phi_0(X_2) + a_{11}\phi_1(X_1)\phi_1(X_2) \\ & + a_{02}\phi_0(X_1)\phi_2(X_2) + \\ & a_{30}\phi_3(X_1)\phi_0(X_2) + a_{21}\phi_2(X_1)\phi_1(X_2) \\ & + a_{12}\phi_1(X_1)\phi_2(X_2) + \\ & a_{03}\phi_0(X_1)\phi_3(X_2) + a_{40}\phi_4(X_1)\phi_0(X_2) + \cdots\end{aligned} \tag{5.18}$$

The above equation is expressed as in Equation (5.16) using multiple indices to denote the corresponding one-dimensional polynomials associated with them. Using the set of Hermite polynomials, $\{1,\ X,\ X^2 - 1,\ X^3 - 3X, \ldots\}$ and Equation (5.17), we can write the terms in Equation (5.18) in a simplified form as

$$\begin{aligned}&\Psi_0(X_1, X_2) = 1 \qquad \Psi_1(X_1, X_2) = X_1 \qquad \Psi_2(X_1, X_2) = X_2 \\ &\Psi_3(X_1, X_2) = X_1^2 - 1 \qquad \Psi_4(X_1, X_2) = X_1 X_2 \qquad \Psi_5(X_1, X_2) = X_2^2 - 1 \\ &\Psi_6(X_1, X_2) = X_1^3 - 3X_1 \qquad \Psi_7(X_1, X_2) = X_2(X_1^2 - 1) \qquad \ldots\end{aligned} \tag{5.19}$$

Using the terms in Equation (5.19), we can express Equation (5.18) as

$$\mathcal{M}(X_1, X_2) = \sum_{k=0}^{\infty} a_k \Psi_k(X_1, X_2) \tag{5.20}$$

This equation is expressed as in Equation (5.17). Except in the difference in the indexing convention, the surrogate models in Equation (5.18) and (5.20) is identified. For example, $a_{30}\phi_3(X_1)\phi_0(X_2)$ in Equation (5.17) is identified as the term $a_6\Psi_6(X_1, X_2)$ in Equation (5.19).

5.2.5 Truncation Scheme

The representation of a random response using Equation (5.17) is exact when infinite series is considered. However, this is not possible for practical implementation and hence a finite dimensional polynomial chaos has to be built by truncating the series up to a certain degree. The total number of terms (N) retained in the expansion can be determined with the dimensionality (n) of input variables, $\boldsymbol{X}$, and the truncation order (p) of the expansion as:

$$N = \frac{(n+p)!}{n!\,p!} \tag{5.21}$$

A PCE of degree $p = 2$ usually provides satisfactory results for moment and sensitivity analysis, whereas a degree $p = 3$ is often necessary when performing a reliability analysis (Blatman & Sudret, 2010a; Sudret, 2008). Hence, the truncated form of PCE can be written as:

$$Y = \mathcal{M}(\boldsymbol{X}) \simeq \tilde{Y} = \widetilde{\mathcal{M}}(\boldsymbol{X}) = \sum_{k=0}^{N} a_k \Psi_k(\boldsymbol{X}) \tag{5.22}$$

5.2.6 Computation of PCE Coefficients

Once the truncated PC basis is established, the coefficients $\{a_k,\ k \in \mathbb{N}\}$ has to be computed. In this study, a non-intrusive method called the projection method is of interest. Non-intrusive

methods rely on the repeated run of the computational model for selected realizations of random vector, $\boldsymbol{X}$, which is similar as in Monte-Carlo simulation. The computation of PC coefficients using the projection approach exploits the orthonormality of the PC basis.

Multiplying Equation (5.22) by $\Psi_l(\boldsymbol{X})$ and by taking its expectation:

$$\mathrm{E}\left[\widetilde{\mathcal{M}}(\boldsymbol{X})\Psi_l(\boldsymbol{X})\right] = \mathrm{E}\left[\sum_{k=0}^{N} a_k \Psi_k(\boldsymbol{X})\,\Psi_l(\boldsymbol{X})\right] \tag{5.23}$$

This can be written as

$$\int_{\mathfrak{T}_X} \widetilde{\mathcal{M}}(\boldsymbol{x})\Psi_l(\boldsymbol{x})\, f_{\boldsymbol{X}}(\boldsymbol{x})d\boldsymbol{x} = \int_{\mathfrak{T}_X}\left[\sum_{k=0}^{N} a_k \Psi_k(\boldsymbol{x})\,\Psi_l(\boldsymbol{x})\right] f_{\boldsymbol{X}}(\boldsymbol{x})d\boldsymbol{x} \tag{5.24}$$

Due to orthonormality condition as indicated in Equation (5.15), only the term when $k = l$ will be retained. Noting that the inner product of an orthonormal basis with itself is equal to one, the right-hand side of the equation gets reduced to:

$$a_k \int_{\mathfrak{T}_X} \Psi_k^2(\boldsymbol{x}) f_{\boldsymbol{X}}(\boldsymbol{x})d\boldsymbol{x} = a_k\langle\Psi_k, \Psi_k\rangle = a_k \tag{5.25}$$

Hence, by using Equation (5.24) and (5.25), the PCE coefficients can be computed as:

$$a_k = \int_{\mathfrak{T}_X} \widetilde{\mathcal{M}}(\boldsymbol{x})\Psi_k(\boldsymbol{x})\, f_{\boldsymbol{X}}(\boldsymbol{x})d\boldsymbol{x} = \langle\Psi_k, \widetilde{\mathcal{M}}\rangle \qquad (k = 0, 1, \dots, N) \tag{5.26}$$

One should note that the calculation of PCE coefficients requires to evaluate an n-dimensional integration. This multidimensional integral may be computed using various quadrature schemes, which differ in the choice of the selected integration points (i.e., the mechanistic model evaluations).

5.2.6.1 Post-processing using PCE coefficients

One of the major advantages of the PCE method is that once all the PCE coefficients are determined, the mean and variance of the response can be approximated in a straightforward manner as follows:

$$\mu_Y \equiv a_0 \tag{5.27}$$

$$\sigma_Y^2 \equiv \sum_{k=1}^{N} a_k^2 \tag{5.28}$$

Another advantage is the possibility to derive the global sensitivity indices of the model response to the input variables in an easy manner (Sudret, 2008). Of particular interest is the total sensitivity index, which quantifies the influence of the variability of each input random variable on the overall variance of the response function. This is estimated by means of:

$$S_i^T = \frac{1}{\sigma_Y^2} \sum_{\boldsymbol{\lambda} \in \mathfrak{T}_i^*} a_{\boldsymbol{\lambda}}^2 \tag{5.29}$$

where $\mathfrak{T}_i^* \equiv \{\boldsymbol{\lambda} \in \mathbb{N}^n, 0 \leq |\boldsymbol{\lambda}| \leq p, \alpha_i \neq 0\}$ denotes the set of all indices with a non-zero i-th component.

5.2.6.2 Computational Cost of PCE Coefficients

One of the easiest quadrature scheme is based on the random sampling, in which Monte Carlo simulation is widely used. Despite its easy to implement nature, MCS relies upon a large number of model evaluations to compute the integration. A well-known drawback of simulation based method for high dimensional integration is the low convergence rate, which makes the method computationally very expensive (Dubourg, 2011). Improvements to MCS were made by

introducing advanced methods such as Latin Hypercube sampling. A significant reduction in model evaluations was possible but can be still expensive for the purpose of PFEA of expensive-to-evaluate FE models (Hosder et al., 2007).

An alternate to the simulation method is the use of multivariate Gauss quadrature techniques, which are computationally less expensive when compared to simulation-based methods. Considering an L-point scheme, a full tensor Gauss quadrature can be used to approximate the multidimensional integration defining each PCE coefficients as:

$$a_k \approx \sum_{i_1=1}^{N} \dots \sum_{i_n=1}^{N} \left[\left(\prod_{L=1}^{n} w_{i_L} \right) . \Psi_k\left(x_{i_1}, \dots, x_{i_n}\right) . \widetilde{\mathcal{M}}\left(x_{i_1}, \dots, x_{i_n}\right) \right] \qquad (5.30)$$

where w_{i_L} and x_{i_L} are an L^{th} Gauss weight and point of random variable X_i, respectively. It is important to note that, considering an L-point scheme to evaluate an n-dimensional integration results in L^n evaluations of the model $\widetilde{\mathcal{M}}$, which means that the total number of model evaluations exponentially increases with respect to the dimensionality of $\boldsymbol{X}$. This is called curse of dimensionality, which leads to intractable computational cost for PCE surrogate model construction (Debusschere et al., 2004). Improvements such as use of Smolyak algorithm was introduced to moderate the curse of dimensionality of full tensor Gauss quadrature but the computational cost still increases strongly with the number of input parameters (Blatman & Sudret, 2010a).

5.2.7 Using PCE for Probabilistic FEA

The advantage of PCE when compared to other uncertainty propagation methods is that one can get a surrogate model of the computationally expensive mechanistic model and then the full

probabilistic characteristics of the output response by performing MCS using the simple-to-evaluate surrogate model. One can also perform reliability analysis using MCS on the surrogate model. However, if there are multiple input random variables, the computational cost of PCE surrogate model construction becomes high for computationally expensive FE codes (e.g., non-linear FEM problems) due to high number of repetitive calls of FE codes to compute the PCE coefficients. For an efficient probabilistic finite element analysis, it is important to reduce the model evaluations significantly. This is not possible while using the currently available PCE coefficient computation techniques.

5.3 Multiplicative Dimensional Reduction Method (M-DRM)

5.3.1 Background

The computation of PCE coefficients involves an n-dimensional integration. For this reason, PCE cannot be considered as an efficient method for reliability analysis of expensive-to-evaluate FE codes which leads to intractable computational cost for PCE surrogate model construction. Several methods have been introduced in literature to overcome the computational cost associated with computing an n-dimensional integration. The point estimate method (Rosenblueth, 1975) and the Taylor series approximation can deal with this problem but the limitations of these methods are that both the uncertainty of random input and the nonlinearity of random output with respect to random input must be small (Rahman & Xu, 2004). A more efficient method is the high-dimensional model representation (H-DMR) (Li, Rosenthal, et al., 2001; Rabitz et al., 1999) or also called as dimensional reduction method (Rahman & Xu, 2004; Xu & Rahman, 2004) in which a function is decomposed in terms of functions increasing dimensions. Using DRM, a

multivariate function can be expressed as a sum of lower order functions in an increasing hierarchy, thus called as additive DRM (A-DRM). Another way of representation is by using multiplicative DRM (M-DRM) in which a multivariate function is expressed as product of lower order functions. In general, it is truncated to one dimensional functions and the evaluation is further simplified by using the cut-point H-DMR method (Rahman & Xu, 2004). Using this formulation, the number of function evaluations can be significantly reduced to nL from L^n .

In M-DRM, the response function $Y = \mathcal{M}(\boldsymbol{X})$ is evaluated with respect to a fixed input point, known as the cut point with coordinates $\boldsymbol{c}$ (Li, Rosenthal, et al., 2001)

$$\boldsymbol{c} = (c_1, c_2, \dots, c_n) \tag{5.31}$$

where $c_1, c_2, \dots, c_n$ corresponds to the mean value of each random variable $X_1, X_2, \dots, X_n$. Thus, an i^{th} cut function is obtained by fixing all the input random variables, except X_i at their respective cut point coordinates, which are generally chosen as the mean values $(c_1, c_2, \dots, c_n)$ such that

$$\mathcal{M}_i(x_i) = \mathcal{M}(c_1, \dots, c_{i-1}, x_i, c_{i+1} \dots, c_n) \tag{5.32}$$

Chowdhury et al. (Chowdhury et al., 2009) used HDMR as a response surface approximation to solve finite element problems, where each cut function was discretely calculated at finite number of points. He then used an interpolation method using moving least squares approximation to compute the output response at a point off the cut points and came up with the approximate response surface. This approach was later combined with FE model by Rao et al. for probabilistic characterization of inner containments of nuclear reactors (Rao et al., 2009, 2010) and to solve fuzzy FE analysis of structures where Lagrange interpolation functions were used to approximate the response surface (Balu & Rao, 2012). Balomenos and Pandey used M-DRM to directly compute fractional moments of the response and then derived the distribution of the response

without the need of expensive FE simulations (Balomenos & Pandey, 2016). They used this approach with FE models of reinforced concrete slab (Balomenos et al., 2015a) and nuclear containment wall segments (Balomenos & Pandey, 2017) for probabilistic analysis. This chapter presents a new approach where M-DRM is coupled with polynomial chaos expansion (PCE), which significantly reduces the computational cost associated with PCE coefficient computation and hence the construction of PCE surrogate model.

5.3.2 Mathematical Setting of M-DRM

The key idea in additive DRM (A-DRM) is to express a high-dimensional function as a sum of functions of lower order in an increasing hierarchy as (Chowdhury et al., 2009; Li, Wang, et al., 2001; Rabitz et al., 1999; Xu & Rahman, 2004)

$$Y = \mathcal{M}(\boldsymbol{X}) = \mathcal{M}_0 + \sum_{i=1}^{n} \mathcal{M}_i(x_i) + \sum_{1 \le i < j \le n} \mathcal{M}_{ij}(x_i, x_j) + \dots \tag{5.33}$$

For a sufficiently smooth function, the influence of higher order terms are negligible than the univariate terms, $\mathcal{M}_i(x_i)$. This results in a simple representation of response function by retaining only up to the univariate functions (Rahman & Xu, 2004):

$$Y = \mathcal{M}(\boldsymbol{X}) \approx \sum_{i=1}^{n} \mathcal{M}_i(x_i) - (n-1)\mathcal{M}_0 \tag{5.34}$$

where $\mathcal{M}_i(x_i)$ is a one-dimensional cut function as defined in Equation (5.32) and $\mathcal{M}_0$ defines the response when all the random variables are fixed to their mean values, i.e.,

$$\mathcal{M}_0 = \mathcal{M}(c_1, c_2, \dots, c_n) = \ a\ constant \tag{5.35}$$

M-DRM follows the same approach with A-DRM, but the response function is first transformed logarithmically, i.e., $\log[\mathcal{M}(\boldsymbol{X})]$, which derives the multiplicative approximation of the response function as

$$Y = \mathcal{M}(\boldsymbol{X}) \approx h_0^{(1-n)} \times \prod_{i=1}^{n} \mathcal{M}_i(x_i) \tag{5.36}$$

Thus, the above equation gives an approximate model of the input-output relation in a product form. This approximate model can be used in polynomial chaos expansion to reduce the computational cost of PCE surrogate model construction.

5.4 Combining the M-DRM with PCE

The high computational cost of PCE surrogate model construction was due to the n-dimensional integration involved in the computation of PCE coefficients. A full tensor Gauss quadrature method requires L^n model evaluations for an L-point scheme with n input random variables, which gives an exponential increase in model evaluations with increase in input random variables. This computational cost can be significantly reduced when M-DRM is coupled with PCE.

Consider a mechanistic model of the random response expressed as:

$$Y = \mathcal{M}(\boldsymbol{X}) \tag{5.37}$$

Using M-DRM, the mechanistic model given above can be approximated as:

$$Y = \mathcal{M}(\boldsymbol{X}) \approx h_0^{(1-n)} \times \prod_{i=1}^{n} \mathcal{M}_i(x_i) \tag{5.38}$$

where $\mathcal{M}_0 = \mathcal{M}(c_1, c_2, \dots, c_n)$, i.e., model evaluated at cut point with all mean values of input random variables and $\mathcal{M}_i(x_i) = \mathcal{M}(c_1, \dots, c_{i-1}, x_i, c_{i+1} \dots, c_n)$, i.e., model evaluated by fixing all the input random variables, except X_i at their respective mean values.

From Equation (5.26), the coefficients of PCE can be computed as:

$$a_k = \int_{\mathfrak{T}_X} \widetilde{\mathcal{M}}(\boldsymbol{x}) \Psi_k(\boldsymbol{x})\, f_{\boldsymbol{X}}(\boldsymbol{x}) d\boldsymbol{x} = \langle \Psi_k, \widetilde{\mathcal{M}} \rangle \qquad (k = 0, 1, \dots, N) \tag{5.39}$$

Substituting the M-DRM approximation of mechanistic model from Equation (5.38) into Equation (5.39), the PCE coefficients can be approximated as:

$$\begin{aligned} a_k &\approx \int_{\mathfrak{T}_X} \left[h_0^{(1-n)} \times \prod_{i=1}^{n} \mathcal{M}_i(x_i) \right] \Psi_k(\boldsymbol{x})\, f_{\boldsymbol{X}}(\boldsymbol{x}) d\boldsymbol{x} \qquad (k = 0, 1, \dots, N) \\ &= h_0^{(1-n)} \times \int_{\mathfrak{T}_X} \left[\prod_{i=1}^{n} \mathcal{M}_i(x_i) \right] \Psi_k(\boldsymbol{x})\, f_{\boldsymbol{X}}(\boldsymbol{x}) d\boldsymbol{x} \qquad (k = 0, 1, \dots, N) \end{aligned} \tag{5.40}$$

Referring to Equation (5.14), recall that a multivariate polynomial Ψ_k with an index k is defined as a tensor product of marginal univariate polynomials $\{\psi_{j_i},\ j \in \mathbb{N}\}$ defined according to the i-th marginal distribution of the respective individual random variables as

$$\Psi_k(\boldsymbol{x}) = \prod_{i=1}^{n} \psi_{j_i}(x_i) \tag{5.41}$$

Noting this relation, Equation (5.40) can be written as

$$a_k \approx h_0^{(1-n)} \times \prod_{i=1}^{n} \left(\int_{\mathfrak{T}_{X_i}} \mathcal{M}_i(x_i)\, \psi_{j_i}(x_i) f_i(x_i) dx_i \right) \qquad (k = 0, 1, \dots, N) \tag{5.42}$$

The integral in the above equation for PCE coefficient computation has now reduced to one-dimensional integrals with respect to each random variables. Each of these integrals can be now computed using an L-point Gauss quadrature scheme and the PCE coefficients in Equation (5.42) can be computed as:

$$a_k \approx h_0^{(1-n)} \times \prod_{i=1}^{n} \left(\sum_{L=1}^{l} \mathcal{M}_{i_L}(x_{i_L}) \psi_{j_i}(x_{i_L})\, w_{i_L} \right) \qquad (k = 0, 1, \dots, N) \qquad (5.43)$$

where w_{i_L} and x_{i_L} are an L^{th} Gauss weight and point of random variable X_i, respectively. This computation requires nL model evaluations for all the cut functions and an additional model evaluation to compute h_0. Thus, only $nL + 1$ mechanistic model evaluations are required in total for PCE coefficient computation. For example, a problem with 10 random variables and 5-point Gauss quadrature will require only 51 model evaluations, whereas a full tensor Gauss quadrature will require 5^{10} model evaluations. Hence, the computational cost of the PCE surrogate model construction can be significantly reduced and the colossal difference in the required model evaluations between the two method proves the advantage of the new method.

Note that while combining the M-DRM and PCE methods, multivariate polynomials were not constructed, and only univariate polynomials were used for computing the PCE coefficients. The multivariate polynomials corresponding to each coefficient are then built based on the already known multi-indices used to compute these coefficients. After obtaining all the coefficients and multivariate polynomials, the final surrogate model can be constructed using Equation (5.17).

5.5 Gaussian Quadrature Scheme for One-Dimensional Integration

A univariate quadrature rule approximates the unidimensional integrals by a weighted sum of L weight values, w_{i_L} and integration points, x_{i_L} as:

$$\int g(x)\, W(x)dx = \sum_{i=1}^{L} w_{i_L}.\mathcal{M}(x_{i_L})W(x_{i_L}) \tag{5.44}$$

The integration scheme for various distributions is shown in Table 5.2. The value of the integration points and weights depends on the integrand and the quadrature selected. For example, for the case of a normal random variable, the Gauss-Hermite integration scheme can be used. The Gauss-Hermite quadrature involves the approximation of an integral of the form (Beyer, 1987; Kythe & Schäferkotterr, 2004; Zwillinger, 2011)

$$\int f(x)dx \;=\; \int e^{-x^2}\mathcal{M}(x)dx \tag{5.45}$$

Where based on Table 5.2, the Gauss-Hermite integral is approximated as

$$\int e^{-x^2}\mathcal{M}(x)dx \approx \sum_{L=1}^{l} w_L\mathcal{M}(x_L) \tag{5.46}$$

where l is the number of evaluation points and w_L $(L = 1, \ldots, l)$ are known as Gauss-Hermite weights. The basic idea is that the function $\mathcal{M}(x_L)$ is evaluated at a few chosen evaluation points x_L and then the integral is approximated as a weighted sum.

The Gauss coordinates (z_L) and Gauss weights (w_L), of the five-order rule $(L = 5)$ of Gauss-Hermite, Gauss-Legendre and Gauss-Laguerre quadrature, are summarized in Table 5.3. If more orders $(l > 5)$ of Gauss coordinates (z_L) and Gauss weights (w_L) based on other orthogonal

polynomials are required, they can be found from literature (Beyer, 1987; Kythe & Schäferkotterr, 2004; Zwillinger, 2011).

From Table 5.2, Gauss-Hermite quadrature can be used for a normal distribution. For a standard normal distribution, the probability density function (PDF) is expressed as

$$f(z) = \frac{1}{\sqrt{2\pi}} e^{\left(-\frac{z^2}{2}\right)} \tag{5.47}$$

A standard Normal random variable Z can be then transformed into a Normal random variable X using the following equation (Ang & Tang, 2007a).

$$X = \mu + \sigma Z \tag{5.48}$$

where μ is the mean and σ is the standard deviation of the Normal distribution.

The Gauss-Hermite coordinate, x_{i_L}, for each normal random variable X_i can be related to the Gauss-Hermite coordinate, z_{i_L}, for the standard normal variable Z_i via the following transformation

$$x_{i_L} = \mu_i + \sigma_i \times z_{i_L} \tag{5.49}$$

where μ_i is the mean value, σ_i is the standard deviation and z_{i_L} is the Gauss-Hermite coordinate of each input normal random variable.

Another frequently used probability distribution in Engineering problems is the Lognormal distribution, which takes only positive values. If a random variable X follows a Lognormal distribution, then $\ln(X)$ follows a normal distribution. The PDF of a Lognormal distribution is expressed as (Ang & Tang, 2007a)

$$f(x) = \frac{1}{x\zeta\sqrt{2\pi}} e^{\left(-\frac{[\ln(x)-\lambda]^2}{2\zeta^2}\right)} \tag{5.50}$$

where λ is the shape parameter and ζ is the scale parameter of the Lognormal distribution. These parameters are related to Normal distribution parameters via the following relations

$$\lambda = \ln(\mu) - \left(\frac{1}{2}\zeta^2\right) \; and \; \zeta = \sqrt{\ln\left(1 + \frac{\sigma^2}{\mu^2}\right)} \tag{5.51}$$

Therefore, a relation between the Standard Normal random variable Z and the Lognormal random variable X can be expressed as

$$Z = \frac{\ln(X) - \lambda}{\zeta} \tag{5.52}$$

Using Equation (5.52), the Gauss-Hermite coordinate, x_{i_L}, for each Lognormal random variable X_i can be related to the Gauss-Hermite coordinate for z_{i_L} for the standard normal variable Z_i via the following transformation

$$x_{i_L} = e^{\left(\lambda_i + \zeta_i z_{i_L}\right)} \tag{5.53}$$

where λ_i is the shape parameter, ζ_i is the scale parameter and z_{i_L} is the Gauss-Hermite coordinate of each input Lognormal random variable.

Equation (5.45) and Equation (5.53) can be used to compute the function evaluation points x_{i_L} for each random variable X_i upon knowing the distribution parameters of Normal and Lognormal distributions. After evaluating the function output $\mathcal{M}(x_L)$ at each evaluation point x_L, they are multiplied with the corresponding Gauss-Hermite weights w_L and are then summed to obtain the approximation of the integral shown in Equation (5.46). Gaussian quadrature is therefore a powerful tool to significantly reduce the computational cost of a unidimensional integral.

Table 5.2: Gaussian integration formula for one-dimensional integration

Distribution	Support domain	Gaussian quadrature	Numerical integration formula
Uniform	$[a, b]$	Gauss-Legendre	$\sum_{L=1}^{l} w_L \left[\frac{1}{2}\xi\left(\frac{b-a}{2}z_L + \frac{a+b}{2}\right)\right]$
Normal	$(-\infty, \infty)$	Gauss-Hermite	$\sum_{L=1}^{l} w_L[\xi(\mu + z_L\sigma)]$
Lognormal	$(0, \infty)$	Gauss-Hermite	$\sum_{L=1}^{l} w_L\{\xi[\exp(\mu + z_L\sigma)]\}$
Exponential	$(0, \infty)$	Gauss-Laguerre	$\sum_{L=1}^{l} w_L \left[\xi\left({}^{z_L}/_{\lambda}\right)\right]$
Weibull	$(0, \infty)$	Gauss-Laguerre	$\sum_{L=1}^{l} w_L \left[\xi\left(\theta z_L^{\,1/\delta}\right)\right]$

Table 5.3: Weights and coordinates of the five order Gauss-Hermite quadrature rule

Gaussian rule	L	1	2	3	4	5
Gauss-Hermite	w_L	0.011257	0.22208	0.53333	0.22208	0.011257
	z_L	-2.85697	-1.35563	0	1.35563	2.85697
Gauss-Legendre	w_L	0.23693	0.47863	0.56889	0.47863	0.23693
	z_L	-0.90618	-0.53847	0	0.53847	0.90618
Gauss-Laguerre	w_L	0.52176	0.39867	0.07594	0.00361	0.00002
	z_L	0.26356	1.4134	3.5964	7.0858	12.641

5.6 Probabilistic FEA using the proposed method

Coupled M-DRM and PCE method will give a significant reduction in the computational cost associated with PFEA of expensive-to-evaluate FE models because: (1) it significantly reduces the number of mechanistic model evaluations; (2) approximately estimates the probability distribution of the output response. The implementation of the proposed method for PFEA is given in Figure 5.1, which describes how to develop a surrogate model and perform a PFEA using the proposed method. A more detailed description on the steps that must be followed to implement the proposed method is also given below.

Step 1: Define the *n* random variables $\boldsymbol{X} = [X_1, X_2, \dots, X_n]^{\mathrm{T}}$**.** Choose the appropriate Gaussian quadrature based on the type of distribution followed by each random variable. e.g., for a normally distributed random variable, choose the Gauss-Hermite quadrature. Gauss quadrature scheme for other type of distributions can be found in Table 5.2.

Step 2: Choose the number of points of the Gauss quadrature scheme. A 5-point scheme is usually adequate (Balomenos et al., 2015a; Zhang & Pandey, 2013b). The weights, w_{i_L}, and the coordinates, z_{i_L}, of a five-point Gauss-Hermite quadrature rule is given in Table 5.3, along with other Gaussian rules.

Step 3: For the chosen Gaussian quadrature of each random variable, compute the corresponding quadrature coordinates, e.g., use Equation (5.45) for the Gauss-Hermite to calculate the Gauss quadrature coordinates, x_{i_L}, from z_{i_L}. Each of these x_{i_L} values along with the fixed mean values of the other random variables forms the M-DRM input grid. Equations associated with other distributions can be found in (Zhang & Pandey, 2013a).

Step 4: Input the first x_{i_L} value along with the fixed mean values of the other random variables to the FEA software, run the analysis and obtain the corresponding output response $\mathcal{M}_{i_L}(x_{i_L})$. Repeat the same process by changing each of the x_{i_L} values listed in the input grid. At the end, set all input random variables to their mean value and run one additional FEA to calculate the response $\mathcal{M}_0$. The collection of these output responses forms the output grid.

Step 5: Select the truncation order, *p*, of the PCE and choose the appropriate orthogonal polynomials based on the distribution type of each random variable given in Table 5.1.

Step 6: Multiply each of the $\mathcal{M}_{i_L}(x_{i_L})$ obtained from step 4 with its associated Gauss quadrature weight, w_{i_L} and the corresponding univariate polynomial obtained from step 5 and use Equation (5.43) to calculate each of the PCE coefficients.

Step 7: Evaluate the mean and the variance using Equations (5.27) and (5.28) and perform a sensitivity analysis using Equation (5.29).

Step 8: Build the multivariate polynomials corresponding to each coefficient based on the already known multi-indices used to determine these coefficients.

Step 9: Construct the final surrogate model using Equation (5.17).

Step 10: Run a MCS using the surrogate model and perform the probabilistic/stochastic analysis.

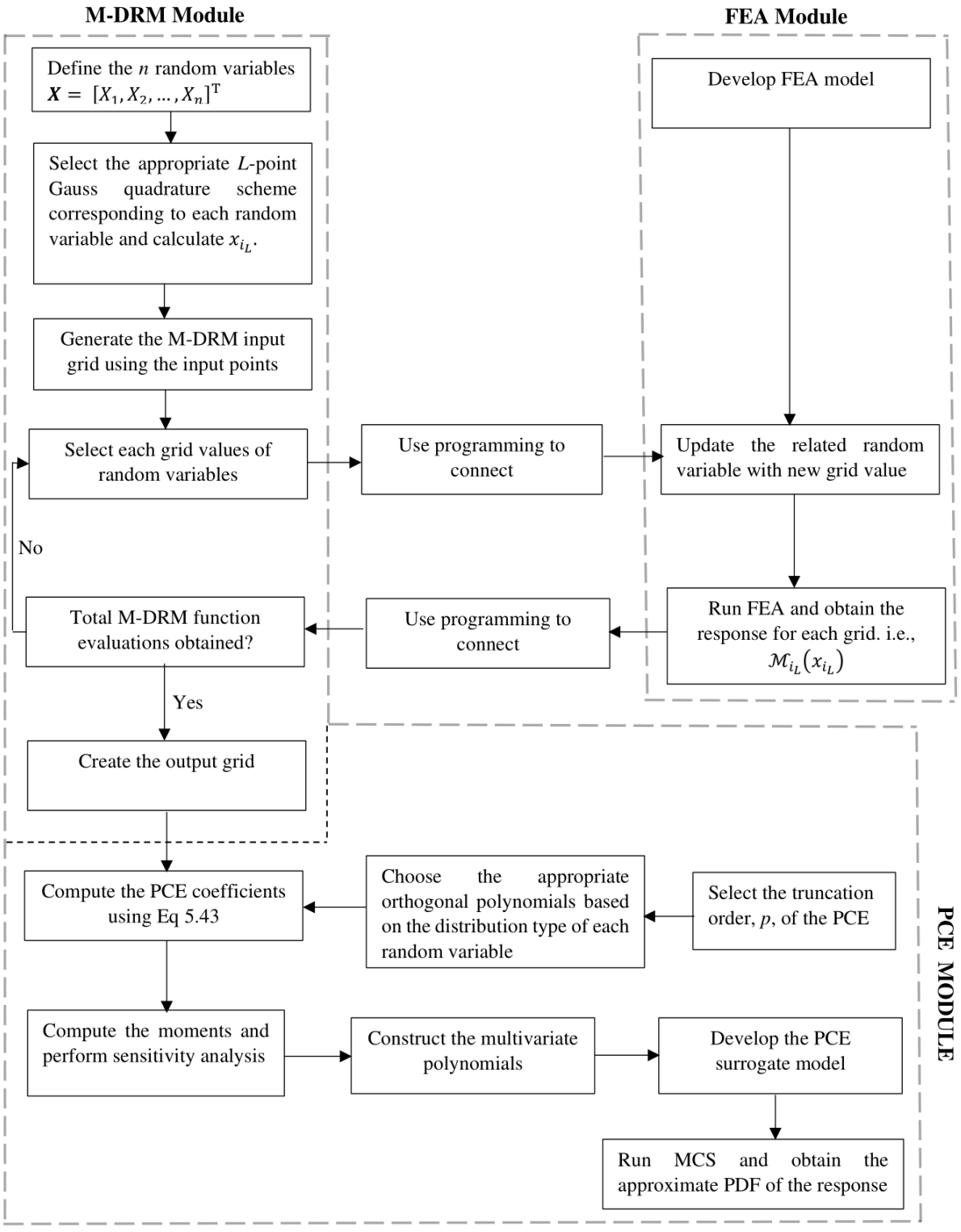

Figure 5.1: Flowchart to conduct PFEA using the proposed method

5.6.1 Application Example

For the illustration purpose of the proposed method, an analytical response function with two random variables is considered. Feeder pipes connect the inlet and outlet headers to the reactor core in CANDU nuclear power plants. A degradation mechanism known as flow accelerated corrosion (FAC) causes wall thinning, which affects the structural integrity of these feeder pipes. Flow accelerated corrosion causes general thinning as well as local thinning. For simplicity, a general thinning case is assumed here. According to the Design by Analysis rules of NB-3221 of ASME Boiler and Pressure Vessel (ASME B&PV) Code, the general primary membrane stress must meet the S_m limit, where S_m is the maximum allowable stress intensity for the material at the design temperature (ASME, 2015). The material used for the fabrication of feeder pipes is SA 106 Carbon Steel and the maximum allowable stress intensity, $S_m = 119$ MPa (Abdelsalam & Vijay, 2010). The general primary membrane stress (i.e., the hoop stress) in the pipe due to internal pressure can be computed as

$$\sigma_h = \frac{P_{int} r}{t} \tag{5.54}$$

where P_{int} is the internal pressure and t is the wall thickness of the pipe. The internal pressure has a coefficient of variation of 0.15 (Gupta & Choi, 2003) and wall thickness has a coefficient of variation of 0.0745, which was computed based on the inspection data. The implementation of the proposed method and the computations involved in each module as given in Figure 5.1 is described in detail next. Note that the FEA module is now replaced by the analytical equation given in Equation (5.54).

5.6.1.1 M-DRM Module

The first step in the implementation of coupled M-DRM and PCE method is to define the distribution type and parameters of the random variables. This is given in Table 5.4.

Table 5.4: Statistics of random variables related to hoop stress in pipes

Random variable	Distribution	Mean	Standard Deviation
P_{int}	Lognormal	10.4	1.56
t	Normal	3.9124	0.2905

The next step in the implementation of coupled M-DRM and PCE method is to form the input grid. Using a 5-point $(L = 5)$ Gauss quadrature, an input grid is generated to evaluate the model response. The Gauss Hermite formula is used since random variables follow normal and lognormal distribution. The total number of model evaluations are $nL + 1 = (2 \times 5) + 1 = 11$. For each of the evaluation point, only one random variable value is changed while other random variables are fixed to their mean value, which forms 10 model evaluations. The 11^{th} or final model evaluation is reserved for the mean case where the function evaluation is carried out by fixing all input random variables to their mean values. The input grid and the output grid are given in Table 5.5. This complete the computations in the M-DRM module.

Table 5.5: Input grid for model evaluation and the corresponding output grid

Random variable	Model evaluations	Gauss Hermite points (z_j)	P_{int}(MPa)	t(mm)	σ_h(MPa)
P_{int}	1	-2.8570	**6.7162**	3.9124	45.0404
	2	-1.3556	**8.4020**	3.9124	56.3459
	3	0	**10.2849**	3.9124	68.9735
	4	1.3556	**12.5899**	3.9124	84.4312
	5	2.8570	**15.7501**	3.9124	105.6241
t	6	-2.8570	10.4	**3.0825**	91.3243
	7	-1.3556	10.4	**3.5186**	78.7152
	8	0	10.4	**3.9124**	69.7452
	9	1.3556	10.4	**4.3062**	62.4158
	10	2.8570	10.4	**4.7423**	55.7191
Fixed mean values	11	N/A	10.4	3.9124	69.7452

5.6.1.2 PCE Module

After completing all the required model evaluations and obtaining the output, the next step is to compute the PCE coefficients. For this, the multivariate polynomial basis must be constructed. Since the random variables have Normal and Lognormal distribution, the Hermite orthogonal polynomials can be used as appropriate basis functions. Truncating the order of polynomial chaos to 3, i.e., $p = 3$, the total number of terms retained in the expansion can be computed using Equation (5.21) as 10. For PC basis construction, let us denote the first random variable, P_{int} as X_1 and the second random variable t as X_2. The corresponding set of univariate Hermite polynomials for each random variable are $\{1, X_1, X_1^2 - 1\}$ and $\{1, X_2, X_2^2 - 1\}$, respectively. The multivariate orthogonal polynomial chaos basis can be now constructed using the tensor product. To use it as a proper basis, the orthogonal polynomials must be factorized with their respective

squared norms. Using the function evaluation values and the constructed PC basis, the PCE coefficients can be computed using Equation (5.30). PC basis construction and the obtained PCE coefficients are given in Table 5.6.

The analytical equation for hoop stress given in Equation (5.54) can be now replaced using the PCE surrogate model expressed using Equation (5.17) as

$$\sigma_h \approx 70.1946 + 10.4707X_1 + \ldots - 0.0347\left(\frac{1}{\sqrt{3!}}(X_2^3 - 3X_2)\right) \qquad (5.55)$$

Table 5.6: Two-dimensional Hermite polynomials and computed PCE coefficients

k	$\boldsymbol{\lambda}$	$p = \sum_{i=1}^{2} \lambda_i$	Orthonormal Chaos Polynomials $[\Psi_k(\boldsymbol{X})]$	PCE Coefficients
0	{0,0}	0	$\Psi_0(\boldsymbol{X}) = \psi_0(X_1)\psi_0(X_2) = 1$	70.1946
1	{1,0}	1	$\Psi_1(\boldsymbol{X}) = \psi_1(X_1)\psi_0(X_2) = X_1$	10.4707
2	{0,1}	1	$\Psi_2(\boldsymbol{X}) = \psi_0(X_1)\psi_1(X_2) = X_2$	-6.0521
3	{2,0}	2	$\Psi_3(\boldsymbol{X}) = \psi_2(X_1)\psi_0(X_2) = \frac{1}{\sqrt{2}}(X_1^2 - 1)$	0.7809
4	{1,1}	2	$\Psi_4(\boldsymbol{X}) = \psi_1(X_1)\psi_1(X_2) = X_1X_2$	-0.9028
5	{0,2}	2	$\Psi_5(\boldsymbol{X}) = \psi_0(X_1)\psi_2(X_2) = \frac{1}{\sqrt{2}}(X_2^2 - 1)$	0.4571
6	{3,0}	3	$\Psi_6(\boldsymbol{X}) = \psi_3(X_1)\psi_0(X_2) = \frac{1}{\sqrt{3!}}(X_1^3 - 3X_1)$	0.0388
7	{2,1}	3	$\Psi_7(\boldsymbol{X}) = \psi_3(X_1)\psi_0(X_2) = \frac{1}{\sqrt{2}}X_2(X_1^2 - 1)$	-0.0673
8	{1,2}	3	$\Psi_8(\boldsymbol{X}) = \psi_3(X_1)\psi_0(X_2) = \frac{1}{\sqrt{2}}X_1(X_2^2 - 1)$	0.0682
9	{0,3}	3	$\Psi_9(\boldsymbol{X}) = \psi_0(X_1)\psi_3(X_2) = \frac{1}{\sqrt{3!}}(X_2^3 - 3X_2)$	-0.0347

5.6.1.2.1 Computation of response statistics

Using the obtained PCE coefficients, the mean and standard deviation can be computed in a straightforward manner using Equation (5.27) and Equation (5.28). For the sake of comparison, MCS of the actual analytical function given in Equation (5.54) is also performed with 100,000 simulations and the statistics were computed. The statistics obtained from each method is summarized in Table 5.7. The results indicate the numerical accuracy and computational efficiency of the proposed method.

Table 5.7: Comparison of statistics of hoop stress based on MCS and proposed method

Method used	Total model evaluations	Mean of σ_h (MPa)	Standard deviation of σ_h (MPa)	Coefficient of variation
M-DRM+PCE	11	70.1946	12.1963	0.1736
MCS	10^6	70.1982	12.1897	0.1736

5.6.1.2.2 Sensitivity Analysis

Another significant advantage of PCE is the straightforward computation of the sensitivity indices using the PCE coefficients and Equation (5.29) (Table 5.8). It is observed that the variance of the internal pressure mostly contributes to the variance of the hoop stress. Therefore, the response σ_h is most sensitive to the input random variable P_{int}, contributing 74.53% of its variance to the variance of σ_h. This higher correlation was also validated from MCS with 100,000 simulations as shown in Figure 5.2. The difference $1 - \sum_j S_j = 0.0056$, which shows a negligible interaction between the random variables.

Table 5.8: Sensitivity indices

Random variable (j)	Sensitivity index (S_j)
P_{int}	0.7453
t	0.2491

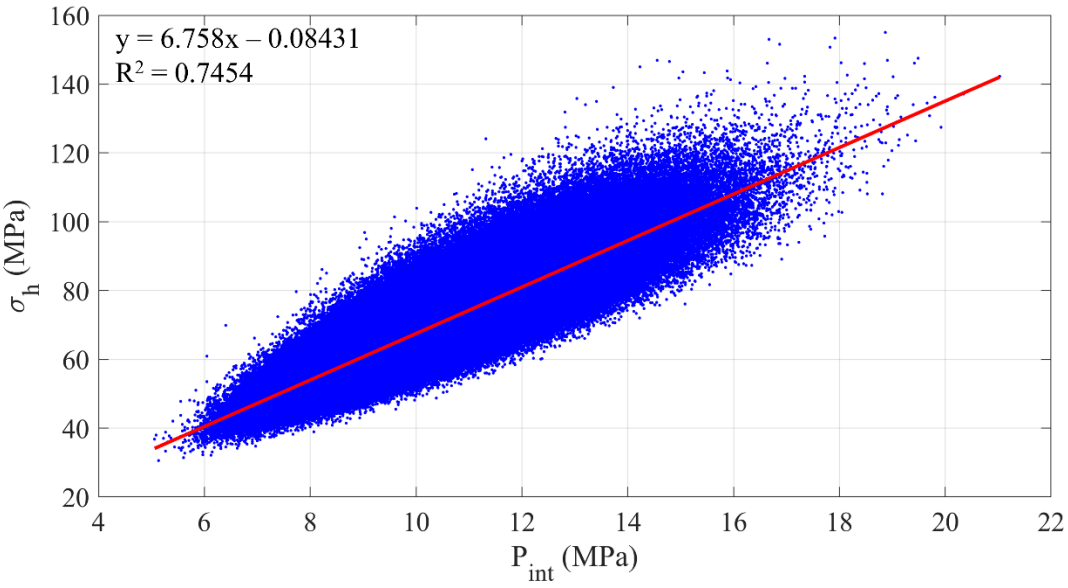

Figure 5.2: Scatter plot and linear fit of internal pressure versus hoop stress

5.6.1.2.3 Response Probabilistic Result

Monte Carlo simulation (MCS) with 100,000 simulations was performed using the surrogate model to get the complete probability distribution. The probability of failure P_f is estimated by plotting the probability of exceedance (POE) as shown in Figure 5.3. It is observed that the coupled M-DRM and PCE method provides a highly accurate approximation for almost the entire range of the output response distribution. For instance, the probability of failure of a degraded feeder pipe can be defined as the probability of hoop stress exceeding the maximum allowable stress intensity of 119 MPa. The probability of failure was computed as 8.72×10^{-4} using coupled M-DRM and

PCE method, which is close to the estimated value using MCS (8.9×10^{-4}). This shows the efficiency of the proposed method.

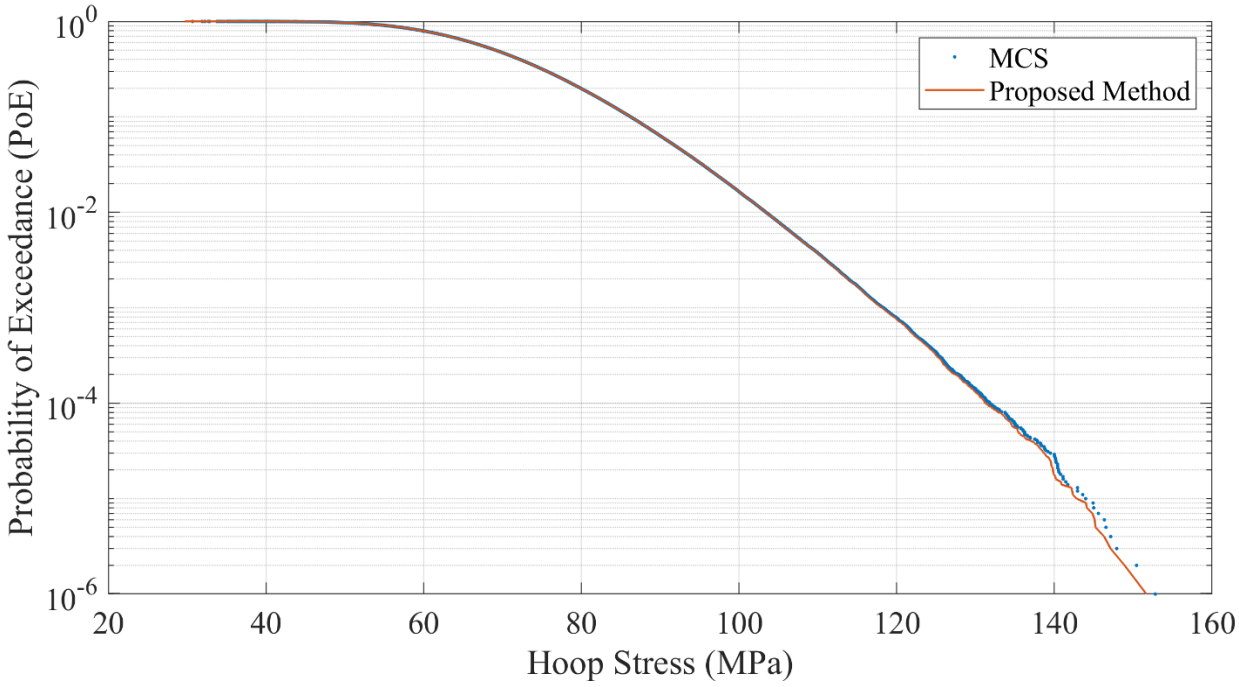

Figure 5.3: Comparison of probability of exceedance of hoop stress

5.6.2 Accuracy and Limitations of the Coupled Approach

The accuracy of the calculations can be affected by: (1) the consideration of only up to univariate functions in the M-DRM representation and (2) the truncation order (p) of the PCE.

For case (1), the coupled approach considers only terms up to the univariate functions in the M-DRM representation. For an accurate representation of the response function, the higher order terms must also be considered as shown in Equation (5.33). Therefore, an error is introduced from ignoring the higher order terms in the M-DRM representation. For case (2), an exact representation

of the surrogate model using PCE is possible only when infinite terms are used. However, for practical implementations, the PCE is built by truncating the series up to a certain degree as give in Equation (5.22). Therefore, an error is introduced by truncating the series up to a certain degree for PCE. The error in the coupled approach could be therefore expressed as a sum of both the errors from case (1) and case (2).

The coupled approach has limitations for approximating highly non-linear functions or model responses. This is because the coupled approach considers only terms up to the univariate functions in the M-DRM representation. However, previous applications involving M-DRM has shown that for applications involving structural problems, the influence of higher order terms is negligible compared to the univariate terms (Balomenos et al., 2015b; Balomenos & Pandey, 2016). Therefore, the coupled approach can be reasonably applied to structural problems. For approximating highly non-linear model responses, the bivariate functions in the M-DRM representation can be included. However, this will increase the computational cost of performing PFEA, but still efficient when compared to the full tensor Gauss quadrature approach.

5.7 Conclusions

This chapter presents a computationally efficient method for performing structural reliability and sensitivity analysis by coupling the multiplicative dimensional reduction method (M-DRM) with polynomial chaos expansion (PCE) method. The computational cost associated with computing the PCE coefficients is significantly reduced by combining the PCE method with M-DRM, which in turn gives a computationally efficient method for developing surrogate models of expensive-to-evaluate finite element models. The coupling of M-DRM with PCE makes the PCE

coefficient computation formulation simple and requiring only one dimensional integrals to be solved. M-DRM is used in concurrence with the Gauss quadrature scheme, which gives a set of selected values of random variables to calculate the output response. During each M-DRM trial, one random variable value is changed while the other random variable values are kept at mean values. Each output response is collected as an output grid. The PCE coefficients are then computed using the output grid and the appropriate orthogonal polynomials. The method uses the advantage of PCE in computing statistical parameters such as mean and standard deviation, and for performing sensitivity analysis in a straightforward manner using the PCE coefficients. The surrogate model is then developed using the known PCE coefficients and the multivariate polynomials to perform MCS and obtain the complete probability distribution of the output response of interest.

The method was demonstrated by applying the proposed method on a simple analytical equation. The statistical and sensitivity analysis results obtained from the proposed method was compared with the results obtained from Monte Carlo simulation (MCS), which showed a very close agreement. The probability of failure results also showed a very good agreement which confirms the efficiency and accuracy of the proposed method.

The proposed method can be extremely powerful while using it for probabilistic finite element analysis (PFEA) due to the requirement of a very small number of FE evaluations. For an L point Gauss quadrature scheme and n random variables, only $nL + 1$ mechanistic model evaluations are required in total for PCE coefficient computation and in developing a surrogate model. Therefore, the proposed method gives a colossal reduction in the computational cost for performing PFEA when compared with MCS.

Chapter 6

Probabilistic Finite Element Analysis of CANDU Fuel Channels

6.1 Introduction

In CANDU reactors, a contact between the "hot" Pressure Tube (PT) and the "cold" Calandria Tube (CT) could cause the development of hydride blisters that may lead to delayed hydride cracking (DHC) of PTs (Byrne et al., 1991). An example of a blister in Zr-2.5Nb PT material is shown in Figure 6.1. To maintain PT integrity, contact between these two tubes must be avoided. Under normal operating conditions (NOCs), the PT-CT contact can occur as a result of in-reactor deformation due to irradiation induced creep, irradiation growth and thermal creep of the FC assembly. Prabhu et. al. described in detail the in-reactor deformation of CANDU FCs and the prediction of PT-CT contact using finite element models (Prabhu et al., 2020, 2022b), and the need of surrogate models in probabilistic contact assessments (Prabhu et al., 2020). Since the prediction of time to contact is influenced by various uncertainties, such as change in, (i) the dimensions of the FC, and (ii) the material properties and boundary conditions of the FC, probabilistic simulation-based methods are necessary to assess the PT-CT contact risk and establish adherence with provisions of the Canadian Standards Association (CSA) Standard N285.8. However, the direct use of FEM models is not a computationally feasible and reliable choice for probabilistic assessments of an entire reactor core with 380 or 480 FCs. For example, the nuclear industry currently uses 1D FEM models with a limited number of MCSs for making risk-informed and life-extension decisions. The limitations of 1D FEM beam models were discussed in Chapter 3 and it was shown that a 1D FEM model significantly underpredicts the gap and a 3D FEM model

is necessary to accurately predict the PT-CT gap. Also, the probabilistic results based on a limited number of MCSs couldn't be used with sufficient confidence for risk-informed decisions. Therefore, a viable approach is sought for performing the probabilistic contact assessment of CANDU FCs and of an entire reactor core using 3D FEA in a computationally efficient manner.

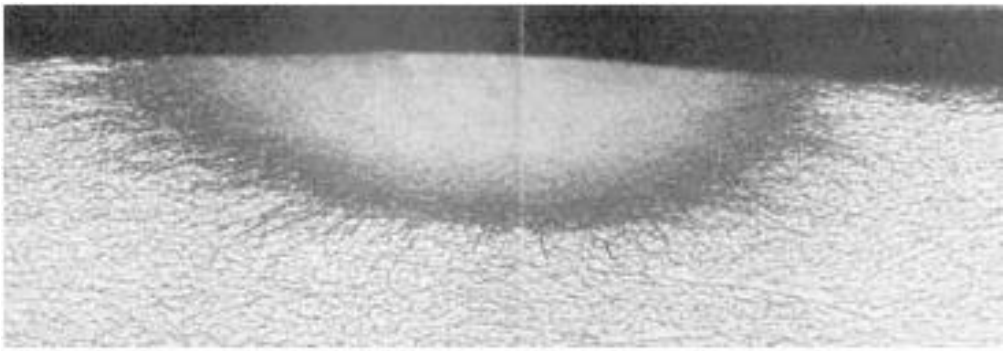

Figure 6.1: Example of a blister in Zr-2.5Nb PT material (blister depth = 0.25 mm from outside surface to lower end of darker region) (Nadeau, 2012)

6.1.1 Objective

The main objective of this chapter is to perform PFEA of CANDU FCs using the coupled multiplicative dimensional reduction method (M-DRM) and the polynomial chaos expansion (PCE) method. The first objective is to apply the proposed method using 1D FEA and validate the obtained statistical and probabilistic results against the MCS results. After validation, the proposed method is used for probabilistic contact assessment. The second objective is to perform a detailed probabilistic contact assessment utilizing the 3D FEA and the proposed method by considering different PT orientations in a CANDU reactor. The final objective is to compare the probabilistic analysis results based on 1D and 3D FEM models to make aware and demonstrate to the nuclear

industry on the associated error in probability of contact prediction using a 1D FEM model, which is the current industry practice.

6.1.2 Organization

The organization of the chapter is as follows. Section 6.2 presents the uncertain parameters and the corresponding distribution of these parameters influencing the PT-CT gap profiles, which will be used for probabilistic FEA using both 1D and 3D FE models. Section 6.3 discusses the application of MCS and coupled M-DRM and PCE method using 1D FEM model for probabilistic FEA of CANDU FCs, where MCS is used as a benchmark to check the accuracy of the coupled M-DRM and PCE method. Section 6.4 presents the deterministic 3D FEA results on PT diametral expansion and PT-CT gap profile based on different PT orientations. Section 6.5 discusses the application of coupled M-DRM and PCE method using 3D FEM model for probabilistic FEA of CANDU FCs by considering different PT orientations. Finally, section 6.6 summarizes the conclusions. The surrogate model development in Chapter 4 utilized the understanding of the nature of the PT-CT gap evolution due to irradiation induced creep phenomena.

6.2 Uncertain Variables Influencing Gap Profile

Most of the model variables such as FC geometry, loading history, weight of nuclear fuel and coolant, etc. can be modeled as deterministic constants due to insignificant variations from their nominal design values. However, there are certain variables which exhibit significant variation and influence the PT-CT contact risk appreciably as discussed next.

The **first** variable is associated with the deformation equation describing PT deformation. A simpler approach is used to model the observed variability due to in-reactor creep given that the statistical distribution of the equation parameters describing the creep component is not available. A factor that multiplies the parameter describing the creep component is used to scale the calculated total strain using the creep deformation equation. This factor, identified here as *the creep factor*, is then modelled as a normally distributed random variable (Nadeau, 2012). In the FE model, the creep factor was incorporated in the UMAT subroutine, and the scaling was performed by multiplying the creep strain increment computed by the corresponding deformation equation with the creep factor at each time increment.

The **second** and **third** variables that significantly influence the gap profile are the end-slopes of the PT at the inlet and outlet ends. The end-slopes are formed due to the tilting of the end-fitting caused during the installation process, which results in a non-zero value at both ends. The variability of end-slopes leads to uncertainties and are therefore treated as normal random variables (Nadeau, 2012). The end-slopes were applied by assigning respective end-slope values to the rotational degree of freedom in the downward direction to the rigid nodes at the centre of the PT ends, leading to a tilt at the ends.

Hence, the gap profile is mostly sensitive to the creep factor (C), the slope at the outlet end (θ_{out}) and the slope at the inlet end (θ_{in}) of the FC. The parameters and the distribution type of these random variables are given in Table 6.1. Note that statistical information in Table 6.1 is based on gap data from CANDU 6 units. The same procedure in this chapter can be extended to other units (e.g., Pickering and Darlington) with the availability of statistical information for those respective units.

Table 6.1: Distribution type and parameters of random variables influencing PT-CT gap profile

Random variable	Distribution	Mean	Standard Deviation
C	Normal	0.87	0.122
θ_{out}	Normal	0.0017	0.00125
θ_{in}	Normal	0.0042	0.002

6.3 Probabilistic FEA of CANDU FCs using 1D FEA

6.3.1 General

In this section, the probabilistic FEA is performed using MCS and coupled M-DRM and PCE method using 1D FEM model. The 1D FEM model used in this section has the same geometry and operating conditions as discussed in Chapter 3. Therefore, the results discussed in this section are based entirely on the use of the same 1D FEM model. This section primarily has two aims:

1) To check the accuracy of coupled M-DRM and PCE method for probabilistic contact assessments by validating the results against MCS.
2) To use the probabilistic results based on 1D FE results to compare against 3D FE results.

6.3.2 Monte Carlo Simulation

MCS is performed here for probabilistic FEA using 1D model to use as a benchmark. The 1D FE model is computationally cheaper (18 minutes for a simulation) compared to 3D FE model (2.5 hours for a simulation) and is therefore used for MCS. A total of 10^3 simulations were performed. For performing probabilistic FEA, the uncertain input parameters must be updated for each FE simulation. The random variables used in the simulation are the creep factor, which must be

updated for each simulation in UMAT and the two end slopes, which must be updated in the deterministic FE code. For this purpose, a link was created between Python, ABAQUS and MATLAB. A ‘mat’ file was initially created using MATLAB containing the set of uncertain parameter values required for each simulation. Python programming was used to develop the deterministic FE model and the input random values of end slopes were updated using Python by accessing the values from the mat file. The Python code also updates the values of creep factor in the UMAT, which is a FORTRAN file (‘.for’ file). Once the parameters are updated, the Python code calls the ABAQUS for performing deterministic FEA and the results are stored in an output file which has an output database format (.odb). Upon completing the FE analysis, the Python code then calls MATLAB which accesses the .odb file and post processes the vertical displacement values of PT and CT for computing PT-CT gap profile. This procedure is repeated as many times as MCS is required, producing the same number of gap profiles as the number of trials.

6.3.3 Application of Coupled M-DRM and PCE Method

Here coupled M-DRM and PCE method is applied using 1D FEA to evaluate the accuracy and efficiency for probabilistic contact assessment of CANDU FCs. Although the Python code was used to repeatedly run the required number of trials using ABAQUS, the proposed method can be also implemented without the use of any programming for linking, since it requires only a small number of trials. The user can manually change the values of random variables for each simulation, as it requires minimal effort. This is advantageous as the proposed method can be used by a user who is not much familiar with advanced programming, which makes it an easy and applicable method.

6.3.3.1 Surrogate Model Form

The PT-CT gap values vary with axial location along the PT as well as with time. Thus, the surrogate model of the gap profile and in turn the PCE coefficients required for the construction of the surrogate model must also be expressed as a function of both the axial location and time. By referring to Equation (5.17), the surrogate model for the gap profile can be written as follows:

$$G(\boldsymbol{X}, d, t) \approx \sum_{k=0}^{N} a_k(d, t)\Psi_k(\boldsymbol{X}) \tag{6.1}$$

where $\boldsymbol{X} = [C, \theta_{out}, \theta_{in}]$ is the vector of random variables, d is the axial location, t is the time, $a_k(d, t)$'s are the PCE coefficients and $\Psi_k(\boldsymbol{X})$'s are the multivariate polynomials.

6.3.3.2 Input and Output Grid Generation

The first step in implementing the proposed method is to define the parameters and type of distribution of the random variables, which is described in section 6.2. The next steps in the proposed model is to form the input and output grid. Using a 5-point ($L = 5$) Gauss quadrature, an input grid was generated to evaluate the model responses. The Gauss Hermite formula is used since random variables follow a normal distribution. The total number of model evaluations is $nL + 1 = (3 \times 5) + 1 = 16$. The input grid is given in Table 6.2. For each evaluation point, only one value of a given random variable is changed while other random variables are fixed to their mean value, which forms 15 model evaluations. The 16th final model evaluation is reserved for the mean case where the function evaluation is carried out by fixing all input random variables to their mean values. But it should be noted that the model evaluations 3, 8 and 13 are the same as the

mean case and hence they need to be evaluated only once, which reduces the total FE evaluations from 16 to 13.

The 13 1D FE evaluations were executed by using each of the input grid values and the corresponding PT-CT gap outputs were collected. Note that the results discussed in this section are from 1D FEA runs for a PT back end placed at the fixed outlet end (BEO). As mentioned before, the gap values vary along the length of the PT and with time. Thus, the FE gap output was recorded at 118 axial locations along the axis of the PT and these values were stored in a matrix form corresponding to various time frames. Therefore, the output grid for this problem is a function of axial location and time. This completes all the steps in the M-DRM module.

Table 6.2: Input grid for model evaluation

Random variable	FEM evaluation	z_j	C	θ_{out}(rad)	θ_{in}(rad)
C	1	-2.8570	**0.5214**	0.0017	0.0042
	2	-1.3556	**0.7046**	0.0017	0.0042
	3	0	**0.87**	0.0017	0.0042
	4	1.3556	**1.0354**	0.0017	0.0042
	5	2.8570	**1.2185**	0.0017	0.0042
θ_{out}	6	-2.8570	0.87	**-0.00187**	0.0042
	7	-1.3556	0.87	**5.46E-06**	0.0042
	8	0	0.87	**0.0017**	0.0042
	9	1.3556	0.87	**0.0034**	0.0042
	10	2.8570	0.87	**0.0053**	0.0042
θ_{in}	11	-2.8570	0.87	0.0017	**-0.0015**
	12	-1.3556	0.87	0.0017	**0.0015**
	13	0	0.87	0.0017	**0.0042**
	14	1.3556	0.87	0.0017	**0.0069**
	15	2.8570	0.87	0.0017	**0.0099**
Fixed mean values	16	NA	0.87	0.0017	0.0042

Note: z_j denotes the Gauss Hermite points

Referring to Table 6.2, every five FE model evaluations are grouped in such a way that only one random variable value is changed by keeping other random variables values fixed at their mean. The influence of each of the random variables on the output gap profile can be visualized by plotting the gap profile results corresponding to each of the grouped five FE model evaluations. Figures 6.2, 6.3 and 6.4 show the gap profile variations at 200 kEFPH for each of the five FEM evaluations. The effect of the creep factor is significant across all five spans. The outlet slope mostly influences the gap at spans S_1 and S_2, and with a slight effect on the central span, S_3. The inlet slope has the most influence on spans S_4 and S_5, and with a slight effect on the central span, S_3. Since the minimum gap is occurring at span S_5, the inlet slope has the most influence on it, followed by the creep factor. The outlet slope has no influence on the minimum gap. A quantification of these observations is discussed in a later section by performing sensitivity analysis.

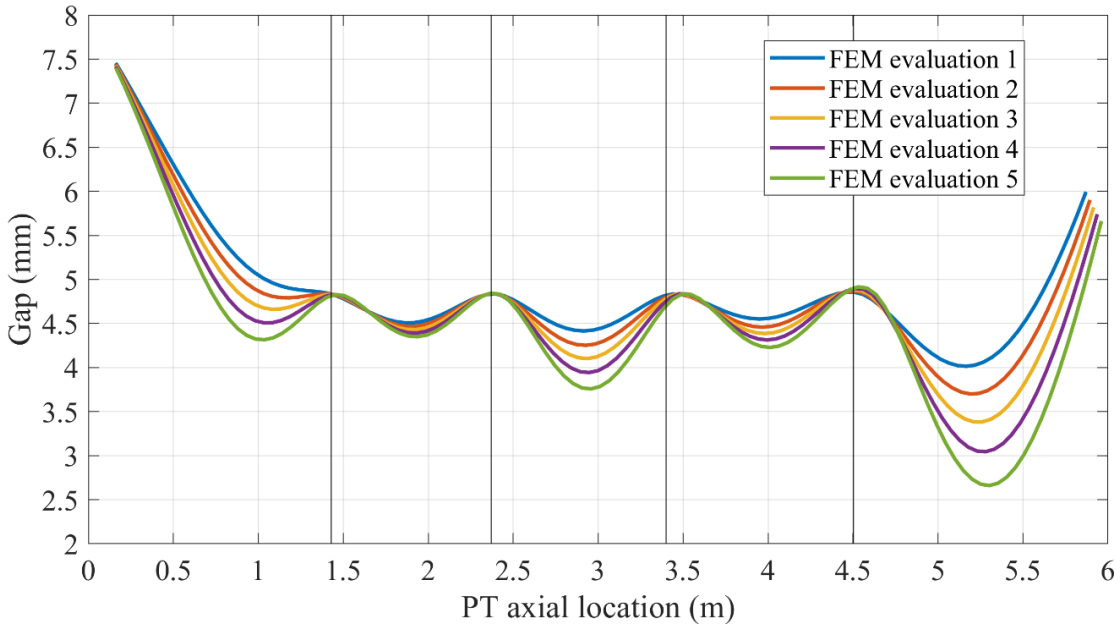

Figure 6.2: Predicted gap profiles from 1D FEA for selected values of creep factors at 200 kEFPH, (inlet slope and outlet slope fixed at mean values and PT with BEO)

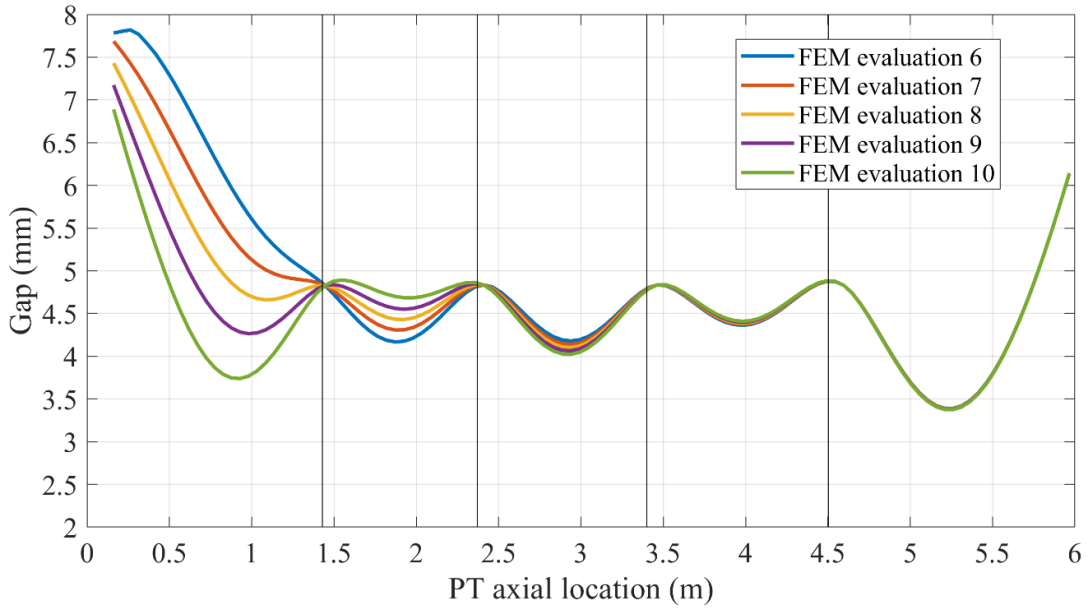

Figure 6.3: Predicted gap profiles from 1D FEA for selected values of outlet slopes at t = 200 kEFPH, (creep factor and inlet slope fixed at mean values and PT with BEO)

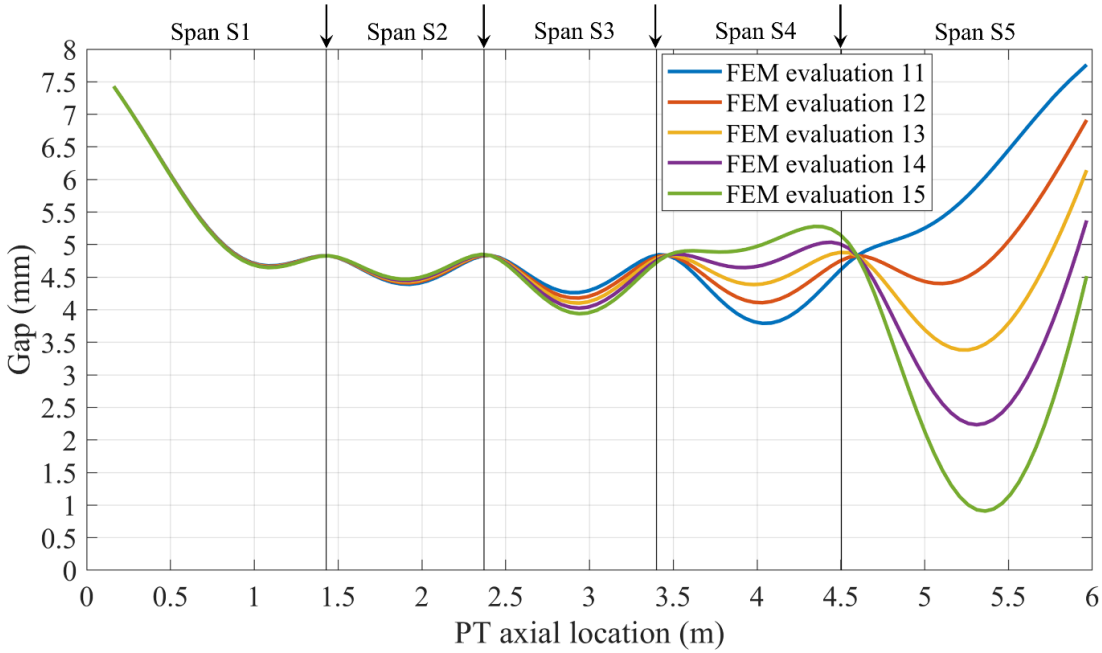

Figure 6.4: Predicted gap profiles from 1D FEA for selected values of inlet slopes at t = 200 kEFPH, (creep factor and outlet slope fixed at mean values and PT with BEO)

6.3.3.3 Computation of PCE Coefficients

After completing all the FE model evaluations, the PCE coefficients were computed using the stored output gap values. Since the random variables are normally distributed, the Hermite orthogonal polynomials were used as appropriate univariate basis functions. Truncating the order of polynomial chaos to 3, the total number of terms retained in the expansion can be computed as 20. Using the gap values and the constructed PC basis, the PCE coefficients were computed using Equation (5.30) as a function of axial location and time. These coefficients were then saved in a data file in a matrix form.

6.3.3.4 Final Surrogate Model based on 1D FE Model

By utilizing the saved data file of PCE coefficients as a function of location and time, the final surrogate model of the PT-CT gap was developed using Equation (6.1). This surrogate model is a function of the random variables, C, θ_{out} and θ_{in} and can predict the PT-CT gap by using the values of these random variables into the surrogate model expression as an input. This equation can be then treated as a substitute for the ABAQUS 1D FE model.

To assess the prediction capability of the proposed surrogate model, the gap profiles at (i) t = 220 kEFPH, C = 0.964, θ_{out} = 0.0032 rad and θ_{in} = 0.0036 rad and, (ii) t = 180 kEFPH, C = 0.867, θ_{out} = 0.0031 rad and θ_{in} = 0.0012 rad were predicted using the surrogate model and compared the results to those predicted by the 1D FEA in ABAQUS as shown in Figure 6.5. An exceptionally close agreement between the surrogate model prediction and that from the 1D FEA can be seen across all five spans, with a maximum difference of 0.025 mm in the inlet (right most) span.

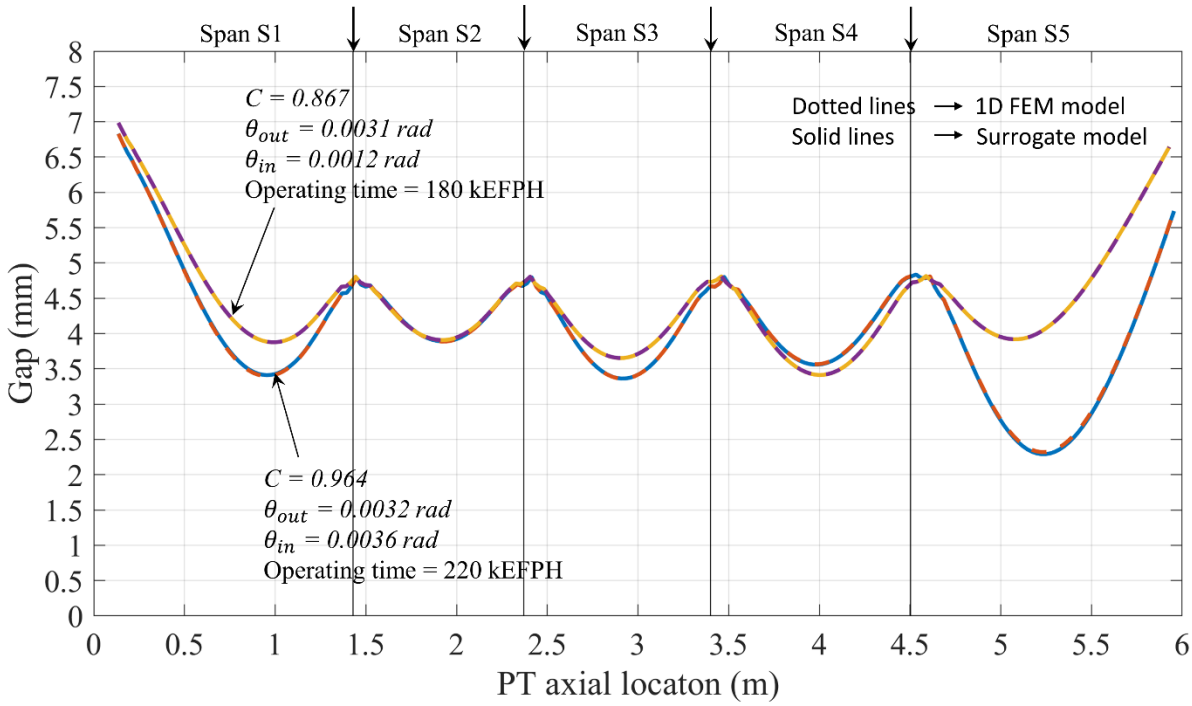

Figure 6.5: Comparison of gap profiles predicted by the surrogate model and the 1D FEA at different time intervals and parameter values

6.3.4 Comparison of Statistical Results

In this section, the statistical and probabilistic results obtained based on MCS and the coupled M-DRM and PCE method is compared. Using the proposed method, the mean and standard deviation can be computed in a straightforward manner by using Equation (5.27) and Equation (5.28). Table 6.3 shows the comparison of statistics obtained from both MCS and coupled M-DRM and PCE method at the minimum gap location for various time points. Figure 6.6 shows the comparison of mean, mean + 2 standard deviation and mean – 2 standard deviation at time 200 kEFPH at all 111 axial locations along the PT. The results from Table 6.3 and Figure 6.6 indicate the numerical accuracy and computational efficiency of the proposed method.

To further analyze the efficiency of the method, a semi-log plot of the cumulative distribution function (CDF) of the minimum gap was plotted as shown in Figure 6.7. A point on this plot gives the probability of the minimum gap falling below a deterministic minimum gap threshold. It is observed that the proposed method provides a highly accurate approximation for almost the entire range of minimum gap, indicating that it is a sufficiently accurate method to be used instead of the time-consuming MCS using FE models.

Table 6.3: Statistics of the minimum gap obtained using MCS and coupled M-DRM and PCE method

Method used	Time (kEFPH)	Mean of minimum gap (mm)	Standard deviation of minimum gap (mm)	Coefficient of variation (cov)	Total number of function evaluations
MCS	50	4.8564	1.7200	0.3541	1000
M-DRM + PCE	50	4.8678	1.7364	0.3567	13
MCS	100	4.1127	1.9081	0.4640	1000
M-DRM + PCE	100	4.1058	1.9024	0.4633	13
MCS	150	3.4955	1.0292	0.2944	1000
M-DRM + PCE	150	3.4907	1.0296	0.2950	13
MCS	200	2.7400	0.5591	0.2041	1000
M-DRM + PCE	200	2.7480	0.5534	0.2014	13

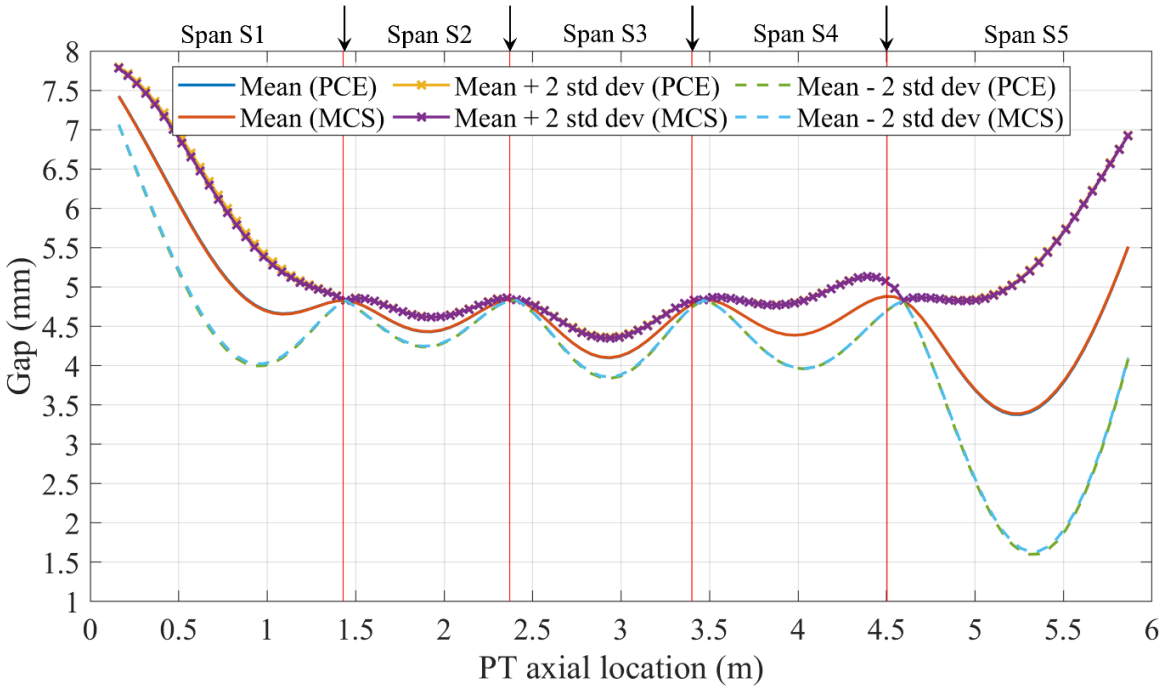

Figure 6.6: Comparison of statistics from MCS and M-DRM + PCE method across the PT axial location at 200 kEFPH

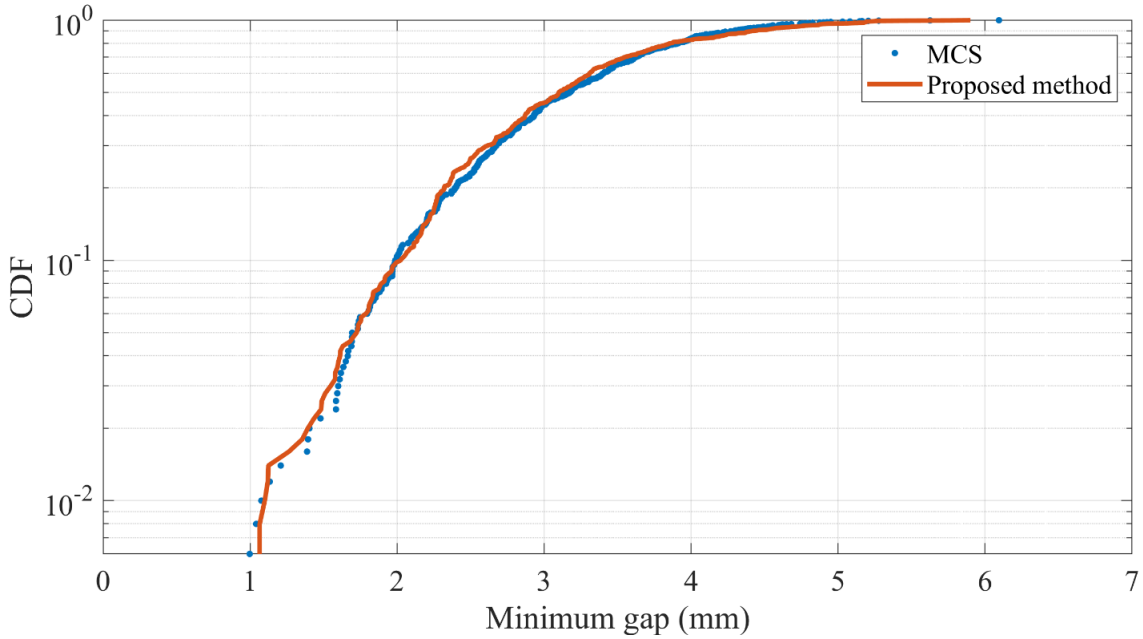

Figure 6.7: Comparison of CDF of the minimum gap at 220 kEFPH using MCS and the proposed method based on 1D FEA

6.3.5 Computational Time

The coupled M-DRM and PCE method provides an enormous saving of computational time. For instance, each deterministic 1D FEA takes approximately 18 minutes to run the analysis up to 220 kEFPH on a computer with Intel Xeon 3.5 GHz Processor and 16Gb of RAM. Therefore, MCS with 1000 simulations requires 12.5 days (i.e., 18000 minutes) to complete, whereas the proposed method requires only 13 simulations, which are completed in less than 3.9 hours. The proposed method also includes the computation of PCE coefficients and performing MCS using the surrogate model, which requires around 15 minutes. Therefore, the total time required for the proposed method is 4.15 hours (i.e., 249 minutes), which is merely 1.38% of the time taken by the MCS. This shows the computational efficiency and the significant advantage of using this method for probabilistic FEA.

6.3.6 Probabilistic Contact Assessment using 1D Surrogate Model

In probabilistic contact assessment, the interest is in computing the probability of PT coming in contact with CT (i.e, PT-CT gap being zero). Being validated, the surrogate model developed using the proposed method can be used for probabilistic contact assessment. MCS using 10^6 trials were run using the surrogate model, which requires only a few seconds to complete. The minimum gap was recorded for each simulation for various reactor operating time intervals. A semi-log CDF plot of minimum gap is shown in Figure 6.8. Therefore, from these CDF curves, the probability of contact (POC) is the point where the curve meets zero on the X-axis. The POC increases with reactor operating time and at 220 kEFPH, the POC is $\sim 1.9\times10^{-4}$ for a PT with the BEO.

An important observation to be conveyed to the nuclear industry here is regarding the number of MCS trials required to obtain a confident result. As mentioned before, the nuclear industry currently uses 1D FEA with limited number of MCS (1000 trials) for assessing probability of contact. By comparing Figure 6.7 (CDF with 1000 MCS trials) and Figure 6.8 (CDF with 1 million MCS trials), it can be observed that an MCS with 1000 simulations is not showing any probability of contact (i.e., zero probability) at 220 kEFPH. The lowest value of minimum gap based on 1000 MCS is ~1mm. However, MCS with 1 million simulation gives a probability of contact of ~1.9×10^{-4} at 220 kEFPH. This shows that a probabilistic result based on 1000 simulations couldn't be used as a reliable estimate, which the nuclear industry must be aware of.

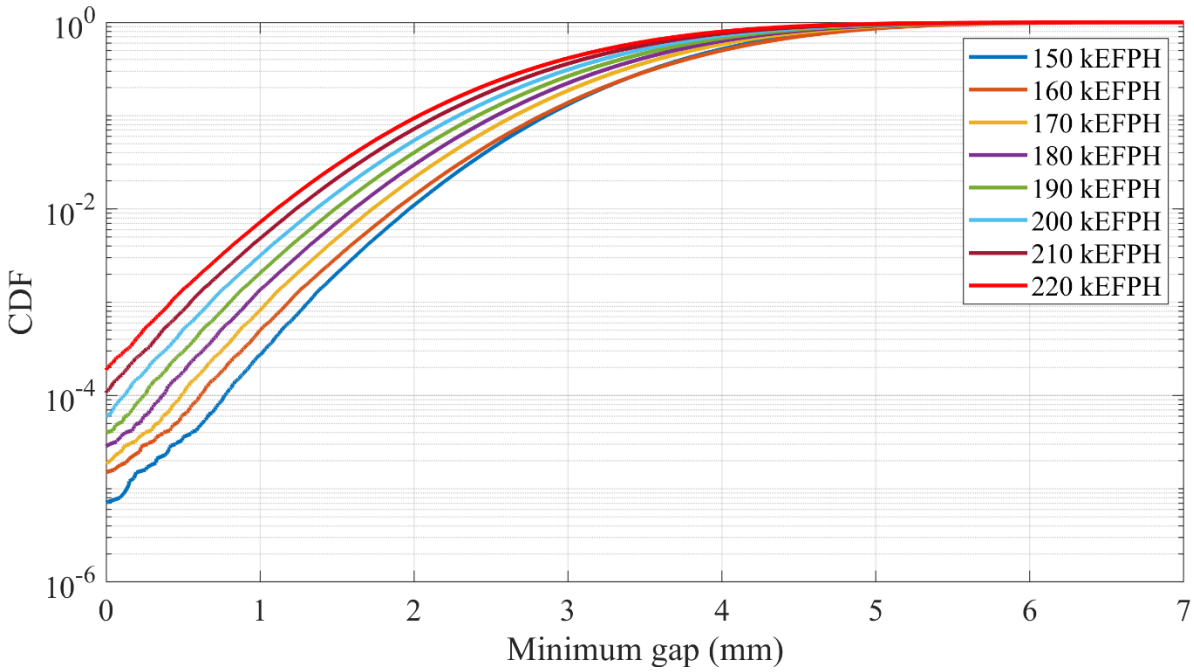

Figure 6.8: CDF at various time intervals during service of FCs (Based on 1D FEA for PTs with the BEO)

6.4 3D FEA Based on Different PT Orientations

In Chapter 3, the focus was on PTs with the back end placed at the outlet. It must be emphasized here that there are two distinct orientations of the PTs within the population of FCs in a reactor core and the deformation behaviour is influenced from the change in orientation with respect to coolant flow. As a consequence of the hot-extrusion process, the end of the PT emerging first from the extrusion press is labeled as the '*front end*' and the end appearing last is referred to as the '*back end*'. The extrusion process leads to differences in the material properties, microstructure and crystallographic texture of the PT along its length (Choubey et al., 1996; R. Fleck et al., 1984), which in turn result in an asymmetrical strain profile when the back end is placed at the outlet (BEO) and a more symmetrical strain profile when the back end is placed at the inlet (BEI). Figure 6.9 shows the measured diametral strain at the mid-bundle location of two PTs with different orientations. The term used to describe this behaviour is "end-to-end material variation". It is important to properly analyse the influence of the PT orientation with respect to the coolant flow on the profile of the PT-CT gap and the time of contact since they depend strongly on this aspect.

In this section, the 3D FEA is extended by considering the difference in orientations of the coolant flow with respect to the manufacturing direction of the PT. To determine this effect, two analyses were conducted:

1) The PT back end placed at the outlet (Same as in Chapter 3)

2) The PT back end placed at the inlet

The FC geometry and the operating conditions are the same as used in Chapter 3 and for both these cases, the boundary conditions were that the outlet end is kept fixed, and the inlet end free. A

separate UMAT file was created based on the deformation model for a PT with BEI. The 3D FEA was run up to 220 kEFPH.

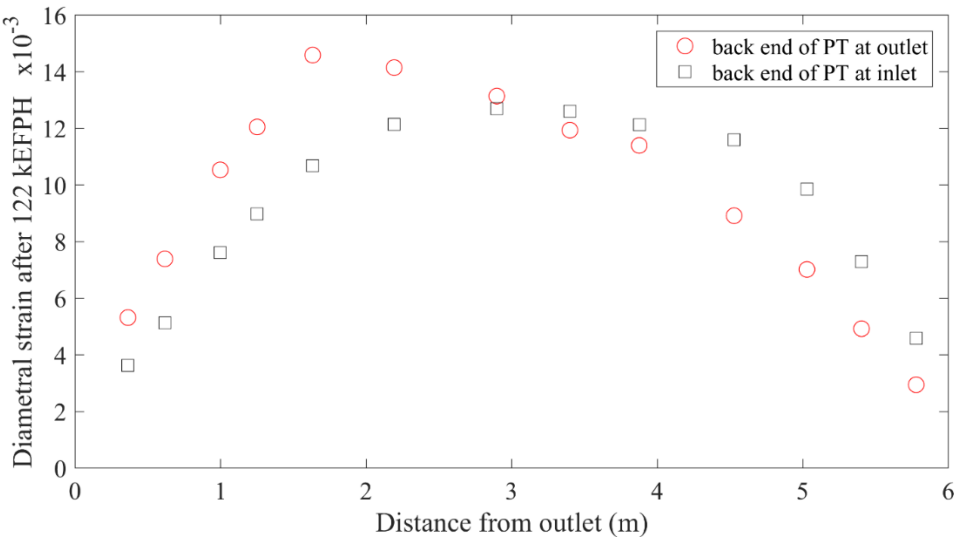

Figure 6.9: Comparison of diametral strain profiles in CANDU PTs with back end at the outlet and back end at the inlet

6.4.1 Deterministic 3D FEA Results

The FC deformation obtained from the FEA output contains the overall sag, axial elongation, diametral expansion and wall thinning of the PT and CT at a given operating time. The axial elongation is less affected by the change in PT orientation and therefore is of no interest. The present section looks in more detail at the diametral expansion and the PT-CT gap profile predictions based on different PT orientations using 3D FEA.

6.4.1.1 Diametral expansion

Figure 6.10 shows the inner diameter prediction of PTs with two different orientations at 220 kEFPH. As expected, the 3D FEA predicts an asymmetric profile when the PT has the BEO

and a symmetrical profile when the PT has the BEI. This difference in the diametral profile could significantly influence the PT-CT gap profile predictions, which is discussed next.

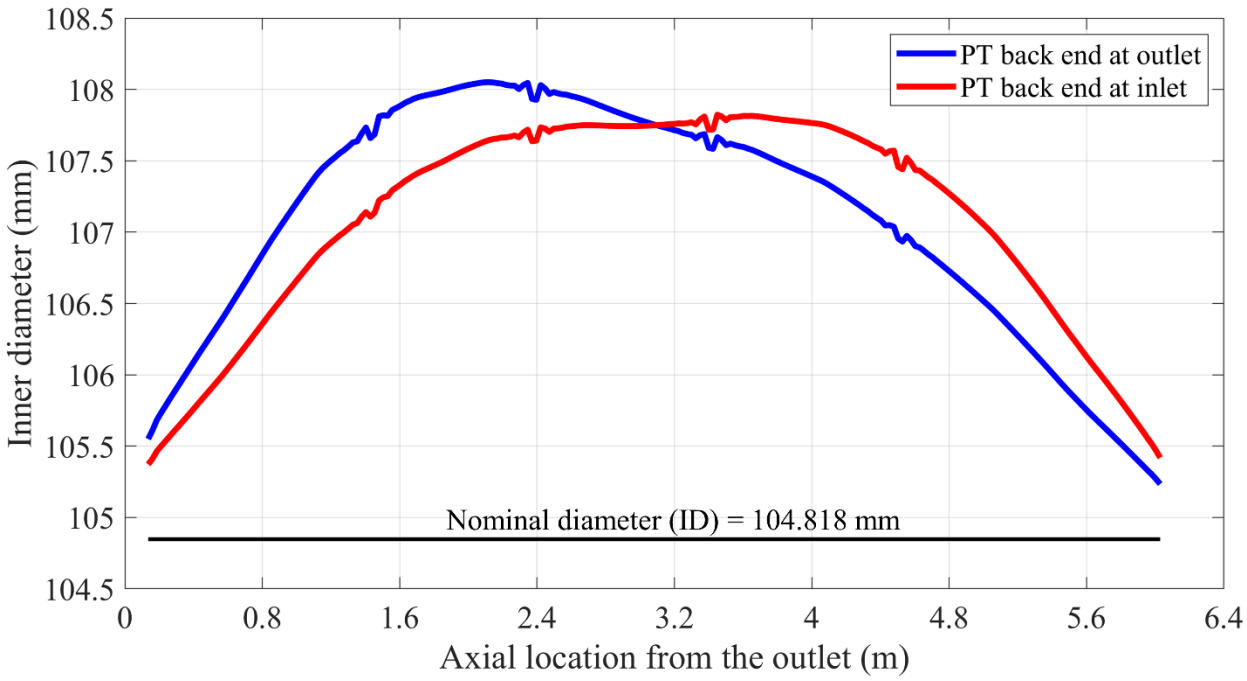

Figure 6.10: Predicted diameter profiles for two different PT orientations with respect to coolant flow at 220 kEFPH

6.4.1.2 Gap profile

The influence of PT orientation on the PT-CT gap profile is shown in Figure 6.11. It is evident that the PT-CT gap at the end spans is significantly influenced by the orientation of the tube with respect to the coolant flow, whereas the gap at the inner spans is almost the same. Span S5 is affected mostly in both cases, whereas the gap is substantially less when the PT has the BEI. This is consistent with the higher diametral expansion at axial locations of Span S5 of a PT with the BEI, as shown in Figure 6.10. Therefore, the likelihood of PT-CT contact during the reactor lifetime is higher for PTs with the BEI that is the free end of the channel. The evolution of gap

profiles with reactor operating time for a PT with BEI is shown in Figure 6.12. As expected, the PT-CT gap at Span 5 is always less for PT with BEI than the gap for PT with BEO (Referring to Figure 3.26) and vice versa at Span1, at all operating intervals.

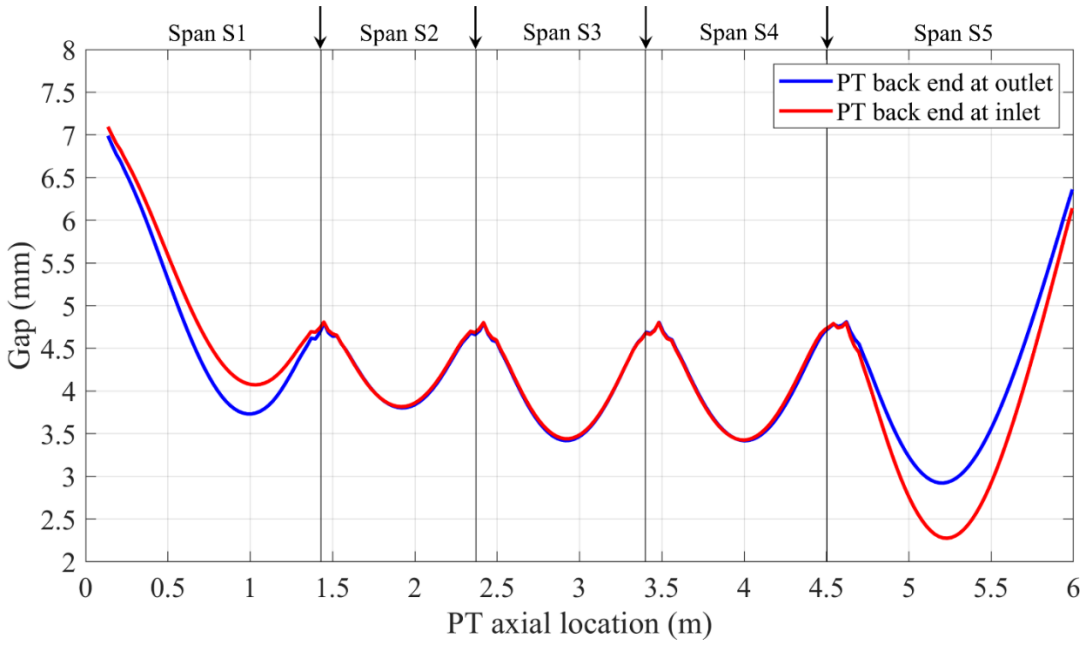

Figure 6.11: Comparison of predicted PT-CT gap profiles at 220 kEFPH for two distinct PT orientations with respect to coolant flow

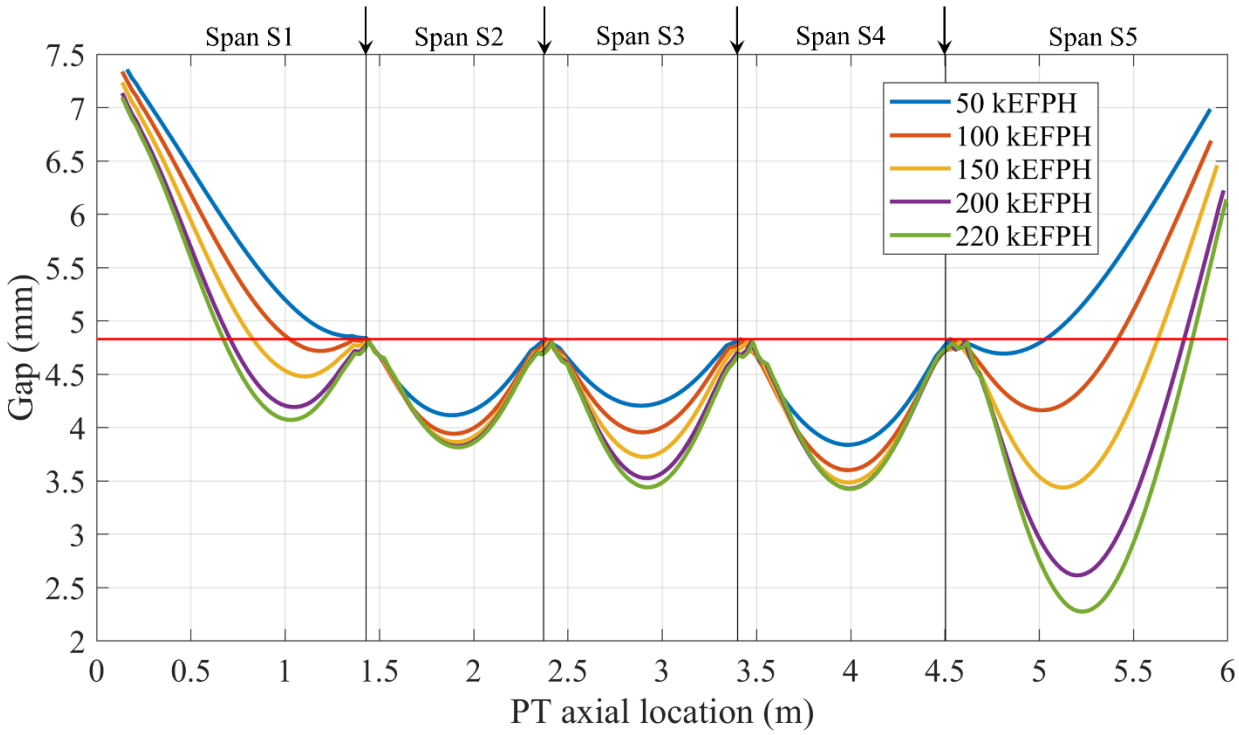

Figure 6.12: Predicted PT-CT gap profiles at various time intervals in the operating life of the FC (PT back end placed at inlet)

6.5 Probabilistic FEA of CANDU FCs using 3D FEA

6.5.1 General

A single 3D FEA simulation takes approximately 2.5 hours to complete, and therefore the computational cost for PFEA using MCS would be colossal, even by using a limited number of trials. Therefore, coupled M-DRM and PCE method is applied for performing probabilistic FEA of CANDU FCs using 3D FEA. The analysis considers different PT orientations (i.e., PT with BEO and BEI) and a detailed probabilistic contact assessment is conducted. The 3D FE model used in this section has the same geometry and operating conditions as discussed in Chapter 3.

Therefore, the results discussed in this section are based entirely on the use of the same 3D FE model.

6.5.2 Application of Coupled M-DRM and PCE Method for 3D PFEA

6.5.2.1 Implementation of the Method

As the random variables (creep factor, outlet end slope and inlet end slope) are the same for 1D and 3D FEA, the initial steps in applying coupled M-DRM and PCE method using 3D FEA are the same as discussed in section 6.3. The surrogate model would be of the form as given in Equation (6.1) and the input grid as given in Table 6.2. As mentioned in section 6.3.3, the total number of FE evaluations required are 13. Therefore, the 13 3D FE evaluations were executed by using each of the input grid values and the corresponding PT-CT gap outputs were collected. Note that the output grid results shown in this section are from 3D FEA runs for a PT back end placed at the fixed outlet end. The same procedure was performed for the analysis of a PT with its back end at the free inlet end. As the gap values vary along the length of the PT and with time, the FE gap output was recorded at 228 axial locations along the axis of the PT. These values were stored in a matrix form corresponding to various time frames. This completes all the steps in the M-DRM module.

Referring to Table 6.2, every five 3D FE model evaluations are grouped in such a way that only one random variable value is changed by keeping other random variables values fixed at their mean. The influence of each of the random variables on the output gap profile can be visualized by plotting the gap profile results corresponding to each of the grouped five 3D FE model

evaluations. Figures 6.13, 6.14 and 6.15 show the gap profile variations at 200 kEFPH for each of the five 3D FEM evaluations.

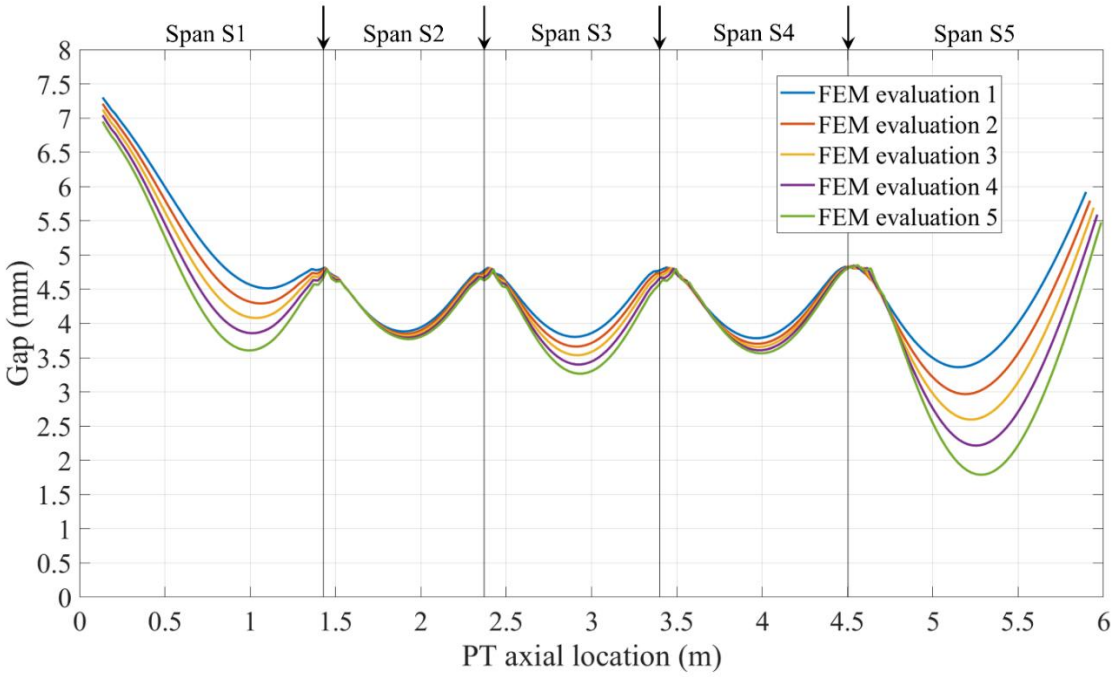

Figure 6.13: Predicted gap profiles from 3D FEA for selected values of creep factors at 200 kEFPH, (inlet slope and outlet slope fixed at mean values and PT with BEO)

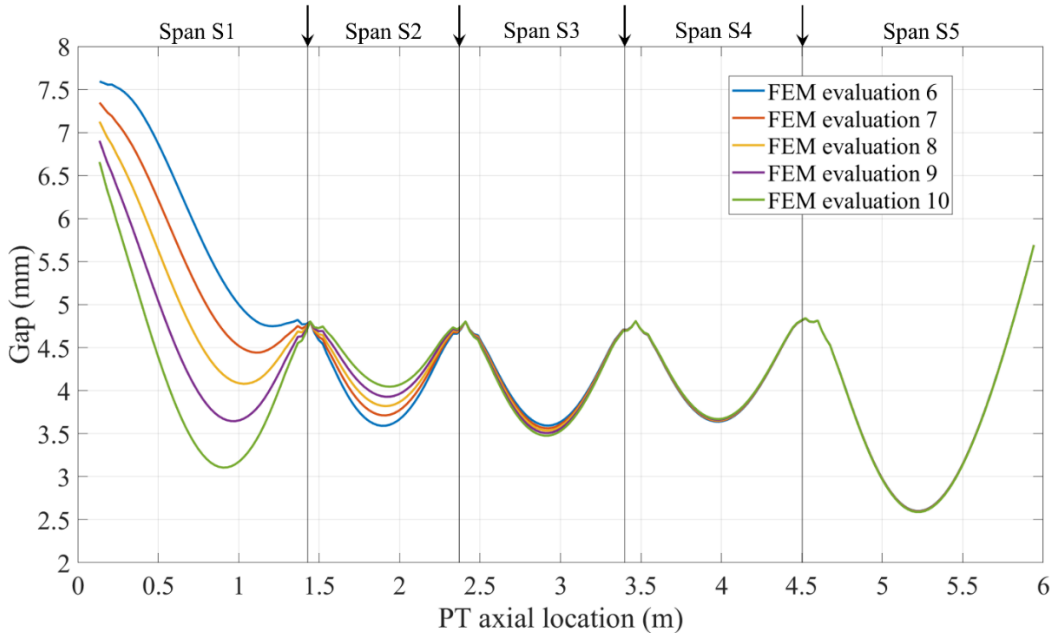

Figure 6.14: Predicted gap profiles from 3D FEA for selected values of outlet slopes at t = 200 kEFPH, (creep factor and inlet slope fixed at mean values and PT with BEO)

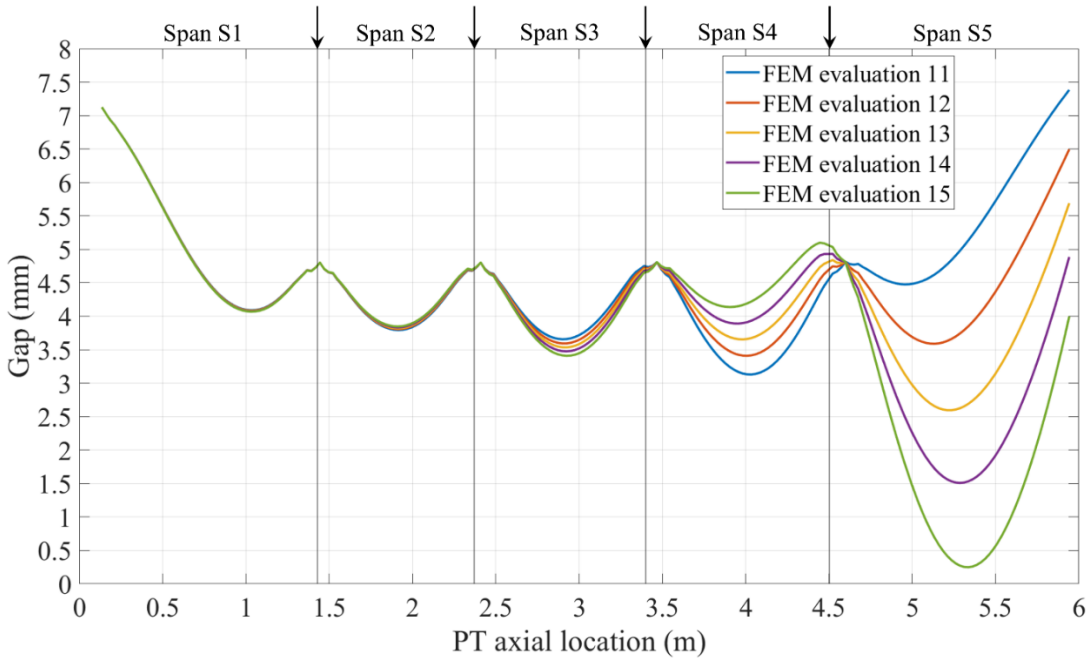

Figure 6.15: Predicted gap profiles from 3D FEA for selected values of inlet slopes at t = 200 kEFPH, (creep factor and outlet slope fixed at mean values and PT with BEO)

After completing all the required 3D FE simulation, the PCE coefficients were computed using the stored output grid gap values. Since the random variables are normally distributed, the Hermite orthogonal polynomials were used as appropriate univariate basis functions. Truncating the order of polynomial chaos to 3, the total number of terms retained in the expansion can be computed as 20. Using the gap values and the constructed PC basis, the PCE coefficients were computed using Equation (5.30) as a function of axial location and time. These coefficients were then saved in a data file in a matrix form.

6.5.2.2 Final Surrogate Model based on 3D FE Model

The final surrogate model of the PT-CT gap was developed by utilizing the saved data file of PCE coefficients as a function of location and time and by using Equation (6.1). This surrogate model is a function of the random variables, C, θ_{out} and θ_{in} and can predict the PT-CT gap by using the values of these random variables into the surrogate model expression as an input. This equation can be then treated as a substitute for the ABAQUS 3D FE model.

To assess the prediction capability of the proposed surrogate model, the gap profiles at (i) t = 220 kEFPH, C = 1.2, θ_{out} = 0.0029 rad and θ_{in} = 0.0048 rad and, (ii) t = 170 kEFPH, C = 0.855, θ_{out} = 0.0022 rad and θ_{in} = 0.0023 rad were predicted using the surrogate model and compared the results to those predicted by the 3D FEA in ABAQUS as shown in . An exceptionally close agreement between the surrogate model prediction and that from the 3D FEA can be seen across all five spans, with a maximum difference of 0.069 mm in the inlet (right most) span.

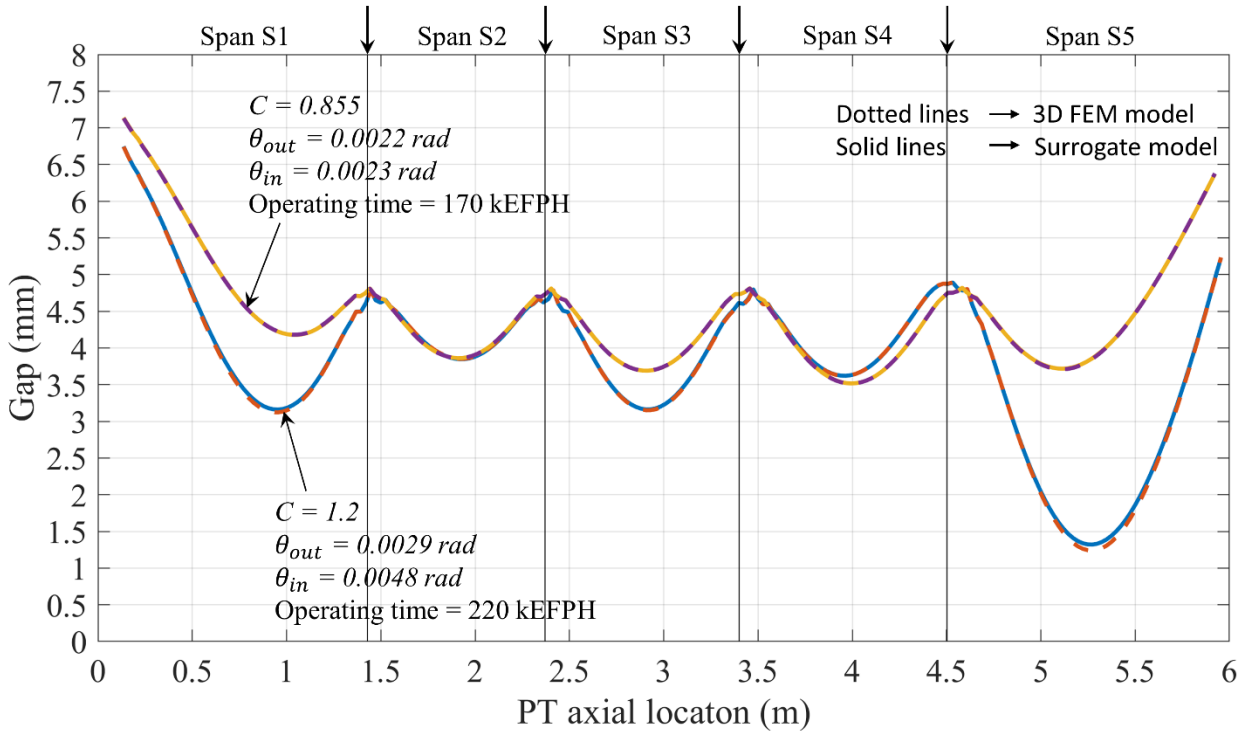

Figure 6.16: Comparison of gap profiles predicted by the surrogate model and the 3D FEA at different time intervals and parameter values

6.5.2.3 Gap statistics

As discussed in Chapter 5, the mean and standard deviation can be determined in a straightforward manner from the PCE coefficients. The mean, (mean + two standard deviations) and (mean – two standard deviations) of gap profiles at 200 kEFPH are presented in Figure 6.17 for both PT orientations. This figure shows the variability introduced by the creep factor and the end slopes to the PT-CT gap profiles at a particular operating time. Compared to other spans, the variability is higher at the inlet (right most) span with the highest variability occurring between 5 and 5.5 m along the PT axial location. This is also the region where the minimum gap occurs and therefore it is the PT-CT region where contact is most likely.

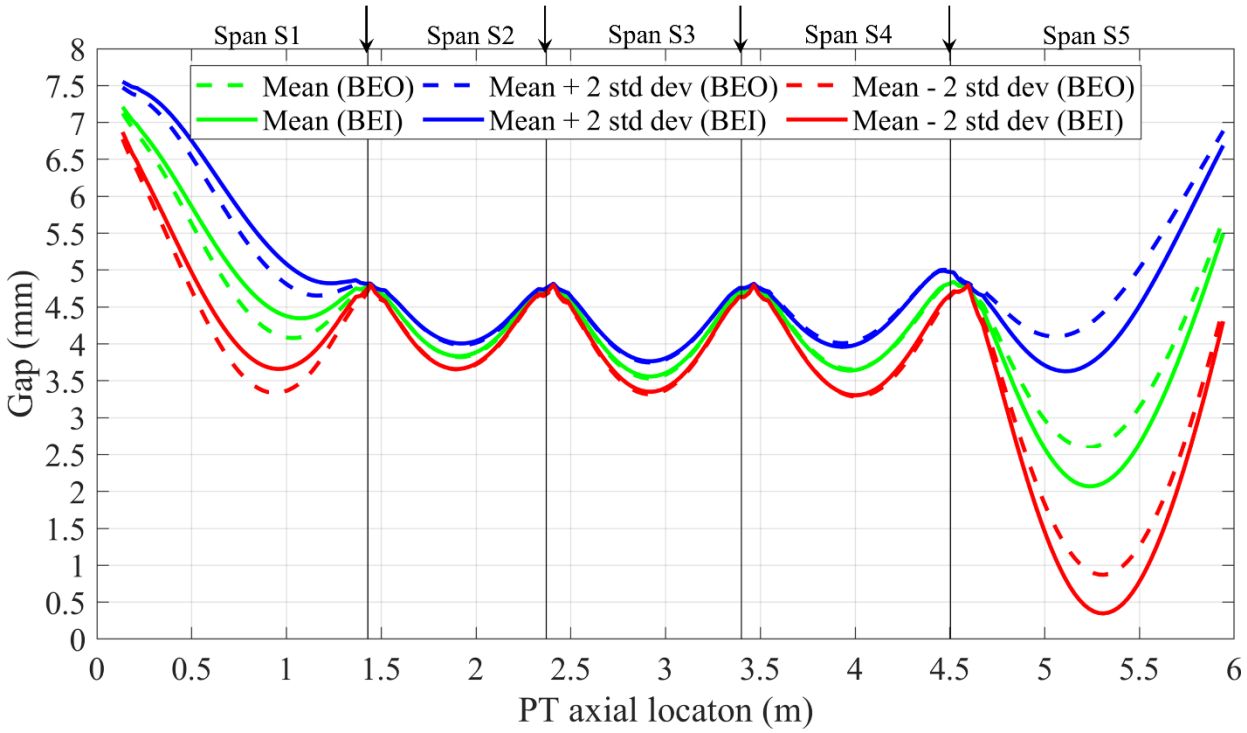

Figure 6.17: Mean and Variability of the gap profile at 200 kEFPH for PTs with the BEO and the BEI

6.5.2.4 Sensitivity Analysis

The sensitivity analysis is performed using Equation (5.29) to quantify the influence of the creep factor and the end-slopes on the gap profile. Figure 6.18 shows the sensitivity indices determined at 220 kEFPH. The outlet slope has a dominant effect on Spans S1 and S2 and no effect on Spans S4 and S5. Similarly, the inlet slope has a dominant effect on Spans S4 and S5 and no effect on Spans S1 and S2. The creep factor has a profound effect on Span S3 but a lesser effect on all the other spans.

To further understand the influence of these variables on PT-CT gap, sensitivity indices were plotted for each variable as a function of time. Figure 6.19 shows an increase in the influence of

creep factor as a function of reactor operation time. The highest influence is happening in Span S3. Figure 6.20 and Figure 6.21 shows the influence of the end slopes. They have a significant effect on the outer spans and lesser on the intermediate spans. Since Span S5 is the area where the probability of a minimum gap is high, it is of special interest. The inlet slope has the highest effect (above 88%) in this span, followed by the creep factor (less than 12%). This shows that the inlet slope is the most important variable influencing the minimum PT-CT gap. This information is important in preventing PT-CT contact by either improving the design in future units such that the end slopes are kept to a minimum or identifying the channels that exhibit high end slope values in existing CANDU units.

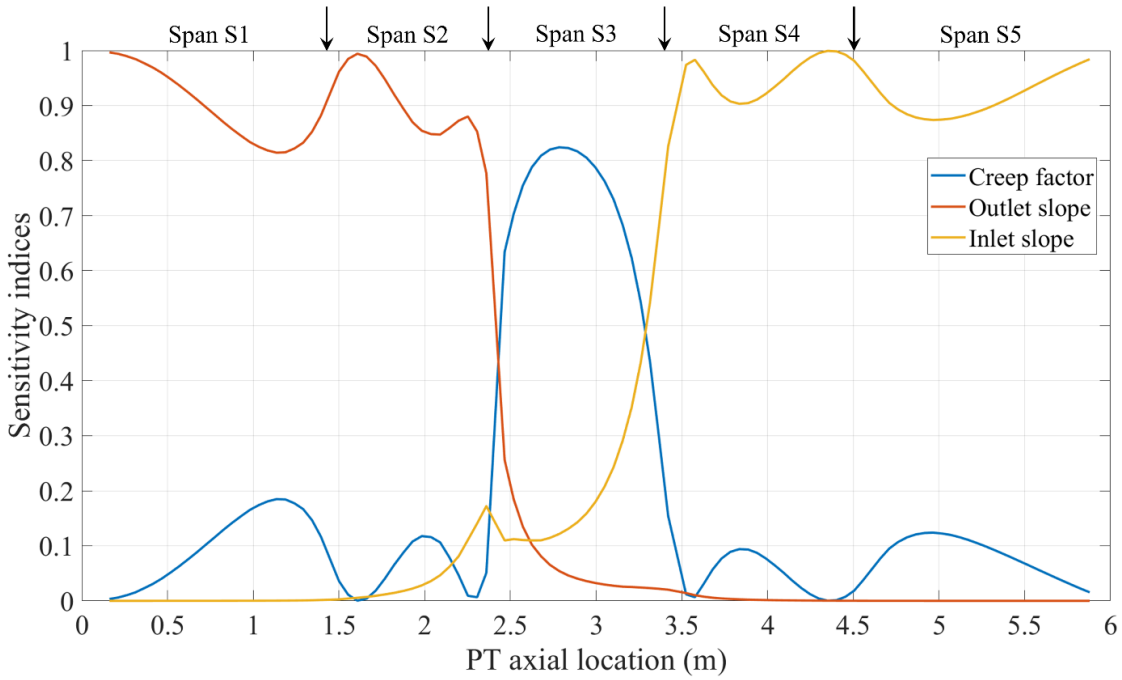

Figure 6.18: Sensitivity indices of the creep factor, outlet slope and inlet slope at 220 kEFPH for a PT with the BEO

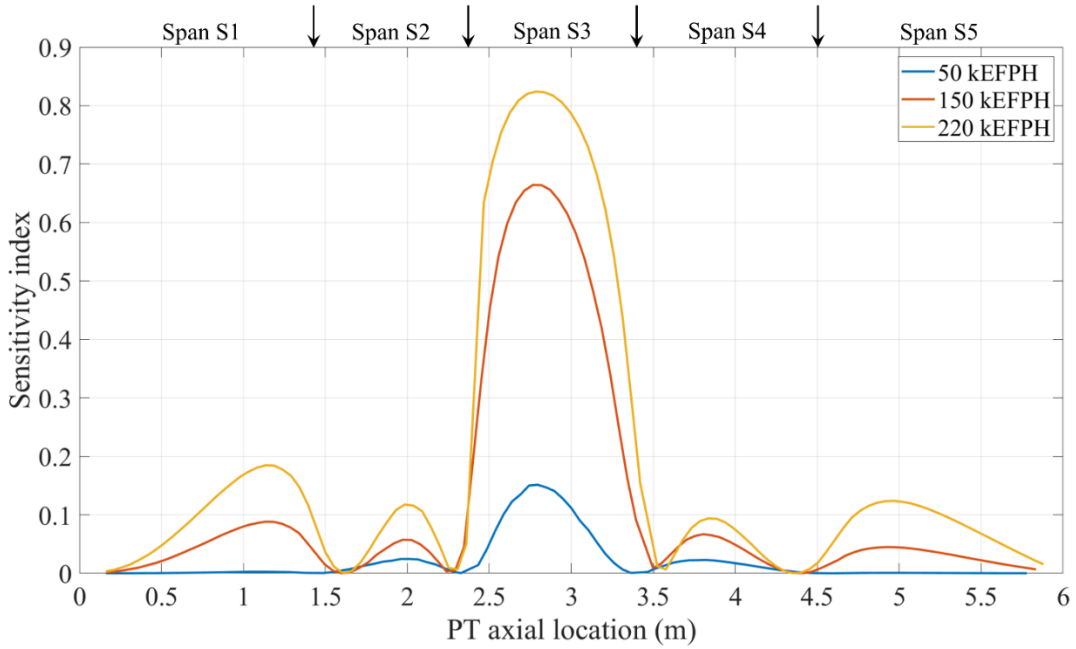

Figure 6.19: Comparison of creep factor sensitivity index at various time interval for a PT with the BEO

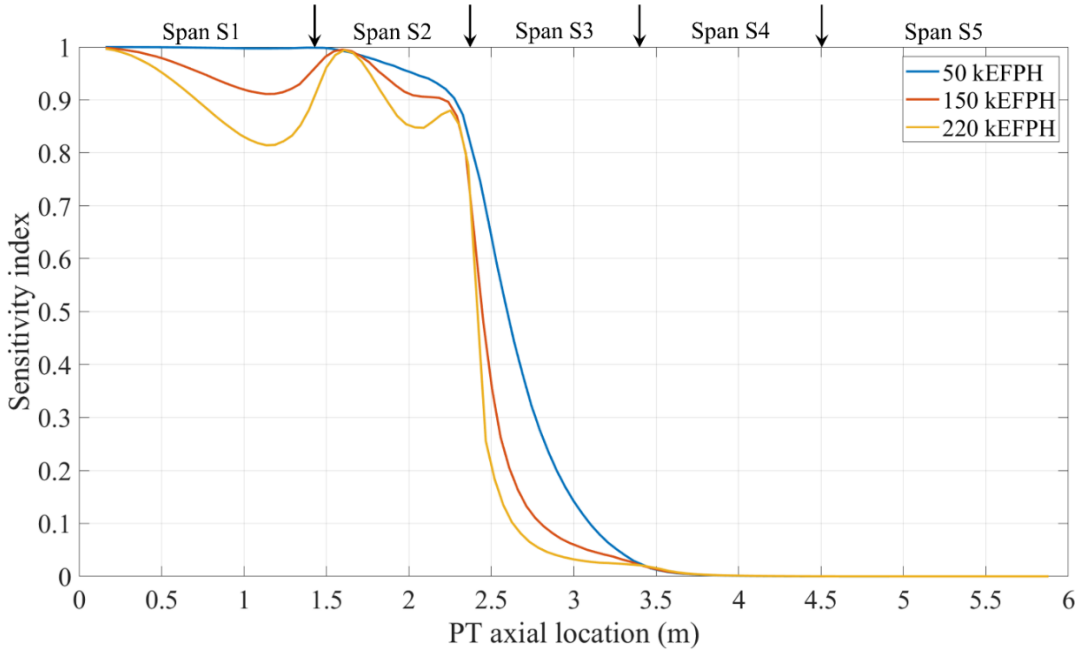

Figure 6.20: Comparison of outlet slope sensitivity index at various time interval for a PT with the BEO

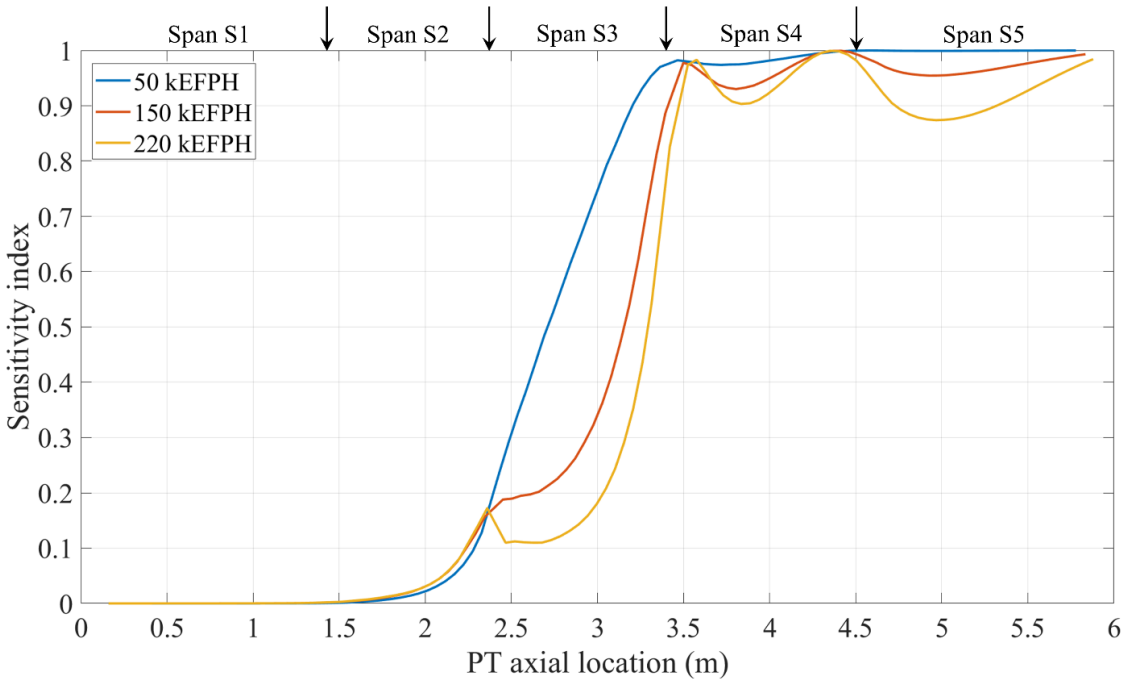

Figure 6.21: Comparison of inlet slope sensitivity index at various time interval for a PT with the BEO

6.5.3 Probabilistic Contact Analysis using the Surrogate Model

The whole purpose of developing a surrogate model was to significantly reduce the computational cost of performing probabilistic assessments by replacing the expensive-to-evaluate 3D FE model with a simpler-to-evaluate surrogate model. The predictive capability of the proposed method was initially validated using the surrogate model developed using 1D FEA and MCS with 10^3 trials. Therefore, the 3D surrogate model developed by means of the approach proposed here was used to perform a probabilistic contact assessment. In probabilistic contact assessment, the interest is in computing the probability of PT coming in contact with CT (i.e, PT-CT gap being zero). One million Monte Carlo simulations were performed using the surrogate model and the minimum gap obtained from the gap profiles were saved for each simulation. Note that the surrogate model is a

simple analytical polynomial chaos expression, and the entire simulation can be completed in a few seconds, which demonstrates how powerful this method is and the significant advantage its use provides. The minimum gap was recorded for various time intervals. An experimental CDF of minimum gap at 150 kEFPH and 220 kEFPH is presented in Figure 6.22. The minimum gap decreases with the operating time and the CDF after 220 kEFPH is substantially higher at low gap values indicating a significantly higher probability of PT-CT contact as the reactor approaches end-of-life.

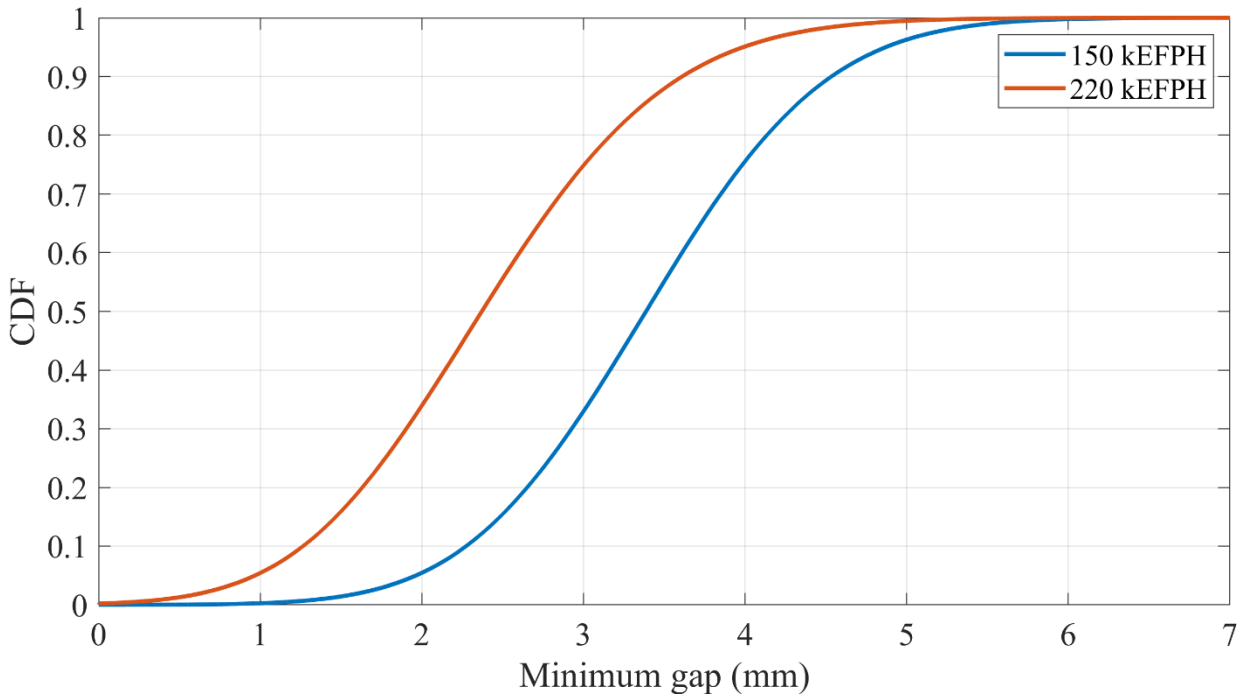

Figure 6.22: Cumulative distribution function (CDF) of minimum gap at two different time intervals for a PT with the BEO

For better understanding of the probability of contact (POC) as a function of reactor operating time, the semi-log CDF plots at given time intervals was plotted as shown in Figure 6.23. A point

on this curve gives the probability of minimum gap becoming less than the minimum gap values on the X-axis. A contact between PT and CT occurs when the minimum gap becomes zero. Therefore, from these curves, the POC is the point where the curve meets zero gap on the X-axis. The POC increases with reactor operating time and at 220 kEFPH, the POC is ~2.2×10^{-3} for a PT with the BEO. These probability curves capture the uncertainty associated with PT-CT contact and will be very important in making risk-based decisions as the reactor approaches end-of-life. These curves not only give the POC but they also provide the probability of gap falling below any minimum gap value of interest. For example, Figure 6.24 shows the probability of minimum gap falling below 2mm at the various operating intervals and as expected, the probability of gap reduction increases with operating interval.

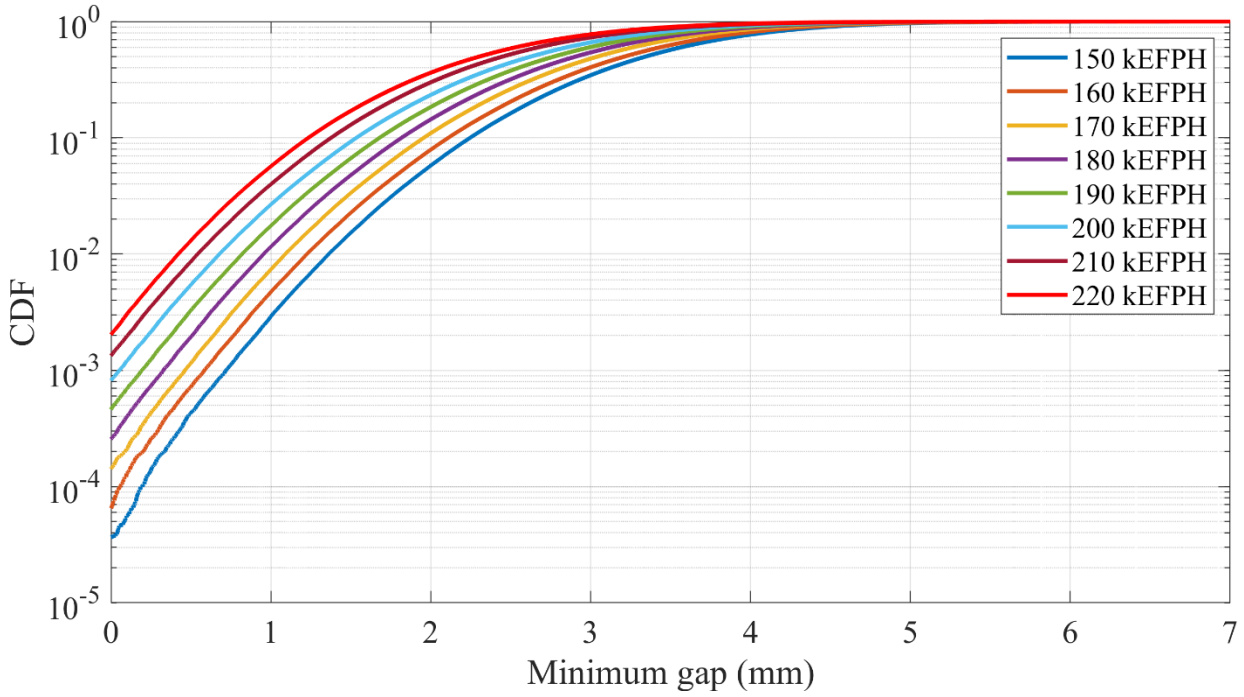

Figure 6.23: Probability of gap reduction at various time intervals during service of FCs (for PTs with the BEO)

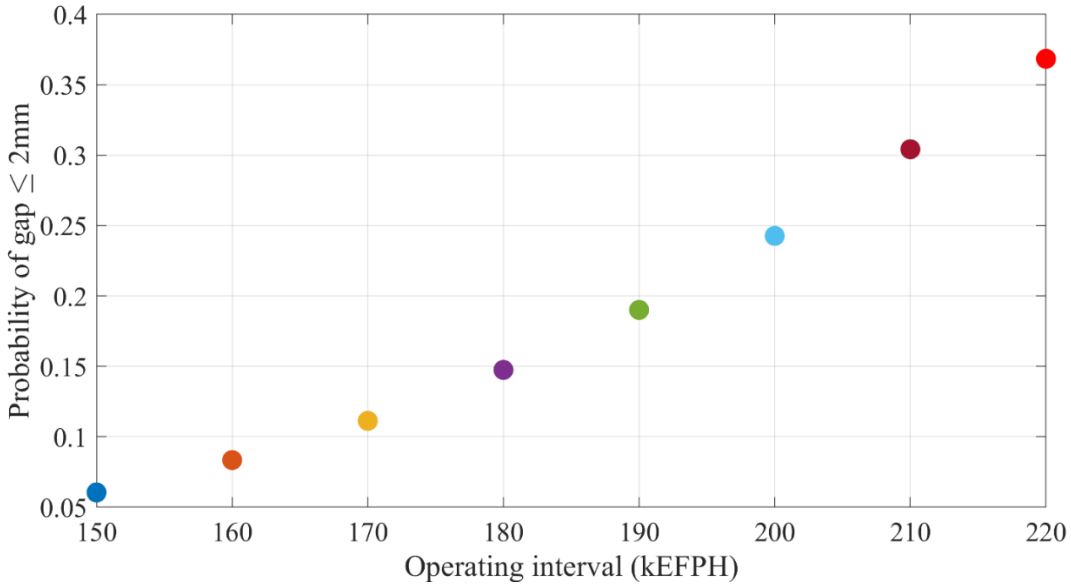

Figure 6.24: Probability of gap falling below 2mm at various time intervals during service of FCs (for PTs with the BEO)

POC predictions were also compared for PTs with different orientations and based on 1D and 3D FEA as shown in Figure 6.25. The POC is high for PTs with the BEI (~1.7×10^{-2} at 220 kEFPH) compared with PTs with the BEO (~2.2×10^{-3} at 220 kEFPH). It appears that nuclear operators should pay increased attention when channels have PTs with their free back end in the inlet. Another important observation is the effect of 1D and 3D FEA on the predicted probability of reaching minimum gap. The current practice by the nuclear industry is to rely on performing 1D FEA using MCS for making risk-based decisions. However, as is shown in Figure 6.25, 1D FEA significantly underestimates the POC (~1.9×10^{-4} at 220 kEFPH) compared to the 3D FEA (~2.2×10^{-3} at 220 kEFPH) and is therefore not a reliable estimate for end-of-life or life-extension decisions. The methodology proposed here is therefore a powerful tool for the nuclear industry to

use for the assessment of reactor units for which their operating life is being extended well beyond the initial design life of 210 kEFPH (Prabhu et al., 2022).

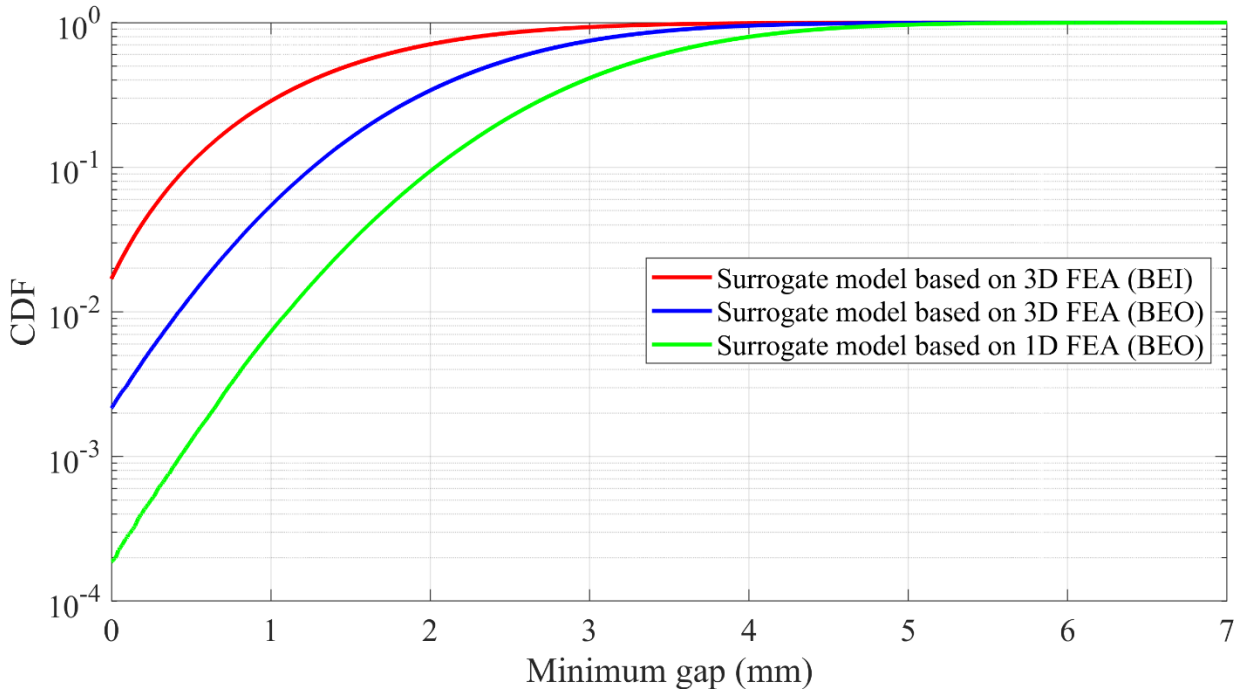

Figure 6.25: Comparison of the probability of gap reduction curves at 220 kEFPH for different PT orientations and type of FE analysis

6.6 Conclusions

This chapter presents a computationally feasible approach for developing a surrogate model of assessing the evolution of PT-CT gap profiles with time and the process to perform probabilistic contact assessments by coupling the multiplicative dimensional reduction method (M-DRM) with the polynomial chaos expansion (PCE). An important advantage of the proposed method is that it requires a significantly smaller number of FE execution runs in the development of the surrogate model. Prior to developing the surrogate model, a deterministic FE model of a fuel channel (FC)

was simulated using ABAQUS and the results of diametral expansion and gap profile predictions with different pressure tube (PT) orientations were discussed. Using the proposed method, the time consuming ABAQUS FEA runs of PT-CT gap predictions were replaced by the simple-to-evaluate surrogate model. The surrogate model is expressed as an additive form of polynomials, which are functions of the creep factor, inlet slope and outlet slope. The model coefficients depend on the axial location along the longitudinal axis of the pressure tube and the reactor operating time, and they were saved as a matrix file for a probabilistic contact assessment of FCs.

A very close agreement was achieved from the comparison between the gap profiles predicted by the 1D FEA and the corresponding surrogate model as well as 3D FEA and its corresponding surrogate model, proving the validity of the method. The results from the sensitivity analysis showed that the inlet slope of the free end of the channel has the strongest effect on the minimum PT-CT gap. The predictive capability of the proposed method for probabilistic assessments was initially examined using the surrogate model that was developed by using 1D FEA and MCS. It was shown that the surrogate model agrees well with the results from the 1D FEA+MCS. Subsequently, using surrogate models that were developed based on 3D FEA simulations, the CDF curves were obtained for both PT orientations. It was shown that these models are significant in making risk-based end-of-life decisions. The results indicate that the probability of PT-CT contact is high for PTs with their back at the free inlet end when compared to PTs with their back placed at the fixed outlet end. The results also show that the current practice of nuclear industry in using 1D FEA for probabilistic FEA using 1000 MCS is not a reliable estimate for making end-of-life or life extension decisions. The 1D FEA results are under-estimating the minimum gap and 1000 MCS trials are not enough to obtain reliable estimates of probabilistic results.

In summary, the low computational cost and predictive capability of the proposed method is suitable for carrying out full probabilistic assessments of CANDU reactor cores for units with 380 or 480 FCs.

Chapter 7

Conclusions and Recommendations

7.1 Summary

Chapter 3 presented the 1D and 3D finite element (FE) modelling details of a CANDU fuel channel (FC) in ABAQUS finite element package and the implementation of pressure tube (PT) and calandria tube (CT) material deformation models in ABAQUS using UMAT. The FC deformations were predicted using both models and a comparison on PT-CT gap profile prediction showed the advantage and need of a 3D FE model in making better predictions.

Chapter 4 presented the importance of surrogate models for replacing the expensive-to-evaluate finite element models. The surrogate models of diametral creep and PT-CT gap profiles had a nonlinear form, and the calibration and validation of these models were conducted by comparing with measured data.

Chapter 5 presented a computationally efficient method for performing structural reliability and sensitivity analysis by coupling the multiplicative dimensional reduction method (M-DRM) with polynomial chaos expansion (PCE) method. The mathematical formulation of PCE and M-DRM along with Gauss quadrature scheme were presented. The steps required in implementing the proposed method was illustrated and the method was demonstrated by applying on a simple analytical equation. The statistical and sensitivity analysis results, along with probability of failure results obtained from the proposed method was compared with the results obtained from Monte Carlo simulation (MCS), which showed a very good agreement.

Chapter 6 presented a computationally feasible approach for developing a surrogate model to assess the evolution of PT-CT gap profiles with time and the process to perform probabilistic contact assessments by coupling the multiplicative dimensional reduction method (M-DRM) with the polynomial chaos expansion (PCE). The predictive capability of the proposed method for probabilistic assessments was initially examined using the surrogate model that was developed by using 1D FEA and MCS, which showed a good agreement. The method was then applied to develop a surrogate model based on 3D FEA and a detailed probabilistic contact assessment by considering different PT orientations was conducted. A critical comparison between the probabilistic analysis results of 1D and 3D FE models showed the downsides of using a 1D FEA with a limited number of Monte Carlo simulations (MCSs) for probabilistic contact analysis. These findings and insights are critical to the nuclear industry.

7.2 Conclusions

This thesis presents 1D and 3D finite element analysis (FEA) of a CANDU fuel channel (FC) to predict the in-reactor deformations due to irradiation induced creep and develops computationally efficient and robust surrogate and probabilistic models based on the FEA of FCs for making better risk-informed decisions. The current industry practices in assessing PT-CT contact risk is critically analyzed, and significant improvements and contributions are made towards assessing the contact risk with confidence. Important conclusions based on this research are categorized into three main categories:

1) Findings regarding the FEA of CANDU FCs

- A full 3D FE model is required for accurately modelling in-reactor deformation and predicting PT-CT gap, contact location and time to contact.
- A comparison between 1D and 3D FEA results showed a significant underestimation of gap by the 1D model. Making end-of-life decisions based on 1D FEM results would therefore be a less reliable estimate.
- Irradiation creep has the most significant contribution to the diametral strain, while thermal creep has only a very small effect. Irradiation growth has a negative contribution to the diametral strain, making it a beneficial mechanism.
- Even though the flux dip at the fuel bundle joints is ~15%, the diametral creep drop by only ~10% due to material continuity.
- The boundary conditions and PT orientations significantly influence the PT-CT gap profiles.

2) Findings regarding surrogate models and probabilistic results of CANDU FCs

- A nonlinear form of surrogate model along with a scale factor is required for calibrating diametral creep, which efficiently captures the fluence dependence on irradiation growth strain rate changes and the variations introduced by material variability.
- The PT-CT gap at a given axial location and time is a linear function of the creep factor if the end-slopes are maintained at their average values, and vice versa.
- The PT-CT gap at a given axial location and time becomes a non-linear function of the creep factor and end slopes when these parameters approach extreme values.

- A nonlinear form of surrogate model captures the PT-CT gap profiles efficiently.
- The probability of PT-CT contact is high for PTs with their back at the free inlet end when compared to PTs with their back placed at the fixed outlet end.
- The surrogate model based on a 1D FEM significantly over-predict (by 14.6 %) the time for PT-CT contact. Given that 7 kEFPH is approximately the number of EFPH in one calendar year, the 1D model overpredicts the time to contact by 38 kEFPH or almost 5.5 calendar years.
- The current practice of nuclear industry in using 1D FEA for probabilistic FEA using 1000 MCS is not a reliable estimate for making end-of-life or life extension decisions. The error is introduced from the simplification of modelling using 1D FE model and by using a small number of MCS.
- For a PT with back end placed at outlet, the probability of contact (POC) using 1D FEA surrogate model is ~1.9×10^{-4} compared to the 3D FEA of ~2.2×10^{-3} at 220 kEFPH. The nuclear industry must be aware of this prediction error using 1D FEA and should therefore rely on probabilistic results from 3D FEA for making confident risk-informed decisions.

3) Findings with respect to coupled M-DRM and PCE method

- The coupled M-DRM and PCE method can be considered as a computationally efficient method for performing probabilistic finite element analysis of expensive-to-evaluate finite element models.

- Combining M-DRM with PCE gives a significant reduction in computational cost involved in computing the PCE coefficients and thereby in the surrogate model construction.
- The surrogate model can be used to obtain the complete probability distribution and the straightforward post-processing using PCE coefficients gives the statistics of the output response of interest and the sensitivity indices of the random variables influencing the output response without any additional computational cost.
- The coupled M-DRM and PCE method requires only a few function evaluations and therefore can be performed using any deterministic FEA software without the use of advanced programming, making the approach flexible and easy-to-implement.

7.3 Recommendations for Future Research

The following are the recommendations for future research:

- The 3D finite element model can be updated by considering through thickness elements for pressure tube. Instead of using shell elements which is based on plane stress condition, solid elements can be considered for accounting the full triaxial stress state. However, the solid elements could significantly increase the computational cost of the analysis.
- The variation of flux and temperature along the circumference of the pressure tube with diametral expansion can be considered to further improve the predictions of diametral strain along the circumference as well as PT-CT gap predictions at locations other than at 6 o'clock position.

- The proposed coupled approach considers only uncorrelated random variables. The analysis can be extended to investigate the application to correlated random variables.
- The developed surrogate models of diametral creep and PT-CT gap doesn't include the operating conditions (fast flux and temperature) in the model. The analysis can be extended further to include the operating condition parameters into the surrogate model to make it more universal.
- Additional analysis can be performed up on availability of in-reactor inspection data to obtain the distribution of certain parameters. For example, the scale factor was obtained for five fuel channels used in the calibration and development of surrogate model of diametral creep. More analysis would give the distribution of this factor and therefore can be used for probabilistic analysis.

References

ABAQUS. (n.d.). *Abaqus UMAT User's Manual. Version 6.12, Dassault Syst. Simulia Corp.*

Abdelsalam, U., & Vijay, D. (2010). ASME Code Qualification of Pipe Bends With Localized Wall Thinning. *In ASME 2010 Pressure Vessels and Piping Division/K-PVP Conference*, 213–220.

Alexander Hrennikoff. (1941). Solution of problems of elasticity by the framework method. *J. Appl. Mech.*

Ang, A., & Tang, W. (2007a). *Probability concepts in engineering: emphasis on applications in civil & environmental engineering*. John Wiley & Sons Inc.

Ang, A., & Tang, W. (2007b). *Probability concepts in engineering: emphasis on applications in civil & environmental engineering* (Vol. 1). Wiley.

ASME. (2015). Rules for Construction of Nuclear Facility Components. In *ASME Boiler and Pressure Vessel Code, Section III*. American Society of Mechanical Engineers.

Badie, N., Holt, R. A., Schulte, C. W., & Sauvé, R. G. (1988). Sag of Zr-2.5% Nb Pressure Tubes. *Proceedings of the Ninth Annual Conference of the Canadian Nuclear Society*.

Balomenos, G. P., Genikomsou, A. S., Polak, M. A., & Pandey, M. D. (2015a). Efficient method for probabilistic finite element analysis with application to reinforced concrete slabs. *Engineering Structures*, *103*, 85–101.

Balomenos, G. P., Genikomsou, A. S., Polak, M. A., & Pandey, M. D. (2015b). Efficient method for probabilistic finite element analysis with application to reinforced concrete

slabs. *Engineering Structures*, *103*, 85–101.

Balomenos, G. P., & Pandey, M. D. (2016). Finite element reliability and sensitivity analysis of structures using the multiplicative dimensional reduction method. *Structure and Infrastructure Engineering*, *12*(12), 1553–1565.

Balomenos, G. P., & Pandey, M. D. (2017). Probabilistic finite element investigation of prestressing loss in nuclear containment wall segments. *Nuclear Engineering and Design*, *311*, 50–59.

Balu, A. S., & Rao, B. N. (2012). High dimensional model representation based formulations for fuzzy finite element analysis of structures. *Finite Elements in Analysis and Design*, *50*, 217–230.

Beyer, W. H. (1987). *CRC standard mathematical tables*. CRC Press, Taylor & Francis Group.

Bickel, G. A., & Griffiths, M. (2007). Manufacturing variability, microstructure, and deformation of Zr-2.5Nb pressure tubes. *Journal of ASTM International*, *4*(10), 1–11.

Bickel, G. A., & Griffiths, M. (2008). Manufacturing variability and deformation for Zr-2.5Nb pressure tubes. *Journal of Nuclear Materials*, *383*(1–2), 9–13.

Blatman, G., & Sudret, B. (2010a). An adaptive algorithm to build up sparse polynomial chaos expansions for stochastic finite element analysis. *Probabilistic Engineering Mechanics*, *25*, 183–197.

Blatman, G., & Sudret, B. (2010b). An adaptive algorithm to build up sparse polynomial chaos expansions for stochastic finite element analysis. *Probabilistic Engineering Mechanics*,

25(2), 183–197.

Bruno, S. (2007). *Uncertainty propagation and sensitivity analysis in mechanical models–Contributions to structural reliability and stochastic spectral methods*.

Byrne, T. P., Metzger, D. R., & Leger, M. (1991). Zirconium Hydride Blister Modelling and the Application to the P2-G16 Failure. *Proc. of the 11th Conf. on Structural Mechanics in Reactor Technology (SMiRT 11 Transactions)*, 335–340.

Cameron, R., & Martin, W. (1947). The orthogonal development of non-linear functionals in series of Fourier-Hermite functionals. *Annals of Mathematics*, 385–392.

Causey, A. R. (1974). In-Reactor Creep of Zircaloy-2, Zircaloy-4 and Zr-1.15 wt % Cr-0.1 wt % Fe at 568 K Derived from their Stress-Relaxation Behaviour. *Journal of Nuclear Materials*, *54*, 64–72.

Causey, A. R. (1981). Anisotropy of irradiation creep of Zr-2.5 wt% Nb and Zircaloy-2 alloys. *Journal of Nuclear Materials*, *98*(3), 313–321.

Causey, A. R., Elder, J. E., Holt, R. A., & Fleck, R. G. (1994). On the Anisotropy of In-Reactor Creep of Zr-2.5Nb Tubes. *Proceedings of the 10th Int. Symp. on Zr in the Nuclear Industry, ASTM STP 1245*, 202–220.

Causey, A. R., Holt, R. A., & MacEwen, S. R. (1984). In-Reactor Creep of Zr-2.5Nb. In D.G. Franklin and R.B. Adamson (Ed.), *Proceedings of the 6th Int. Symp. on Zr in the Nuclear Industry, ASTM STP 824* (pp. 269–288). American Society for Testing of Materials.

Causey, A. R., Norsworthy, A. G., & Schulte, C. W. (1985). Factors Affecting Creep Sag of

Fuel Channels in Candu-PHW Reactors. *Canadian Metallurgical Quarterly*, *24*(3), 207–214.

Causey, A. R., Woo, C. H., & Holt, R. A. (1988). The Effect of Intergranular Stresses on the Texture Dependence of Irradiation Growth in Zirconium Alloys. *Journal of Nuclear Materials*, *159*, 225–236.

Choubey, R., Aldridge, S., Theaker, J., & Cann, C. (1996). Effects of extrusion-billet preheating on the microstructure and properties of Zr-2.5 Nb pressure tube materials. *Zirconium in the Nuclear Industry. Eleventh International Symposium, ASTM STP 1295, E.R. Bradley and G.P. Sabol, Eds., American Society for Testing of Materials*.

Chowdhury, R., Rao, B. N., & Prasad, A. M. (2009). High-dimensional model representation for structural reliability analysis. *Communications in Numerical Methods in Engineering*, *25*, 301–337.

Christodoulou, N., Causey, A. R., Holt, R. A., Tome, C. N., Badie, N., Klassen, R. J., Sauve, R., & Woo, C. H. (1996). Modeling In-Reactor Deformation of Zr-2.5Nb Pressure Tubes in CANDU Power Reactors. *Zirconium in the Nuclear Industry: Eleventh International Symposium, ASTM STP 1295, E.R. Bradley and G.P. Sabol, Eds., American Society for Testing and Materials*, 518–537.

Christodoulou, N., Causey, A. R., Woo, C. H., & Tomé, C. N. (1993). Modelling the Effect of Texture and Dislocation Structure on Irradiation Creep of Zirconium Alloys. *Proceedings in Effects of Radiation on Materials, 16th Int. Symp., ASTM STP 1175*, 1111–1128.

Clough, R. W. (1960). The finite element method in plane stress analysis. *Proceedings of 2nd*

ASCE Conference on Electronic Computation.

Coleman, C. E., Causey, A. R., & Fidleris, V. (1976). In-reactor Creep of Zirconium-2.5 wt% Niobium at 570 K. *Journal of Nuclear Materials*, *60*, 185–194.

Courant, R. (1943). Variational methods for the solution of problems of equilibrium and vibrations. *Bulletin of the American Mathematical Society*, *49*, 1–23.

CSA N285.4. (2010). *Periodic Inspection of CANDU Nuclear Power Plant Components*.

CSA N285.8. (2015). *Technical Requirements for in-service Evaluation of Zirconium Alloy Pressure Tubes in CANDU Reactors*.

Debusschere, B. J., Najm, H. N., Pébay, P. P., Knio, O. M., Ghanem, R. G., & Le Maitre, O. P. (2004). Numerical Challenges in the Use of Polynomial Chaos Representations for Stochastic Processes. *SIAM Journal on Scientific Computing*, *26*(2), 698–719.

Der Kiureghian, A., & Liu, P. (1986). Structural Reliability under Incomplete Probability Information. *Journal of Engineering Mechanics*, *112*(1), 85–104.

Ditlevsen, O., & Madsen, H. O. (1996). *Structural reliability methods*. Wiley.

Dubourg, V. (2011). *Adaptive surrogate models for reliability analysis and reliability-based design optimization. Ph.D.thesis*. Université Blaise Pascal, Clermont-Ferrand, France.

Ellingwood, B. (2006). Structural safety special issue: General-purpose software for structural reliability analysis. *Structural Safety*, *28*, 1–2.

Ells, C. E., Coleman, C. E., & Chow, C. K. (1985). Properties of a Candu Calandria Tube. *Canadian Metallurgical Quarterly*, *24*(3), 215–223.

Fanjoy, G. R. (1984). *Pressure tube failure-Pickering NGS unit 2 (No. CNS--75)*.

Fidleris, V. (1988). The Irradiation Creep and Growth Phenomena. *Journal of Nuclear Materials*, *159*, 22–42.

Fidleris, V., Causey, A., & Holt, R. (1985). Factors affecting in-core dimensional stability of Zircaloy-2 calandria tubes. *Optimizing Materials for Nuclear Applications*, 35–50.

Fleck, R. G., Elder, J. E., Causey, A. R., & Holt, R. A. (1994). Variability of Irradiation Growth in Zr-2.5Nb Pressure Tubes. *Proceedings of the 10th Int. Symp. on Zr in the Nuclear Industry, ASTM STP 1245*, 168–182.

Fleck, R., Price, E., & Cheadle, B. (1984). Pressure tube development for CANDU reactors. *Zirconium in the Nuclear Industry. ASTM International*.

Fraser, D. E., Ross-Ross, P. A., & Causey, A. R. (1973). The Relation Between Stress-Relaxation and Creep for Some Zirconium Alloys During Neutron Irradiation. *Journal of Nuclear Materials*, *46*, 281–292.

Gerstner, T., & Griebel, M. (1998). Numerical integration using sparse grids. *Numerical Algorithms*, *18*(3–4), 209–232.

Ghanem, R. (1998). Probabilistic characterization of transport in heterogeneous media. *Comput. Methods Appl. Mech. Engrg*, *158*, 199–220.

Ghanem, R., & Spanos, P. (1991). *Stochastic finite elements: a spectral approach*. Springer - Verlag.

Griffiths, M., Davies, W., Causey, A., Moan, G., Holt, R., & Aldridge, S. (2002). Variability

of In-Reactor Diametral Deformation for Zr-2.5Nb Pressure Tubing. *Proceedings of the 13th International Symposium on Zirconium in the Nuclear Industry, ASTM STP 1423, American Society for Testing and Materials*, 796–810.

Gupta, A., & Choi, B. (2003). Reliability-based load and resistance factor design for piping: An exploratory case study. *Nuclear Engineering and Design*, *224*(2), 161–178.

Haldar, A., & Mahadevan, S. (2000). *Reliability assessment using stochastic finite element analysis*. John Wiley & Sons.

Hasofer, A., & Lind, N. (1974). Exact and invariant second-moment code format. *Journal of the Engineering Mechanics Division*, *100(1)*, 111–121.

Haukaas, T. (2003). *Finite element reliability and sensitivity methods for performance-based engineering*.

Haukaas, T., & Der Kiureghian, A. (2006). Strategies for finding the design point in non-linear finite element reliability analysis. *Probabilistic Engineering Mechanics*, *21*, 133–147.

Haukaas, T., & Der Kiureghian, A. (2007). Methods and Object-Oriented Software for FE Reliability and Sensitivity Analysis with Application to a Bridge Structure. *ASCE Journal of Computing in Civil Engineering*, *21*(3), 151–163.

Hill, R. (1998). *The Mathematical Theory of Plasticity*. Oxford University Press.

Hohenbichler, M., & Rackwitz, R. (1981). Non-normal dependent vectors in structural safety. *Journal of the Engineering Mechanics Division*, *107.6*, 1227–1238.

Holt, R. A. (1979). Effect of Microstructure on Irradiation Creep and Growth of Zircaloy

Pressure Tubes in Power Reactors. *Journal of Nuclear Materials*, *82*, 419–429.

Holt, R. A. (2008). In-reactor deformation of cold-worked Zr-2.5Nb pressure tubes. *Journal of Nuclear Materials*, *372*(2–3), 182–214.

Holt, R. A., & Causey, A. R. (1997). The effects of intergranular constraints on irradiation growth of Zircaloy-2 at 320 K. *Journal of Nuclear Materials*, *150*, 306–318.

Holt, R. A., Causey, A. R., Griffiths, M., & Ho, E. T. C. (2000). High-Fluence Irradiation Growth of Cold-Worked Zr-2.5Nb. *Zr in the Nuclear Industry, Twelfth International Symposium, ASTM STP 1354*, 86–105.

Holt, R. A., Christodoulou, N., & Causey, A. R. (2003). Anisotropy of In-Reactor Deformation of Zr 2.5Nb Pressure Tubes. *Journal of Nuclear Materials*, *317*, 256–260.

Holt, R. A., & Fleck, R. G. (1991). The Contribution of Irradiation Growth to Pressure Tube Deformation. *Proceedings in 9th Int. Symposium on Zr in the Nuclear Industry, ASTM STP 1132*, 218–228.

Holt, R. A., Holden, T. M., Causey, A. R., & Fidleris, V. (1989). Intergranular Constraints in Polycrystalline Zircaloy-2. *Proceedings of the 10th Risø International Symposium on Metallurgy and Materials Science: Materials Architecture, Risø National Laboratory, Roskilde*, 383–390.

Holt, R. A., & Wong, H. W. (2002). Life management of CANDU fuel channels. *Nuclear Energy*, *41*(02), 69–74.

Hosder, S., Walters, R. W., & Balch, M. (2007). Efficient Sampling for Non-Intrusive

Polynomial Chaos Applications with Multiple Uncertain Input Variables. *In 48th AIAA/ASME/ASCE/AHS/ASC Structures, Structural Dynamics, and Materials Conference.*, 1939.

Hurtado, J. E., & Barbat, A. H. (1998). Monte Carlo techniques in computational stochastic mechanics. *Archives of Computational Methods in Engineering*, *5*(1), 3–29.

Ibrahim, E. F., & Holt, R. A. (1980). Anisotropy of Irradiation Creep and Growth of Zirconium alloy PTs. *Journal of Nuclear Materials, 91*, 311–321.

Kim, T. R., & Sohn, S. M. (2004). Computation and measurement of calandria tube sag in pressurized heavy water reactor. *Nuclear Engineering and Design*.

Koduru, S. D., & Haukaas, T. (2010). Feasibility of FORM in finite element reliability analysis. *Structural Safety*, *32*(2), 145–153.

Kythe, P. K., & Schäferkotterr, M. R. (2004). *Handbook of computational methods for integration* (C. and H. CRC Press (ed.)).

Le Maˆıtremaˆıtre, O. P., Reagan, M. T., Najm, H. N., Ghanem, R. G., & Knio, O. M. (2002). A Stochastic Projection Method for Fluid Flow II. Random Process. *Journal of Computational Physics*, *181*, 9–44.

Leitch, B. W. (2004). Deformation Behaviour of a Transversely Loaded Garter Spring. *Pressure Vessels and Piping Conference*, 53–58.

Li, G., Rosenthal, C., & Rabitz, H. (2001). High Dimensional Model Representations. *The Journal of Physical Chemistry, American Chemical Society*, *105*(33), 7765–7777.

Li, G., Wang, S. W., Rosenthal, C., & Rabitz, H. (2001). High dimensional model representations generated from low dimensional data samples. I. mp-Cut-HDMR. *Journal of Mathematical Chemistry*, *30*(1), 1–30.

Lopez, R. H., Torii, A. J., Miguel, L. F. F., & Souza Cursi, J. E. (2015). Overcoming the drawbacks of the FORM using a full characterization method. *Structural Safety*, *54*, 57–63.

Madsen, H., Krenk, S., & Lind, N. (2006). *Methods of structural safety*. Courier Corporation.

Maître, O. Le, & Knio, O. (2010). *Spectral methods for uncertainty quantification: with applications to computational fluid dynamics*. Springer Science & Business Media.

Melchers, R., & Beck, A. (2018). *Structural reliability analysis and prediction*. John Wiley & Sons.

Metropolis, N., & Ulam, S. (1949). The Monte Carlo Method. *Journal of the American Statistical Association*, *44*(247), 335–341.

N Wiener. (1938). The homogeneous chaos. *American Journal of Mathematics*, *60*(4), 897–936.

Nadeau, E. (2012). Derivation of input distributions for probabilistic evaluation using in-reactor measurements. *Proceedings of the ASME 2012 Pressure Vessels & Piping Conference*, 285–294.

Nadeau, E., Byrne, T., Khajehpour, S., Lupia, E., & Araujo, E. (2007). Probabilistic Evaluation in Support of Risk-Informed Pressure Tube Maintenance. *Structural Mechanics in*

Reactor Technology-19.

Northwood, D. O., London, I. M., & Bahen, L. E. (1975). Elastic Constants of Zirconium Alloys. *Journal of Nuclear Materials*, *55*, 299–310.

Orszag, S. A., & Bissonnette, L. R. (1967). Dynamical Properties of Truncated Wiener-Hermite Expansions. *Physics of Fluids*, *10*(12), 2603.

Pan, Z. L., Wang, N., & He, Z. (2010). Measurements of Elastic Modulus in Zr Alloys for CANDU Applications. *11th International Conference on CANDU Fuel*.

Pandey, M. D., Tallavo, F. J., Christodoulou, N. C., Leitch, B., & Bickel, G. A. (2018). Understanding the mechanics of creep deformation to develop a surrogate model for contact assessment in CANDU® fuel channels. *Nuclear Engineering and Design*, *330*(January), 141–156.

Papadrakakis, M., & Kotsopulos, A. (1999). Parallel solution methods for stochastic finite element analysis using Monte Carlo simulation. *Computer Methods in Applied Mechanics and Engineering*, *168*(1–4), 305–320.

Pellissetti, M. F., & Schuëller, G. I. (2006). On general purpose software in structural reliability-An overview. *Structural Safety*, *28*, 3–16.

Prabhu, S. R., Pandey, M. D., & Christodoulou, N. (2022a). An efficient method for probabilistic finite element analysis with application to contact assessment of CANDU fuel channels. *Nuclear Engineering and Design*, *387*(September 2021), 111609.

Prabhu, S. R., Pandey, M. D., & Christodoulou, N. (2022b). Computational modeling of in-

reactor deformation in CANDU fuel channels. In Jovica Riznic (Ed.), *Pressurized Heavy Water Reactors* (pp. 135–169). Elsevier.

Prabhu, S. R., Pandey, M. D., Christodoulou, N., & Leitch, B. W. (2020). A surrogate model for the 3D prediction of in-service deformation in CANDU® fuel channels. *Nuclear Engineering and Design*, *369*, 110871.

Rabitz, H., Aliş, Ö. F., Shorter, J., & Shim, K. (1999). Efficient input-output model representations. *Computer Physics Communications*, *117*(1–2), 11–20.

Rackwitz, R., & Fiessler, B. (1978). Structural reliability under combined load sequences. *Computer & Structures ASCE*, 2195–2199.

Rahman, S., & Xu, H. (2004). A univariate dimension-reduction method for multi-dimensional integration in stochastic mechanics. *Probabilistic Engineering Mechanics*, *19*(4), 393–408.

Rao, B. N., Chowdhury, R., Prasad, A. M., Singh, R. K., & Kushwaha, H. S. (2009). Probabilistic characterization of AHWR Inner Containment using High Dimensional Model Representation. *Nuclear Engineering and Design*, *239*, 1030–1041.

Rao, B. N., Chowdhury, R., Prasad, A. M., Singh, R. K., & Kushwaha, H. S. (2010). Reliability analysis of 500 MWe PHWR inner containment using high-dimensional model representation. *International Journal of Pressure Vessels and Piping*, *87*, 230–238.

Reddy, J. N. (2010). *An introduction to the finite element method*. McGraw-Hill.

Reh, S., Beley, J.-D., Mukherjee, S., Khor, H., & Khor, E. H. (2006). Probabilistic finite

element analysis using ANSYS. *Structural Safety*, *28*, 17–43.

Rosenblatt, M. (1952). Remarks on a multivariate transformation. *The Annals of Mathematical Statistics*, *23*(3), 470–472.

Rosenblueth, E. (1975). Point estimates for probability moments. *Proceedings of the National Academy of Sciences*, *72*(10), 3812–3814.

Ross-Ross, P. A., Fidleris, V., & Fraser, D. E. (1972). Anisotropic creep behaviour of zirconium alloys in a fast neutron flux. *Canadian Metallurgical Quarterly*, *11*(1), 101–111.

SA Smolyak. (1963). Quadrature and interpolation formulas for tensor products of certain classes of functions. *Doklady Akademii Nauk*, *148*(5), 1042–1045.

Saibaba, N., Vaibhaw, K., Neogy, S., Mani Krishna, K. V., Jha, S. K., Phani Babu, C., Ramana Rao, S. V., Srivastava, D., & Dey, G. K. (2013). Study of microstructure, texture and mechanical properties of Zr-2.5Nb alloy pressure tubes fabricated with different processing routes. *Journal of Nuclear Materials*, *440*(1–3), 319–331.

Sauvé, R. G. (1987). Predicting Creep Response of CANDU Fuel Channel Assemblies. *Proceedings of the 13th Annual Reactor Simulation Symposium, AECL-Chalk River National Laboratories Report*.

Sauvé, R. G., Badie, N., & R. A. Holt. (1989). Simulation of Fuel Channel Creep Response in CANDU Nuclear Reactors. *Proc. 10th Int. Conf. on Structural Materials in Reactor Technology (SMiRT 10), Vol. L (Inelastic Behaviour and Constitutive Laws of Materials)*,

219–224.

Schuëller, G. I., & Pradlwarter, H. J. (2006). Computational stochastic structural analysis (COSSAN)-a software tool. *Structural Safety*, *28*, 68–82.

Sobol, I. (1994). *A primer for the Monte Carlo method*. CRC Press.

Soize, C., & Ghanem, R. (2005). Physical Systems with Random Uncertainties: Chaos Representations with Arbitrary Probability Measure. *SIAM Journal on Scientific Computing*, *26*(2), 395–410.

Stefanou, G. (2009a). The stochastic finite element method: past, present and future. *Computer Methods in Applied Mechanics and Engineering*, *198*(9–12), 1031–1051.

Stefanou, G. (2009b). The stochastic finite element method: Past, present and future. In *Computer Methods in Applied Mechanics and Engineering*.

Sudret, B. (2008). Global sensitivity analysis using polynomial chaos expansions. *Reliability Engineering and System Safety*, *93*(7), 964–979.

Sudret, B., & Der Kiureghian, A. (2002a). Comparison of finite element reliability methods. *Probabilistic Engineering Mechanics*, *17*(4), 337–348.

Sudret, B., & Der Kiureghian, A. (2002b). Comparison of finite element reliability methods. *Probabilistic Engineering Mechanics*, *17*(4), 337–348.

Thacker, B. H., Riha, D. S., Fitch, S. H. K., Huyse, L. J., & Pleming, J. B. (2006). Probabilistic engineering analysis using the NESSUS software. *Structural Safety*, *28*, 83–107.

Tomé, C. N., Christodoulou, N., Holt, R. A., Woo, C. H., Lebensohn, R. A., & Turner, P. A.

(1994). Deconvolution of Experimental Data of Aggregates Using Self-Consistent Models. In S. I. Andersen, J. B. Bilde-Sørensen, T. Lorentzen, O. B. Pedersen, & N. J. Sørensen (Eds.), *Proceedinsg of the 15th Risø International Symposium on Materials Science: Numerical Predictions of Deformation Procecesses and the Behaviour of Real Materials* (pp. 169–204).

Tomé, C. N., So, C. B., & Woo, C. H. (1993). Self-consistent Calculation of Steady-State Creep and Growth in Textured Zirconium. *Philosophical Magazine A*, *67*, 917–930.

Walters, L., Bickel, G. A., & Griffiths, M. (2015). The Effects of Microstructure and Operating Conditions on Irradiation Creep of Zr-2.5Nb Pressure Tubing. *Proceedings of the 17th International Symposium on Zirconium in the Nuclear Industry, American Society for Testing and Materials*, 693–725.

Woo, C. H. (1985). Polycrystalline Effects on Irradiation Creep and Growth in Textured Zirconium. *Journal of Nuclear Materials*, *131*, 105–117.

Woo, C. H. (1987). Effects of Intergranular Interaction on the Anisotropy of Irradiation Creep and Growth in Zirconium. *Proceedings of the British Nuclear Society*, 65–71.

Xiu, D., & Em Karniadakis, G. (2002). Modeling uncertainty in steady state diffusion problems via generalized polynomial chaos. *Computer Methods in Applied Mechanics and Engineering*, *191*(43), 4927–4948.

Xiu, D., & Karniadakis, G. E. (2002). The Wiener--Askey Polynomial Chaos for Stochastic Differential Equations. *SIAM Journal on Scientific Computing*, *24*(2), 619–644.

Xiu, D., & Karniadakis, G. E. (2003). Modeling uncertainty in flow simulations via generalized polynomial chaos. *Journal of Computational Physics*, *187*(1), 137–167.

Xu, H., & Rahman, S. (2004). A generalized dimension-reduction method for multidimensional integration in stochastic mechanics. *International Journal for Numerical Methods in Engineering*, *61*, 1992–2019.

Zhang, X., & Pandey, M. D. (2013a). Structural reliability analysis based on the concepts of entropy, fractional moment and dimensional reduction method. *Structural Safety*, *43*, 28–40.

Zhang, X., & Pandey, M. D. (2013b). Structural reliability analysis based on the concepts of entropy, fractional moment and dimensional reduction method. *Structural Safety*, *43*, 28–40.

Zhang, X., & Pandey MD. (2014). An effective approximation for variance-based global sensitivity analysis. *Reliability Engineering & System Safety*, *121*, 164–174.

Zhao, Y.-G., & Ono, T. (1999). A general procedure for first/second-order reliability method (FORM/SORM). *Structural Safety*, *21*(2), 95–112.

Zwillinger, D. (2011). *CRC standard mathematical tables and formulae*. CRC Press, Taylor & Francis Group.

Appendix A

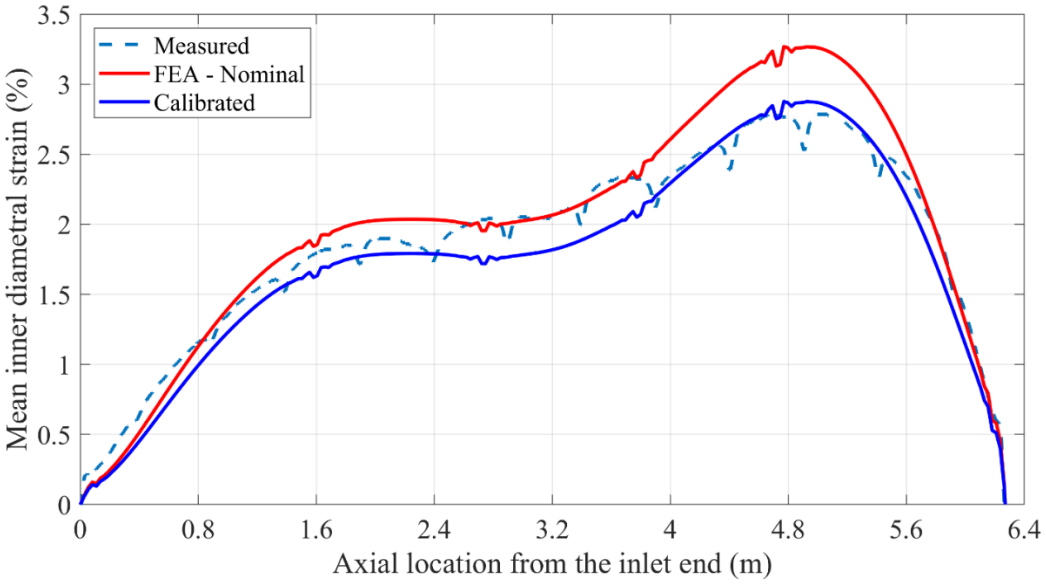

Figure A.1: Comparison of measured, nominal, and calibrated diametral strain of PT2 at 161615 EFPH

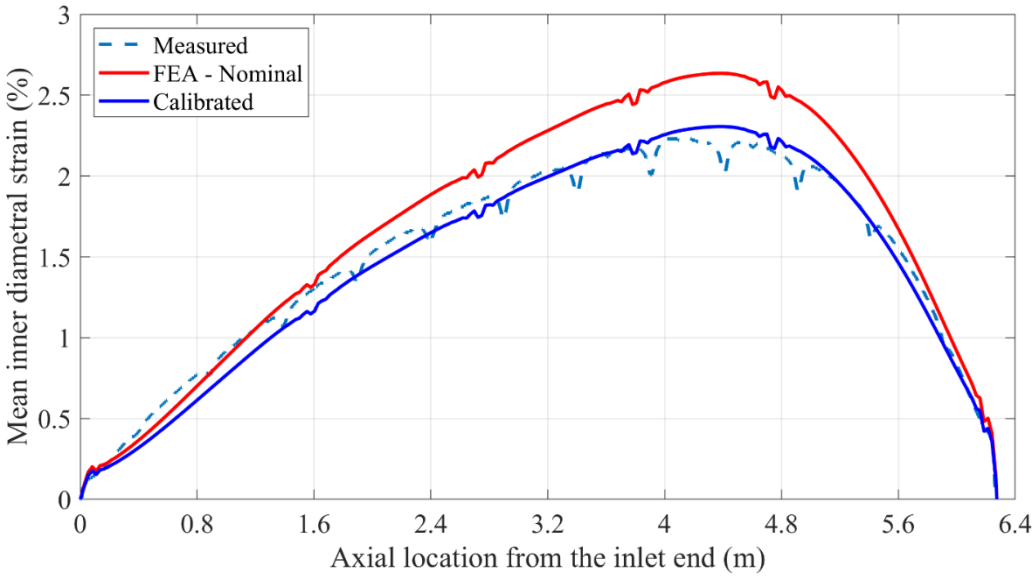

Figure A.2: Comparison of measured, nominal, and calibrated diametral strain of PT3 at 161615 EFPH

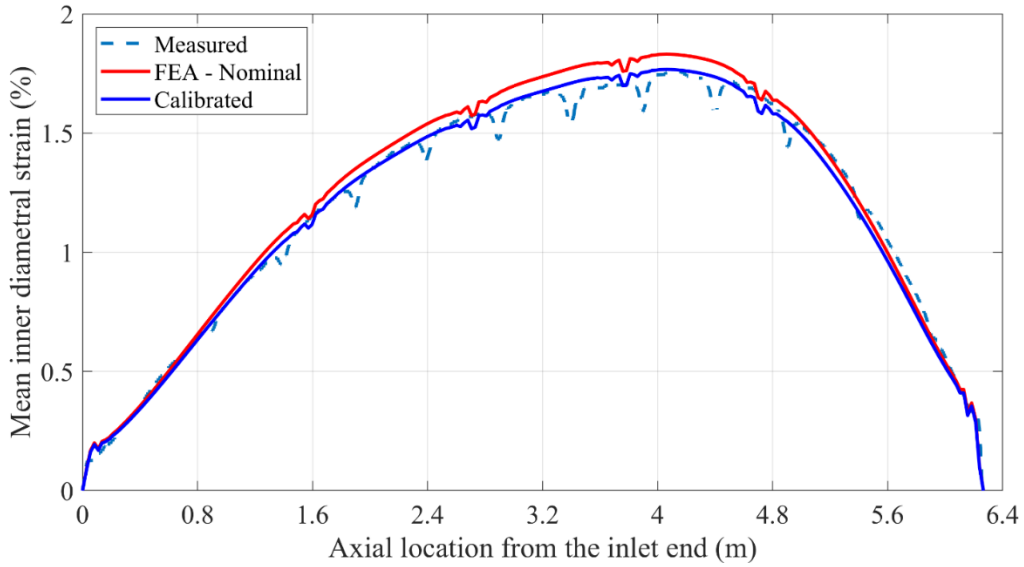

Figure A.3: Comparison of measured, nominal, and calibrated diametral strain of PT4 at 161615 EFPH